University of Nottingham
UK | CHINA | MALAYSIA

High-Powered Electric Motorcycle Integrated Performance Studies

Louis Flanagan, MEng

Thesis submitted to the University of Nottingham for the degree of

Doctor of Philosophy

31/05/2022

Abstract

Electric vehicles and low carbon technology are currently at the forefront of research due to the need to rapidly reduce global carbon emissions. Significant effort has been invested into the improvement of electric cars but comparatively little for electric motorcycles, especially high-performance electric motorcycles.

To achieve high-performance it is important to capture relevant design trade-offs and plan for vehicle optimisation prior to starting detailed design. These design trade-offs typically involve optimal sizing of the vehicle battery, electric motor, and motor drive, as well as the determination of the optimum lift-to-drag ratio. A full vehicle analysis including pertinent mechanical and electrical elements is required to perform this properly, as the system is highly interdependent. Existing models are shown to be lacking in key areas, notably the integration of an appropriate battery model, a realistic electric motor model (reflecting modern high-performance electric motorcycle design practices), and an appropriate tyre model, amongst other issues.

The work in this thesis builds and validates a full vehicle model of a modern high-performance electric motorcycle. This is accomplished by first developing a rigid body dynamics motorcycle model that includes a full tyre model, the effects of downforce, differing front and rear tyres, and front-wheel drive. Further work is then undertaken to increase the depth and suitability of the electric powertrain modelling for high-performance electric motorcycles. Here, the battery thermal and electrical responses are modelled as well as the powertrain torque response, including saturation and loss modelling of the motor, motor drive and final drive. To validate these models both motor dynamometer testing and battery cycle testing is performed. An accelerated battery testing procedure is also developed to reduce the time required to properly evaluate and characterise test cells for performance evaluation.

Having developed the vehicle model, a lap simulation procedure is then developed, implemented, and validated. Validation uses lap data acquired at multiple events including the Isle of Man TT Zero, Pikes Peak International Hillclimb (PPHIC) and Elvington Airfield Land speed record attempts. The lap simulation is then extended to include the effects of energy deployment strategy on lap time. This includes a different methodology for designs that are limited by the battery thermal performance

and those that are not. This deployment strategy implementation is shown to significantly affect lap time.

The work continues with lap time simulations of the Isle of Man TT Zero and PPHIC, investigating the respective influence of energy management on battery sizing. This shows that it is important to include the energy management strategy into the design evaluation and that the energy management trade-offs are specific to each race event. Additionally, analysis shows that situations where battery temperature management strategies dominate energy management strategies should be avoided by the proper design of a battery cooling system. This is because the penalty associated with reducing battery temperature through power and velocity limitations is higher than that of including sufficient cooling.

The lap time sensitivity to mass, motor inertia, winglet lift-to-drag ratios and other design variables are explored with recommendations made for the Isle of Man TT Zero race and PPHIC. It is shown that by properly including representations of the underlying physics using a holistic modelling approach, and utilising a quantifiable objective, the relative contribution of individual elements can be quantified and directly compared. The significance of this from a full vehicle design standpoint is large as now vehicle development can be accurately targeted into areas that provide significant benefit. This can greatly improve the efficiency of the development process and the ultimate performance of the motorcycle.

Acknowledgements

My thanks are extended to my project supervisors Prof. Atanas Popov, Prof. Pat Wheeler and Dr Miquel Gimeno-Fabra who throughout the project have always been approachable and willing to provide assistance.

Gratitude must also be extended to the Engineering and Physical Sciences Research Council, which provided the funding necessary for this project.

Additionally, the support of my fellow students; Jonathan Blissett, provider of many a tip and mad project suggestion and Felix Biertümpfel, provider of many a much-needed coffee break.

The final and significant thank you must go to the race team members who without their tireless dedication to not sleeping and getting things done just in time, there would have been no project to work on.

Table of Contents

List of Figures

Nomenclature

Variables:

R_{squat}	Squat ratio
σ_{squat}	Squat angle
τ	Load transfer angle
M_b	Mass matrix
P_b	Stiffness matrix
N_b	Damping matrix
q	Vector of generalised coordinates
J_u	Jacobian matrix of motorcycle equations with respect to the input vector
u	Control input vector
ψ	Motorcycle yaw angle
$\dot{\psi}$	Motorcycle yaw rate
$\ddot{\psi}$	Motorcycle yaw acceleration
ϕ	Motorcycle roll angle
$\dot{\phi}$	Motorcycle roll rate
$\ddot{\phi}$	Motorcycle roll acceleration
θ	Motorcycle pitch angle
$\dot{\theta}$	Motorcycle pitch rate
$\ddot{\theta}$	Motorcycle pitch acceleration
∂	Motorcycle steer angle
$\dot{\partial}$	Motorcycle steer rate
R_{1-yaw}	Yaw rotation matrix
R_{2-roll}	Roll rotation matrix
R_{3-rake}	Rake rotation matrix
$R_{4-steer}$	Steer rotation matrix
x	Longitudinal position
y	Lateral position

T_{xy}	Translation matrix for the motorcycle in global x, y coordinates
T_{rcg}	Translation matrix to the rear centre of gravity
H_{01}	Example homogenous transformation matrix from axes 0 to axes 1
ω_{rf}	Angular velocity vector for motorcycle rear frame
ω_{ff}	Angular velocity vector for motorcycle front frame
ϵ_{n}	Deflection of tyre contact patch centre normal to the road surface
ϵ_{n0}	Positive smoothing parameter for tyre contact patch deflection
$\tilde{\epsilon}_{\mathrm{n}}$	Smoothed tyre contact patch deflection normal to the road [m]
σ_{long}	Tyre relaxation length
$\sigma_{long,0}$, $\sigma_{long,1}$	Tyre relaxation length determination parameters
I	In-plane inertia of a body
m	Object mass
d_{filar}	The separation distance between filars for the bifilar pendulum technique
L_{filar}	Length of filars for bifilar pendulum technique
g	Gravitational constant
ω	Angular velocity
θ_p	Angle separating body principal axes and motorcycle reference axes
$I_{r,xx}$	Moment of inertia, rear frame, about motorcycle x-axis
$I_{r,zz}$	Moment of inertia, rear frame, about motorcycle z-axis
$I_{r,xz}$	Moment of inertia, rear frame, about motorcycle xz-axis cross couple
$I_{r,xxp}$	Moment of inertia, rear frame, about body principle x-axis
$I_{r,zzp}$	Moment of inertia, rear frame, about body principle z-axis
F_{x0}, F_{y0}	Maximum longitudinal and lateral tyre forces
F_x, F_y	Longitudinal and lateral tyre forces

D_x, D_y	Pacejka tyre model peak value coefficients
C_x, C_y, C_γ	Pacejka tyre model shape factor coefficients
B_x, B_y, B_γ	Pacejka tyre model stiffness factor coefficients
E_x, E_y, E_γ	Pacejka tyre model curvature factor coefficients
α_y	Tyre slip angle
κ	Longitudinal tyre slip
γ	Tyre camber angle
S_{vx}	Pacejka tyre model vertical shift coefficient
R_{rt}	Rear tyre effective radius
R_{tc}	Rear tyre crown radius
$R_{t\phi}$	Rear tyre effective radius due to camber angle
R_{t0}	Rear tyre undeformed zero camber radius
K_{rtyre}	Rear tyre vertical stiffness
F_z	Tyre vertical load
F_{z0}	Tyre reference vertical load
F_{rr}	Tyre rolling resistance force
q_{sy1}	Rolling resistance torque coefficient
q_{sy2}	Rolling resistance torque depending on F_x
q_{sy3}	Rolling resistance coefficient depending on speed
q_{sy4}	Rolling resistance coefficient depending on speed^4
V_x	The velocity of the tyre contact patch
V_0	Reference velocity
F_{fx}	Front tyre longitudinal force
F_{fy}	Front tyre lateral force
F_{fz}	Front tyre vertical force
F_{rx}	Rear tyre longitudinal force
F_{ry}	Rear tyre lateral force
F_{rz}	Rear tyre vertical force
F_{bx}	Body aerodynamic force in x-axis
F_{bz}	Body aerodynamic force in z-axis
M_{by}	Body aerodynamic pitching moment about y-axis

F_{wx}	Winglet aerodynamic force in x-axis
F_{wz}	Winglet aerodynamic force in z-axis
M_{wy}	Winglet aerodynamic pitching moment about y-axis
a_x	Acceleration in x-axis
a_y	Acceleration in y-axis
h_b	Height of body aerodynamic centre from the ground plane
h_w	Height of winglet aerodynamic centre
h_{cg}	Height of body mass centre from the ground plane
l_b	Distance of body aerodynamic centre in x-axis from front tyre centre
l_w	Distance of winglet aerodynamic centre in x-axis from front tyre centre
l_{wb}	Length of motorcycle wheelbase
l_{cg}	Distance from front tyre centre to body centre of gravity
α	Front to Rear longitudinal tyre force distribution coefficient
μ_{fx}, μ_{fy}	Front tyre friction coefficients in x and y axes
μ_{rx}, μ_{ry}	Rear tyre friction coefficients in x and y axes
μ_x, μ_y	General tyre friction coefficients in x and y axes
P_{max}	Maximum motor power
V	Generalised velocity term
$E1, E2, E3$	Coefficients used for simplification of rigid body tyre limit equations
m_{eff}	Effective mass due to inertia of accelerating rotating body
$m_{r,eff}$	The effective mass of the rear wheel and powertrain inertias
m_{mc}	Motorcycle mass
m_{eq}	Equivalent mass of motorcycle including effective mass contributions
r	Generalised radius term
r_{fw}	The radius of the front wheel
r_{rw}	The radius of the rear wheel
I_{pt}	Inertia of powertrain
I_{fw}	Inertia of front wheel

I_{rw}	Inertia of rear wheel
I_{mot}	Inertia of motor rotor
N_1	Motor sprocket tooth count
N_2	Rear-wheel sprocket teeth count
κ_r	Rear-wheel longitudinal slip
$T_{w,max}$	Maximum wheel torque
T_{mot}	Motor torque
x_{lg}	Data logger displacement from the centre of gravity in motorcycle x-axis
y_{lg}	Data logger displacement from the centre of gravity in motorcycle y-axis
z_{lg}	Data logger displacement from the centre of gravity in motorcycle z-axis
a_{lgx}	Data logger measured acceleration in motorcycle x-axis
a_{lgy}	Data logger measured acceleration in motorcycle y-axis
a_{lgz}	Data logger measured acceleration in motorcycle z-axis
V_q	Peak voltage in quadrature axis
V_d	Peak voltage in direct axis
V_s	Peak phase voltage
$V_{s,lim}$	Maximum achievable peak phase voltage
V_{batt}	DC Voltage available at motor drive capacitor terminals
λ_{mod}	DC voltage modulation index
i_q	Peak current in quadrature axis
i_d	Peak current in direct axis
i_s	Peak phase current
i_{smax}	Maximum peak phase current
p_e	Number of pole pairs in the motor rotor
ψ_e	Flux linkage
L	General inductance term
L_q	Inductance in quadrature axis
L_d	Inductance in direct axis
ω_e	Rotor electrical frequency

ω_{base}	Motor base speed
N_{turns}	Number of turns in motor coil
C_f	Skin friction coefficient
ρ	Air density
Re	Reynolds number
r_{rotor}	Rotor outer diameter
l_{rotor}	Rotor core length
$T_{l,wind}$	Torque loss to windage
$T_{l,seal}$	Torque loss due to lip seal
$T_{l,br}$	Torque loss in bearings
$T_{l,rr}$	Torque loss (frictional moment) due to bearing rolling resistance
$T_{l,sl}$	Torque loss (frictional moment) due to sliding friction
$T_{l,brseal}$	Torque loss (frictional moment) due to bearing seals
$T_{l,drag}$	Torque loss (frictional moment) due to bearing drag losses in an oil bath
$T_{l,ch}$	Torque loss due to chain tension on motor bearings
$T_{l,rot}$	Combined torque loss of rotor
k_1, k_2, k_3	Torque loss coefficients
μ_{frict}	Static friction coefficient
D_{IDb}	Bearing inner diameter
R_{msproc}	Radius of the motor sprocket pitch circle
f_{AC}	Motor fundamental frequency
$P_{l,rs}$	Power lost due to winding losses
f_{sw}	Motor drive switching frequency
$T_{stat,ref}$	Stator reference temperature
T_{stat}	Stator temperature
α_{rs}	Stator resistance variation coefficient
R_{s0}	Stator resistance at reference temperature
R_s	Stator resistance
$P_{l,hyst}$	Power loss to magnetic hysteresis in the stator core
K_{hyst}	Stator core hysteresis constant

B	Magnetic flux density
β	Steinmetz constant
$P_{\mathrm{l,eddy}}$	Power loss to eddy currents in the stator core
K_{eddy}	Stator core eddy current constant
$P_{l,sw}$	Power loss from motor drive switching module switching
$P_{l,CT}$	Power loss from motor drive switching module conduction
$P_{l,CD}$	Power loss from motor drive diode conduction switching
E_{on}	Switching module switch-on energy
I_{on}	Equivalent direct current in the switching module at turn on
E_{off}	Switching module switch-off energy
I_{off}	Equivalent direct current in the switching module at turn off
E_{Don}	Diode switch-on energy
I_D	Equivalent direct current in the diode at turn on
I_{ref}	Data sheet reference current
V_{ref}	Data sheet reference voltage
$N_{parallel}$	Number of switching modules in parallel
u_{CE0}	IGBT on-state zero-current collector-emitter voltage
ϕ_e	Separation angle between voltage and current vectors in 'dq' frame
Mod	Modulation index
$I_{C,rms}$	Capacitor ripple current
$I_{N,rms}$	RMS phase current in the stator
F_{ch}	Chain tension
$T_{ch,inp}$	Input sprocket torque
$r_{ch,inp}$	Input sprocket radius
F_{cf}	Force due to centripetal acceleration of roller chain links
m_{cl}	Mass of individual roller chain link
r_{sproc}	Pitch circle radius of sprocket
ω_{sproc}	Sprocket angular velocity
μ_p	Roller chain articulation friction coefficient
r_b	Roller chain average articulation diameter
$W_{articulate}$	Work done per roller chain link articulation

α_{pin}	Articulation angle of roller chain link
M_0	Instantaneous battery cell voltage hysteresis coefficient
M_1	Exponential battery cell voltage hysteresis coefficient
γ_{hyst}	Battery cell voltage hysteresis decay constant
h_0	Instantaneous battery voltage hysteresis state
h_1	Time dependant battery voltage hysteresis state
Q_{cell}	Battery cell capacity in ampere-hours
i_{cell}	Battery cell current
η_c	Battery cell coulombic efficiency
Q_{heat}	Battery cell heat energy
V_{cell}	Battery cell output voltage
$V_{oc,cell}$	Battery cell open-circuit voltage
T_{cell}	Battery cell temperature
$A_{SA,cell}$	Battery cell surface area
M_{cell}	Battery cell mass
C_p	Battery cell specific heat capacity
ε	Battery cell emissivity
h_{conv}	Convective heat transfer coefficient
T_{air}	Ambient air temperature
σ_{bm}	Stefan-Boltzman constant
k_{wire}	Thermal conductivity of load wires
$A_{CSA,wire}$	Cross-sectional area of load wires
l_{wire}	Length of load wire to exit of insulation
dV_0	Instantaneous change in battery cell voltage
dV_{tot}	Total battery cell recovery voltage change
$R_{0-RC0fixed}$	Fixed internal resistance value, single resistor battery model,
a_{1-9}	Fitted coefficients to capture temperature and state of charge dependency for cell parameters
R_{0-RC0}	Temperature and state of charge dependant resistance value, single resistor battery model
i_{R1}	Current in resistor-capacitor circuit 1

R_1	Resistance in resistor-capacitor circuit 1
C_1	Capacitance in resistor-capacitor circuit 1
τ_1	Time constant for resistor-capacitor circuit 1
i_{R2}	Current in resistor-capacitor circuit 2
R_2	Resistance in resistor-capacitor circuit 2
C_2	Capacitance in resistor-capacitor circuit 2
τ_2	Time constant for resistor-capacitor circuit 2
dl_{euc}	Euclidian distance between points
dx	Change in x coordinate
dy	Change in y coordinate
dz	Change in z coordinate
dl_{arc}	Arc length distance determination between points
$r_{arcpath}$	Radius of arc used to determine path length
θ_1, θ_2	Arc path segment angle
r_{2Dpath}	2-dimensional path radius
$\widehat{N}$	Generic unit normal vector to plane
U, V, W	Generic three-dimensional coordinate vectors used to describe arc in global coordinates x_0, y_0, z_0
$\widehat{UV}, \widehat{VW}$	Vectors between points U, V, W
u, v, w	Generic two-dimensional coordinate vectors used to describe arc in local plane x_{arc}, y_{arc}
o_{arc}	Orogin of arc in local plane x_{arc}, y_{arc}
$\overrightarrow{o_{arc}u}, \overrightarrow{o_{arc}v}$	Vectors between points u, v, o_{arc}
$\lvert o_{arc}u\rvert, \lvert o_{arc}v\rvert$	Vector magnitude of vectors between points u, v, o_{arc}
κ	Path curvature
F_{hill}	Force representing the longitudinal component of gravity due to road inclination
$F_{d,duct}$	Drag force in duct
Nu_{lam}	Nusselt number for laminar flow
Nu_{turb}	Nusselt number for turbulent flow
Pr	Prandtl number
Pe	Peclet number

W_{duct}	Width of cooling duct
H_{duct}	Height of cooling duct
D_{hyd}	Hydraulic diameter of duct
h_{cool}	Heat transfer coefficient of duct
ρ	Air density
v_{duct}	Fluid velocity in duct

Abbreviations:

ABS	Anti-lock Braking System
AC	Alternating Current
BST	Brake Steer Torque
CAN	Controller Area Network
CFD	Computation Fluid Dynamics
CVT	Continuously Variable Transmission
DC	Direct Current
EIS	Electrochemical Impedance Spectroscopy
ESR	Equivalent Series Resistance
EV	Electric Vehicle
FEA	Finite Element Analysis
FEM	Finite Element Method
FIM	Fédération Internationale de Motocyclisme
GPS	Global Positioning System
GVM	Global Vehicle Motor
HPPC	Hybrid Pulse Power Characterisation
HV	High Voltage
IC	Internal Combustion
IGBT	Insulated Gate Bipolar Transistor
IM	Induction Machine
IMU	Inertial Measurement Unit
IoM	Isle of Man
IPM	Interior Permanent Magnet
MF	Magic Formula
MFMC	Magic Formula Motor-Cycle

MTPV	Maximum Torque Per Volt
OCV	Open Circuit Voltage
PM	Permanent Magnet
PMAC	Permanent Magnet Alternating Current
PPHIC	Pikes Peak International Hillclimb
QSS	Quasi Steady State
RC	Resistor Capacitor
RMS	Root Mean Squared
SOC	State of Charge
SPM	Surface Permanent Magnet
TT	Tourist Trophy

1. Introduction

1.1. Motivation

Electric vehicles are at the forefront of current research efforts due to the need to reduce carbon emissions [1]. This is a result of a general increase in environmental awareness [2, 3], as well as the increased availability and performance of lightweight energy storage devices, such as the Lithium Polymer battery and high-power density power electronics. However, as with most nascent technologies, examples are generally existing machines converted to a different power source with the existing development methodologies retained. This is usually done without much thought for the sensitivities of the replacement technology as an integrated system.

This lack of vehicle level optimisation generally leads to a system that is sub-optimal. The lack of performance then feeds into a general perception that electric motorcycles are slow, boring, and a bit of a gimmick. This then compounds into lower sales and lower electric vehicle adoption rates than might otherwise be achieved as motorcycle sales carry a proportionally higher weight on performance metrics. This is evidenced by the majority of UK motorcycle owning households also having a car, suggesting that motorcycles are mostly used for enjoyment rather than commuting [4]. This sentiment is reflected in the market penetration of new electric cars (10.6% - UK 2020 registrations) when compared to that of electric motorcycles (2.2% UK 2020 registrations) [5, 6].

Improvements in the performance of electric motorcycles are likely to assist in increasing market penetration as it is perfectly possible for an electric motorcycle to meet or exceed the performance of its internal combustion counterpart. Wider electric vehicle adoption can be driven by improved electric vehicle performance and is key to reduced carbon emissions; ideally when properly coupled to renewable energy generation. However, the benefits of electrification have been shown even for fossil fuel-intensive electricity grids such as Poland [7].

A benefit of focusing on high-performance machines is that pushing the boundaries of performance is where true development and innovation lies. Any improvements found here can trickle down to lower performance machines improving vehicle performance across the board. This is a proven development path evidenced by the rapid

development of technologies such as traction control, active suspension, and hybrid powertrains achieving over 50% thermal efficiency in Formula 1 [8]. Although not usually a direct transfer, the underlying learning has often found its way into improving the mass market.

The pinnacle of performance is racing. A vehicle is optimised for ultimate performance at great expense and then directly compared to the competition. This is a breeding ground of innovation as every competitor is constantly attempting to gain an edge over his or her rivals. Therefore, if attempting to improve high-performance electric motorcycles, the obvious starting point is through competitive racing events.

There are very few events that allow electric motorcycles to race, but an electric vehicle race team set up at the University of Nottingham, the University of Nottingham Electric Superbike race team, managed to race at several. The timeline of these events is handled in more detail in Appendix A, but the most prominent of these is the Isle of Man TT (IoM TT) [9], a 37.7-mile race around the Isle of Man. Other events included the Pikes Peak International Hillclimb (PPHIC) [10], which is a 12.4 mile hill climb race in Colorado USA, and a successful attempt at Fédération Internationale de Motocyclisme (FIM) land speed records for un-faired electric motorcycles [11].

As a package, this selection of events covers the entire spectrum of high-performance electric motorcycle design. Ranging from short low-speed high-acceleration events, PPHIC, to long high-speed high-power race events, IoM TT, and finally, to ultimate speed trials, namely land speed record attempts. Participation in these events allows for experience and data collection on all aspects of high-performance electric motorcycles.

The IoM TT race is held over a 37.7-mile-long section of road in the Isle of Man and competitors average lap speeds in excess of 130 mph. These roads are not specially prepared and are public roads when they are not used for racing. As an overview, to give context to this race, the course map is shown in Figure 1.1.

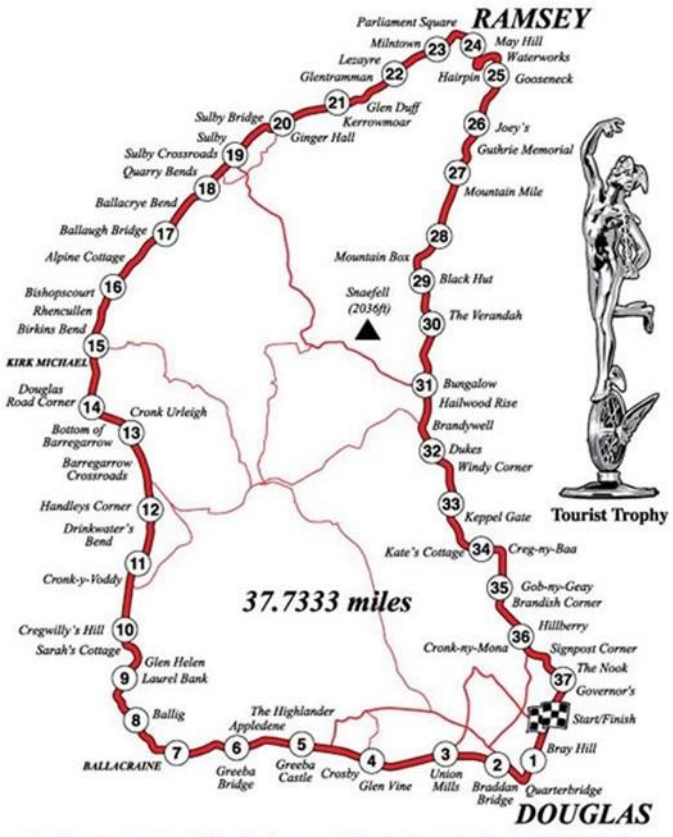

Figure 1.1 - Pictorial representation of the 37.7-mile-long Isle of Man TT course [12]

The effect of design compromises with regards to the electrical powertrain is magnified by the high-power high-speed requirements of the race. The race is also directly applicable to on-road performance since it is held on public roads. Therefore, it follows that a technology showing promise at the IoM TT is likely to be a useful technology for road machines.

The electric class at this race is called the Isle of Man TT Zero. Most existing work on high-performance electric motorcycles has focused on this race. This event is an electric-only event where electric motorcycles compete for the fastest single timed lap around the Isle of Man TT Mountain Course. This was one of the few events that allowed virtually unrestricted development of prototype electric vehicles and was organised by several forward-thinking individuals in the Isle of Man government who realised the truth in the age-old moniker ‘competition breeds innovation’. With the goal of driving rapid advancements in electric motorcycle technology the ‘TT Zero challenge’ was added to the events list in 2010 [13]. Since then, average lap speeds have increased from 96.8 mph in the first year to 121.9 mph in the last 2019 event [9].

An example used extensively throughout this thesis is the University of Nottingham TT Zero 2018 electric superbike. This machine came second at the Isle of Man TT Zero 2018, breaking the previous lap record in the process. Then, when stripped of its fairings and re-optimized for high speed, the motorcycle achieved the land speed record mentioned earlier. A different specification Nottingham machine also raced PPHIC in 2017, 2018 and 2019 taking class wins in the final two years and setting the fastest ever recorded motorcycle speed trap speed at the event.

However, these machines could have been significantly improved with further system-level optimisation as detailed in this thesis. This machine is used as a focus primarily due to the author's familiarity with the machine and availability of data, as a member of the team that designed, built, and raced it.

1.2. Aims and Objectives

Electric motorcycles are fundamentally different from ICE motorcycles. Current high-performance electric motorcycle design is, however, based on techniques developed for IC machines. To best understand and therefore successfully develop high-performance electric vehicles, the electric-specific compromises need to be more fully understood from an integrated design standpoint.

This thesis investigates the modelling of high-performance electric motorcycles with an aim of developing tools and techniques appropriate for modelling and improving the performance of high-performance electric motorcycles. That aim is achieved and the utility is demonstrated with reference to real-world examples.

The overall approach has been to investigate the current state of high-performance electric motorcycle system modelling, identifying any shortcomings, and developing appropriate techniques for achieving the stated goal. More specifically, analysis and modelling has been targeted against the following objectives:

1. Investigation into the performance of existing IC modelling techniques when applied to a contemporary high-performance electric motorcycle. This includes:
    - Determining if powertrain-specific compromises such as the inclusion of an abnormally large rear sprocket results in fundamentally different vehicle design requirements.

    - Determining if existing stability analysis techniques are appropriate for use on electric motorcycles.
2. Investigation into and implementation of appropriate vehicle performance modelling techniques for high-performance electric motorcycles. This includes:
    - Derivation of an appropriate vehicle model including tyres, downforce and mass distribution and integration into the full system model.
    - Determination of appropriate electric motor, motor drive, battery and transmission models and integration into the full system model.
3. Validation of models developed, using data collected using a contemporary high-performance electric motorcycle. This includes:
    - Validation of powertrain component models using experimental data.
    - Validation of the full vehicle simulation performance over target operating cycle using experimental data.
    - Comparison with previous electric motorcycle modelling attempts.
4. Investigation of potential performance development pathways using the validated model. This includes:
    - The significance of energy deployment strategies.
    - Event-specific design compromises such as:
        - Battery sizing
        - Powertrain design choices
        - Mass
        - Lift to drag ratio

1.3. Thesis Outline

Chapter 2 summarises the current literature surrounding motorcycle modelling, electric powertrain modelling, electric motorcycle modelling and highlights relevant electric motorcycle technologies that could provide additional performance.

Chapter 3 handles the benchmarking of the electric racing superbike at the University of Nottingham which is used as a research machine throughout this thesis. This

chapter also handles the evaluation of classic motorcycle models such as the Sharp 71 model [14], using appropriate values for the modern high-performance electric motorcycle. This is used to determine if existing modelling attempts are appropriate for use on high-performance electric motorcycles. This chapter also includes an investigation into the squat response of the electric motorcycle. The contribution within this chapter is the provision of a dataset appropriate for use on a modern high-performance electric motorcycle as well as the determination that existing stability analysis techniques are appropriate for use on modern high-performance electric motorcycles

Chapter 4 details the development of a quasi-steady-state (QSS) mechanical system model appropriate for use with a modern high-performance electric motorcycle. This includes a full Pacejka tyre model [15], downforce generation and two-wheel drive. Here, the potential for improved acceleration on corner exit as well as regenerative braking utilising two-wheel drive is demonstrated. Model performance is verified with reference to both data collected in Chapter 3 and data available in the literature. The contribution here is primarily with regards to the development of a rigid body motorcycle model capable of representing a motorcycle with different front and rear tyres, downforce generating winglets and two-wheel drive.

Chapter 5 details the development of an electrical system model capable of representing most contemporary electrical motorcycle drivetrains and the performance of individual subsystems. The model includes an electric motor, motor drive, battery, and transmission modelling. It is based loosely on the model developed by Blissett [16] but with some notable improvements to expand both the scope and accuracy of the model, with regards to electric motor operation, transmission and battery modelling. Issues associated with the linear battery model used by Blisset and by Dal Bianco *et al*. [16, 17] are highlighted and improved models are implemented. These are evaluated and validated using data collected during laboratory testing. Models are again verified with reference to research machine data as appropriate, and the utility of the model is demonstrated with reference to the land speed record achieved by the UoN motorcycle using this model [11].

Chapter 6 combines the mechanical and electrical system models developed earlier. This is combined into a lap simulation tool. A common lap simulation method [18] is

expanded to incorporate electric vehicle specific areas such as powertrain evolution and regenerative braking as well as rider deployment strategies. This combined model is then verified with reference to the data collected from the research machine. The model performance is also compared to existing motorcycle models, and the resulting differences are evaluated. The Isle of Man TT Mountain course is used here as direct comparisons can be drawn to prior modelling attempts. The contribution here is the development of a validated simulation tool that is more capable of, and more appropriate to, accurately representing the performance of a high-performance electric motorcycles, than previous modelling attempts.

Chapter 7 uses this lap simulation tool to develop appropriate energy and temperature management strategies that are used to perform a retrospective analysis of the 2018 Nottingham University machine, highlighting the need to consider energy management carefully during the design phase. The tool is then used to delve further into potential development pathways and design sensitivities. The battery temperature limitation approach taken by Blissett [16] is shown to be sub-optimal, and recommendations for lap position dependant energy deployment strategies to improve lap time are given. The contribution here is through the provision of an integrated methodology for determining lap time sensitivities incorporating energy management strategies. Additionally, the provision of suggestions for the design and appropriate sizing of different vehicle components for differing drive cycles highlights the utility of the tool developed within this thesis.

2. Literature Review

Motorcycles have been around for a long time and there is a large quantity of literature devoted to most aspects of mechanical motorcycle design, with several good summaries available [19-21]. However, due to increasing climate consciousness, there has been a recent surge in interest in electric vehicle technology. This has primarily been directed at cars and low powered vehicles. Electric motorcycles, particularly high-performance electric motorcycles, have largely been ignored.

Several manufacturers have begun to offer electric motorcycles, but the performance of these machines is often inferior to the internal combustion examples that they compete with. This immediately raises the question of why, and additionally, is this an unavoidable consequence of electrification?

The investigation into the performance of high-powered electric motorcycles is ideally suited to simulation as the design space can be thoroughly and effectively explored before having to invest in expensive components. To avoid the duplication of existing internal combustion (IC) literature, Section 2.1 begins with a look into current IC motorcycle modelling. Here, the state of play regarding multibody models, rigid body models and motorcycle lap time simulation is summarised. This includes vehicle models described by Sharp [14], Biral and Lot [22], as well as the lap time simulation methods described by Hauser and Saccon [18] and the optimal manoeuvre method by Cossalter *et al.* [23].

This is followed by electric powertrain modelling in Section 2.2. Here the elements that should be included in a modern full electric motorcycle system model are identified and highlighted.

The simulation of the high-performance electric motorcycle has had some previous attempts. Section 2.3 analyses the current state of play. Here, the focus is on the models published by Dal Bianco *et al.* [17], as well as the Blissett model [16, 24]. Both models focus on the challenge of the Isle of Man TT Zero as this was, until recently, the highest-profile electric motorcycle race in the world. The race also has a particularly interesting challenge with regards to powertrain sizing. Other comparatively high-performance electric motorcycle modelling attempts are briefly discussed but those relating to scooters, motocross and e-bikes are not considered as the low power and range requirements require a less detailed compromise.

Section 2.4 expands this review to include a summary of some recent electric motorcycle subsystem investigations. Here, several investigations into electrical subsystems that show promise for an electric motorcycle adoption are addressed. Section 2.5 then involves a summary of the literature.

2.1. Motorcycle Models

To properly understand any system and be able to usefully develop it, it is common to create a mathematical model that represents the underlying system. Originally, calculations would be performed by hand, and the models would therefore require extensive simplifications to make this feasible. However, as the power of modern computing has progressed, so has the ability to simulate ever more complex models. This complexity is used to represent the underlying system more accurately, improving the utility of the simulation exercise.

The motorcycle has been studied in great detail with several excellent books on the subject of motorcycle modelling, such as that by Cossalter [19], Lot [20] and Foale [21]. The reader is directed first to these for a more comprehensive overview of the field. The following section is targeted at highlighting specific areas of the field of motorcycle modelling that are relevant to this thesis as a whole.

2.1.1. Multibody modelling

A common method of investigating the response of a complex non-linear system is first to obtain the equations of motion for the system. The state space method can then be used to reduce the system of equations to first order, making them solvable by numerical means. A system of equations describing the motion of bicycles was derived by Whipple [25] in 1899. An updated version of this method was implemented for use on motorcycles by Sharp in 1971 [14]. This has been the basis of modern motorcycle stability and control research. The model implemented is a two-frame model with a revolute joint at the headstock of the motorcycle. It includes a simple tyre model and the gyroscopic effects of rotating wheels. A diagrammatic representation of this model, Figure 2.1, is taken from [26] to illustrate the main features, the wheels and mass locations, of the model.

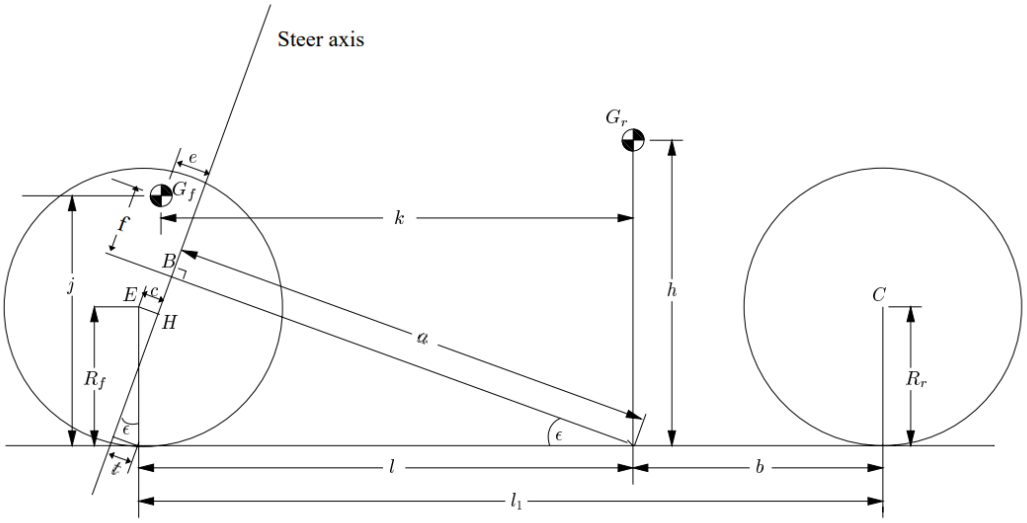

Figure 2.1 – Diagrammatic representation of the Sharp 71 model taken from [26]

The Sharp model has been well documented in its use for IC motorcycles, particularly for stability and control work [27-31]. The model is directly transferable to electric motorcycles. So far there has been no published investigation into the effects of a high-performance electric motorcycle's mass and dynamic setup on its stability when compared to a conventional IC machine. The Sharp model is the ideal tool for an initial investigation into the differences.

The Sharp model has however already been used to model the effect of the electric powertrain on a low-powered scooter by Hsien-Chung *et al*. [32]. The investigation attempted to determine the effect of the lower and rearward centre of gravity on a production electric scooter's controllability and comfort. Hsien-Chung *et al*. concluded that the CoG position influences these parameters and that a position that is high and rearwards is worse for stability, and unsurprisingly that careful placement of the scooter batteries should be considered.

There have been many improvements on the original model and many variations on the theme including models published by Meijaard and Popov [33]; inclusions of frame flexibilities and further updates including suspension deflections by Sharp [34-37]; and further flexibilities, rider modelling and tyre geometries by Cossalter and associates [38, 39]; and others not mentioned here. Each of these has their own improvements and benefits.

However, given the simplicity and widespread use of the original Sharp model, it is possible to determine if this route is worthwhile pursuing in depth with regards to high-performance electric motorcycles. There is already a comprehensive body of work dealing with most aspects of IC motorcycle stability, control and geometry optimisation and further work would only be a worthwhile use of this thesis if the existing work is not applicable to modern high-performance electric motorcycles. A good summary of the field covering multi-body modelling with a particular focus on rider control is given by Popov *et al*. in [40].

2.1.2. Tyres

Tyre forces represent the primary external forces on the motorcycle system and therefore are fundamental to the accurate modelling of a motorcycle. Tyre models typically relate the tyre load, lateral and longitudinal slips, and camber angle to the tyre forces and moments. More advanced models can include further sensitivity to vehicle speed, tread wear, inflation pressure [41] and temperature [42, 43], amongst other parameters.

The options available when choosing a tyre model range from empirical and physical models of varying complexity to finite element models with millions of elements. The finite element model approach and similar computationally expensive models are typically only used when the ultimate accuracy of tyre modelling is of utmost importance.

For models that are less concerned with detailed tyre design and simply wish to represent the tyre's grip response, it is common to use the Pacejka tyre model as developed by TU Delft and Prof. Pacejka [44]. This is sometimes referred to as a semi-empirical model, as it incorporates some structures that have their origin in physical models and are used to extrapolate the data between successive fitted points. The Pacejka tyre model is based around the sin(arctan) formula and uses many fitted scaling factors to modify this base curve to fit test data.

The significant difference between motorcycle and car tyres is the lateral force generation through camber and the large camber angles experienced [15, 45]. The Pacejka tyre model was originally developed for car tyre models and required modification to incorporate the large camber angle behaviour typical of motorcycles. This was accomplished initially by De Vires and Pacejka [15] who published a

version of the Pacejka tyre for motorcycles. These equations were then modified and used as the basis of the Delft-Tyre MFMC (Magic Formula Motor-Cycle) tyre models. In subsequent years, car and motorcycle tyre models were combined into the MF-Tyre 6.2 model that encompasses both tyre constructions [46].

One drawback to the use of the Pacejka tyre model is the large number of parameters that are required to be fitted and the resultingly large quantity of data required. In addition, the separation from physical force generation mechanisms by their empirical nature can lead to increased difficulty understanding the process of force generation. These shortcomings are outlined and addressed with an enhanced string model by Meijaard and Popov in [47]. However, the Pacejka tyre model is still an extremely useful and valid tool, and its widespread use ensures that data in this format is readily available.

2.1.3. Performance Envelope

A vehicle performance model requires a method of determining the limits of vehicle performance. There are many ways to determine these full vehicle response limits. Examples range from a simple point mass with a given friction circle and defined trajectory [18] to a full multi-body model with multiple degrees of freedom, free trajectory, rider modelling and road previews [27]. As with tyre modelling, there are variations in accuracy and complexity with associated computational penalties.

Massaro and Limebeer provide a good summary of modern and historic minimum lap time simulation techniques in [48]. A useful rule of thumb contained within this paper is that a free trajectory full dynamic model approach solved as an optimal control problem will take two orders of magnitude more time than a fixed trajectory Quasi-Steady-State (QSS) approach. A QSS approach simplifies the solution of the equations of motion of the vehicle by assuming that the vehicle is in a momentary equilibrium. As a middle ground, a free trajectory QSS approach has also been developed in [49] but this is still an order of magnitude more computationally expensive than the fixed trajectory approach.

Direct simulation using a multibody model and rider would be highly computationally expensive for the IoM TT, a 37.7-mile course, and likely provide little benefit over a simpler technique, especially during the concept phases of design. A common technique originally used to evaluate racing cars is the use of a ‘GGV’ surface to

describe the limiting vehicle performance and then interpolating this performance envelope to determine the performance over a full lap. GGV stands for the three axes of the plot in question, lateral acceleration in ‘g’, longitudinal acceleration in ‘g’ and vehicle velocity, commonly m/s.

A GGV surface is a method of illustrating the maximal lateral and longitudinal steady-state acceleration combinations of a vehicle with respect to velocity. This was first introduced by Milliken and Milliken [50] and has been adapted for use with motorcycles by Biral and Lot [22]. The method outlined in [22] derives the limiting accelerations from a rigid body model that includes tyre friction coefficients but neglects suspension displacements, steering angles, body inertias and other finer details. This is simple and effective but has some limitations, particularly with regards to the lack of downforce inclusion and the assumption that the front and rear tyres have identical friction coefficients. Additionally, the possibility of a front-wheel-drive motorcycle is ignored in both models.

A two-dimensional illustration of this approach applied to both motorcycles and cars is taken from [49]. Here the diagram is referred to as a GG plot as the third (velocity) dimension is not illustrated.

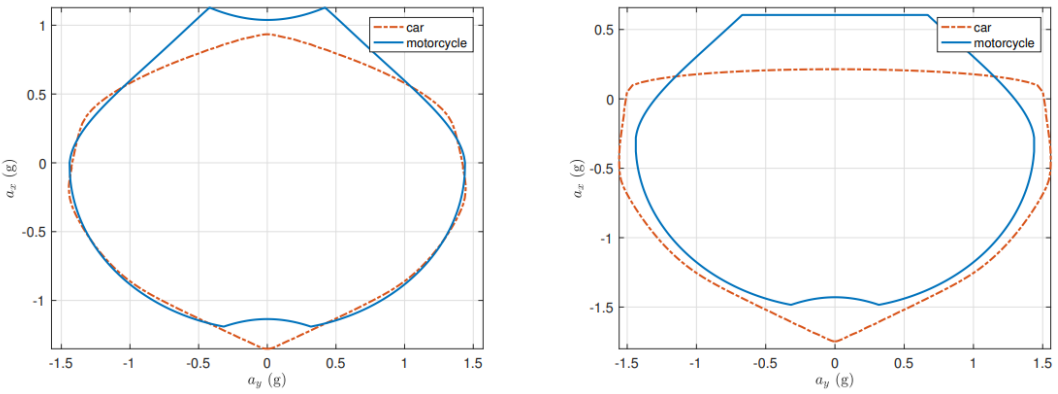

Figure 2.2 - GG diagrams for both cars and motorcycles at v=20 m/s (left) and v=80 m/s (right), taken from [49].

Although the quasi-steady state method is shown to give an acceptable approximation of the limit performance of a high-performance motorcycle [18] there are areas where caution should be exercised. This is particularly with regard to roll rate limitations, as well as the highly transient switch from acceleration to braking phases, where tyre load variation is assumed instantaneous by the quasi-steady-state method. In reality, it takes time to fully develop the front tyre load and resultant force.

2.1.4. Optimal Manoeuvre Method

A body of literature published by Cossalter, Lot, Biral and co-workers [17, 23, 51-53] makes use of the 'Optimal Manoeuvre Method' to calculate the optimal trajectory and rider inputs to generate the minimum lap time, given a set of boundary conditions such as tyre grip, CoG position and motor torque, encapsulated within a vehicle model. The optimal inputs are then determined with a penalty function used to ensure the vehicle remains within a given circuit boundary. The initial description of the method is given by Cossalter *et al*. [23].

The approach has been used with good success for a variety of events optimising CoG positioning [51] and even electric motorcycle battery sizing [17]. It has also been extended to include 3D road profile modelling [54]. This approach is extremely useful for the design of high-performance motorcycles, but the computational burden of this approach is large when applied to the full IoM TT Course with a detailed electric powertrain model, given the length of the lap. This fact is reinforced by Dal Bianco *et al*. [17] and again by Massaro and Limebeer [48].

2.2. The Electric Powertrain

Electric vehicles have been around for a considerable amount of time with Ferdinand Porsche himself having marketed his first electric car in 1898 and the in-wheel electric hub motor in 1900 [55]. As a result, there is a multitude of different models with a multitude of differing advantages and disadvantages, and it would be inefficient to attempt to investigate them all and summarise them here.

The overarching aim here is to identify useful learnings that have been generated through the development of dedicated powertrain, car, aircraft, and other vehicle type models and summarise the benefits and drawbacks of these approaches, if applied to a high-performance electric motorcycle. As such the pertinent learnings with regard to powertrain modelling and energy deployment strategies as part of the design process are included here as follows.

2.2.1. Electric Motor and Drive Modelling

The major components of an electric powertrain are an electric motor, which transforms electrical energy into mechanical energy; a motor drive, which regulates the flow of energy from the battery to the motor; and the battery itself, a DC source

that electrochemically stores energy. The accurate modelling of the states and losses within these components is key to modelling the powertrain.

Electric motors have been around for longer than IC powered vehicles, and there is a myriad of different designs. One of the major forks in motor design is between alternating current (AC) and direct current (DC) motors. Early vehicle motor designs used DC due to the lack of power electronics required to control variable speed AC motors, particularly when considering onboard storage is commonly a battery (DC source). Historically, the requisite power electronics were heavy, difficult to control and limited in their power capabilities. And as a result, early electric vehicles tended towards DC motors with some success [56].

To generate a changing magnetic field in a DC motor, commutators and brushes are used. The physical rotation of the rotor changes the direction of current flow through the armature. The drawback here is limited efficiency due to the losses within and maintenance required for the commutator. Additionally, there is reduced power density and overload capacity due to the difficulty in extracting heat from the rotating armature [57]. In comparison, the AC motor excels here as it does not require brushes and commutators, and motor windings are fixed. This leads to greater flexibility in cooling design. Relatively recent advancements in power electronics and AC motor design have notably improved their availability, performance, and cost [58]. As a result, most electric vehicles have now switched to using AC motors.

The most common AC machines used in vehicles are the Induction (IM) and Permanent Magnet (PM) machines. Contemporary machines have focused on Permanent Magnet Alternating Current (PMAC) designs for reasons of efficiency and torque density. Electrical machine types and their respective suitability for vehicle applications are discussed in more detail by Finken *et al.* [57]. Of these, variations include Interior Permanent Magnet (IPM) and Surface Permanent Magnet (SPM) rotor technologies. IPM rotors have permanent magnets embedded in an iron rotor core and are a combination of the IM and PM design.

An example of IPM construction is shown in Figure 2.3, this photograph is of the Parker GVM-210-150 [59] as used on the Nottingham electric motorcycle. As can also be seen surrounding the rotor is the stator which has been potted in a resin. This

is commonly done to help manage the temperature in the stator windings by providing a thermal mass and improving thermal conductivity to the coolant passageways [60].

In this case, the cooling system involves water passed through copper tubes surrounding the stator. It should also be noted that the coolant circuit to this motor had failed, resulting in severe overheating, hence the blackened appearance of the resin.

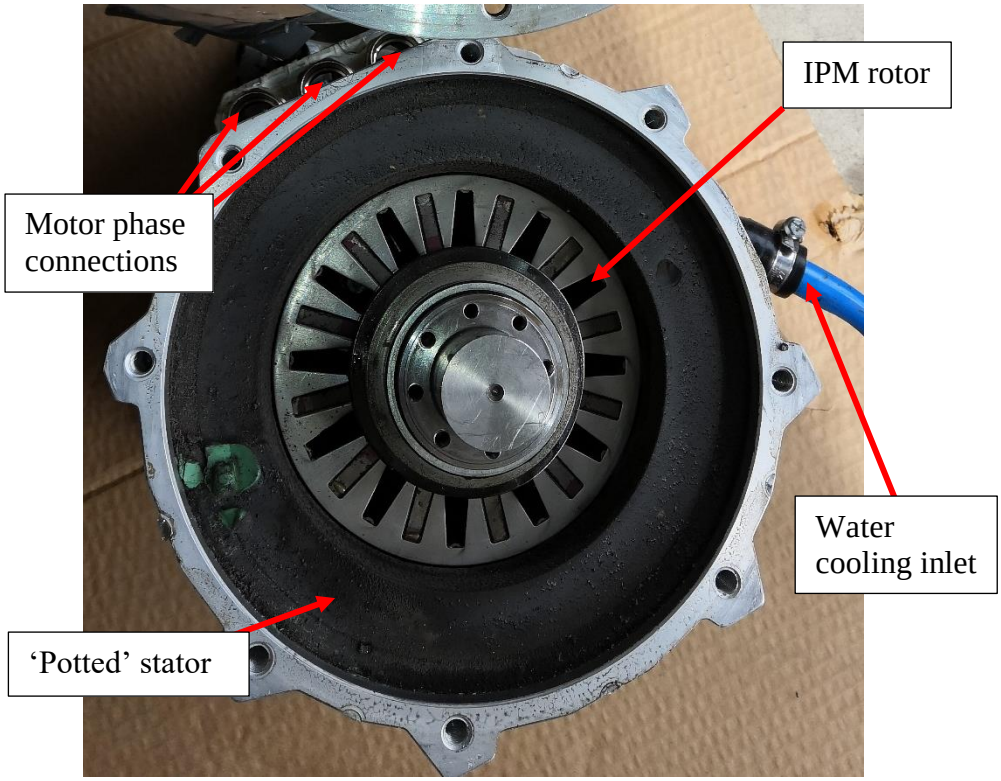

Figure 2.3- Example of the IPM motor construction technique. Image is of the Parker GVM-210-150 used on the University of Nottingham electric motorcycle

SPM rotors usually comprise a ring of surface-mounted permanent magnets on the outside of a rotor, retained by either an Inconel or carbon fibre sleeve. SPM motors generally have increased torque density and higher efficiency but also higher cost, mainly due to increased magnet volume. As an example, the design of a particularly high torque density motor using a dual rotor arrangement for electric motorcycles is outlined in [61].

To create an accurate representation of the torque output and motor current inputs to an inverter fed PMAC machine throughout the operating regions of the motor, the approaches used in [62-64] can be combined. Winding losses and core losses generally form the bulk of the motor losses [65] and can be approximated using the approaches in [66, 67].

The next item is the motor controller/motor drive/inverter - the terms are often incorrectly used interchangeably. An inverter simply converts DC to AC and is not necessarily used to drive a motor. A motor drive consists of capacitors and high current switches and is used to drive a motor. These capacitors smooth the input voltage, and the switches are controlled by a motor controller to regulate the output current to the motor phases by manipulating the voltage applied to each phase. This is done in accordance with the desired torque versus speed output. The major loss component here is the switching and conduction losses associated with the operation of these switches [68]. To give reference to the typical motor drive construction a CAD image of a typical motor drive is shown in Figure 2.4 [69].

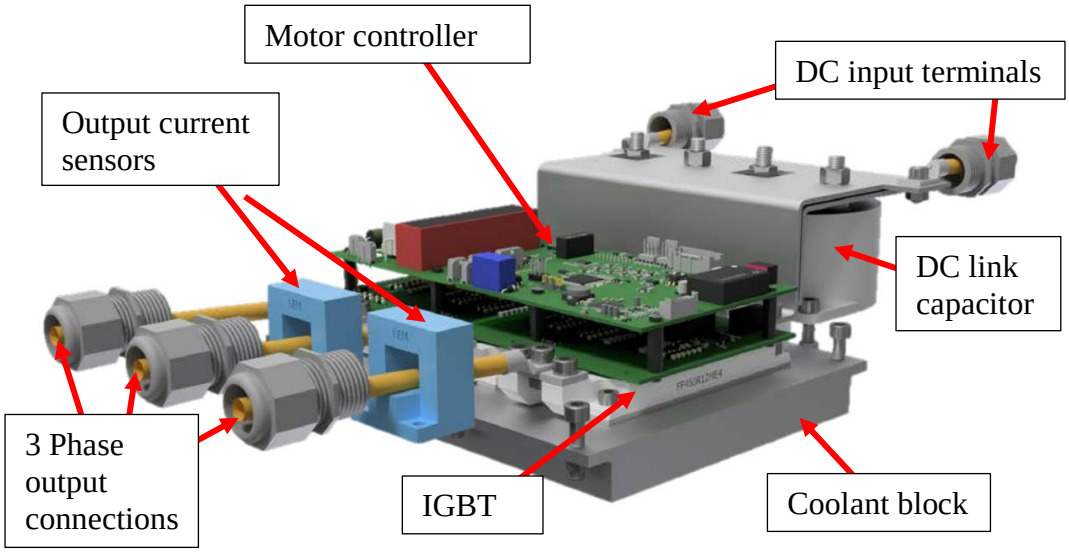

Figure 2.4 – Illustration of typical three-phase motor drive construction, taken from [69]

Traditionally insulated-gate bipolar transistors (IGBTs) have been used for high-powered motor drives but Silicon Carbide MOSFETs, metal–oxide–semiconductor field-effect transistors, are now becoming the norm for high-power, high-efficiency drives. This is due to the potential efficiency gain from the reduction in switching energies amongst other reasons. These losses are commonly approximated for IGBTs and MOSFETs, with reference to the motor operating condition, using the methods outlined by Graovac [68, 70].

2.2.2. Battery Modelling

The battery is arguably the element which contains the biggest compromise in terms of competing requirements in an electric vehicle. Battery design requires a balance of energy density, power density and total storage capacity against mass and cooling requirements, with associated mass and drag penalties. A different solution exists for

each drive cycle. The battery must provide all the energy to propel the vehicle and its associated losses as well as store any regenerated energy without overheating. In a high-performance machine, it must do so efficiently for the minimum mass possible.

Relatively recent advancements in the commercialisation of improved battery chemistries have significantly improved their energy density [71]. As can be seen in Figure 2.5, taken from [71], the more recent lithium-ion (Li-ion) based chemistries significantly outperform the traditional lead-acid and Nickel-Cadmium (Ni-Cd) chemistries. This is in terms of gravimetric and volumetric energy density; these are key factors to reducing the mass and volume of a high-performance electric motorcycle. As a result, the Lithium-ion chemistry is the focus of the remainder of this thesis.

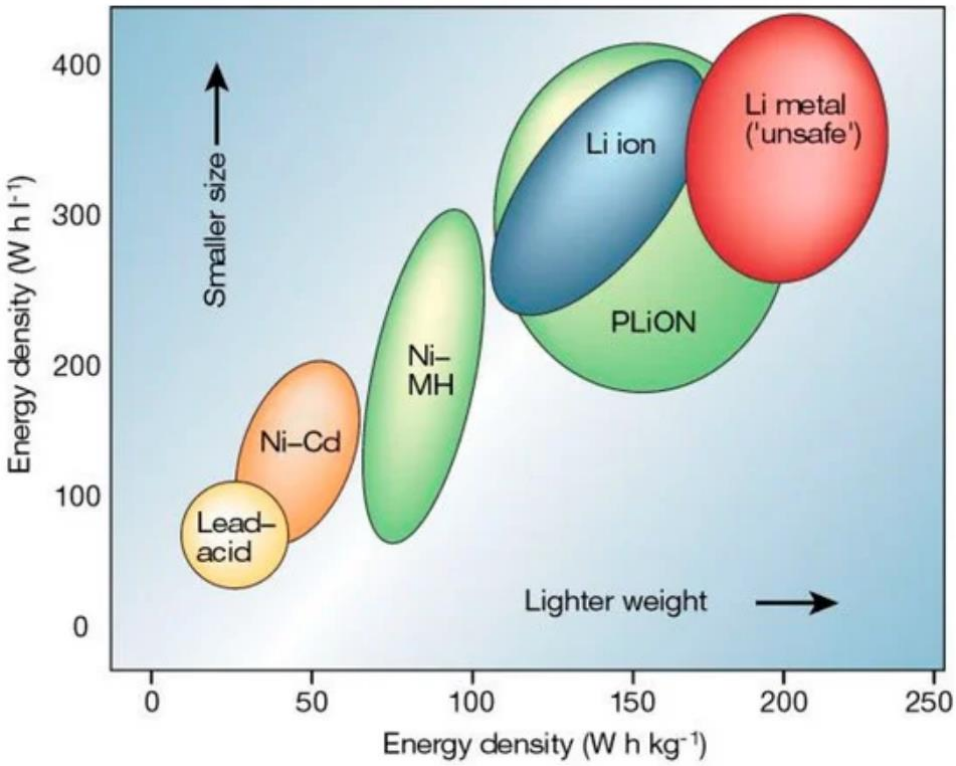

Figure 2.5 - Plot of volumetric and gravimetric energy densities of common battery chemistries from [71]

A battery utilises a reversible electrochemical reaction and as such its performance is governed by the chemical processes and diffusion rates within the cell as well as the external electrical demands placed on it. A battery's response is dependent on several factors including its construction, temperature, and state of charge [72].

When considering performance optimisation it is important to understand the limits of safe operation, and in the case of batteries, the limiting factor is the point at which the

electrode coating material begins to degrade [73] leading to internal short circuits and thermal runaway. This typically begins around 80 ˚C. It is worth noting different cell constructions have differing self-ignition temperatures [74].

The battery model that is commonly used, from a simplicity standpoint, is a model that considers the battery as an idealised voltage source with a series resistance, as used before by Blisset, Dal Bianco and Lot [16, 17, 24, 75] and others. This gives an instantaneous approximation of battery response. However, this series resistance value is in reality, affected by battery temperature and state of charge [76]. Additionally, the time-dependant response over multiple seconds caused by the underlying electrochemical reaction is omitted. The combination of these factors gives a poor approximation of the battery voltage which is important for determining the motor field weakening performance and the battery and inverter losses. This is in turn responsible for determining both the battery temperature state of charge and the motor output torque, critical parameters in a high-performance machine.

In addition to this, the assumption of fully reversible battery behaviour is also an oversimplification. Plett and Birkl *et al.* [76, 77] highlight an open circuit voltage hysteresis effect that is also overlooked by the singular directional approach and by other contemporary electric motorcycle models. Due to the use of regenerative braking, the battery current will be bidirectional, resulting in increased voltage prediction errors, if not accounted for.

In addition to the voltage hysteresis, a state of charge related battery temperature variation can also be found, due to the entropy variation within the cell. This is due to the altering chemical state of cell components during discharge. A common method to determine this relationship is the potentiometric method where a cell is placed in a climatic chamber and the temperature varied at multiple states of charge (SoC) [78]. This method takes days to complete each test. A faster calorimetric method is proposed by Damay *et al.* [78] that claims similar levels of accuracy.

The caloric method is simply an energy balance method. Thomas and Newman [79] derive an expression for the heat sources in a lithium-ion cell. The heat sources considered are ohmic (resistive) heating, entropic heating, and the heat of mixing. The heat of mixing is generally neglected as insignificant in a properly designed cell [79]. A simplified version of this equation, neglecting the heat of mixing, is also given by

Damay *et al.* [80]. The method outlined by Damay *et al.* [78] is the method explored and expanded upon in Chapter 5.

2.2.3. Energy Management

The energy management of an electric vehicle is extremely important given the mass penalty associated with additional storage. A constant trade-off between battery power, energy density, heating and mass is in play when designing an electric vehicle. However, as there is complete freedom over battery design, the goal is to determine: a) what battery management is required; and, b) what optimal deployment is achievable by a normal rider. Battery design decisions primarily relate to the energy density of the battery pack, the energy sensitivity to lap time and the mass sensitivity to lap time.

The optimal control approach as used by Biral, Lot, Cossalter and others [17, 23, 51, 52] for motorcycles, as well as similar approaches used by Herrmann [81] for high-performance electric cars, is useful here as it is possible to determine the optimal rider control inputs that result in the optimal energy deployment. However, the solution time, especially with increased model complexity, is of concern.

Rider integration is an important part of any control strategy, and it is important to remember that a rider will not be able to perfectly follow a prescribed trajectory or modulate the throttle exactly to achieve a perfect lap. The temptation is to use the vast array of electronics available to manage this deployment removing the rider's reaction time as a constraint. This is attractive until the realisation that a rider's confidence and ultimately lap time correlates to his ability to have ultimate authority over the predictable behaviour of his machine. This is no more keenly felt than when road racing due to the increased risks involved. In response to this, a suitable energy deployment strategy is restricted to only allow intervention in a limited form (power clipping and velocity limitation), and only when the machine is well past the corner exit phase. This simplified requirement reduces the benefit of the full optimal control approach and fits well with the simplified direct approach from Sheard [82]. An additional point to note is that most race series restrict the use of sophisticated control systems attempting to make the racing 'about the drivers' [83].

Sheard [82] uses a simple direct method to determine lap time sensitivity to energy deployment. Here the straights are identified and incrementally the difference in

energy usage and lap time is computed for multiple points along the ‘straight’. By comparing the deployment sensitivity of each point around the lap, a global deployment threshold value can be set corresponding to the maximal energy available in the battery and used to determine the deployment map. This has benefits of simplicity, however, issues can arise with the automated definition of ‘straights’, and the vehicle model used by Sheard omitted any form of consideration of battery temperature, motor operating condition, lateral tyre force or braking. These omissions make the gains identified unachievable, as demonstrated in Chapter 7. A particular benefit of this approach is that the energy lap time sensitivity for a given powertrain and mechanical setup, required for the battery sizing determination, is already computed.

2.3. The Electric Motorcycle

There have been many attempts to build electric motorcycles throughout the years, some with great success. Until relatively recently most were forced to use DC motors and lead-acid batteries, as this was the only commercially available technology suitable for the purpose.

The advent of the lithium polymer cell led to a step-change in the energy density achievable from the battery pack (see Figure 2.5). This in turn led to a significant improvement in the viability of electric motorcycles as the whole vehicle could be made smaller and lighter as a result. These early machines still featured DC motors however with advancements in motor power density led by the Agni motor [84]. The combination of these factors resulted in a surge in interest in building electric motorcycles. In tandem with any new technology comes a sense of competition, and therefore an interest in racing.

The first mass participation electric motorcycle race, that the author is aware of, is the 2009 TTXGP, held on the Isle of Man TT Mountain Course. This was won by Rob Barber riding a converted Suzuki GSX-R750 [85]. The machine featured two Agni 95R motors and a 12 kWh lithium-polymer battery pack [86]. The race was won with an average lap speed of 87.4 mph. As can be seen below, Figure 2.6, its construction involved the retrofitting of an electric powertrain to an existing internal combustion machine. This is typical of the design of many of the early modern electric motorcycles.

Figure 2.6 - Agni TTXGP inaugural winner, image from [85]

This type of construction was copied by many contemporary machines. However, it was not long before the search for superior performance led to the adoption of PMAC motor technology. Notable examples of this include the partnership between Mission Motors and Mugen Honda on the Shinden San [87] which won the 2014 TT Zero race (the successor to the TTXGP at the Isle of Man TT) with a 117.366 mph lap [88]. A picture of this machine without fairings to illustrate the step-change in technology levels is shown in Figure 2.7.

Figure 2.7 illustrates the rapid pace of development from the initial converted IC machines to the fully integrated custom carbon fibre chassis design encompassing the 100 kW PMAC powertrain only five years later. This rate of development is a common side benefit of effective competition. This is one of the reasons why electric motorcycle racing is an important area of focus when developing high-performance machines. The current state of vehicle modelling for these high-performance machines is outlined in the following section.

Figure 2.7 - Picture of Mugen Shinden San without fairings, from [89]

2.3.1. High-Performance Electric Motorcycle Modelling

The only published examples of existing high-performance electric motorcycle models are race-focused. Of these, the Isle of Man TT Zero is the most common choice of circuit. This is because the IoM TT Zero is a particularly difficult race for high-performance electric motorcycles, due to its long-distance and high-speed nature. This means that the effect of design compromises with regards to the electrical powertrain is magnified.

Another advantage of focusing on the IoM TT, with it being a long road race, is that any improvements realised here will be directly transferable to the safety and performance of road-going machines. Range anxiety is a common issue that faces electric vehicle adoption. When attempting to match an internal combustion (IC) motorcycle in road driving range (150-200 miles), it quickly becomes apparent that similar levels of stored energy to those used on the TT Zero machines are required. This makes the learnings from TT specific motorcycle designs particularly applicable to wider use beyond racing.

The first motorcycles that raced at the IoM TT Zero were converted IC engine machines featuring a small lithium-Polymer battery pack combined with a DC motor, most commonly the ‘Agni’ Motor [90]. Examples of this type of construction and some early powertrain modelling can be found in papers published by the Brunel Racing team [17] and the MIT [91] entry for the 2011 TT Zero. Many of the other machines were constructed without the use of any real performance modelling. As a

result, there are a few published examples and of those, the most relevant are examined here.

The earliest published electric motorcycle performance model was constructed by Rodgers *et al.* This was used as the basis of a 2011 entry into the TT Zero [91]. The model is a highly simplified model that determined the input and output power from a single DC motor. It then determined a battery capacity requirement by using the track profile and assuming the motorcycle maintained a constant velocity throughout the lap. A second approximation was made by assuming the motorcycle maintained a constant power throughout the lap and determining a battery capacity for this cycle. The discrepancies between these two were resolved by simply assuming the real lap would lie between the two. The full lap power consumption estimate was within 5% of the measured value, and the modelling was reported to be a success. However, this is a poor model performance indicator as the rider's aim is to hit the power consumption target thereby maximising the effect of the onboard storage.

An improvement on this model is the model proposed by Dal Bianco *et al.* which is a retrospective look at the early Brunel University entry for the TT Zero [17]. Again, this model concerns a DC motor and a somewhat simplified approach by modelling a mono-wheel. This decision was sensibly taken as a simulation time-saving exercise. The approach is appropriate for the machine under consideration and allows the effect of gross design changes to be quantified objectively. However, modern machines are significantly more powerful, and when operated at the extremes of performance it is common for wheel lifting limitations to be a key performance limitation. In addition, the low fidelity battery model and lack of battery temperature monitoring is a further issue as this can be a major contributor to machine performance. As an example, the optimum lap speed predicted by the model is an 85.7 mph lap, however, the Nottingham student-built machine achieved a 109mph lap in the same year that the paper was released.

The initial DC motorcycles mentioned above have been quickly superseded by much higher-powered, highly efficient, PMAC (Permanent Magnet Alternating Current) motors [92], where dedicated chassis designs to accommodate the increased volume and weight of battery are required [93, 94]. These higher-powered, more efficient machines have led to the lap speeds increasing along with the required battery

capacity. The average lap speed increased from 96 mph to 121.8 mph average in the 9 years that the race was running [95]. A comparison of this increase and the corresponding increase in IC motorcycle speeds over the same period is neatly illustrated in Figure 2.8, taken from [96].

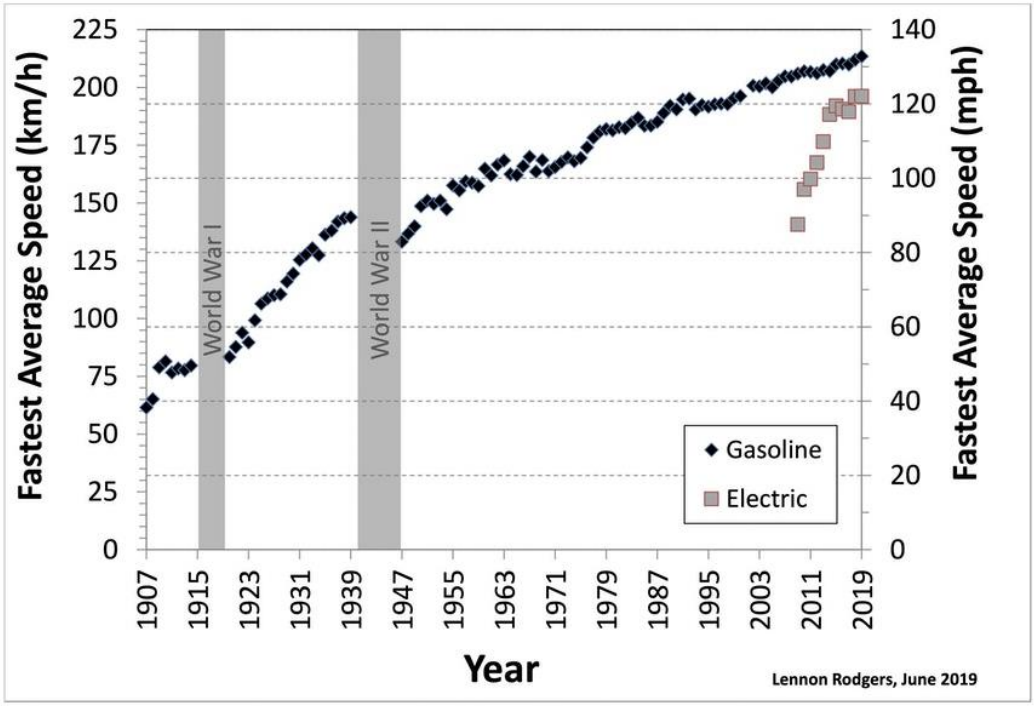

Figure 2.8 - Plot of fastest lap speeds at the Isle of Man TT by year, taken from [96].

There are two published examples of a powertrain optimisation exercise utilising a PMAC motor around the IOM TT course. The first example was developed by Bonnel-Kangas of Ohio State University for the 2014 IoM TT. Here an axial flux PMAC motor was used to record a 3rd place finish [97]. The second is by Blissett [16, 24].

The model by Bonnel-Kangas attempts to follow a prescribed velocity profile using a lookup table of motor performance. Motor drive losses are neglected and battery power limits are considered as a function of the state of charge, but it is not made clear exactly how. This led to an appreciation of the motor settings and battery capacity required to reach the target lap profile but is of limited use. This is because not only is the lap limited by the reference performance of an entirely different machine, but major losses are neglected, battery temperature is not considered, and neither is tyre performance.

In a paper published by Blissett [24], a modern PMAC motorcycle powertrain is modelled and the effect of motor design, efficiency, vehicle mass and pack capacity for the TT course is modelled and grid searched. This model considers the electrical system in more detail than any previous attempt directly modelling the motor torque generation as a function of the battery voltage, including motor drive conduction and switching losses, and approximating the battery temperature.

There are several issues with this approach. Firstly, the lack of a tyre model will contribute to a motor load profile that is shifted from reality. Secondly, the battery model is basic with a fixed internal resistance used in conjunction with a lookup table of open-circuit voltage and state of charge, resulting in the model response being unaffected by temperature variation and requiring 'fine tuning' at each event. This reduces its predictive ability and contributes to the need for performance limitation through battery temperature management strategies at the race event. Thirdly, the motor model used assumes surface permanent magnet (SPM) control strategy is appropriate even though the motor is of Interior Permanent Magnet (IPM) design. Lastly, the motor regeneration torque is simply an assumed fixed value unresponsive to rear tyre load variation.

The simulation strategy in Blissett [16] is based around using previously recorded corner speeds and effectively simulating a drag race between corners. The approach assumes that a small difference in corner speed will likely have little impact on the sizing of electrical components. This is true if the reference lap and actual lap are extremely close in profile and there are no significant lateral accelerations between the points defined as corners that serve to reduce the longitudinal tyre force available. This approach soon becomes invalid if motor power is changed significantly or the reference rider does not perform a perfect lap. Additionally, if the lap speed increases beyond that which is modelled, road curvature that was non-limiting at a lower speed can become limiting to performance at higher speeds.

A separate electric motorcycle battery investigation was used by Brodsky for Pikes Peak International Hill-climb (PPHIC) [98]. Here the process of optimising the battery pack for a specific event is discussed but the powertrain and vehicle performance are ignored. The design again focuses on using previously collected lap

data as opposed to simulating the updated performance and designing to that requirement.

An additional investigation by Möller into PPHIC [99] is focused primarily on sprocket sizing using previous lap data with little consideration for increased loss modelling, battery temperature, powertrain response or tyre modelling.

In summary, there is no available model that considers both the modern electric powertrain in sufficient detail and correctly determines the lap performance based on physical machine limitations, such as tyre performance. This is required to be able to effectively predict performance, particularly with regards to the expansion of the performance envelope and use at multiple events.

2.4. Relevant Performance Investigations into Electric Vehicles

As electric motorcycles are a relatively fertile area for new performance investigations, several potential subsystem developments have been investigated and their potential applicability is summarised here.

2.4.1. Regenerative Braking Traction Control

One obvious starting point is the use of the electric motor as a regenerative brake that converts kinetic energy into electrical energy for storage in the onboard battery pack. This is useful as any energy that can be recuperated in this manner is energy that does not need to be carried around the track in the form of extra cells.

Several authors [100-102] have attempted to model the use of the electric motor as a regenerative brake. The modelling in question was used to show how active control can be used to mitigate an issue that arises with the overuse of rear regeneration. The issue is that adverse conditions, i.e. high weight transfer to the front wheel, can cause the rear wheel to lock under braking. Without adaptive control, there comes a compromise between the desire to maximise regeneration and the desire to have the rear wheel not lock.

This is useful, and the core requirement of optimal braking distribution is also explored by Cossalter [19] and others. This highlights that any model used must consider the unloading of the rear tyre and resulting changing tyre performance to correctly capture the regeneration performance.

2.4.2. Two-Wheel Drive

When attempting to increase the amount of regenerative braking available it is evident that most braking energy is expended through the front brakes. To harvest this energy a motor linked to the front wheel is required.

Detailed modelling of the corner braking scenario was undertaken by Bauman *et al.* [100] and the potential stability improvements of having an electrically controllable front and rear brake were investigated. This model was partially validated through the construction of a demonstrator [101], however, the demonstration vehicle is low powered and not used for racing.

The algorithm employed by Bauman *et al.* [100] aimed to increase the corner braking stability of a motorcycle by minimising the brake steer torque (BST) gradient. It utilised an electric hub motor to modulate the ramp rate of torque applied to the front wheel whilst also maximising the rear wheel braking effect. The model also considers the motorcycle tyre friction ellipse to prevent the locking of either wheel. This is the part of the model that is likely to be most useful in a racing scenario as an experienced racer should be able to pre-empt and deal with any BST spikes.

A pure Anti-lock Braking System (ABS) style approach to two-wheel-drive (2WD) electric motorcycles was also undertaken by Lin and Weng-Ching in [103]. Here a simple upright slip ratio control algorithm is implemented. This can be improved by the consideration of camber angle [104, 105].

Further investigations to see if front-wheel-drive can be used to improve the motorcycle's cornering or acceleration phases were undertaken by Griffin and Popov [31] who concluded that there may be a slight benefit in the efficiency of power delivery. They did not determine a performance benefit in terms of ultimate acceleration performance. Interestingly separate anecdotal evidence claims an increase in cornering stability with a 2WD motorcycle [106].

Work on the use of 2WD in electric motorcycles was also undertaken by Abumi and Murakami [104] where a slip ratio control algorithm that considers camber angle is developed and evaluated. This control method showed promise in dealing with variations in road grip levels and was further expanded to include the effect of rider position through the double inverted pendulum model [105]. An example of the second method on an electric scooter was proposed by Chen *et al.* [107].

One issue remains, however, how to transfer the drive to the front wheel? There are two relatively well known attempts that have involved hydraulic motors [106] or a system of telescoping shafts and bevel gears to transfer the drive to the sprung portion of the motorcycle [108]. These systems have the benefit of comparatively low un-sprung mass increase but lack efficiency. To date these systems have been designed to handle low torque, approximately 15% of the motorcycle's total traction force, this also somewhat limits the regenerative capability using existing systems.

Again, the takeaway here is that full utilisation of the tyre performance envelope is key to maximal performance and by the powering of the front wheel it is possible to increase the size of this performance envelope. Therefore, this functionality should be included in an electric motorcycle model to evaluate the design trade-offs associated with it.

2.4.3. Hub Motors

The simplest and most efficient method of implementation for the front-wheel-drive electric motor is the incorporation of the electric motor into the front wheel hub. The effect of increased un-sprung mass on the road holding performance of a vehicle is understandably widely reported to be negative [109-111]. To give context to this motor integration technique an image of a commercially available hub motor is shown in Figure 2.9.

Figure 2.9 - Electric hub motor integration into motorcycle wheel [112]

Some studies have attempted to quantify the effect of the un-sprung mass on vehicle handling performance. One paper [111] used the half motorcycle model to evaluate

the effect of a 10kg electric motor in varying configurations. The motor was mounted in three positions, in the vehicle body, rigidly mounted to the wheel and suspended independently within the wheel. The conclusion was that the best solution in terms of roadholding is having the electric motor mounted within the vehicle body, the worst is rigidly mounted to the wheel but the inclusion of a well-tuned suspension element between the motor and the wheel mitigated some of the issues. Further research into suspending the motor relative to the wheel is conducted by Luo and Tan [109] this time establishing that there is a benefit (relative to a rigidly mounted motor) to the motors performance as well as the vehicle road holding from suspending the motor.

The quantification of the benefits of this system is not possible without a full cycle efficiency investigation that includes variation in tyre performance, so this functionality will be advantageous in a full system model.

2.4.4. Electronically Actuated Suspension

Research into the use of active suspension has shown that it can have a beneficial effect over a simple passive spring-damper system. T.H. Pham *et al.* indicate that the RMS suspension displacement can be reduced by as much as 31% by the implementation of active suspension [113]. As the electronic vehicle has a large power source available the use of electronic active suspension becomes a more enticing possibility.

T.H. Pham *et al.* [113] investigate the use of active suspension to increase the driveline efficiency by reducing the kinetic energy expended through the suspension. They achieve this by calculating the increased power requirement as a function of the RMS suspension displacement. However, the system model determined that the power required to run the active system was larger than a) the energy saved in driveline efficiency and b) the energy regenerated by an active suspension system even when both were combined.

Amati *et al.* [114] also investigated the implementation of an active electromagnetic suspension as an energy recovery device. The electrical machine was specified to deliver the required performance with minimal mass. The result of this exercise was encouraging with an electronic active suspension that fitted within the confines of the original spring damper unit and had a mass that is only a 20% increase over standard.

Assuming that the approximate suspension energy usage reported in [114] is correct, 100% recovery would recoup 200-300 W. Expanding this to the entire TT Zero lap yields an ideal maximum of 85 Wh. This equates to approximately 460g of battery [115] saved at the cost of a 20% increase in the suspension element mass. This plus the additional complexity quickly negates its use from an energy recovery standpoint even with highly optimistic assumptions.

Semi-active suspension systems have also been shown to provide benefits to the road holding of road vehicles with a lower energy cost than that of the fully active systems. Balamurugan and Jancirani [116] suggest that an electro-rheological damper may suit the HV nature of the electric motorcycle and that both active and semi-active may have the potential for offsetting the problems associated with increased un-sprung mass inherent to hub motors.

In summary, the benefits to electronically actuated suspension are limited to the road holding with negligible benefits for the powertrain. Although, an interesting avenue for research, this has been well explored and it does not satisfy the aims of this thesis. For further reading on active suspension Balamurugan and Jancirani [116] have prepared an in-depth summary.

2.5. Summary

The literature review has covered a wide range of areas concerned with electric motorcycle performance. These have been broadly defined as motorcycle modelling, electric powertrain modelling and finally the combination of these elements the electric motorcycle.

The first of these, motorcycle modelling, particularly multi-body modelling of motorcycles, is a widely researched field that has been extensively studied for many years. There has been significant effort invested into developing ever more complex structural models and control techniques and as such, there is limited scope to establish novel and constructive avenues here for further research.

However, the development of enabling electric vehicle technologies such as the lithium polymer battery and modern power electronics have permitted the relatively recent development of high-performance electric motorcycles. The key to understanding and optimising the design trade-offs inherent in the development of electric vehicles is the full vehicle modelling and simulation of these vehicles.

The full vehicle level system modelling of a high-performance electric motorcycle is not fully explored by existing literature and given the growing interest in electric transportation and high-level competition, there is utility in investigating these more thoroughly. There are a few previous attempts that handle individual elements well. Notably from Blissett [16] who focuses on SPM motor development, and Dal Bianco *et al.* [17] who analyse the lap time response of an early competitor in the TT Zero race. Both have their merits, however, neither manages to fully capture the whole vehicle response of a modern high-performance electric motorcycle.

Therefore, the following two knowledge gaps with regards high-performance electric motorcycles have been identified:

The fully integrated vehicle performance modelling approach, with regard to high-performance electric motorcycles, has yet to be researched in detail. This is particularly with regards to a model featuring a detailed battery model, modern PMAC powertrain, vehicle body response, and tyre modelling.

No previous work has focused on the stability of high-speed high mass electric motorcycles however there is considerable work concerning internal combustion examples and little to add in this regard if the response of an electric motorcycle is similar to that of its internal combustion counterpart.

3. Electric Motorcycle Benchmarking and Stability Analysis

Several areas of high-performance electric motorcycle design have not been fully explored by the current literature. One of these areas identified is the stability analysis of the high-speed, high-mass electric motorcycle and its specific compromises in terms of high inertia and non-standard gear ratios. However, as there is considerable literature regarding the stability and control analysis of internal combustion machines, initial investigations are required to determine the utility of exploring this further.

The first step in this process is understanding and benchmarking a representative high-performance electric motorcycle. Through participation in electric motorcycle racing activities with the University of Nottingham (UoN) and the University of Bath the author gained access to contemporary electric motorcycle data and the ability to perform vehicle and component testing. As a result, much of the following work is focused on lessons learnt from these race events. To give background to the work and introduce the particular trade-offs faced by electric motorcycles, this chapter begins by describing the University of Nottingham Electric Racing motorcycle and other high-performance machines in Section 3.1.

Section 3.2 then takes a deeper look into the powertrain performance over a target lap with an investigation into the effect of gearing changes on full-cycle efficiency as well as the potential inclusion of a Continuously Variable Transmission (CVT). This demonstrates that it can be beneficial to retain a direct drive arrangement from an efficiency standpoint leading to the selection of a large reduction ratio in a single stage. This necessitates the use of non-standard sprocket ratios.

Section 3.3 then evaluates the compromise induced by the non-standard sprocket choice. An investigation into squat response reveals that conventional squat response can be restored by altering the swingarm pivot position and motor shaft position.

Section 3.4 compares the body modes of the UoN electric motorcycle with reference values from literature using Sharp's model [14]. The principal body inertias are measured using the bifilar pendulum technique and the response evaluated with reference to the published data from the original model.

Section 3.5 will present the main conclusions from the conducted research in the chapter.

3.1. Research Machine

The major components of an electric motorcycle are outlined in Figure 3.1. Starting with the rider the throttle takes the rider's torque demand signal and inputs that to the motor drive. The motor drive takes this demand signal and determines the correct inputs to the motor to achieve this demand. More detail on this process is included in Chapter 5. The energy used to drive the motor is contained in the battery and its deployment is regulated by the actions of the motor drive. The battery is a DC source and the motor used is a three-phase AC machine. Therefore, the motor drive must also convert this DC into a suitable AC waveform.

Having determined and applied the correct motor inputs, the motor transforms this electrical energy into mechanical torque and supplies this to the transmission. As the motor and rear wheel operate at different speeds the transmission must transform the motor torque-speed output into a form suitable for the rear wheel. Having achieved this, and transferred the torque to the rear wheel, the wheel and tyre transfer this torque to the road. This generates the longitudinal force required to accelerate the machine.

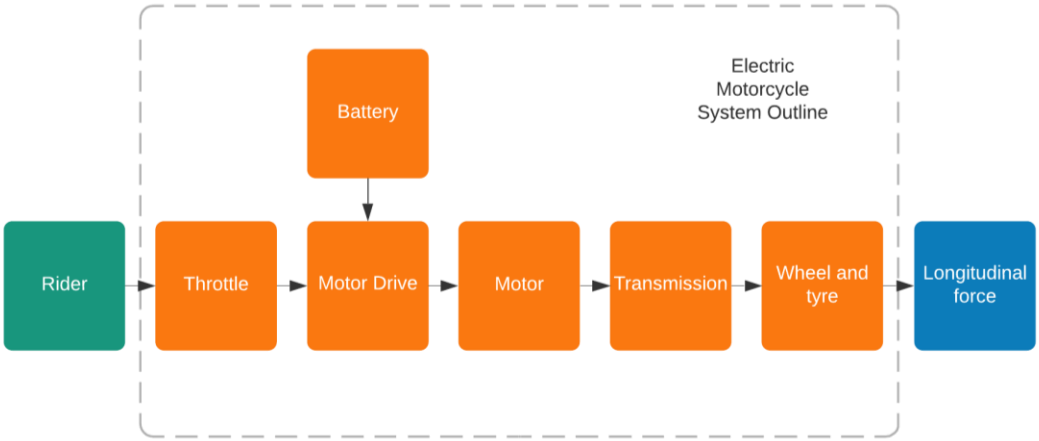

Figure 3.1- Electric motorcycle system outline showing major elements of the powertrain

A modern high-performance electric motorcycle typically consists of a three-phase electric motor and motor drive with a lithium polymer (Li-Po) battery pack [24]. This battery pack is a high-voltage DC source and is built from many individual cells. Each cell has a working voltage range of 4.2-3 Vdc and a capacity typically ranging from 3 to 30 Ah depending on the design. These cells can be stacked in series, which has the effect of summing the voltages, or parallel, which has the effect of summing the capacity of the individual cells. In the case of the University of Nottingham machine

in 2018 TT Zero specification 171 cells are stacked in series (171S) and 4 in parallel (4P) giving a nominal pack voltage of 633Vdc and 40 Ah capacity for a nominal stored energy of 25.3 kWh.

A scaled-down example of this pack building technique is shown in Figure 3.2. This module is only 6S2P but is one of many that are then assembled in series to form the full battery. The same concept applies to the motorcycle albeit with a different number in series and parallel. Other common pack constructions make use of cylindrical cells which have busbars spot-welded or ultrasonically bonded to their terminals to connect them in the required series/parallel arrangement [98].

The battery pack heats up as it is discharged due to its internal resistance. In most applications, the cells are cooled using a variety of methods ranging from direct air-cooling to immersion oil cooling. However, in the case of the Nottingham machine, the cell specification was set intending to eliminate the need for cell cooling, simplifying the design as well as reducing the packaging volume requirements. As an example of the extreme nature of the packaging constraints, images of the Nottingham machine without fairings can be found in Figure 3.3.

Figure 3.2 - Example battery pack construction.

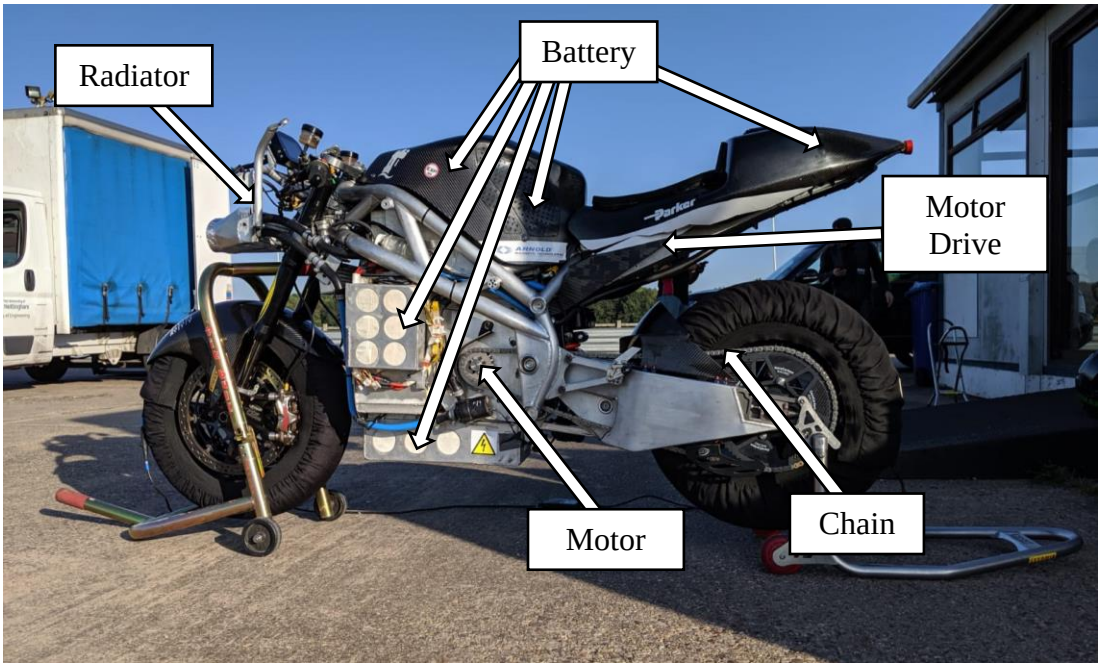

Figure 3.3 - Image of Nottingham electric motorcycle with fairings removed

The battery output (DC source) is transformed into a variable frequency and amplitude sine wave by the motor drive and used to drive the three-phase motor. This motor can be directly coupled to the rear wheel using a chain drive, as per the machines built by Nottingham University [24, 61] and Sarolea [94]. Others utilise a reduction gearbox between these two elements, a good example being the Mugen Honda [93].

Several differing vehicle setups and combinations of battery voltage, motor drive, motor and other changes were used throughout the years on the project as can be seen in Appendix A – Timeline of Electric Motorcycle Racing Activities. However, to keep this thesis focused, only the motorcycle setups used at the 2018 TT Zero, 2019 PPHIC and 2019 Elvington land speed record attempts are used here. These all share a common motor drive and motor architecture with the only change being the number of winding turns in the motor used for PPHIC. The effect of this change is to alter the torque-speed relationship of the motor for a given motor drive current and battery voltage, as detailed in Chapter 5. A table of values for the different models and configurations used throughout this thesis is given in Appendix B – Nottingham Electric Motorcycle Parameters.

The motor used on the Nottingham machine is a three-phase, brushless, PARKER GVM210-150 IPM motor capable of producing a peak torque of 257 Nm and

operating up to 10,500 rpm [117]. This was used to produce up to 170 kW at the rear wheel through a direct chain drive arrangement. The motor drive is a SEVCON Gen4 Size10 [118] which can operate up to 800 Vdc. It has a continuous power output of up to 150 kW and a peak output exceeding this.

The major differences in motorcycle construction between the events surround the battery capacity. This was varied according to the individual requirements of the event. For the TT Zero, the capacity used is 25.3 kWh. This brings the full motorcycle mass to close to 295 kg without the rider. The Land Speed record attempt utilised the battery from the TT Zero. In comparison when racing at Pikes Peak International Hillclimb (PPHIC) the reduced battery requirements reduce the vehicle mass to 220kg.

This variation was achieved by changing the cell type to a higher power density cell and reducing the number of cells in parallel. This maintains the same pack voltage but reduces the capacity. To compensate for the reduced capacity and corresponding increased power demand per cell a cell with higher power density is selected. A table of battery construction details (Table 3.1) is included below, Battery specifications have been taken from the manufacturer's data sheets [115, 119]:

Parameter	*TT Zero*	*PPHIC*
Cells in series	171	171
Cells in parallel	4	2
Cell Model Number	HGB8665155-10C	HGB8665155-20C
Cell capacity	10 Ah	8 Ah
Cell 'Nominal' voltage	3.7 Vdc	3.7 Vdc
Cell Mass	198g	178g
Pack 'Nominal' capacity	25.3 kWh	10.1 kWh
Total pack cell mass	135 kg	75 kg

Table 3.1 – Comparison of battery pack constructions used at the TT Zero 2018 and PPHIC 2019

3.1.1. Race Event Specific Setups

This thesis uses data collected during racing events at the Isle of Man TT Zero, Pikes Peak Hillclimb and land speed record attempts at Elvington Airfield. To familiarise

the reader with the specific challenges and compromises of each event the following section is dedicated to outlining the challenge imposed by each event.

3.1.1.1. Isle of Man TT Zero

This event is a time trial held once a year at the Isle of Man. It is held as part of the TT race week and consists of a single lap of the 37.7-mile-long TT Mountain course. The course average speed for a competitive electric entry is approximately 120 mph and takes approximately 18 to 19 minutes to complete. The race is held on closed public roads but there are large sections of relatively straight road where motorcycles can approach 200 mph. This long duration and high speeds require a large battery capacity to sustain the high-power demands required for a competitive entry.

The University of Nottingham's electric motorcycle performance steadily improved year on year. In 2016 the average speed achieved by Nottingham was 99.884 mph, achieving a 3rd place finish and the fastest ever lap by a university team. In 2017 the machine was reworked with a focus on reliability and achieved a 109.209 mph average lap, again achieving a 3rd placed finish. The final successful year at the TT Zero was the 2018 event where the machine broke the previous lap record with a 119.294 mph lap and achieved a 2nd place finish to Honda Mugen. This lap time could still be significantly improved upon as detailed in Section 7.2, but the race has since been cancelled for the foreseeable future.

3.1.1.2. Pikes Peak International Hillclimb

This race is a Hillclimb held once a year in Colorado Springs USA. The race is again a time trial event however the course is much shorter at 12.4 miles long, typically taking just over 10 minutes to complete. The course is at a high altitude and contains a significant elevation change, the start is at 2860 m and the finish is at 4302 m. The course itself is also much tighter than the TT course with many more hairpin corners that reduce the course average speed to only 70mph. This combination of low speed and short duration means that the energy demands are significantly reduced, and a significantly smaller battery can be used.

Again, the Nottingham team steadily improved year on year. The first year of attendance was 2017. This challenge was beset by multiple logistical and technical issues and resulted in a 785 s run for the team. The second year of attendance, 2018, was much more successful, winning the electric motorcycle division. However, the

lap time of 674 s could still be improved upon. In 2019 the team returned and achieved a 619 s run and achieved the fastest motorcycle ever through the speed trap. This lap time could still be significantly improved upon as detailed in Section 7.3, but the race has since stopped accepting motorcycle entries.

3.1.1.3. Land Speed Record Attempt

This event was held at Elvington Airfield in Yorkshire UK. Each attempt at a record consisted of two runs up and down a 3 km runway. For a flying kilometre attempt, the goal is to achieve the maximum speed measured over a flying kilometre. For a standing mile, the goal is the shortest time to complete a mile from a standing start.

For this event, the motorcycle was raced with the TT Zero battery pack, motor and drive. A smaller 'tank' fairing was used to reduce the frontal area of the machine and the machine was run in both naked and faired configurations.

Some of the records achieved in 2019 with Zef Eisenburg riding the UoN Motorcycle include: the FIM Naked Electric Motorcycle Flying Kilometre, with a speed of 185.103mph and a best one-way speed of 194.086mph; and the FIM Electric Motorcycle Standing Mile with an official speed of 135.277 mph [11]. These were achieved using gear ratio optimisation guided by an early version of the model developed in this thesis.

3.2. Initial Powertrain Analysis

The goal when designing any high-performance motorcycle powertrain is to provide the maximum power possible for the minimum mass and importantly for the full duration of the desired use. This second point is particularly important when considering electric powertrains as the battery mass is a significant contributor to the full powertrain mass. This is in sharp contrast to IC machines which are dominated by the mass of the motor, not the energy storage. When attempting to reduce the weight of the entire electric powertrain both reductions to the electric motor, motor drive and the energy storage requirements need to be considered.

Electric motors are limited in their torque density. To increase power with minimum mass, increasing the motor speed is an effective method. In the case of the UoN motorcycle, a moderately high-speed motor requires a total reduction ratio of approximately 5:1 from the electric motor to the rear wheel. This is typical of many high-performance electric motorcycles using a radial flux motor. In comparison, a

conventional IC motorcycle will have a primary reduction gearbox between the IC motor and the chain drive with a chain drive reduction ratio in the region of 2-2.5:1.

Common methods used to achieve the 5:1 ratio for electric machines are a 2:1 primary reduction gearbox followed by a standard chain drive reduction ratio [93], or a single-stage 5:1 chain reduction. With limited energy storage, it is evident that driveline efficiency is important. Blissett [24] compares the efficiency of both methods and the conclusion is that 5:1 direct reduction is the preferred method. This evaluation, however, is made without considering the full machine sensitivities. A gearbox would allow the use of a higher speed motor and therefore a potential mass reduction.

Other potential improvements could be realised by using a CVT. By adjusting the transmission ratio, it is possible to keep the motor operating at its most efficient point for a larger portion of the lap potentially improving total lap efficiency. The inclusion of a CVT would drop the peak efficiency but could allow areas of lower efficiency to be shifted into a more efficient motor region. Additionally, this would introduce a primary reduction allowing the use of conventional ratios for final drives.

To help give context to the references to electric motor efficiency maps an example provided by the motor manufacturer Parker for the GVM-210-150 electric motor in the constant torque region [59] is shown in Figure 3.4. This illustrates the sharp drop off in motor efficiency as it is operated near to its limits.

By taking the torque-speed trace recorded at the 2018 TT Zero race and interpolating the published motor efficiency plot it is possible to approximate the full cycle efficiency for the motor. A total cycle efficiency of 88.7% can be found.

Searching for the most efficient gear ratio from a motor efficiency standpoint determined that the optimum gear ratio of 18:79 would have had a full cycle efficiency of 88.8%, a very small increase, see Figure 3.5.

The effect of a frictionless CVT which could vary the gear ratio from 2:1 to 16:1 was then included. This achieves the required torque demand trace while delivering a cycle efficiency of 90.39%. However, as soon as one includes a representative maximum CVT efficiency of 94%, Figure 3.6, it becomes apparent that the losses in the CVT offset any gain that might be made elsewhere. To match the initial cycle

efficiency a 97.5% efficient CVT would be required. This is beyond even the peak efficiency (96%) seen in manual transmissions [120].

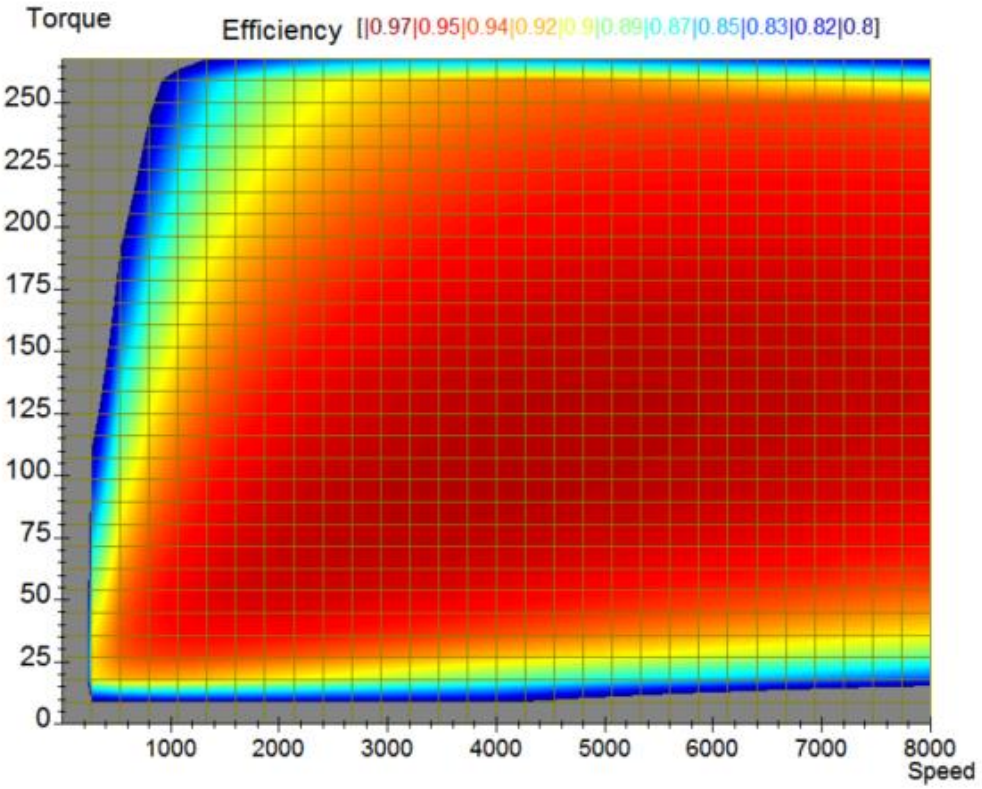

Figure 3.4 - Typical Parker GVM-210-150 efficiency plot for the constant torque region [59]

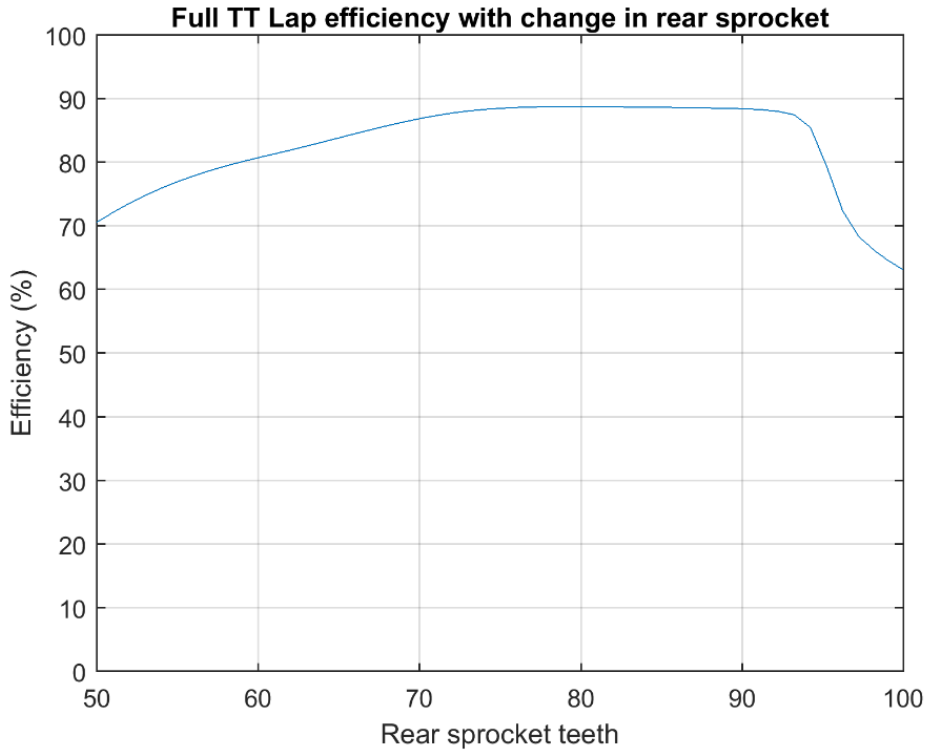

Figure 3.5 - Plot of the effect of rear sprocket size on the full lap cycle efficiency for the TT Zero race 2018

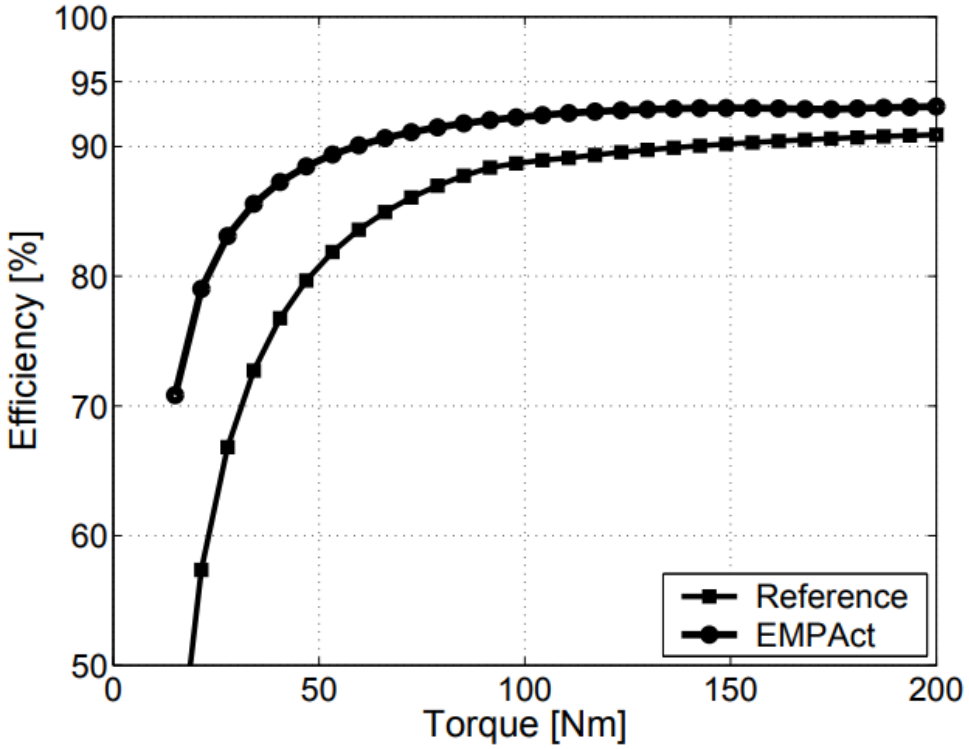

Figure 3.6 - Plot of CVT efficiency including standard 'Reference' CVT and advanced electronic actuated CVT 'EMPAct System' plot [121]

The most efficient transmission system is therefore the single reduction ratio. However, due to the size of the reduction, a corresponding large rear sprocket is required and the impact of this is investigated in the following section.

It should be pointed out here that the use of a motor efficiency lookup table is an over-simplification as not only will the motor output vary with battery voltage, the efficiency of the remainder of the powertrain such, as the motor drive and battery response, is unaccounted for and will also vary with the motor operation and lap distance. This will be addressed in detail in later chapters.

3.3. Squat Ratio

One of the most immediately apparent changes due to the adoption of a single reduction ratio is the presence of an extremely large rear sprocket to achieve the reduction ratio required. Changing the size of the rear sprocket changes the angle of the chain and as a result the reaction of the rear suspension to the application of load. The reaction of the rear suspension under load is important to the acceleration response of the full vehicle. It is important, therefore, to understand if there is an inherent issue with this large rear sprocket selection that cannot be addressed using existing techniques.

The reaction of the rear suspension of the motorcycle to driving force can be characterised as a 'squat ratio'. A summary of the calculations involved for an initial investigation is included here but for further detail please refer to Cossalter [19].

By calculating the sum of moments about the swingarm pivot, the squat ratio of a chain-driven motorcycle 'R_{squat}' can be defined as the ratio between the moment generated by the load transfer, and the moment generated by the sum of the chain force and the driving force. A method used by Cossalter [19] to calculate this squat ratio uses the squat angle and load transfer angle. These angles are illustrated in Figure 3.7.

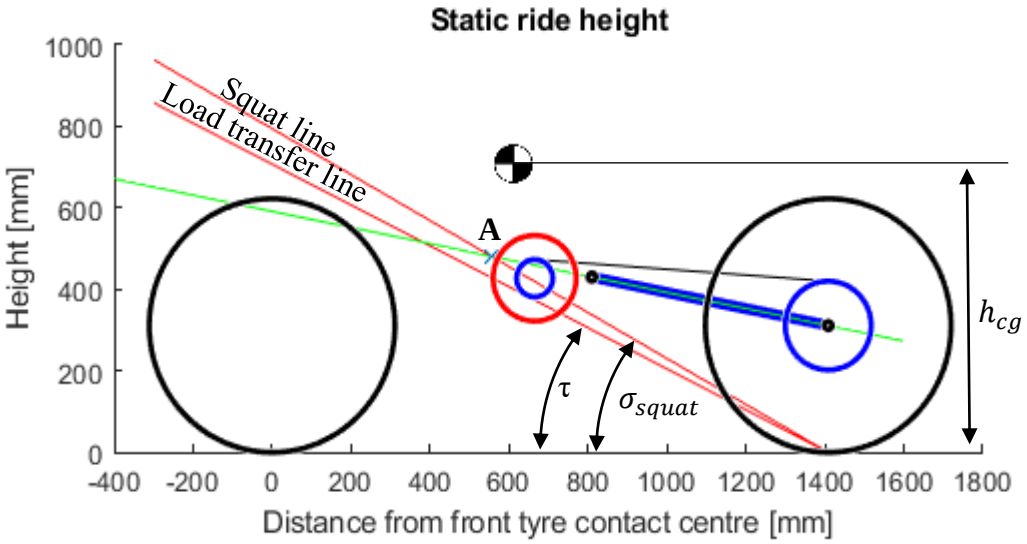

Figure 3.7 - Diagrammatic representation of reference vehicle squat ratio determination

The Squat line is defined as the line connecting the rear tyre centre patch to the point 'A'. Here, point 'A' is the intersection of the chain top line and a straight line passing through the centre of the rear wheel and the swingarm pivot. The squat angle is the angle between this line and the ground plane '$\sigma_{squat}{}'$.

The load transfer line is the line of action corresponding to the combination of the driving force and the load transfer force at an angle 'τ', the load transfer angle, to the horizontal plane as defined in [19]. Here 'h_{cg}' is the height of the centre of gravity and 'l_{wb}' is the length of the motorcycle wheelbase. The corresponding load transfer angle and squat ratio is given by the following equations [19]:

$$\tau = \arctan\left(\frac{h_{cg}}{l_{wb}}\right) \tag{3.1}$$

$$R_{squat} = \frac{tan(\tau)}{tan(\sigma_{squat})} \tag{3.2}$$

The squat ratio is important to the trim of the motorcycle. If $R_{squat} = 1$, there are no additional moments on the swingarm. If $R_{squat} > 1$, an additional moment that acts to compress the rear suspension is created under drive torque application. If $R_{squat} < 1$, a moment that acts to extend the rear suspension is created.

MATLAB was used to determine the rear squat ratio for the full rear suspension travel. The model defines the motorcycle Centre of Gravity (CoG) position, rake angle, wheelbase, swingarm pivot location, and sprocket centre location, as well as front and rear sprocket diameter and wheel sizes. The squat ratio is calculated from the position of point 'A'. This is achieved by calculating the position of a line tangent to the upper surface of the front and rear sprockets, then computing the intersection of this line with that of the line connecting the rear wheel centre to the swingarm pivot. The load transfer line is simply a function of the CoG height and wheelbase.

To include the effect of rear suspension travel, the rear wheel vertical movement is modelled as a rotation of the chassis and associated geometry around the front tyre contact patch. Allowances can be made for the movement of the front suspension/motorcycle trim at this point, but these are kept fixed here. The change in swingarm angle and wheelbase required to achieve the new position is then calculated, and the new squat ratio is found as described previously.

A target ratio was generated using the standard gear ratio and geometry for a 2008 Yamaha R1, the machine that the UoN motorcycle was based on. The squat ratio is then calculated for the updated electric motor setup, an error term generated and least-squares fitting used to manipulate the updated setup to achieve the target profile. Limits for the swingarm and motor positions as well as chain length variation limit are used to constrain the analysis. Additionally, the swingarm length is altered to give the same wheelbase at the static ride height for all combinations.

The effect of the change on the rear squat ratio, if simply swapping sprockets, can be seen in Figure 3.8. By re-optimising the motor and swingarm position the squat response can be returned to its original form. This can be seen in Figure 3.9.

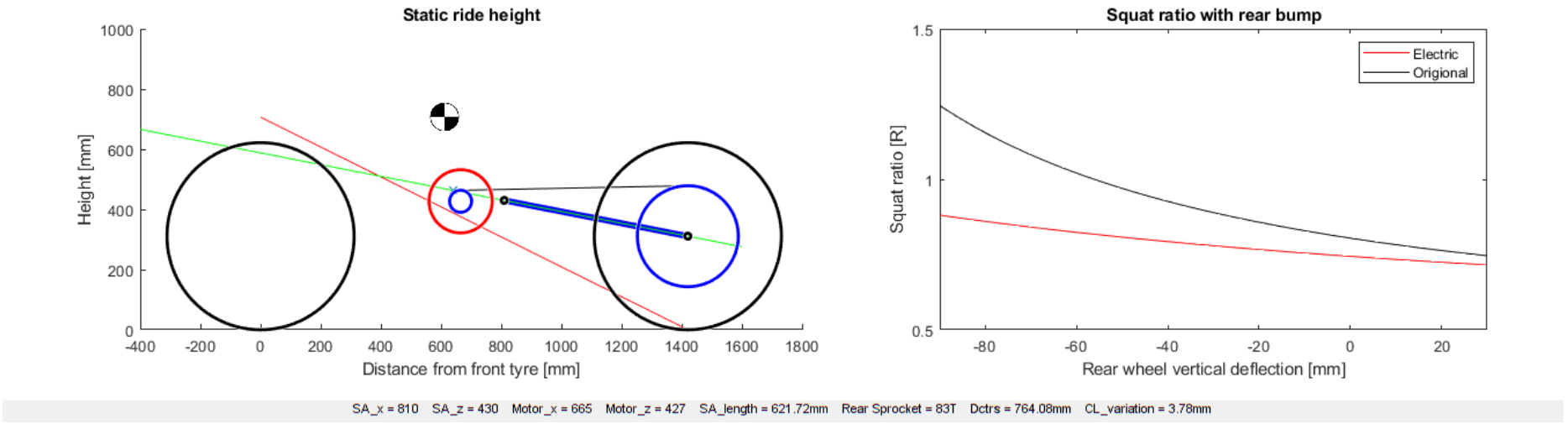

Figure 3.8 - Plot of electric powertrain using R1 motor and swingarm position.

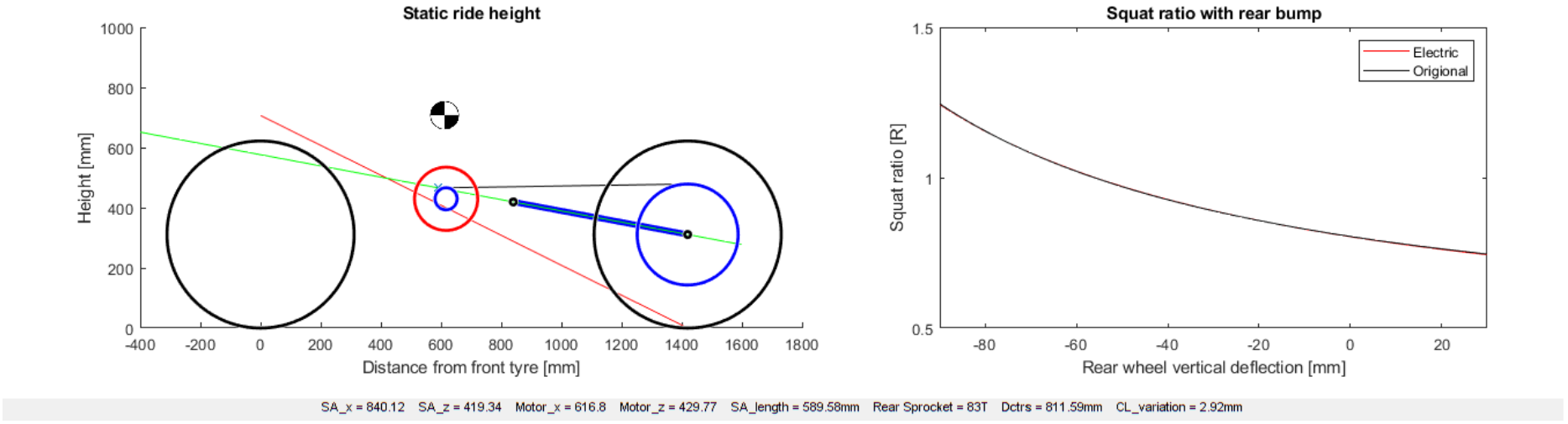

Figure 3.9 - Plot of electric powertrain with matched squat response

Figure 3.9 recommends moving the motor forwards and shortening the swingarm to recapture the original response. Further weighted optimisations can be undertaken that prioritise swingarm length, or conversely packaging volume, by prioritising a rearwards position for the motor.

While interesting for an initial look, proper design work should be undertaken to utilise a more detailed motorcycle model. The purpose of this was to determine if there is an electric specific chassis design compromise that is not well addressed by the existing literature. The result and conclusion here is that the existing squat ratio determination techniques do not require changes to deal with electric powertrain specific compromises.

3.4. Multibody Modelling:

A common method of investigating the response of a complex non-linear system is first to obtain the equations of motion for the system. A system of equations describing the motion of bicycles was derived by Whipple [25]. An updated version of this method was implemented for use on motorcycles by Sharp in 1971 [14] and has been the basis of modern motorcycle multi-body dynamics.

3.4.1. Sharp's Model

The model involves the linearised equations of motion for a bicycle representation of a motorcycle. The initial Sharp model published in 1971 [14] is a two-frame model with a revolute joint at the headstock of the motorcycle, separating the steered mass from the rear frame lumped mass model. It includes a simple tyre model as well as the gyroscopic effects of rotating wheels. The position of both bodies relative to each other is illustrated in Figure 3.10.

The Sharp 71 model involves a simple tyre model and was used in an initial exploration of the wobble, weave and capsize modes of the motorcycle. The identified modes are described as follows. Capsize is a non-oscillatory mode whereby the motorcycle falls onto its side like an inverted pendulum. Wobble is categorised as the rapid oscillation of the steering head in a 'shimmy' like motion. The third and final mode identified is the weave mode, it is a full vehicle mode. This mode is present only when a tyre model is included in the simulation. This mode involves the combined roll and yaw of the entire machine.

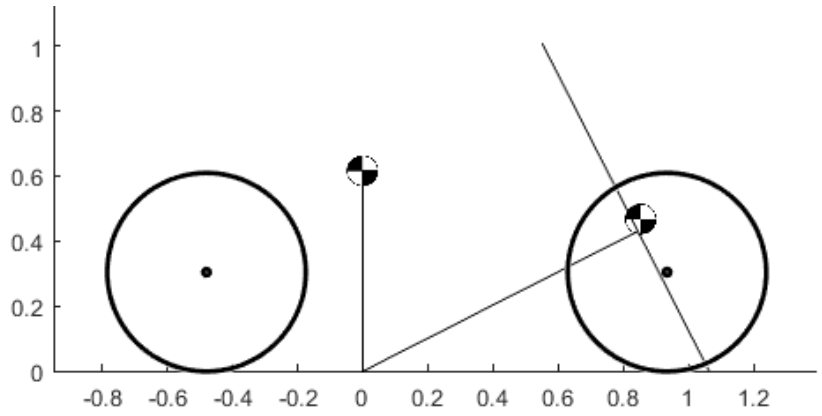

Figure 3.10 - Diagram outlining the main elements of the Sharp model [14]

Here, the equations of motion are initially re-derived symbolically in MATLAB. This is done with a view to potential future use. The use of MATLAB symbolic toolbox is used to eliminate errors in the method of deriving these equations for enhanced models and is validated by comparison to the original model.

3.4.2. Equations of Motion

For the motorcycle model in question, the equations of motion are developed via Lagrange's method [122]. Fundamentally, the system is idealised into an array of rigid bodies and kinematic relationships. The position and velocity of these bodies as well as the constraints upon the relative movement between these bodies are used to derive an expression for the energy of the system with respect to the degrees of freedom within the model.

The implementation of Lagrange's theory can be sumarised in a few steps [14, 27]:

1. Choose fixed reference frame and local coordinate frames at each mass centre or joint.
2. Define the physical properties of the rigid bodies and the kinematic relationships between them including the degrees of freedom within the model.
3. Define the body positions and rotations and differentiate to find the respective velocities.
4. Construct equations describing the kinetic ('T') and potential energy ('V') of each mass centre as well as the external forces acting such as damping ('R').
5. Calculate the effect of external forces such as tyre forces ('Q').

6. Symbolically perform the differentiations required to form Lagrange's equation as stated below and assemble:

$$\frac{d}{dt}\left(\frac{\partial T}{\partial \dot{q}_i}\right) - \frac{\partial T}{\partial q_i} + \frac{\partial V}{\partial q_i} + \frac{\partial R}{\partial q_i} = Q_i \tag{3.3}$$

To investigate the body modes of the system and validate against published data it is necessary to transform the equations of motion into state space form and determine the eigenvalues and associated eigenvectors of the state space matrix [40].

1. The first stage is to linearize the equations of motion by applying small angle approximations to the dependant variables and removing any second and higher-order terms.
2. The equations of motion are organisable into the general form shown below. Therefore, the 5x5 mass (M_b), stiffness (P_b) and damping (N_b) matrices are formed by collecting the coefficients of the respective acceleration, velocity, and position terms. Here (q) is a vector of generalised coordinates. (J_u) is the matrix relating the system inputs vector (u) to the generalised coordinates of the system.

$$M_b\ddot{q} + N_b\dot{q} + P_b q = J_u u \tag{3.4}$$

3. Having derived these matrices, it is a simple matter to invert the mass matrix and express the system in first-order form by forming the standard state space model.

$$\begin{bmatrix}\dot{q}\\ \ddot{q}\end{bmatrix} = \begin{bmatrix}0 & I\\ -M_b^{-1}K_b & -M_b^{-1}C_b\end{bmatrix}\begin{bmatrix}q\\ \dot{q}\end{bmatrix} + \begin{bmatrix}0\\ M_b^{-1}J_u\end{bmatrix}u \tag{3.5}$$

4. The final stage is to convert the matrix from symbolic to numerical and input the motorcycle parameter values. Plots of the real parts of the eigenvalues taken from the 'A' matrix, representing the damping ratios of the modes, can then be compared to the original work of Sharp.

In this model, the origin is defined as the intersection of the rear frame centre of mass with a line projected vertically down from the motorcycle with zero roll angle. The base coordinate system is defined as per the SAE system with the Z-axis positive vertically down, the X-axis positive in the direction of forward motion and the Y-axis positive to the right-hand side of the vehicle. The yaw, pitch and roll rotations are

taken in that order and are positive right-hand rule rotations about the global x,y and z axes respectively.

Suspension deflections are neglected to simplify the model eliminating pitch motions. A steering input also has the effect of changing the motorcycle pitch, but the effect is small and ignored here.

Coordinate systems are assigned as follows. The base coordinate system is defined as above. System 1 involves a yaw rotation and is defined as the base system rotated by an angle 'ψ' about the base z-axis. Pitch is neglected, therefore roll (system 2) is the next rotation and is defined as a rotation of system 1 in the local x-axis by an angle 'ϕ'.

This is where the front and rear centre of mass position derivations diverge. The rear mass position is simply a translation in 'z' to the correct height in the roll axis system. To determine the position of the front centre of mass it is necessary to include a further rotation about system 2 by an angle 'ε' (the rake angle) and then a translation to the steer axis (system 3). Here the position undergoes a rotation in the steer axis system z-axis, of an angle '∂' (the steer angle), followed by a translation in the local x and y-axis to give the position of the front frame centre of mass. Homogeneous transformation matrices are used to perform all these transitions and rotations. Having found the relationship to the position of the rigid bodies in the original coordinate frame, the position is differentiated to find the local translational velocities. As an example, the rear mass position is derived below, for a fuller description Lot has published a detailed breakdown of the required formulations [30]:

$$T_{xy} = \begin{bmatrix} x \\ y \\ 0 \end{bmatrix} = H_{01} = \begin{bmatrix} 1 & 0 & 0 & x \\ 0 & 1 & 0 & y \\ 0 & 0 & 1 & 0 \\ 0 & 0 & 0 & 1 \end{bmatrix} \tag{3.6}$$

$$R_{1-yaw} = \begin{bmatrix} cos\,\psi & -sin\,\psi & 0 \\ sin\,\psi & cos\,\psi & 0 \\ 0 & 0 & 1 \end{bmatrix} = H_{12} = \begin{bmatrix} cos\,\psi & -sin\,\psi & 0 & 0 \\ sin\,\psi & cos\,\psi & 0 & 0 \\ 0 & 0 & 1 & 0 \\ 0 & 0 & 0 & 1 \end{bmatrix} \tag{3.7}$$

$$R_{2-roll} = \begin{bmatrix} 1 & 0 & 0 \\ 0 & cos\,\phi & -sin\,\phi \\ 0 & sin\,\phi & cos\,\phi \end{bmatrix} = H_{23} = \begin{bmatrix} 1 & 0 & 0 & 0 \\ 0 & cos\,\phi & -sin\,\phi & 0 \\ 0 & sin\,\phi & cos\,\phi & 0 \\ 0 & 0 & 0 & 1 \end{bmatrix} \tag{3.8}$$

$$T_{rcg} = \begin{bmatrix} 0 \\ 0 \\ -h_r \end{bmatrix} = H_{34} = \begin{bmatrix} 1 & 0 & 0 & 0 \\ 0 & 1 & 0 & 0 \\ 0 & 0 & 1 & -h_r \\ 0 & 0 & 0 & 1 \end{bmatrix} \quad (3.9)$$

$$H_{04} = H_{01}.H_{12}.H_{23}.H_{34} \quad (3.10)$$

$$H_{04} = \begin{bmatrix} cos\,\psi & -cos\,\psi\,cos\,\phi & sin\,\psi\,sin\,\phi & x - h_r\,sin\,\psi\,sin\,\phi \\ sin\,\psi & cos\,\psi\,cos\,\phi & -cos\,\psi\,sin\,\phi & y + h_r\,sin\,\psi\,sin\,\phi \\ 0 & sin\,\phi & cos\,\phi & -h_r\,sin\,\phi \\ 0 & 0 & 0 & 1 \end{bmatrix} \quad (3.11)$$

The kinetic energy terms required for the Lagrange method include both the angular velocity and the translational velocity of the rigid bodies. The angular velocity of each mass centre is determined by calculating the combined effect of the rotations acting on that mass centre.

Therefore, the angular velocity of the front and rear frames is given by the calculation below:

$$\omega_{rf} = \begin{bmatrix} \dot{\phi} \\ 0 \\ 0 \end{bmatrix} + \left(R^T_{2-roll}. \begin{bmatrix} 0 \\ 0 \\ \dot{\psi} \end{bmatrix} \right) = \begin{bmatrix} \dot{\phi} \\ sin(\phi)\dot{\psi} \\ cos(\phi)\dot{\psi} \end{bmatrix} \quad (3.12)$$

$$\omega_{ff} = \begin{bmatrix} 0 \\ 0 \\ \dot{\delta} \end{bmatrix} + \left(R^T_{4-steer.} R^T_{3-rake.} \begin{bmatrix} \dot{\phi} \\ 0 \\ 0 \end{bmatrix} + \left(R^T_{4-steer}. R^T_{3-rake}. R^T_{2-roll}. \begin{bmatrix} 0 \\ 0 \\ \dot{\psi} \end{bmatrix} \right) \right) \quad (3.13)$$

To determine the various modes of oscillation the state space form of Sharp's equations was formed, and the 'A' matrix eigenvalues and eigenvectors were extracted. It is then possible to identify the modes of oscillation from the shape of the eigenvectors. References for the expected shapes can be found in Rowel and Cossalter *et al.* [27, 28]. Having identified the modes, the natural frequency and damping ratio of the various modes are extracted from the corresponding eigenvector.

3.4.3. Parameter Values

3.4.3.1. Tyres

Sharp outlines the strong dependence of wobble mode damping on the value taken for relaxation length [14], it is known that a tyre's relaxation length is load dependent [33]. An electric motorcycle, particularly the example studied in this thesis, is significantly heavier than an equivalent IC machine. It is important to include this variation. The following equations taken from Meijaard and Popov [33] are used to

determine the relaxation length 'σ_{long}'. Here the overall deflection of the tyre contact patch centre in the direction normal to the road surface is given by 'ϵ_n' this can be easily obtained from tyre stiffness and normal load. A small positive smoothing parameter 'ϵ_{n0}' introduced by Meijaard and Popov [33] is used to obtain the smoothed nominal deflection '$\tilde{\epsilon}_n$'. Negative deflections are ignored as this represents a tyre no longer in contact with the road and therefore the deflection will be zero (ignoring tyre expansion at high speeds). The following equations are used to obtain the relaxation length.

$$\tilde{\epsilon}_n = \frac{1}{2}\epsilon_{n0}\left[\frac{\epsilon_n}{\epsilon_{n0}} + \sqrt[4]{\left(\frac{\epsilon_n}{\epsilon_{n0}}\right)^4 + 1}\right] > 0 \tag{3.14}$$

$$\sigma_{long} = \sigma_{long,0} + \sigma_{long,1}\tilde{\epsilon}_n \tag{3.15}$$

3.4.3.2. Bifilar Pendulum

A Bifilar Pendulum can be used to calculate the in-plane inertia of an object that is suspended by two 'filars' or strings. This technique has previously been used by Sharp [37] to determine the rear frame inertia of modern motorcycles, therefore utilising the same technique helps maintain concurrency with existing literature. The object is suspended above its centre of mass and disturbed by introducing a small angular displacement about the centre of mass in a plane perpendicular to the 'filars' themselves. By measuring the mass of the object - 'm', the separation distance between - 'd_{filar}', and the length of the 'filars' - 'L_{filar}' as well as the angular velocity – 'ω'. It is possible to determine the inertia of the suspended object about the rotation axis as follows [123].

$$I = \frac{mg{d_{filar}}^2}{4L_{filar}\omega^2} \tag{3.16}$$

This technique was used to measure the inertias about the yaw and roll axis of the UoN electric racing motorcycle. The lifting straps seen in Figure 3.11 remained on the motorcycle in case of 'filar' failure but are expected to have a negligible contribution to the inertial measurement.

Figure 3.11 - Image of Nottingham motorcycle suspended as part of the measurement process

Although a motorcycle has symmetry about the XZ plane it does not have symmetry about either the XY or ZY planes. This means that the principal axis of the roll and yaw inertias cannot be determined by inspection. The fact that the Inertia will be largest about the principal axis is used to determine the angle and magnitude of the principal axes as follows.

The inertia is measured in three planes corresponding to 0, 32 and 90 degrees from the motorcycle *z* axis. This allows the determination of the principal axis and therefore the cross product through the subsequent rotation from the body principal axis to the motorcycle axis system.

Offset angle [Degrees]	*Inertia [kg.m^2]*
0	27.3
32	21.4
90	12.2

Table 3.2 – Measured rear frame inertia

By plotting $1/\sqrt{I}$ as the magnitude and the axis inclination angle as the phase on a polar plot it is possible to see that the magnitude of inertia, when inclined from the

principal axis, describes an ellipse (Figure 3.12) [124]. By fitting an ellipse to this data, it is possible to identify the principal axes of the body.

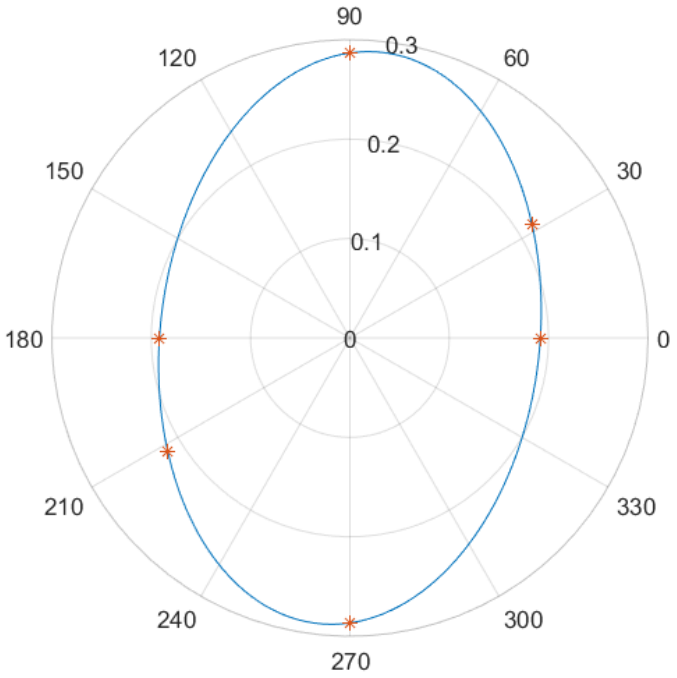

Figure 3.12 - Plot of the 'Inertial ellipse' showing the measured points in the motorcycle axis system and the fitted ellipse.

The minor and major axis of the ellipse corresponds to the magnitude of the inertia in the principal axes and the angle of these axes to the reference axes the rotational offset. The principal axis inclination relative to the rear frame axis system and the magnitudes $I_{r,xxp}$ and $I_{r,zzp}$ in the principal axes are found using a least-square ellipse fit. The effect of moving from the principal axes to an axis inclined at an angle 'θ_p ' to the principal axis is as described below and allows the determination of the respective inertias in the motorcycle rear frame axis system [124].

$$I_{r,xx} = \frac{I_{r,xxp} + I_{r,zzp}}{2} + \frac{I_{r,xxp} - I_{r,zzp}}{2} cos(2\theta_p) \tag{3.17}$$

$$I_{r,xz} = \frac{I_{r,xxp} - I_{r,zzp}}{2} \sin(2\theta_p) \tag{3.18}$$

This is used to determine the required values of $I_{r,xx}$, $I_{r,zz}$, and $I_{r,xz}$. The calculated results used in the subsequent investigation are tabulated in Table 3.3:

Variable	*Inertia [kg.m^2]*
$I_{r,xx}$	12.2
$I_{r,zz}$	27.3
$I_{r,xz}$	1.75

Table 3.3 – Measured rear frame inertias in the motorcycle axis system

3.4.3.3. Rider

The rider's inertial contribution to the rear frame is non-negligible and should be included. The rider's centre of gravity position is determined by measuring the machine tyre loads with and without a rider, in both the inclined and level positions.

It was not possible to situate the rider on the motorcycle during the pendulum testing and so for this analysis, the rider is modelled as a rectangular box of length 1.25 m, width 0.5 m and height 0.2 m with the same mass as the measured rider and protective equipment, measuring 85 kg. It is assumed that the rider is in the tucked position for this analysis and therefore his torso is approaching horizontal and aligned with the principal axes. The combination of inertias is dealt with via the parallel axis theorem and the resulting rear frame inertias shown below, Table 3.4:

Variable	*Inertia [kg.m^2]*
$I_{r,xx}$	24.5
$I_{r,zz}$	29.8
$I_{r,xz}$	0.61

Table 3.4 – Rear frame inertias including rider

3.4.4. Vehicle Response

A good match between the original Sharp model and the rederived model was achieved using the original Sharp parameters with some minor differences. Further work to resolve these differences was not undertaken as initial results directly utilising the original model equations indicated that this was of limited value. For concurrency with existing literature, the results achieved using the original model are included here.

The specific values used to represent the UoN electric racing machine in this model are included in Appendix B – Nottingham Electric Motorcycle Parameters. The determination of these values involved taking physical measurements of motorcycle geometry, determining the centre of mass position as per [19, 125] by raising the front

wheel of the motorcycle and measuring the resultant change in wheel load. This was performed with and without a rider. The Bi-filar measurement technique as outlined earlier was used to obtain the rear frame inertias.

The wheel inertias and front frame inertias are taken from Mejaard and Popov [33] as these are representative of a modern high-performance racing machine and these parts are common between both electric and internal combustion machines. Additionally, the relaxation length has been calculated as outlined earlier to reflect the increased mass contribution as outlined earlier using values representative of the modern machine. The motor rotor inertial contribution is taken from the electric motor datasheet [117] and scaled by the gear ratio 18:83, representing a typical ratio for the UoN machine, and is added to the rear wheel inertia. The tyre cornering, cambering stiffnesses and steer damping has been retained from Sharp's original work to maintain alignment with existing literature and highlight the electric motorcycle-specific variance. A comparison between the response of the Nottingham parameters and the standard Sharp parameters directly using the equations published in [14] is shown in Figure 3.13.

As can be seen the capsize modes are very similar, with the UoN machine having slightly higher damping for a small period of the 10-20 m/s speed range. The weave mode response is also extremely similar again with increased damping for the heavier higher inertia machine throughout the higher speed range of operation of interest for high-performance machines. Neither of these results is particularly surprising however the wobble response shows a greater variation. The wobble mode is significantly more damped than in the reference machine. This is due to a combination of several factors, the major one being the differing front-end geometry. This is shown by replacing the UoN front frame geometry, mass distribution and front-wheel inertia with that initially used by Sharp, see Figure 3.14.

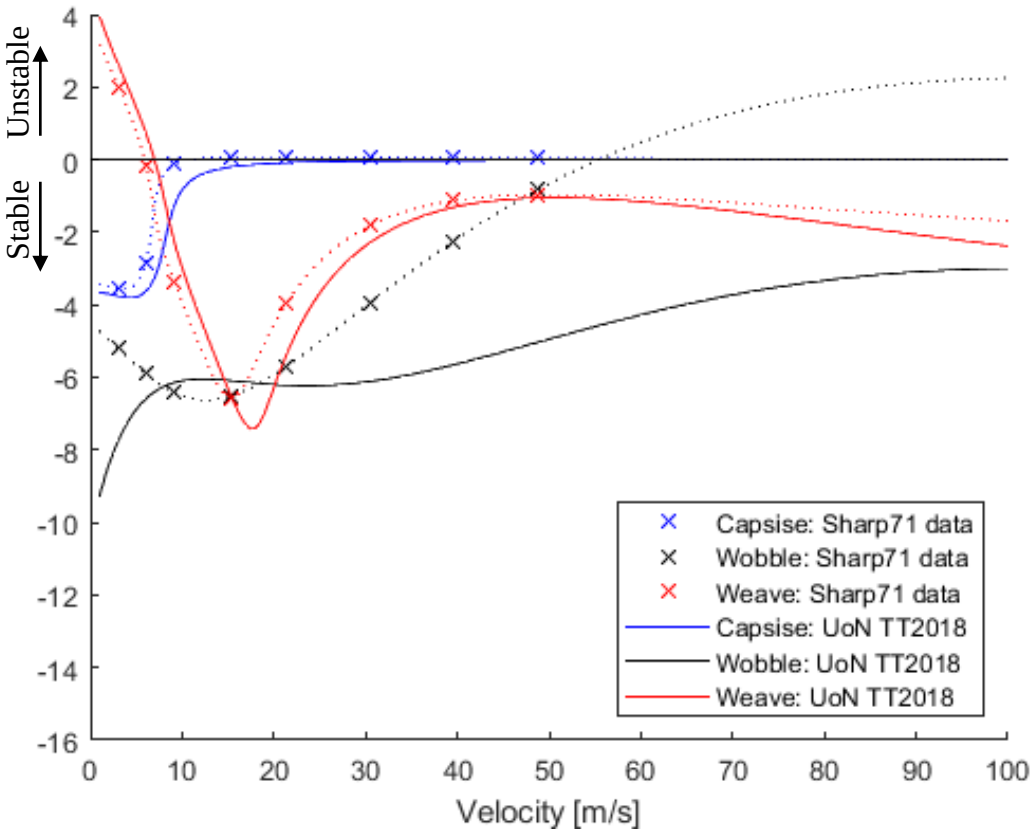

Figure 3.13 - Comparison of the stability of the original Sharp model (dotted) and the measured UN_02 machine (solid)

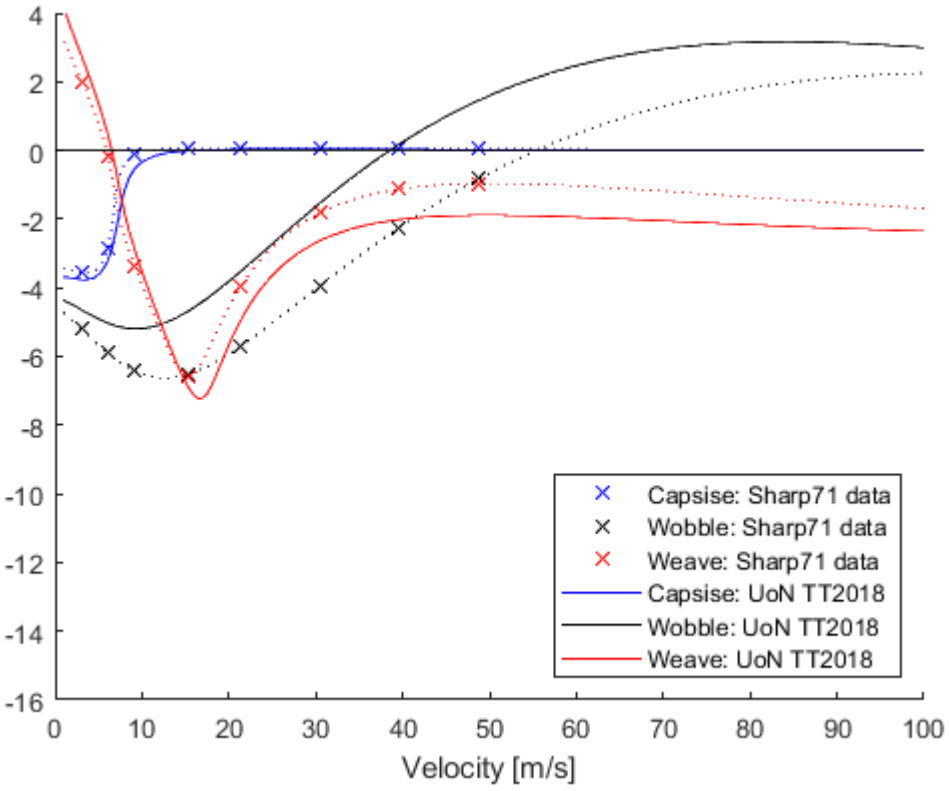

Figure 3.14 - Comparison of the Sharp model with the UoN rear frame and Sharp front end.

3.5. Conclusion

The general layout and construction techniques used in the electric motorcycle have been outlined and specific trade-offs examined. The rationale behind a single reduction transmission, as used by the Nottingham motorcycle has been explained and the resulting compromise of an unusually large rear sprocket investigated and shown to be well handled by existing work. However, this investigation highlighted the need for a more in-depth powertrain investigation to capture the powertrain compromises and their effect on full vehicle performance.

A contribution here has been in the construction of a representative high-performance electric motorcycle model, which has been used for an investigation into the stability of high-performance electric motorcycles. It has revealed that, although the increased battery mass leads to slightly increased levels of vehicle inertia, existing models do not require significant changes to accommodate this. The response of the UoN machine is compared to that of the original Sharp machine using the Sharp 71 model, and substantial differences are found with regards to increases in wobble damping. However, the majority of these can be traced to the design of the front-end geometry. The conclusion is that there is very little novelty to be explored focusing purely on mechanical multibody modelling of high-performance electric motorcycles. There are major similarities with existing internal combustion motorcycles, which have already been explored in detail elsewhere and have several dedicated software packages available for use.

In summary, the first aim of this thesis has been completed and it is found that the stability and control of high-performance electric motorcycles are not vastly different to that of their IC counterparts. This is a useful finding as this demonstrates that the existing techniques remain appropriate for use in this area with the advent of new technologies.

A contribution has also been made through the investigation of electric powertrain torque transmission techniques using a simplified electric powertrain model concluding that the direct chain drive is the most efficient method of torque transfer.

It has also been found that the powertrain specific compromises are significantly different for electric motorcycles, and this does require further investigation. Due to the high gravimetric energy density of petrol, efficiency is of limited concern to the

internal combustion designer. However, efficiency is key to the performance of an electric motorcycle to mitigate the high battery mass. To model the performance of an electric motorcycle, it is important to capture both the mechanical and electrical vehicle response elements as they are co-dependent.

Therefore, the remainder of this thesis will develop a holistic vehicle model that can combine both mechanical and electrical elements to explore the full vehicle compromise as one entity. This is key to achieving an optimum electric motorcycle design.

4. Electric Motorcycle Performance envelope

Investigation of electric motorcycle performance requires a model that captures significant detail of both powertrain and chassis performance. The vehicle model developed in this thesis has been separated into two parts. The first, the chassis model, is described in this chapter. The second, the powertrain, is contained in the following chapter, Chapter 5. Together these modelling elements are combined and used to describe the full vehicle response for a given demand, this process is described in Chapter 6.

The goal of this chapter then is to develop and verify a model that can represent the features of a modern high-performance motorcycle at the limit of performance. This must be completed with an eye to reducing complexity where possible as significant additional complexity will be added with the introduction of the electric powertrain model. To be a useful simulation, it must be able to provide results in a timely manner. To this end, the following elements are dealt with as follows.

Tyre performance is handled in Section 4.1. Tyre performance has a significant influence on both the powertrain and chassis performance. The tyre model is required to properly reflect the limit handling. The most influential elements are the effect of camber, longitudinal slip, and load dependency. In this regard, the Pacejka tyre model developed in [15] is selected, implemented, and its performance verified.

Lap time optimisation is targeted at answering lap specific compromises such as Centre of Gravity (CoG) position, optimum lift-to-drag ratio, and powertrain trade-offs. To simplify the longitudinal and lateral dynamics the Quasi-Steady-State approach is used. This has been shown in [18] to give a good approximation of a full motorcycle response under limit manoeuvring, appropriate for a race vehicle.

Section 4.2 details the implementation of a rigid body model used to develop a response surface corresponding to maximal accelerations in the x and y axes (in units of ‘g’) with respect to the vehicle velocity. This surface is commonly known as the GGV surface. This is an approach commonly found in racing car optimisations and has previously been applied to motorcycles in [22, 49]. This basis is expanded upon for motorcycles and the resulting improved model is evaluated using track data. The new model includes aerodynamic effects such as downforce, drag and pitching

moment, as well as allowing for differences in front and rear tyre construction and two-wheel drive.

Section 4.3 is a short section outlining the inclusion of motorcycle powertrain and wheel inertias as an equivalent mass and the handling of regenerative braking.

Section 4.4 handles the verification of the completed model using data gathered from the UoN electric motorcycle, as well as parameter variations performed to demonstrate the model sensitivity to input changes. The performance is validated with reference to the research machine described in Chapter 3.

4.1. Tyres

Tyres models are essential for accurate modelling of vehicle dynamics. Tyres are responsible for transmitting lateral and longitudinal forces between the motorcycle and the ground. Models typically relate the tyre load, lateral and longitudinal slips and camber angle to the tyre forces and moments. More advanced models can include variations due to vehicle speed, tyre wear and temperature.

The options available when choosing a tyre model range from empirical and physical models of varying complexity to finite element models with millions of elements. The finite element model approach, and similar computationally expensive models, are typically only used when the ultimate accuracy of tyre modelling is of utmost importance.

It is sometimes possible to use a linear tyre stiffness coefficient, a simplification of the tyre model that works well at low to medium tyre forces. However, the racing tyre is operated at the tyre limit, a non-linear region, and therefore requires the full tyre model. For models that are less concerned with detailed tyre design and simply wish to represent the tyre response, it is common to use the Pacejka semi-empirical model as developed by TU Delft, Prof. Pacejka and collaborators. This decision is supported by the availability of some published representative data for this model.

4.1.1. Pacejka Tyre Model

The Pacejka tyre model is a form of empirical model that was developed to address the large deviations between simulation and reality in many analytical models such as the brush model [44].The Pacejka tyre model is based around the sin(arctan) formula and uses many fitted scaling factors to modify this base curve to fit test data. It is also

referred to as a semi-empirical model, as it incorporates some structures that have their origin in physical models and are used to extrapolate the data between successive fitted points.

The Pacejka tyre model was originally developed for car tyre models and requires modification to properly model the large camber angle behaviour typical of motorcycles. This was accomplished initially by De Vries and Pacejka[15] which published a version of the Pacejka tyre model for motorcycles. These equations were then modified and used as the basis of the Delft-Tyre MFMC (Magic Formula Motor-Cycle) tyre models.

Subsequently, the car and motorcycle models were combined into the MF-Tyre 6.2 model that encompasses both tyre constructions [46]. However, since the fitted parameters do not correlate exactly between the different models, it is important to ensure that the correct model version is used.

The general form of the Pacejka tyre equations for longitudinal 'F_{x0}' and lateral force 'F_{y0}' is as follows:

$$F_{x0} = D_x \, sin(C_x \arctan[B_x\kappa - E_x\{B_x\kappa - arctan(B_x\kappa)\}]) + S_{vx} \tag{4.1}$$

$$F_{y0} = D_y \sin\begin{pmatrix} C_y \arctan\left[B_y\alpha_y - E_y\{B_y\alpha_y - \arctan(B_y\alpha_y)\}\right] \\ +C_\gamma \arctan\left[B_\gamma\gamma - E_\gamma\{B_\gamma\gamma - \arctan(B_\gamma\gamma)\}\right] \end{pmatrix} \tag{4.2}$$

The model parameters 'B_x, B_y, B_γ' are stiffness factors, '$C_x, C_y,$'are shape factors, 'D_x, D_y' peak values, 'E_x, E_y, E_γ' the curvature factors and 'S_{vx}' the vertical shift.

The equations used at present are more complex than this with 55 fitting parameters required for the version of the MF model proposed by De Vires and Pacejka [15]. The model also includes expressions to allow for mixed longitudinal and lateral slip as well as aligning moment. The reader is referred to [44] for more detail.

Little representative data is available and tyre manufacturers guard their data tightly. It is always possible to update model data after construction so the data published in [15] was used and is shown here. By recreating the model published in [15] the response of the motorcycle tyres with respect to vertical load used to verify the proper operation of the model. The response of a 160/70 tyre can be seen in Figure 4.1.

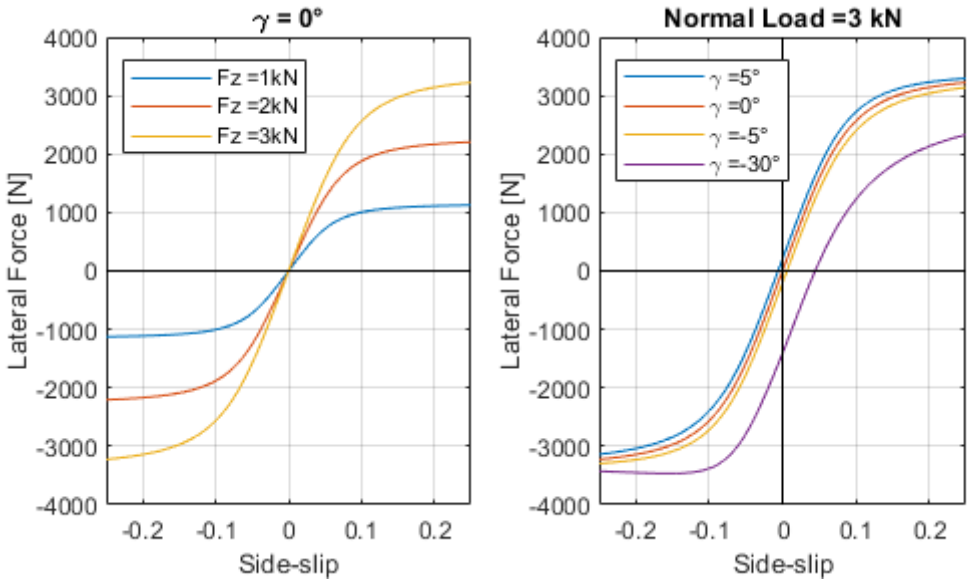

Figure 4.1 - Lateral force response of 160/70 tyre to normal load and camber variation

As motorcycles developed, there has been a move towards wider tyres to deal with the higher power outputs available with modern machines. Therefore, the data available for 120/70 and 180/55 tyres have been used in this thesis. A tyre cannot generate maximum longitudinal force and maximal lateral force at the same time. The longitudinal and lateral forces for a given normal load are illustrated in Figure 4.2 for the 180/55 tyre.

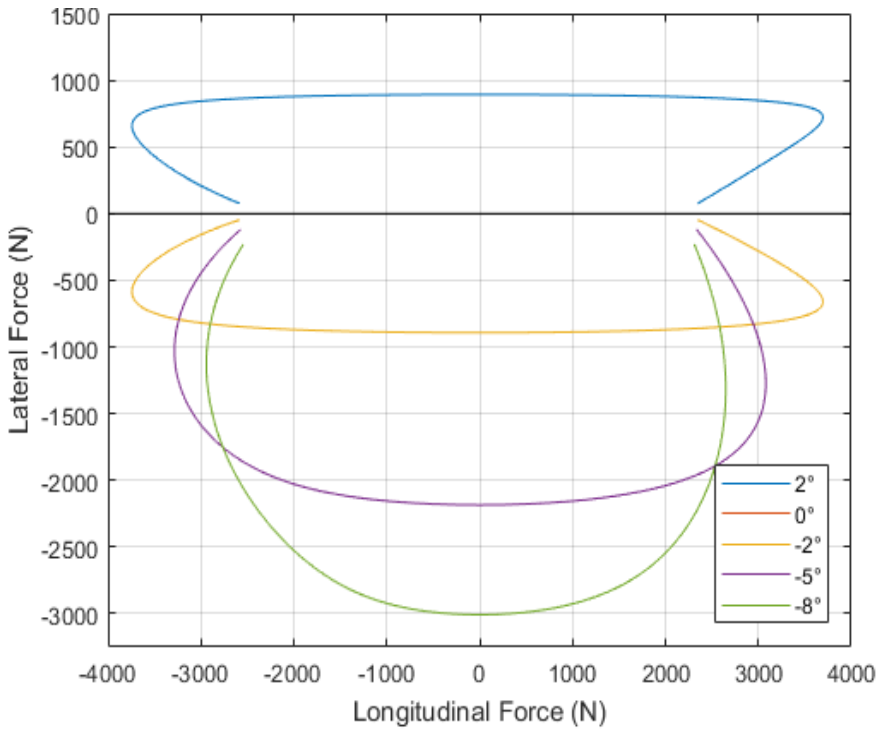

Figure 4.2 - A plot of the lateral and longitudinal force combinations at different values of sideslip for the 180/55 tyre.

The outer envelope of these curves represents the maximum available traction and cornering forces. This envelope is commonly known as the friction ellipse. The friction ellipse can be simply described by the following equation and this is the basis of the point mass lap simulation described in [18]:

$$\left(\frac{f_{long}}{f_{long}^{max}}\right)^2 + \left(\frac{f_{lat}}{f_{lat}^{max}}\right)^2 \leq 1 \qquad (4.3)$$

The goal of the racing rider is to be at the limit of performance at all points to maximise lap time. This corresponds to the limit of the friction ellipse. When the value of slip is unimportant only the 'D' and 'S_v' values in equations [4.1,4.2] need to be evaluated to determine the peak tyre force.

However, the slip value at which peak force occurs varies with the combination of lateral, longitudinal and vertical loading. Figure 4.3 highlights this effect with reference to the rear tyre longitudinal force response under load. This is important when determining the relationship between road speed and motor speed. This response is required to accurately determine the motor operating point.

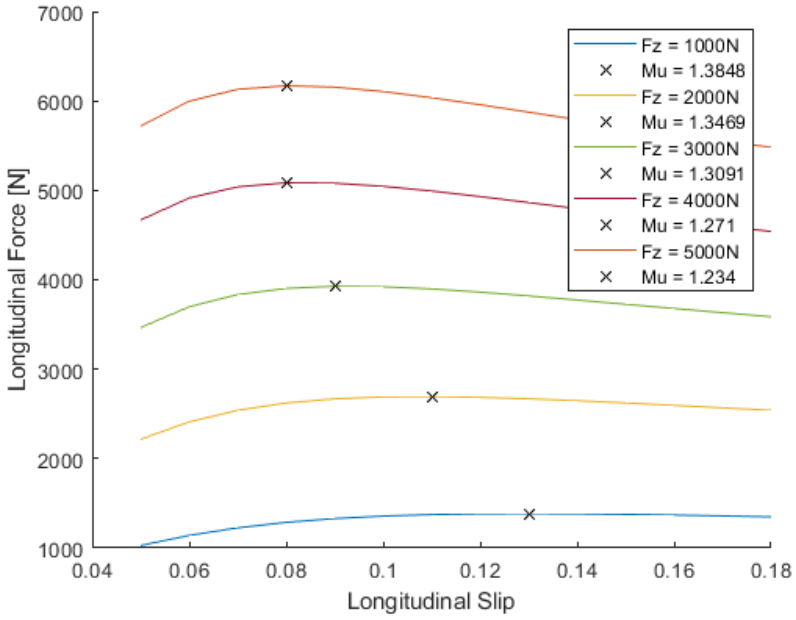

Figure 4.3 - Tyre longitudinal force as a function of vertical force and longitudinal tyre slip with peak values highlighted.

4.1.2. Rolling Radius

As the effective radius of the rear tyre (R_{rt}) changes with the camber angle of the motorcycle, it is important to capture this effect for use in combination with the

powertrain model. The radius of the tyre crown (R_{tc}) is determined from the width and height of the tyre, assuming the tyre profile is circular. The change in rear tyre radius due to lean can be determined from the chord length of the segment of the tyre profile.

This chord length is obtained through simple trigonometry using the camber angle of the motorcycle. The change in height is then given by this chord and the crown radius, as illustrated in Figure 4.4. The tyre effective radius due to camber angle $R_{t\phi}$ is given by the following formula:

$$R_{t\phi} = R_{t0} - R_{tc}(1 - cos(\phi)) \tag{4.4}$$

The tyre is a compliant structure and vertical load also affects the rolling radius of the tyre. The tyre deflection can be modelled as a simple vertical spring and this additional reduction in rolling radius is included as follows, where F_{rz} is the tyre vertical load and K_{rtyre} the equivalent stiffness, as follows:

$$R_{rt} = R_{t0} - R_{tc}(1 - \cos(\phi)) - \frac{F_{rz}}{K_{rtyre}\, cos(\phi)} \tag{4.5}$$

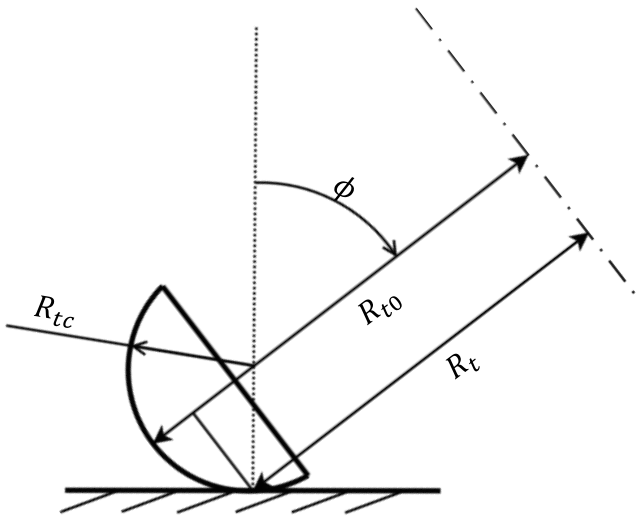

Figure 4.4 - Diagram of the rear tyre as the motorcycle rolls

4.1.3. Rolling Resistance

The effects of drag and rolling resistance reduce the force available to accelerate the vehicle. The rolling resistance calculation is performed using the Pacejka tyre model [44]. Rolling resistance 'F_{rr}' is determined as a function of vertical load 'F_z',

longitudinal force'F_x', and velocity 'V_x'. These are used in conjunction with four fitted coefficients 'q_{sy}', the reference vertical load 'F_{z0}' and reference velocity 'V_0', as follows:

$$F_{rr} = -F_z\left(q_{sy1} + q_{sy2}\frac{F_x}{F_{z0}} + q_{sy3}\left|\frac{V_x}{V_0}\right| + q_{sy4}\left(\frac{V_x}{V_0}\right)^4\right) \tag{4.6}$$

As the rolling resistance coefficients vary between the front and rear tyres it is important to determine the motorcycle tyre load distribution. This is accomplished by determining the weight transfer due to vehicle acceleration, drag and downforce accounting for the change in centre of gravity height due to the motorcycle camber angle. This is covered in more detail in the following section.

4.2. Performance Envelope Generation

The model requires a method of determining the limits of vehicle performance so that the ultimate performance of the machine can be evaluated. There are many ways to determine these full vehicle response limits. Examples range from a simple point mass with a given friction circle [18] to a full multi-body model with multiple degrees of freedom and rider modelling. As with tyre modelling, there are variations in accuracy and complexity with associated computational penalties.

The use of a multi-body motorcycle model with a rider is highly computationally expensive for a 37.7-mile (60 km) course such as the TT [17, 48]. This was discounted as it was deemed likely too computationally intensive for the equipment available. A common technique used to evaluate racing cars is the use of a GGV surface to describe the limiting vehicle performance. This was first described by Milliken and Milliken [50] and has been adapted for use with motorcycles by Biral and Lot [22]. Here, the method outlined in [22] has been expanded to increase its fidelity, particularly in response to tyre modelling and aerodynamic effects.

Other methods such as those described by Hauser and Saccon [18] are available but they either lack the higher fidelity available from the chosen method or require higher computational effort. The decision was taken early on to focus on a single method.

4.2.1. Rigid Body Performance Envelope

The rigid body performance envelope is commonly illustrated as a GGV plot. This is a method of illustrating the maximal lateral and longitudinal acceleration

combinations of a vehicle with respect to velocity. These plots are commonly used to explore the effect of vehicle changes on the limit performance of the machine.

Initially, this technique was derived for use in racing car performance optimisation as set out by Milliken and Milliken [50]. These plots are a useful tool in analysing rider performance, as the perfect rider will be able to track the limit of these plots and thus achieve the ultimate lap time.

A simple motorcycle model used to generate these plots is derived by Biral and Lot as well as Veneri and Massaro [22, 49]. However, neither are entirely appropriate for the vehicle at hand. The possibility of a front-wheel-drive motorcycle and differing front and rear tyres are ignored in both models as well as the inclusion of downforce generating winglets.

The simple steady state rigid body model is re-derived here for completeness. The model ignores the effect of suspension deflections and tyre thickness. The SAE coordinate system is used. The geometric parameters associated with the simplified rigid body motorcycle are illustrated in Figure 4.5. The values used from the measuring machine are given in Appendix B – Nottingham Electric Motorcycle Parameters.

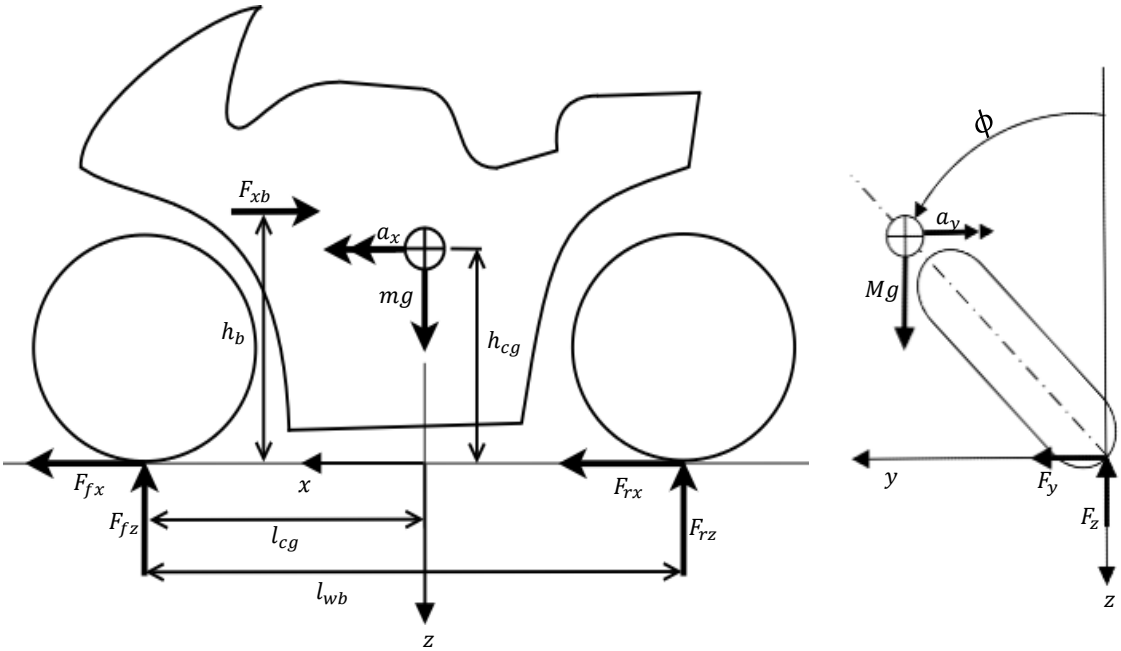

Figure 4.5 - Simple Rigid Body Motorcycle model

The equations of motion are derived according to the Newton-Euler approach and are as follows:

$$ma_x = F_{rx} + F_{fx} - F_{bx} \tag{4.7}$$

$$ma_y = F_{ry} + F_{fy} \tag{4.8}$$

$$0 = mg - F_{rz} - F_{fz} \tag{4.9}$$

$$a_y \cos\phi = g sin\phi \tag{4.10}$$

$$ma_x h_{cg} cos\phi = F_{zr}\left(l_{wb} - l_{cg}\right) - F_{zf} l_{cg} - F_{xb} h_b cos\phi \tag{4.11}$$

$$ma_x \mathrm{h_{cg}} \sin\phi = F_{yr}\left(\mathrm{l_{wb}} - \mathrm{l_{cg}}\right) - \mathrm{F_{yf}} \mathrm{l_{cg}} - \mathrm{F_{xb}} \mathrm{h_b} \sin\phi \tag{4.12}$$

A motorcycle can apply torque to both the front and rear wheels through combined braking, or through a front-wheel-drive mechanism in addition to the traditional rear-wheel-drive. It is useful to include a relationship between the front and rear longitudinal forces, as follows:

$$\alpha = \frac{F_{rx}}{F_{rx} + F_{fx}} \tag{4.13}$$

The relationship between the lateral and longitudinal grip available from a tyre at the limit of adhesion can be given as a friction ellipse. Here the front and rear tyre friction ellipses are given by the following equations:

$$\left(\frac{F_{rx}/F_{rz}}{\mu_{rx}}\right)^2 + \left(\frac{F_{ry}/F_{rz}}{\mu_{ry}}\right)^2 \leq 1 \tag{4.14}$$

$$\left(\frac{F_{rx}/F_{fz}}{\mu_{fx}}\right)^2 + \left(\frac{F_{fy}/F_{fz}}{\mu_{fy}}\right)^2 \leq 1 \tag{4.15}$$

The roll angle of the motorcycle is readily obtained from the equations of motion, here $\tan\phi = a_y/g$. It is then possible to develop the equations relating the limiting longitudinal and lateral accelerations for the front and rear tyres, which are given as follows:

$$\left(\frac{\alpha l_{wb}(ma_x + F_{bx})\sqrt{g^2 + a_y^2}}{\mu_{rx} g\left(m l_{cg}\sqrt{g^2 + a_y^2} + ma_x h_{cg} + F_{bx} h_b\right)}\right)^2 + \left(\frac{a_y}{\mu_{ry} g}\right)^2 \leq 1 \tag{4.16}$$

$$\left(\frac{(1-\alpha) l_{wb}(ma_x + F_{bx})\sqrt{g^2 + a_y^2}}{\mu_{fx} g\left(m\left(l_{wb} - l_{cg}\right)\sqrt{g^2 + a_y^2} - ma_x h_{cg} - F_{bx} h_b\right)}\right)^2 + \left(\frac{a_y}{\mu_{fy} g}\right)^2 \leq 1 \tag{4.17}$$

Typically, a motorcycle will drive only the rear wheel during acceleration, and the majority of braking is performed by the front wheel. The limiting performance can then be determined by considering the operation of the single tyre at the limit of adhesion - if the magnitude of the friction ellipse = 1, α = 1 under traction, and α = 0 under braking.

However, to evaluate the optimal machine performance utilising both front and rear tyres it is necessary to determine an optimum value for α. This is obtained by assuming that the front and rear tyre friction coefficients are the same ($\mu_x = \mu_{fx} = \mu_{rx}, \mu_y = \mu_{fy} = \mu_{ry}$) and that the longitudinal tyre friction engagement of the front tyre is the same as that of the rear one [22, 49]. i.e., $F_{fx}/F_{fz} = F_{rx}/F_{rz}$. It is then possible to determine the following expression for α:

$$\alpha = \frac{ml_{cg}\sqrt{g^2 + a_y^2} + ma_x h_{cg} + F_{bx}h_b}{ml_{cg}\sqrt{g^2 + a_y^2}} \tag{4.18}$$

Combining this with the friction circle equation yields the following expression for the longitudinal acceleration of the rigid body as limited by the tyres.

$$a_x = g\mu_x\sqrt{1 - \left(\frac{a_y}{g\mu_y}\right)^2} - \frac{F_{bx}}{m} \tag{4.19}$$

Additional factors that need to be included in this model are the front and rear wheel lifting limits. Here, it is possible to solve analytically for $F_{fz} = 0$ and $F_{rz} = 0$ and determine the acceleration limits. For the 'wheelie' limit - front wheel lifting, $F_{fz} = 0$, which leads to the following:

$$a_x = \frac{(l_{wb} - l_{cg})\sqrt{g^2 + a_y^2}}{h_{cg}} + \frac{F_{bx}h_b}{mh_{cg}} \tag{4.20}$$

Conversely, for the 'stoppie' limit – rear wheel lifting under braking, $F_{rz} = 0$, and this leads to the following limit acceleration:

$$a_x = -\left(\frac{ml_{cg}\sqrt{g^2 + a_y^2} + F_{bx}h_b}{mh_{cg}}\right) \tag{4.21}$$

It is assumed that the motorcycle's brakes can achieve this limit performance and therefore no further terms to reduce this limit for braking are required.

This is not true for positive acceleration due to powertrain limitations. However, a motorcycle powertrain power limit can easily be included by the following expression. The following equation is used to implement a further positive acceleration limit to match the existing model [22], but is replaced by a more advanced powertrain model at a later stage.

$$a_x = \frac{P_{max}}{mV} - \frac{F_{bx}}{m} \tag{4.22}$$

To ensure the model is performing as expected the results in [49] are recreated in Figure 4.6.

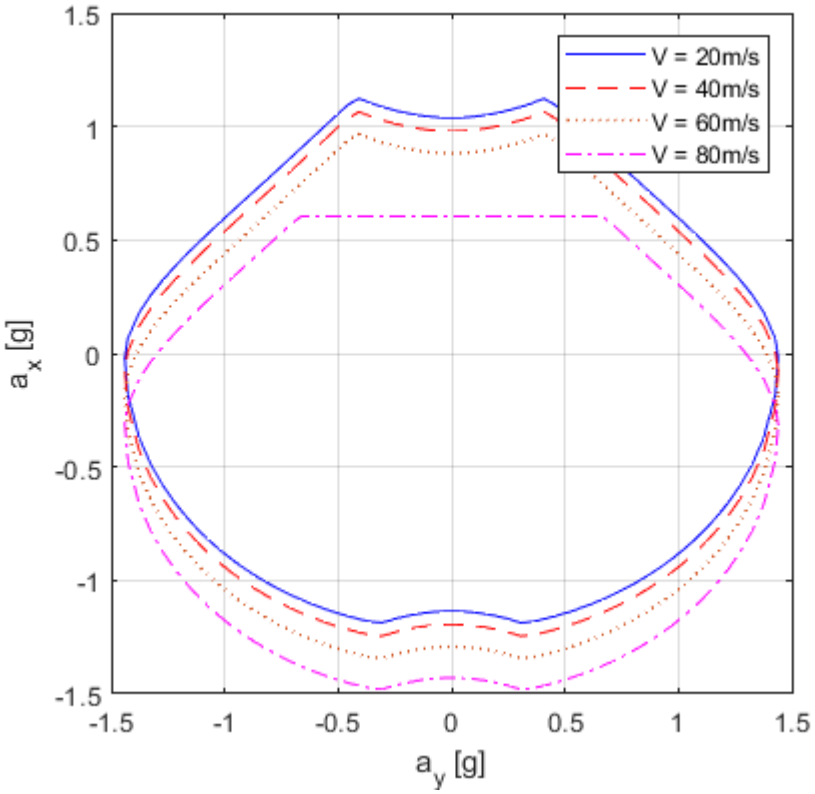

Figure 4.6 - GGV plot used to show the match with the published model in [49]

When analysing the assumptions required to derive these simple performance envelopes, a few issues arise. One, the assumption that both the front and rear tyres are the same is hard to justify given the large differences between the modern front and rear racing tyres. Two, the aerodynamic effects of lift and pitching moment are neglected. This is again in sharp contrast to modern high-performance motorcycles that employ significant effort in perfecting the downforce generation of their motorcycles.

To remove these limitations, the aerodynamic forces of lift drag and pitching moment on the motorcycle body, as well as a proposed winglet, are included in the analysis and the resulting equations of motion are solved without assuming that the front and rear tyres are identical. The revised free body diagram is shown in Figure 4.8.

Although uncommon, it is also possible to create a two-wheel-drive motorcycle. To investigate the resulting performance differential, the optimal longitudinal force distribution can be used under traction as well as braking. The resulting influence of the addition of front-wheel-drive to the model is shown in the GG plot, Figure 4.7.

Figure 4.7 shows that there is a significant benefit to this inclusion at moderate to high lateral accelerations. This is expected as the effective height of the CoG is lowered when the motorcycle is cambered reducing weight transfer and therefore the maximum force available at the rear wheel. By allowing front-wheel-drive this performance can be recovered through using additional longitudinal force applied through the front tyre contact patch. The additional freedom adds no benefit when the wheelie limit is approached; again this is expected as the front tyre is unloaded.

This leads to an interesting conclusion. An electric motor sized for this front-wheel application will likely have to deliver a drive-cycle that consists of several short high-power bursts corresponding to braking and corner exit, but the continuous power requirements are likely to be comparatively low. This has motor topology implications which should be considered in the design of a front-wheel-drive system. The relative merits of different topologies for this particular application are outside the scope of this thesis but would prove interesting for further work.

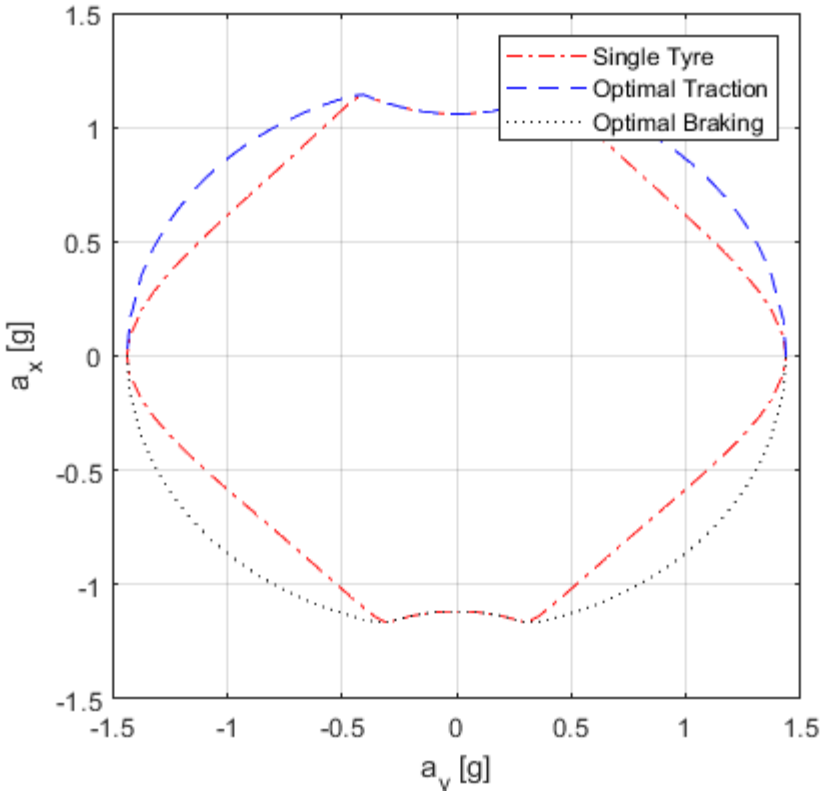

Figure 4.7 - Effect of optimal longitudinal force distribution over both tyres on the GG envelope

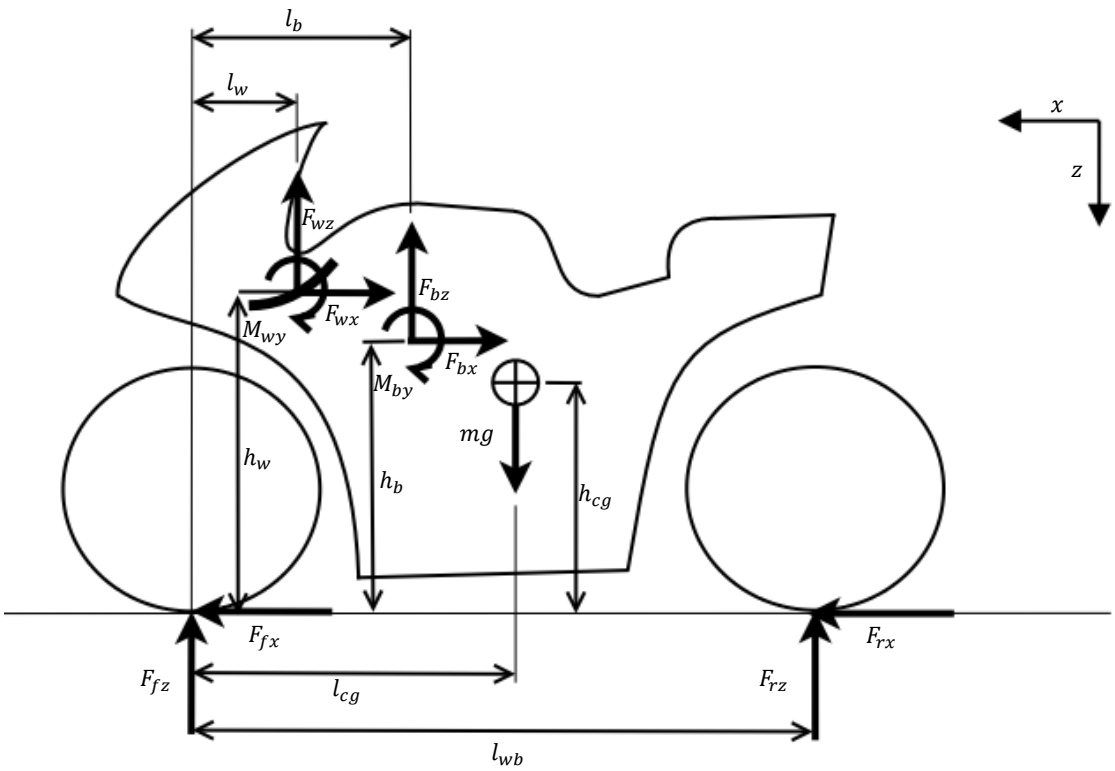

Figure 4.8 - Free body diagram of the expanded model showing inclusion of aerodynamic winglet and body forces

The revised equations of motion, including the effects of lift and pitching moment, as well as the inclusion of a dedicated winglet and associated aerodynamic performance, are given as follows:

$$ma_x = F_{rx} + F_{fx} - F_{bx} - F_{wx} \tag{4.23}$$

$$ma_y = F_{ry} + F_{fy} + (F_{bz} + F_{wz})sin\phi \tag{4.24}$$

$$0 = mg - F_{rz} - F_{fz} - (F_{bz} + F_{wz})cos\phi \tag{4.25}$$

$$a_y cos\phi = gsin\phi \tag{4.26}$$

$$\begin{aligned} ma_x h_{cg} cos\phi = F_{rz}(l_{wb} - l_{cg}) - F_{fz} l_{cg} \\ -(F_{bx}h_b + F_{wx}h_w + F_{bz}(l_{cg} - l_b) + F_{wz}(l_{cg} - l_w) + M_{by} + M_{wy})cos\phi \end{aligned} \tag{4.27}$$

$$\begin{aligned} ma_x h_{cg} sin\phi = F_{ry}(l_{wb} - l_{cg}) - F_{fy} l_{cg} \\ -(F_{bx}h_b + F_{wx}h_w + F_{bz}(l_{cg} - l_b) + F_{wz}(l_{cg} - l_w) + M_{by} + M_{wy})sin\phi \end{aligned} \tag{4.28}$$

When determining the limitations of a single tyre, the same process as before is repeated. To simplify the resulting equations, the following terms have been introduced.

$$\begin{aligned} E1 = ml_{cg}\sqrt{g^2 + a_y^2} + ma_x h_{cg} + F_{bz}(-l_b) + F_{wz}(-l_w) + F_{bx}h_b \\ +F_{wx}h_w + M_{by} + M_{wy} \end{aligned} \tag{4.29}$$

$$\begin{aligned} E2 = m(l_{wb} - l_{cg})\sqrt{g^2 + a_y^2} - ma_x h_{cg} - M_{wy} - F_{bz}(l_{wb} - l_b) \\ -F_{wz}(l_{wb} - l_w) - F_{bx}h_b - F_{wx}h_w - M_{by} \end{aligned} \tag{4.30}$$

$$E3 = l_{wb}(ma_x + F_{bx} + F_{wx})\sqrt{g^2 + a_y^2} \tag{4.31}$$

The resulting inequalities are then given as follows:

$$\left(\frac{\alpha(E3)}{\mu_{rx} g(E1)}\right)^2 + \left(\frac{a_y}{\mu_{ry} g}\right)^2 \leq 1 \tag{4.32}$$

$$\left(\frac{(1-\alpha)(E3)}{\mu_{fx} g(E2)}\right)^2 + \left(\frac{a_y}{\mu_{fy} g}\right)^2 \leq 1 \tag{4.33}$$

When determining the optimal performance utilising both tyres, it is necessary to ensure that both tyres are fully engaged. This is resolved by equating the full tyre inequalities and obtaining an expression for α in terms of a_x. The resultant acceleration is then obtained by solving either of the tyre inequalities numerically using MATLAB's solver 'vpasolve' [126] and the expression for α.

The following expressions are used depending on the magnitude of the respective input μ_y values. If μ_{fy} equals μ_{ry}.

$$\alpha = \frac{\mu_{rx}(E1)}{\mu_{rx}(E1) + \mu_{fx}(E2)} \tag{4.34}$$

If not; the two equations (4.32 and 4.33) are equated to each other and the MATLAB symbolic toolbox in conjunction with solver 'vpasolve' [126] is used to solve for both α and a_x.

Having determined the optimal longitudinal force distribution and roll angle, the lateral and longitudinal tyre friction coefficients can be iterated to account for the load sensitivity of the tyres using the full tyre model described earlier. Tyre slip values are also obtained in this manner. These slip values can then be used in conjunction with the tyre rolling radius to obtain the necessary relationship between motor speed and resultant road speed.

The wheel lifting limits are obtained in the same manner as previously and are given as follows. For wheelie, $F_{fz} = 0$:

$$a_x = \frac{\begin{array}{c} m\left(l_{wb} - l_{cg}\right)\sqrt{g^2 + a_y^2} - F_{bz}(l_{wb} - l_b) - F_{wz}(l_{wb} - l_w) - F_{bx}h_b \\ -F_{wx}h_w - M_{by} - M_{wy} \end{array}}{mh_{cg}} \tag{4.35}$$

And for the 'stoppie' limit where $F_{rz} = 0$:

$$a_x = -\left(\frac{ml_{cg}\sqrt{g^2 + a_y^2} + F_{bz}(-l_b) + F_{wz}(-l_w) + F_{bx}h_b + F_{wx}h_w + M_{by} + M_{wy}}{mh_{cg}}\right) \tag{4.36}$$

To demonstrate the effect of the influence of this additional model fidelity the effect of downforce coefficient variation a winglet was placed at 0.3 m from the front wheel tyre centre patch and 1 m in height. This winglet was simulated with a '$C_{lw}A$' (combined lift coefficient and effective area term) of 0, -0.1 and -0.2. This winglet's contribution to the UoN electric motorcycle GG plot at 50 m/s is shown in Figure 4.9. The tyre parameters are taken from [15] and are unscaled. The equation used to determine the relationship between this coefficient and the winglet force is as follows, where 'ρ_{air}' is air density.

$$F_{wx} = \frac{1}{2}\rho_{air} v^2 C_{lw} A \tag{4.37}$$

This is a useful additional design sensitivity as the winglet downforce level and position can be varied to tune to the desired characteristics. The wheelie limit is increased as well as the 'stoppie' limit as expected. It is also possible to see the forward bias to the winglet position causes a larger increase in front tyre force showing it is possible to increase both the traction and the braking performance with additional downforce. This is a useful tool for tuning the vehicle performance envelope. The additional drag has been neglected for this plot to highlight the effect of the single parameter, but this is considered later in Chapter 7.

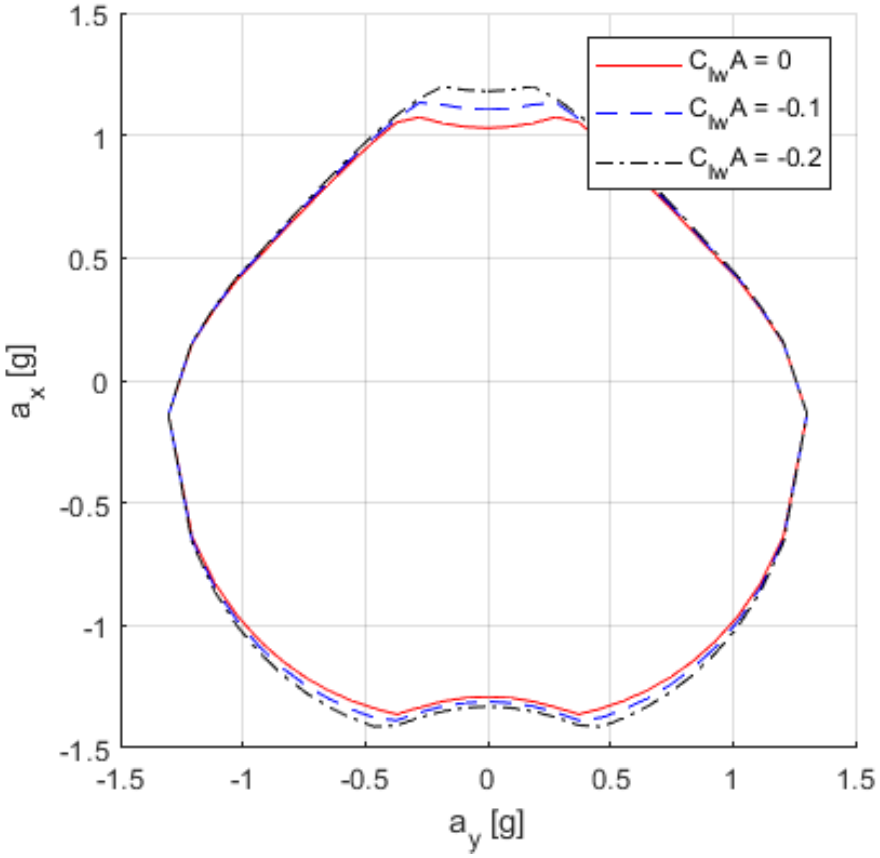

Figure 4.9 - GG plot illustrating the effect of winglet downforce contribution to motorcycle performance.

The individual tyre friction coefficients can also be varied to account for differences in the front and rear tyres which impacts the full vehicle performance envelope. This impact is shown in Figure 4.10. As can be seen, the tyre limited braking force is directly related to the longitudinal tyre friction modification coefficient '$\lambda_{\mu xf}$' and this is independent of the rear tyre performance. Additionally, when the lateral friction

coefficient is modified by the coefficient '$\lambda_{\mu yf}$' this has an impact on the lateral performance of the machine, particularly under braking. These are both expected behaviours but are important to include as part of the full vehicle response not captured in [22, 49].

Another important feature not captured in [22, 49] that is included with the adoption of a full tyre model is the load dependant variation in tyre performance. Although the limitations of the tyre data available do not capture the variation in lateral performance, the variation in longitudinal performance can be seen. For purposes of comparison, the effect of the increased mass of the UoN TT2018 machine is compared to that of a typical IC-powered superbike and rider in Figure 4.11. The effect of the electric powertrain limitation on both machines has also been included for reference.

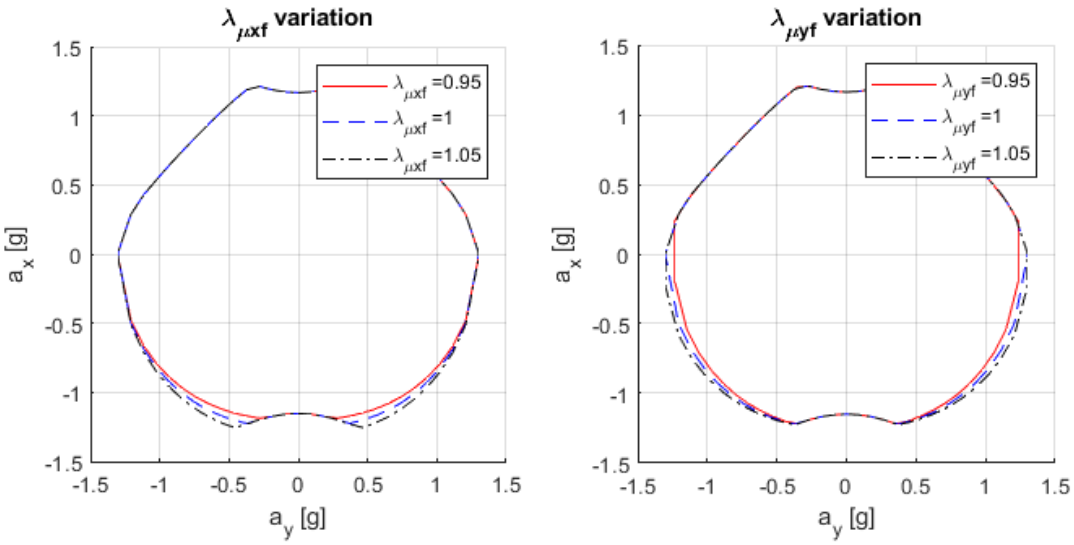

Figure 4.10 – Effect of scaling the front longitudinal and lateral tyre friction coefficient

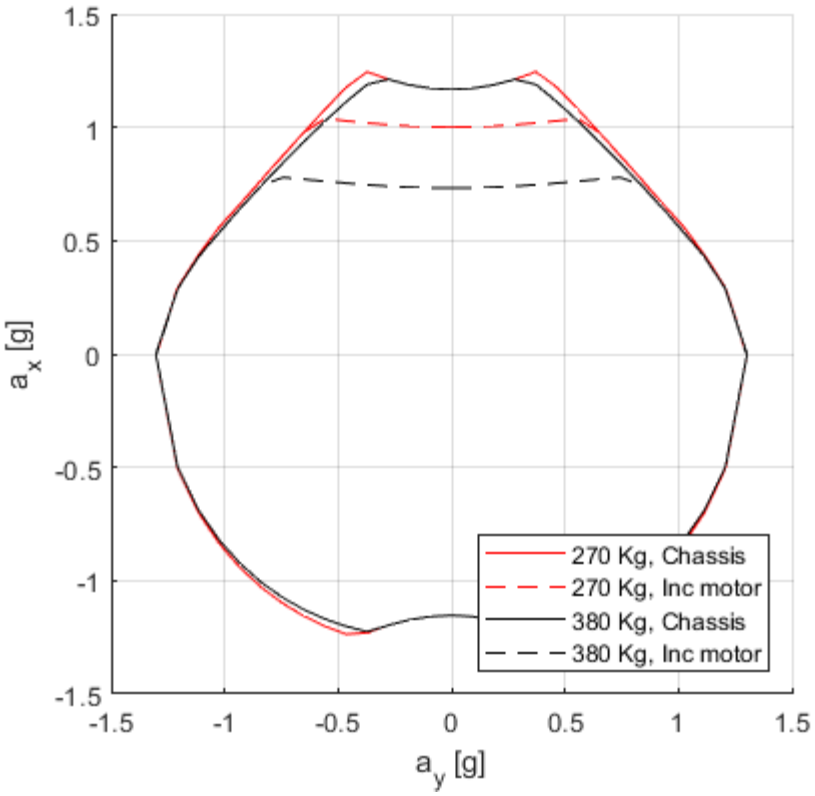

Figure 4.11 - Plot of the impact of vehicle mass on the TT2018 performance envelope using un-scaled tyre data [15]

As has been outlined in the previous section, the model developed in this thesis captures several significant effects that have been ignored in the previous models [22, 49]. The goal here was to include the effect of many of the current vehicle performance tuning parameters omitted from the previous work into a vehicle model. This has been achieved and the resulting increased fidelity model capabilities demonstrated with reference to the research machine. This is extremely useful for investigating some of the more detailed effects of the full vehicle response. Effects such as the effect of differing front and rear tyres, tyre load sensitivity and inclusion of aerodynamic devices can now be investigated. This has all been achieved while retaining the simplicity of the rigid body model.

To demonstrate the overarching goal of this piece of work, the generation of the full vehicle performance envelope for a given set of input parameters and speeds, the full GGV performance envelope for the UoN 2018 TT Zero motorcycle with unscaled tyre parameters, is shown in Figure 4.12. The tyre model used the model and dataset published by De Vries and Pacejka [15]. This can now be used in conjunction with the powertrain model developed in Chapter 5 to predict vehicle performance. An

interesting, but expected, effect highlighted in the plot, is how the ultimate acceleration performance degrades with speed and how the powertrain performance is affected by roll angle at high speeds. The former is due to the inclusion of aerodynamic drag while the latter is due to the interaction of the motor speed limiter and the camber angle of the motorcycle in conjunction with the rear tyre profile. Motorcycle performance can now be quickly evaluated for a range of vehicle setups.

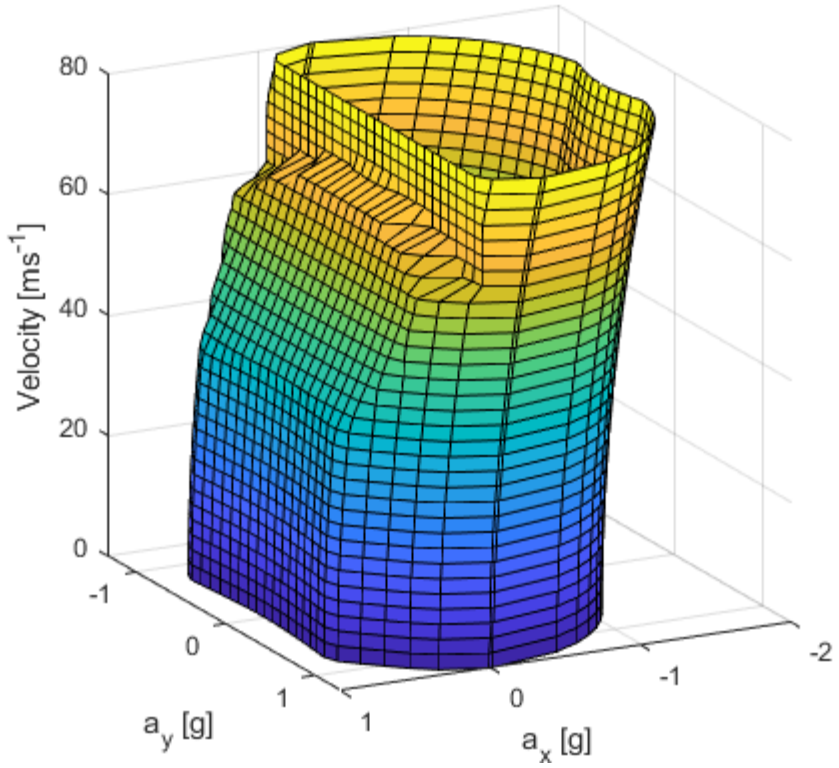

Figure 4.12 - G-G-V plot of the 2018 UoN TT2018 contender with un-scaled tyre model

4.3. Powertrain Integration

The limiting longitudinal tyre force and associated longitudinal slip are determined in the previous section. The motor speed is simply a function of the rolling radius, gear ratio, and longitudinal tyre slip. To determine the maximum acceleration, and thus the maximum usable driving torque as limited by the tyres, the powertrain inertia also needs to be accounted for.

The use of linear effective mass is a method of including the motor and wheel inertia contributions to linear acceleration. Here the effective linear mass 'm_{eff}' is determined from the object's inertia 'I' and its radius of gyration 'r'.

$$m_{eff} = \frac{I}{r^2} \tag{4.38}$$

As the powertrain has a single-speed transmission the powertrain inertia 'I_{pt}' can be determined from the rear wheel inertia 'I_{rw}' and the electric motor rotor inertia 'I_{mot}'. The effect of the gear ratio is determined from 'N_1' the motor sprocket number of teeth and 'N_2' the rear wheel sprocket number of teeth as follows.

$$I_{pt} = I_{rw} + I_{mot}\left(\frac{N_2}{N_1}\right)^2 \tag{4.39}$$

The effect of tyre slip means that the rotational velocity of the powertrain during the acceleration phase is above what it would be if the powertrain speed was simply fixed to the road speed. The opposite is true during regenerative braking. The equivalent mass determination is therefore modified as follows, where 'κ_r' is the quasi-steady-state rear-wheel longitudinal slip value [18]

$$m_{r,eff} = \frac{I_{pt}(1+\kappa_r)}{r_{rw}^2} \tag{4.40}$$

The equivalent mass of the vehicle 'm_{eq}' is then given by the following where 'm_{mc}' is the motorcycle mass:

$$m_{eq} = m_{mc} + \frac{I_{fw}}{r_{rw}^2} + \frac{I_{pt}(1+\kappa_r)}{r_{rw}^2} \tag{4.41}$$

The maximum motor torque the vehicle can utilise is derived from the sum of the tyre force, the rolling resistance force 'F_{rr}' and the force required to accelerate the linear equivalent mass. The resulting maximum wheel torque '$T_{w,max}$' is thus:

$$T_{w,max} = \left(a_x m_{eq} + F_{bx} + F_{wx} + F_{rr}\right) r_{rw} \frac{N_1}{N_2} \tag{4.42}$$

If the motor cannot supply this limit torque, then the acceleration of the machine is instead determined by the motor limitation as follows, where T_{mot} is motor torque.

$$F_w = \frac{T_{mot}}{r_{rw}} \frac{N_2}{N_1} \tag{4.43}$$

$$a_x = \frac{F_w - F_{bx} - F_{wx} - F_{rr}}{m_{eq}} \tag{4.44}$$

4.3.1. Braking

An electric motorcycle can drive in both forward and reverse directions. An unexpected reverse is particularly disconcerting for the rider in the author's experience! The reason for including this here is the importance of regenerative braking. An electric motor, such as the one used by the Nottingham Race team, can be operated as a generator. As an electric vehicle is significantly influenced by battery mass any method of recuperating energy that would otherwise be wasted should be analysed.

The optimum distribution of combined braking forces is determined as shown previously. The tyre slip under braking is determined using the vehicle model. This is used to determine electric motor speed. In the case of a rear-wheel-drive motorcycle, the regeneration torque that the motor can apply is significantly less than what it can apply in traction, due to weight transfer. In the case of the UoN motorcycle at the TT Zero race, the limit was approximately 20% of the forward torque.

Due to this comparatively low torque requirement, the electric motor will likely be able to supply this torque throughout the vehicle speed range, without impact from the voltage dependant torque drop off. There is therefore little to be gained from computing the exact voltage dependant motor operating point as a function of the state of charge during regeneration. Instead, a simplification is made, whereby a lookup table is generated at the nominal battery voltage and is used to determine the regeneration power developed throughout the lap.

It is worth noting that the centre of gravity placement and aerodynamic loads influence the optimum braking distributions. By moving the CoG, it is possible to increase the rear wheel regenerative braking capability but this movement influences the traction performance. The model allows for the effect of CoG placement to be investigated as part of a full lap analysis.

4.4. Model Correlation

To generate validation data for the GGV plots and parts of the powertrain model, an AIM Evo5 datalogger [127] was attached to the motorcycle for the Isle of Man TT Zero race 2018, as well as a separate CAN logger for the motor drive data. This race data as well as separate test data from a coast down test performed at Bruntingthorpe testing grounds is used for validation.

The vehicle drag coefficient is obtained by fitting a simple drag model to coast down test data collected at Bruntingthorpe. Here the motorcycle was accelerated to a high speed and allowed to coast to a lower speed as far as the track limits would allow. Regenerative braking was disabled for this test and the rider was instructed to remain in the tucked position throughout the manoeuvre. A model of the motorcycle drag and rolling resistance is then fitted to the coasting portion of the data and an approximate motorcycle 'C_dA' of 0.335 (drag coefficient 'C_d' times area 'A') is obtained, see Figure 4.13. This value is only valid for the Elvington configuration and TT2019 as the fairings, rider size and tank size are all different for the TT2018 data.

It was not possible to run in both directions as the track is single direction only for safety reasons. This introduces some systematic error into the measurement due to the potential effects of wind speed and road gradients. However, the track is an old airfield, and it was a calm day, so the error is likely to be small, but were no further opportunities to quantify and rectify this.

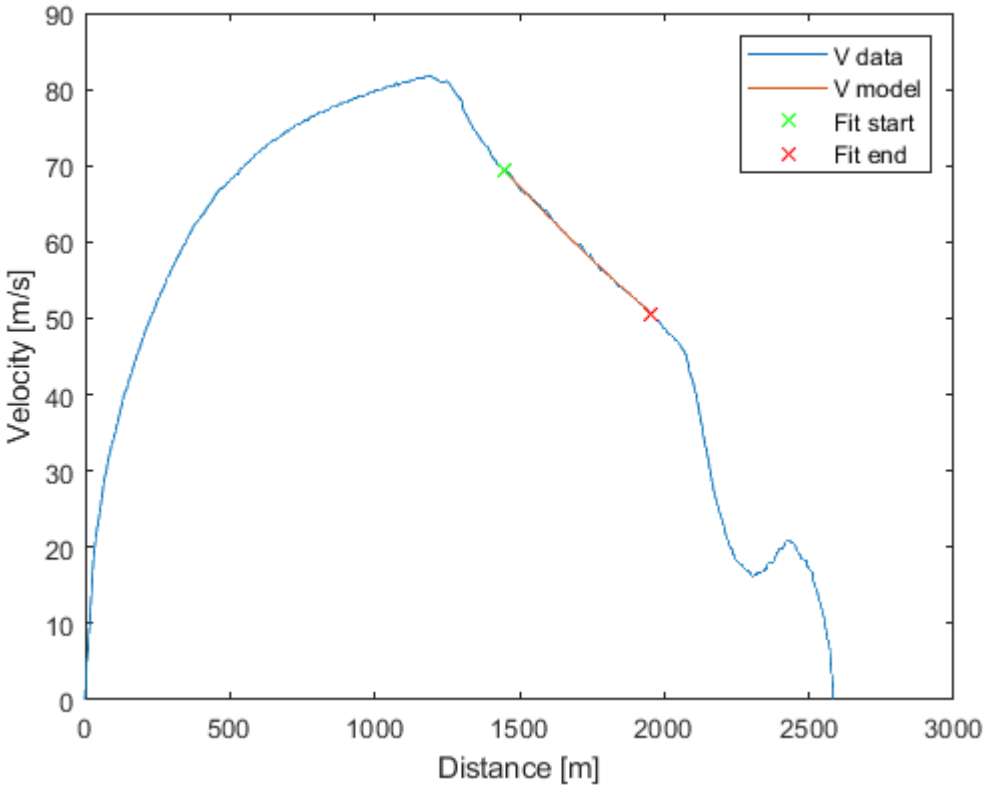

Figure 4.13 - Plot showing coast down test profile velocity and model fitted section.

To validate the vehicle performance envelope, it was first necessary to collate and condition the available data. This begins by combining separate race data streams

from the vehicle data logger and the powertrain data logger. It was planned to utilise a wheel speed measurement in the AIM logger to compare to motor rpm in the drive log, but the sensor was destroyed prior to the race. The combination thus involves aligning the start points of the lap in both streams and resampling the same frequency, using the respective timestamps for reference.

The AIM data logger contained an internal Inertial Measurement Unit (IMU) but this was placed in the tail of the motorcycle due to lack of available space closer to the centre of mass. To obtain the true acceleration at the vehicle centre of mass this displacement is accounted for as follows [128].

To obtain vehicle accelerations at the centre of mass, the raw acceleration data, as well as the roll, pitch and yaw angular rates and accelerations, are required. The angular rates are available from the vehicle IMU however the angular accelerations are not. As the raw acceleration data is significantly noisy it is first filtered using the inbuilt 'Savitzky-Golay' filtering algorithm in MATLAB [126] reducing noise as shown in Figure 4.14.

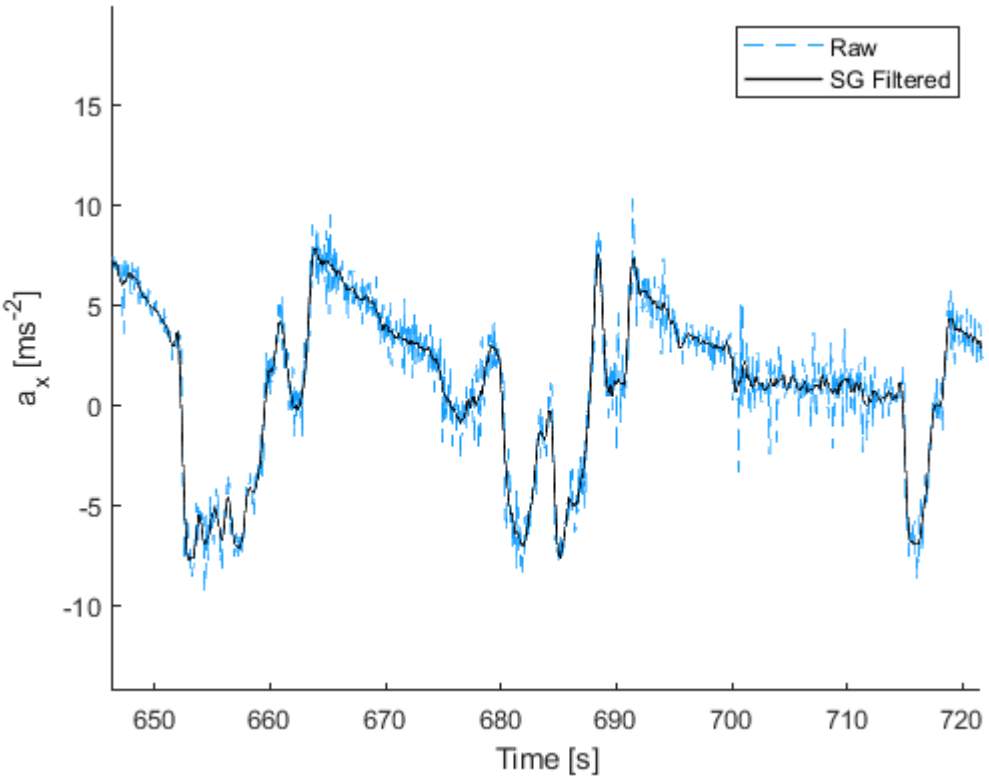

Figure 4.14 - Extract of filtered and raw data for longitudinal x-axis acceleration

The resulting smoothed data can then be differentiated to obtain the angular accelerations. Utilising the angular rates and accelerations the translational accelerations at the centre of mass can be determined with the following formula where the displacement $[x_{lg} \quad y_{lg} \quad z_{lg}]^T$ of the logger from the centre of gravity is given in the vehicle body axes. The angular velocities and accelerations are given in radians.

$$g\begin{bmatrix} a_x \\ a_y \\ a_z \end{bmatrix}_{cg} = g\begin{bmatrix} a_{lgx} \\ a_{lgy} \\ a_{lgz} \end{bmatrix} + \begin{bmatrix} (\dot{\theta}^2 + \dot{\psi}^2) & -(\dot{\phi}\dot{\theta} - \ddot{\psi}) & -(\dot{\phi}\dot{\psi} + \ddot{\theta}) \\ -(\dot{\phi}\dot{\theta} + \ddot{\psi}) & (\dot{\phi}^2 + \dot{\psi}^2) & -(\dot{\theta}\dot{\psi} - \ddot{\phi}) \\ -(\dot{\phi}\dot{\psi} - \ddot{\theta}) & -(\dot{\theta}\dot{\psi} + \ddot{\phi}) & (\dot{\phi}^2 + \dot{\theta}^2) \end{bmatrix}\begin{bmatrix} x_{lg} \\ y_{lg} \\ z_{lg} \end{bmatrix} \quad (4.45)$$

The data logger included GPS but no dedicated roll angle sensor. As the Inertial Measurement Unit (IMU) moves with the motorcycle axes it is important to determine the motorcycle roll angle. This can be approximated from the GPS yaw rate (in $rads^{-1}$) by the following equation.

$$\phi = atan\left(\frac{v\dot{\psi}}{g}\right) \quad (4.46)$$

An additional approximation can be obtained by an integration of the vehicle roll rate measured by the IMU. Both approaches have issues, the IMU roll rate integration has an issue with drift and the GPS signal is noisy and is only an approximation. To combat this a moving average filter is used to determine the drift correction required for the IMU roll rate integration from a comparison of both inputs. This roll angle is then used to transform the IMU 'z' and 'y' axis accelerations into the global axes required for comparison to the GGV plots as shown in Figure 4.15.

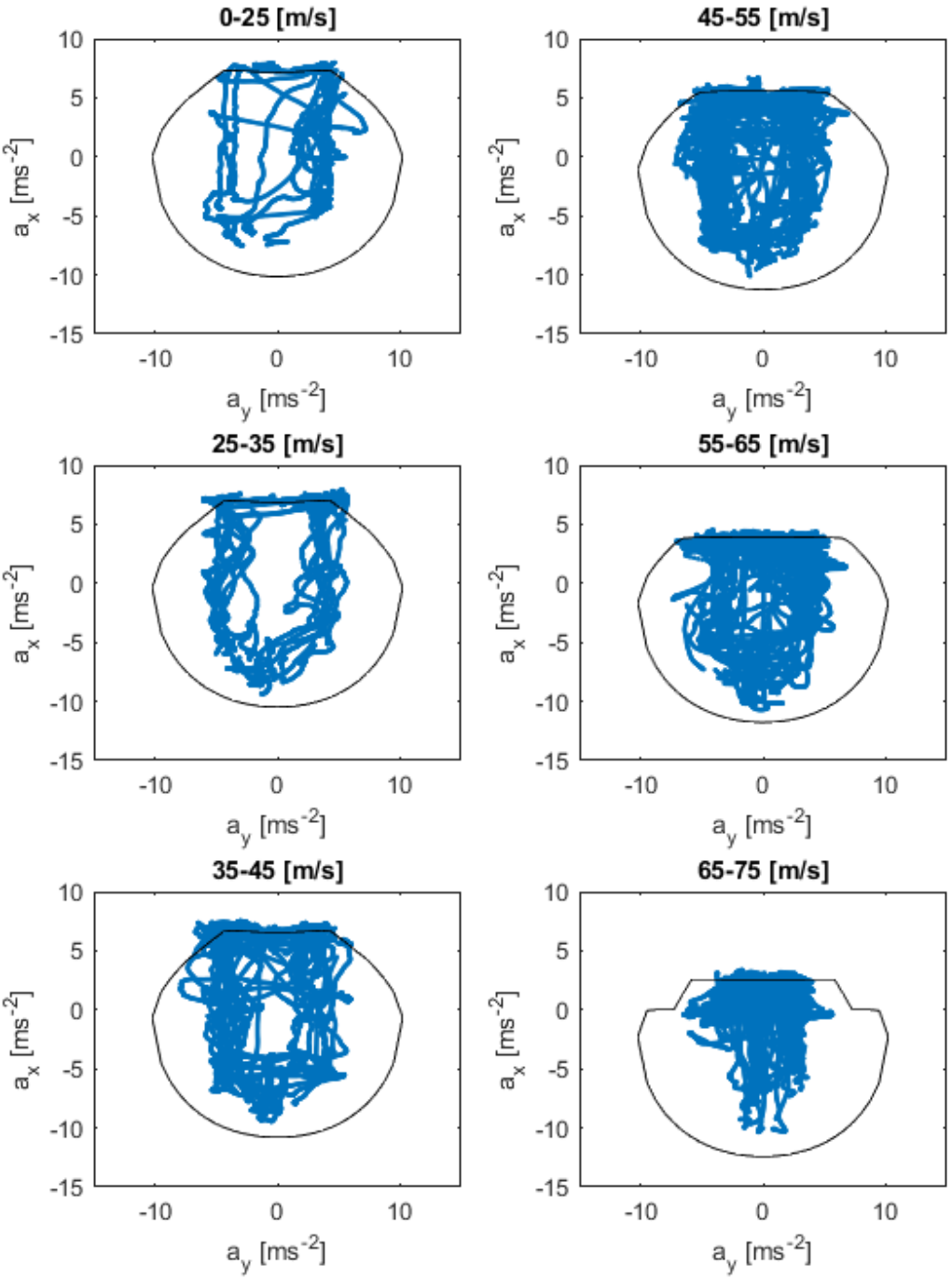

Figure 4.15 - Comparison of measured 2018 TT Zero Acceleration data (blue 'x') and simulated limit performance (black line) in 10m/s velocity bands as appropriate.

Despite a good match between simulation and data for the motorcycle longitudinal performance the lateral performance of the motorcycle struggles to match the simulated motorcycle limit. Several factors contribute to this discrepancy. Firstly, there is no lateral force load dependency in the tyre model. Additionally, the race is held on closed public roads instead of a dedicated track meaning that the road surface is not in optimum condition. Informal discussions with other racing teams have

revealed that a tyre friction coefficient in the region of 0.9 could be more reasonable in sharp comparison to the 1.3 in the dataset used here taken from De Vires and Pacejka [15] this is a significant reduction.

It is possible to scale the peak tyre response using scaling parameters as outlined by Pacejka [44]. This has been done here with peak longitudinal values scaled by the scaling factors $\lambda_{\mu xf} = \lambda_{\mu xr} = 0.8$ and the lateral values scaled by the scaling factors of $\lambda_{\mu yf} = \lambda_{\mu yr} = 0.9$. The selection of these factors was performed in conjunction with the alignment of predicted apex speeds seen later in Section 6.4.3.

Contributing factors to this reduction include the limited size and budget of the university race team. They often struggled to find the time and resources for proper testing. Inevitably this results in significantly compromised setup with tyres not operating at their optimum as well as reduced rider confidence. Rider confidence is paramount at a race with such high penalties for mistakes. For the race in question, the rider had only completed one practice lap of the course on the UoN machine before the race lap. When these additional factors are considered the deficit in lateral and braking performance is understandable.

4.5. Conclusion

In this chapter a new, simple, and effective, rigid body chassis model has been developed and partially validated with reference to experimental data. The model shows a good match to the experimental data and is a significant enhancement over the mechanical model described by Blissett [16] which does not include any tyre modelling, aerodynamics, or the effects of weight transfer.

The model described by Dal Bianco *et al.* [17] is that of a monowheel, and although appropriate for a low-performance motorcycle model with low levels of weight transfer, it is no longer appropriate for the modern high-performance machines capable of performing ‘wheelies’ and ‘stoppies’. In this chapter, the model developed responds to the effects of acceleration braking and aerodynamic load distribution and the effect due to the load sensitivity of the tyres. This is particularly important for determining the correct traction limits as well as the effect on regenerative braking levels.

The rigid body model developed in this chapter is a significant enhancement over the GG models described in [22, 49] due to the inclusion of the ability to handle different front and rear tyres, the inclusion of downforce and drag, and the introduction of a Pacejka tyre model. The inclusion of the tyre model allows for an accurate powertrain to road speed and load dependant response modelling. The addition of the other sensitivities and their influence on the resulting performance envelope is also demonstrated. The full vehicle response is then investigated showing a good correlation to experimental data collected at the 2018 TT Zero race.

The intention for this model is to be used as a part of a whole vehicle model. As such the goal is to capture the necessary level of detail without requiring excessive computational power. This goal has been met with notable improvements over existing available models.

Chapter 5, which follows, builds and validates the electrical powertrain model and combines it with the vehicle model developed here. The effect of tyre slip on full vehicle response is a particularly important improvement as will be demonstrated. This combined model is then used for lap simulation in Chapter 6 and finally energy deployment strategy and lap sensitivity studies in Chapter 7.

5. Powertrain Modelling

This thesis aims to develop a robust high-fidelity model of a modern high-performance superbike. The development of a mechanical system model is covered in Chapter 4. To investigate the full vehicle response an electric powertrain model is also required and is developed and validated in this chapter.

The model must be able to accurately predict the response for common contemporary electric powertrains throughout the entire range of useful operation. As the aim of this thesis is to simulate high-performance machines, it follows that it is also important to model, as far as practical, the non-linearities that arise at the limit of performance. This model is subsequently used in Chapters 6 and 7 to help identify the sensitivity of the full vehicle response to changes in individual components allowing for a more complete design and development process.

The powertrain consists of five major components, the battery, the motor, the motor drive, the transmission, and finally the wheel. A graphical representation of the different parts of the powertrain is shown in Figure 5.1. As energy is transferred from each component to the next and used by each component there are losses. The summation of these losses determines the total efficiency of the transfer from battery to tyre and vice versa.

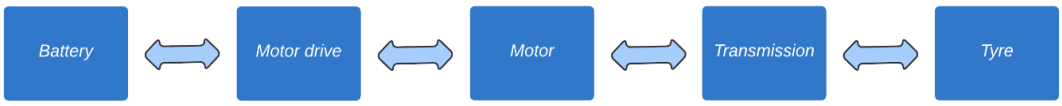

Figure 5.1 - Graphical representation of the key elements of the powertrain and the energy transfer pathway

This chapter begins in Section 5.1 by using the well-proven method of vector control of permanent magnet motors to determine the idealised motor torque for IPM and SPM motors. Section 5.2 details the motor loss modelling and saturation effects that push the motor away from these ideal operating conditions. These are dealt with through empirical methods and serve to reduce the motor output torque and increase the input power requirements.

Section 5.3 further expands the loss modelling to the motor drive switching and conduction losses and evaluates the contribution of more minor losses such as capacitor current ripple. These sections have some similarities to the model described by Blissett [16] however with some notable enhancements. It is expanded to cover a

wider range of motor types and now includes magnetic saturation and iron losses. By doing so it is possible to expand the scope of the model to include most contemporary powertrains and achieve a better understanding of the powertrain performance at the limit of the performance envelope.

Section 5.4 deals with additional losses arising from the chain transmission as used on most motorcycles and raises some issues with the published data. The cumulative effect of the motor and transmission losses is evaluated in Section 5.5 with a breakdown of the common methods of addressing these inefficiencies provided.

The final part of the powertrain, the battery, is dealt with in Section 5.6. In previous works [16, 17] the battery has been modelled as an ideal voltage supply with a series resistor. This is shown to be a poor approximation of the voltage response and instead is replaced by a model that includes a resistor-capacitor (RC) circuit to approximate the time dependant behaviour of the battery.

Battery temperature is a critical parameter that can significantly affect the system's performance. This has been omitted by Dal Bianco and Lot [17] and a simple approximation used by Blissett [16]. Temperature and state of charge variation of model parameters as well as entropic heating are included to improve accuracy, particularly around temperature prediction. This model is validated using battery testing data generated through laboratory cell testing with a DC load.

5.1. Motor Torque Output

There are a wide variety of motor designs and control techniques. Contemporary machines have focused on Permanent Magnet Synchronous Machine (PMSM) designs for reasons of efficiency and torque density. This is discussed in more detail by Finken *et al.* [57]. Of these designs, the Interior Permanent Magnet (IPM) and Surface Permanent Magnet (SPM) rotor designs are of interest here due to their power density.

The ability to include both of these is an advancement over prior electric motorcycle powertrain models which have been concerned with DC [17] and SPM [16] machines only. The torque output of an inverter fed Permanent Magnet Synchronous Machine (PMSM) throughout the operating regions of the motor is modelled as follows [62].

The use of a Permanent Magnet Synchronous Machine (PMSM) from a DC source (battery) requires the use of an inverter or motor drive to transform this DC source into a sinusoidal current suitable for driving the Synchronous Machine (SM). The current and voltage in the stator are controlled through switching devices by Pulse Width Modulation (PWM). The control of these switching devices is critical to the successful operation of the motor and drive. As the machine is operating at a variable speed with a variable torque requirement the amplitude and frequency of these sinusoidal currents require precise control to deliver the demand torque.

To deliver this control it is useful to obtain the current and voltage equations in a form that is time-independent, as the flux linkage, induced voltages and currents all change continuously as the electric motor rotates. This is achieved through the principle of current vector control, here the three sinusoidal phased stator currents are first transformed into two components in an orthogonal stationary frame by the use of the Clarke transform [129]. The Park transform is then used to transform these currents into equivalent DC currents in the rotor rotating reference frame. These current vectors are commonly referred to as the quadrature and direct axis currents (i_d and i_q). The 'direct' axis corresponds to the direction of the magnetic pole of the rotor, the quadrature axis is perpendicular to this. The voltage (V_d,V_q) and current (i_d, i_q) vectors in the 'd' and 'q' axes are shown in Figure 5.2 below.

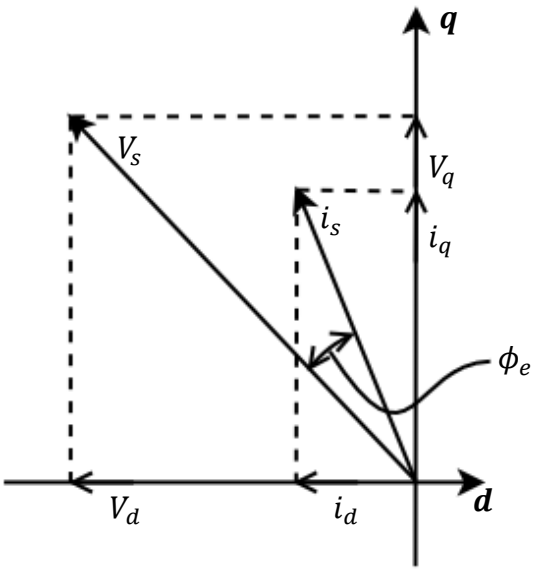

Figure 5.2 - Vector representation of PMSM voltage and current in the 'dq' frame

Obtaining the current vectors in this form eliminates the time-varying parameters and expresses the variables in orthogonal or decoupled axes [58]. This simplifies the construction of the motor control algorithm. Having determined the optimal current distribution in the 'dq' frame the inverse Park and Clarke transforms are then used to transform this demand back into the time-dependent demand used to drive the motor.

The equivalent circuit diagrams for the 'd' and 'q' axes are shown in Figure 5.3. Here stator winding resistance is given as 'R_s', d and q axis inductances (L_d, L_q), flux linkage (ψ_e) and the rotor electrical frequency $\omega_e = \omega p_e$, where 'p_e' is the number of pole pairs in the motor.

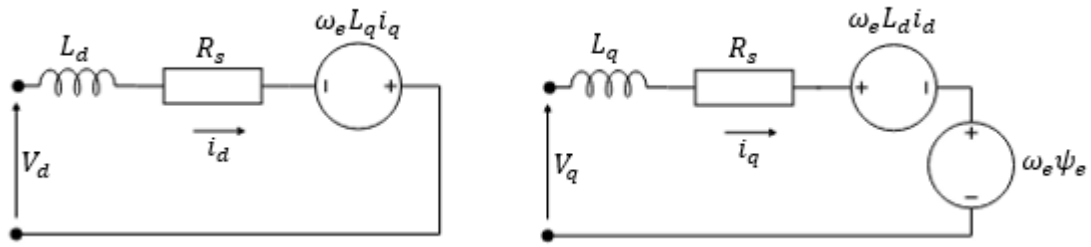

Figure 5.3 - Equivalent circuit diagram for 'd' and 'q' axes

A summary of the motor torque equations is included here. A fuller description of the equations are covered in detail in Appendix C – Description of Electric Motor Torque Equations. The motor voltages are given by the following equations.

$$V_q = R_s i_q + \omega_e (L_d i_d + \psi_e) \tag{5.1}$$

$$V_d = R_s i_d - \omega_e L_q i_q \tag{5.2}$$

$$V_s = \sqrt{V_q^2 + V_d^2} \tag{5.3}$$

The motor torque is given by the following equation [62].

$$T_{mot} = \frac{3}{2} p_e \left[\psi_e i_q + \left(, L_d - L_q\right) i_d i_q \right] \tag{5.4}$$

For an SPM motor $L_d = L_q$ and for an Induction machine $\psi_e = 0$. An IPM machine typically comes between the two and can have differing L_d and L_q by design. This can be used to tailor the machine characteristics. As the model developed here is concerned with both SPM and IPM designs the $i_q$and i_d current determination

involves both terms in all motor operation regions and is determined as per Appendix B – Nottingham Electric Motorcycle Parameters.

The optimal motor current vectors vary depending on the motor operation region and optimisation target. Here the use of MTPA control implies the optimisation of copper losses. Other strategies that include iron and inverter losses and optimise for full powertrain efficiency are available but not considered here for simplicity [62].

The voltage supplied to the motor drive is limited by both the source (batteries in this case) and the voltage rating of the switching devices (commonly IGBTs) therefore there is a limit to the voltage that the motor drive can apply. It is important to remember that as the motor rotates the permanent magnets in the rotor induce a voltage in the stator. As the motor speed increases there comes a point where the peak induced voltage from the rotor rotational speed matches that of the voltage source. This reduces the ability of the motor drive to control the stator current. To drive the motor past this point, the motor drive must reduce the induced voltage. It accomplishes this by suppressing the rotor magnetic field through the injection of d-axis current, commonly referred to as field weakening. In this region, the maximal motor torque is reduced but the motor speed increased allowing a wider band of operation.

In some IPMSM where the characteristic current is less than the rated current, as the motor speed increases further there comes a point where the optimal current vector no longer follows the MTPA line. This is called the Maximum Torque Per Volt region (MTPV). In this operation region the optimum current vector is below the maximum limit but increasing the current would only serve to increase losses and reduce the output torque. Here the stator current and voltage vectors are determined as per M. Fadel *et al.* [64]

The current vector distribution throughout the full operation envelope as well as the effect of MTPV control on a simplified GVM210-150-P6 motor model is evaluated in Figure 5.4 at a battery voltage of 650 VDC. MTPV has a positive but limited effect on output torque in the operation range of this motor at this voltage. An important point to note however, is the reduction in total phase current and therefore losses. This loss reduction is important to the system efficiency at high speed.

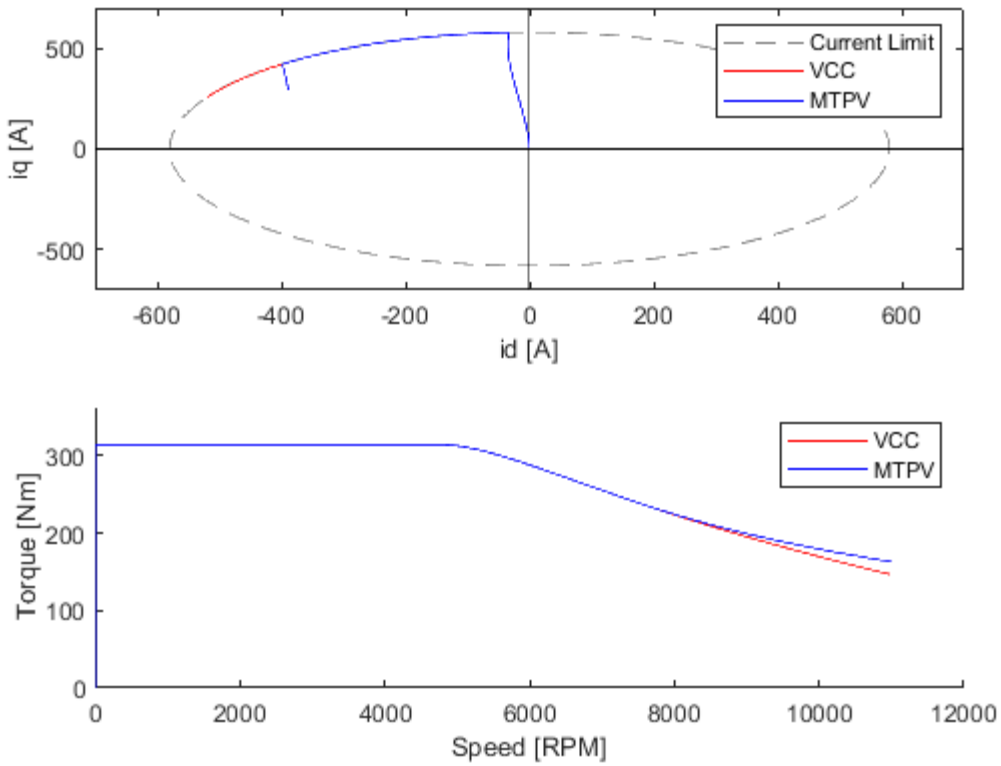

Figure 5.4 - Plots of motor torque and current vectors with and without MTPV control on simplified GVM 210 Model

The motor inductances L_q, L_d, also vary as a function of the motor currents. To simplify the model the change in inductance is modelled as a cubic polynomial function of i_s fitted to either supplied data or estimated using measured V_d and V_q response under load. In this case, motor data was supplied by the manufacturer who had generated it using Finite Element Modelling (FEM). The correlation between this data and the measured data was then improved by adjusting the initial parameters.

Motors commonly come with a variety of different winding configurations differentiated by the number of 'turns' per slot. This is a quick way for a manufacturer to vary the motor's response to different input requirements.

The UoN machine used 5 different winding configurations throughout multiple seasons. For reference the Parker GVM-210-150-P6 motor designation is broken down as follows: 210 refers to the stator diameter, 150 to the rotor active length and P6 the winding designation.

It is useful to include an approximation of this scaling into the model to allow for quick analysis of multiple winding configurations without requiring FEM data for each variation, see Figure 5.5 as an example. Note in one case the drive current limit

prevents the motor from reaching full torque (257 Nm) but that same motor has improved performance at higher rpm. Optimising the full powertrain for the application is important.

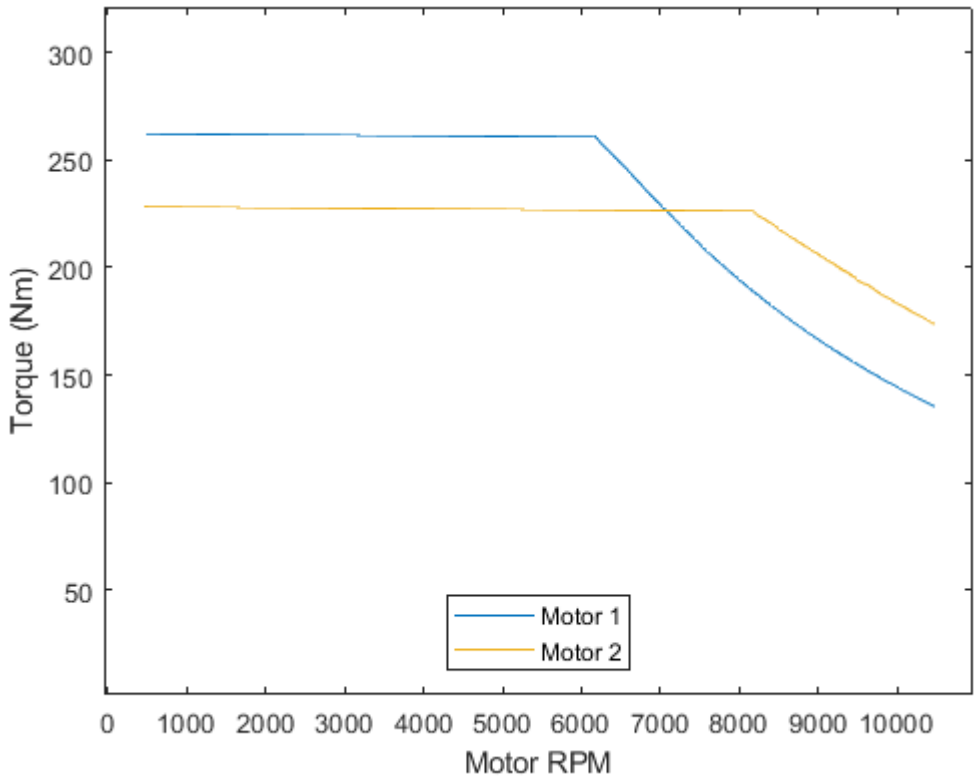

Figure 5.5 - Motor Torque Speed response for two different GVM210-150-P6 and R6 winding options

The motor inductances are simply scaled using the relationship that inductance $L \propto N_{turns}^2$ where N_{turns} is the number of turns in the coil [130]. The resulting scaled inductance variation with stator current for the UoN Parker GVM210-150-P6 winding, as used on the UoN machine, is shown in Figure 5.6. This scaling also applies to the motor flux ($\psi_e \propto N_{turns}$) and as well as maximum current ($i_{smax} \propto N_{turns}$) and stator resistance ($R_s \propto N_{turns}$) accordingly.

If possible, it is important to check the motor parameters post scaling. The zero current flux linkage is verified with reference to the PMSM voltage equations introduced earlier. It is determined from a portion of the V_q data where the motor is coasting to a stop from high speed, Figure 5.7.

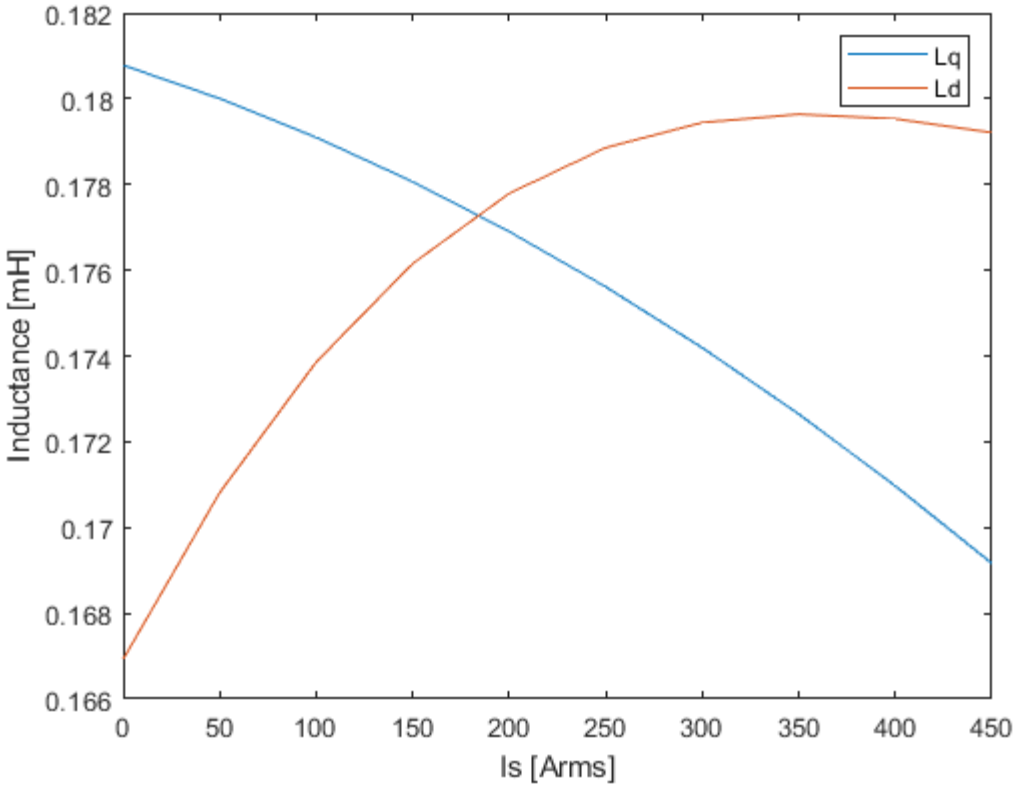

Figure 5.6 - Plot of 'Ld' and 'Lq' variation with 'i_s' scaled from Parker FEA data [130]

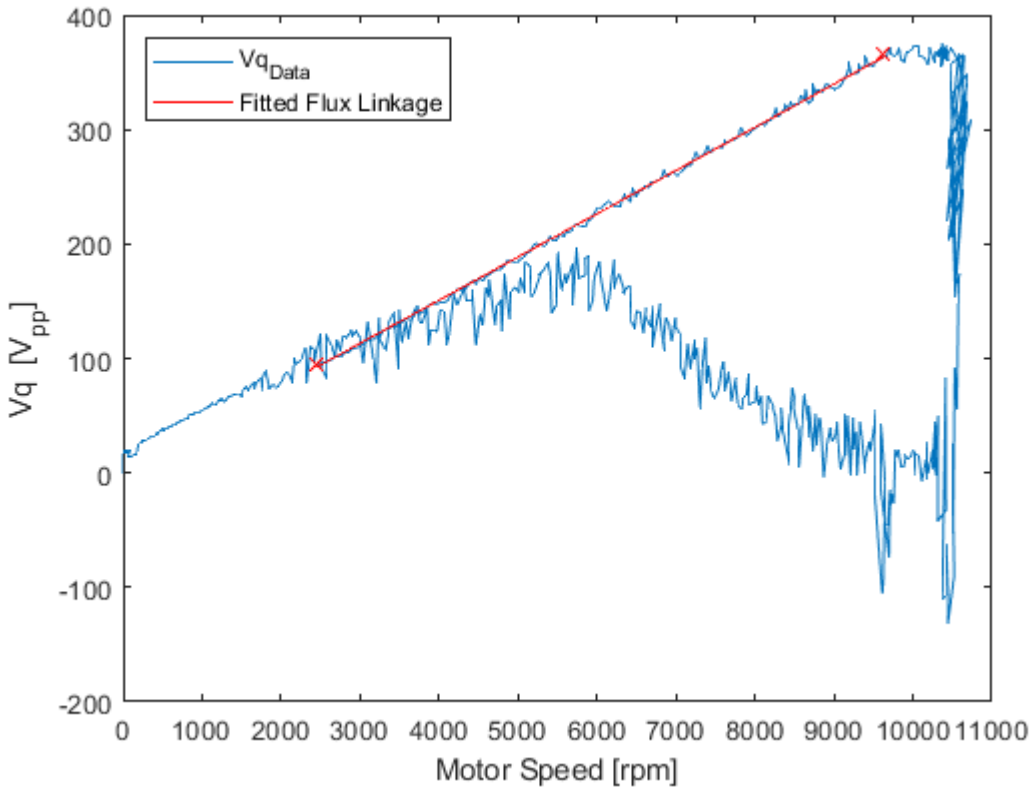

Figure 5.7 - Plot of measured 'Vq' during a dynamometer run and used to match machine parameters

The actual torque developed by the motor is lower than the ideal due to losses and magnetic saturation. The effect of magnetic saturation due to a change in magnetic permanence [131] serves to reduce the torque developed with increasing stator current. This effect can be modelled as a simple function of $\psi_e = f(i_s)$ fitted to FEM data or measured data as follows.

To quantify the motor saturation the existing motorcycle motor was mounted on a back-to-back motor dynamometer with a torque meter built into the coupling shaft. A picture of this setup is shown in Figure 5.8. The setup features two motors with an HBM T40B torque meter [132] integrated into the coupling between them. One motor is used as the load motor and one as the test motor. The shaft torque between the two is measured by the torque meter. This allows direct measurement of the motor torque.

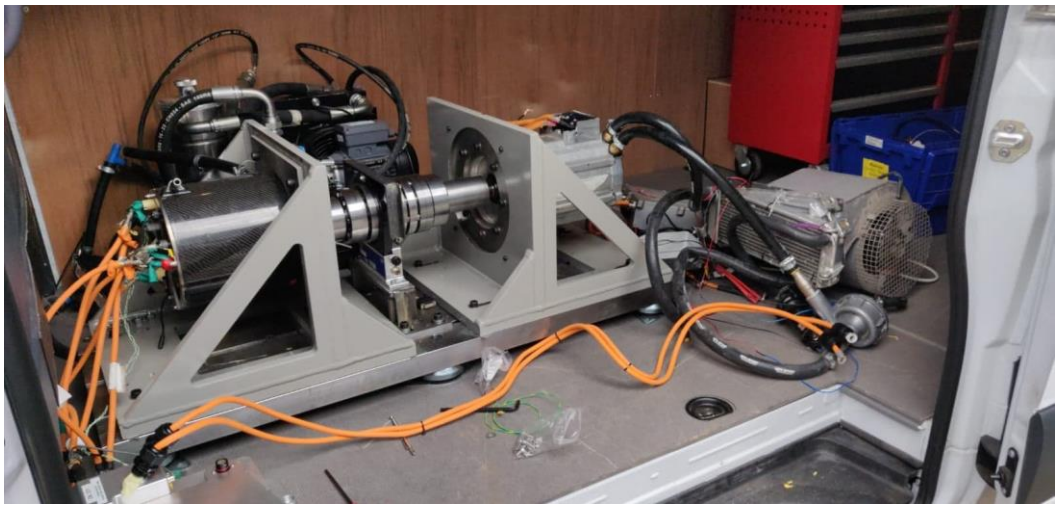

Figure 5.8 - Image of the back-to-back motor dynamometer with torque meter directly mounted

By utilising the torque equation at $i_d = 0$ the motor torque output is given as $T_{mot} = \frac{3}{2} p_e \psi_e i_q$. This corresponds to SPM motor configuration in the constant torque region $i_q = i_s$. The motor drive in this setup approximates i_s demand to a constant relationship with T_{mot}. The drive torque demand and actual torque delivered was recorded at several speeds. The motor was only tested at speeds below field weakening allowing the testing of the motor at $i_d = 0$. This is shown in Figure 5.9.

Using the simplified torque equation, Figure 5.10 shows the calculated flux linkage variation with i_q. A second-order polynomial is fitted to this data as shown. This polynomial is used to describe the flux variation within the motor model for this motor.

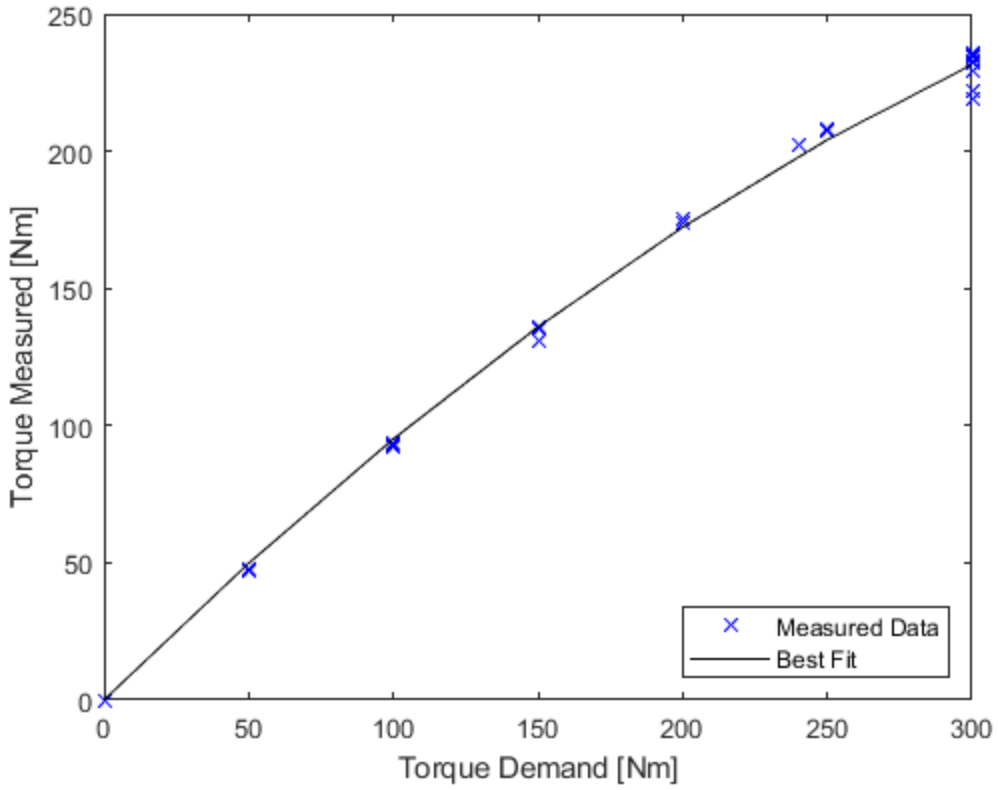

Figure 5.9 - Plot of the 'geometric mode' demand torque vs measured torque by a torque meter

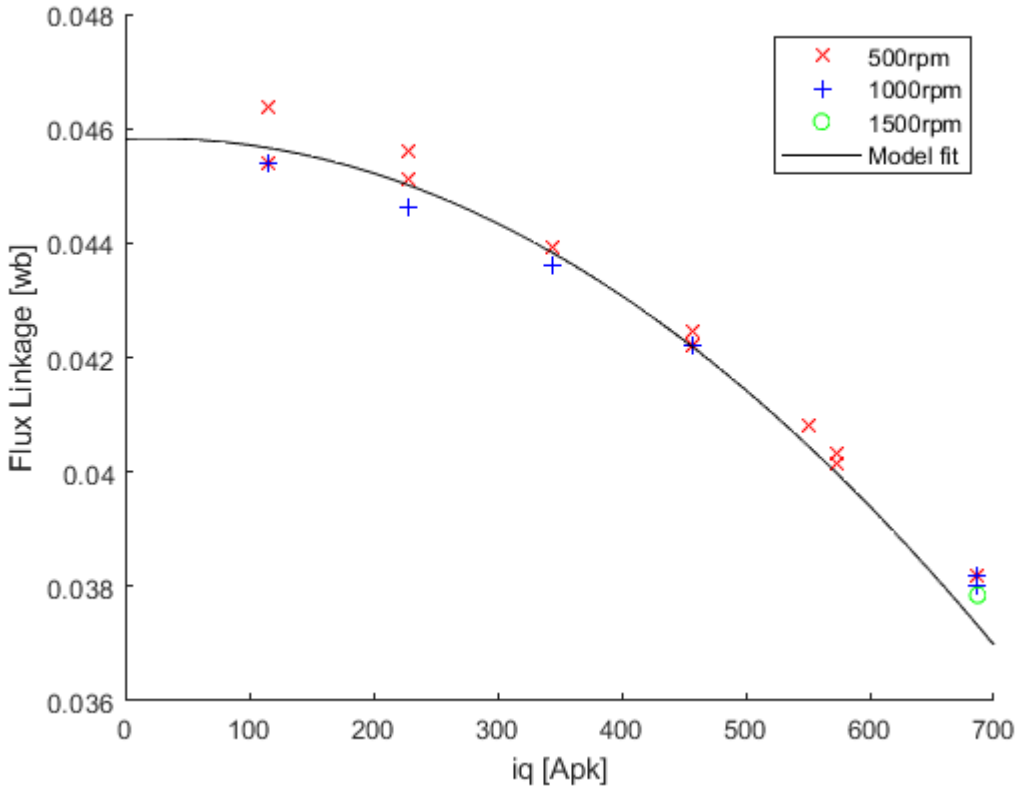

Figure 5.10 - Effect of calculated 'iq' on flux linkage from simplified torque equation

5.2. Motor Losses

To properly model the input and output power from the motor it is important to include significant losses into the powertrain model. These are required to ensure accurate modelling of the state of charge as well as being useful for determining the cooling requirements of the powertrain.

The motor losses can be divided into two categories. These are mechanical losses such as windage and bearing losses and electrical losses such as core and resistive losses. The losses vary with the torque and speed output of the motor.

The mechanical losses are incorporated as a reduction in output torque and the electrical losses as an additional input power requirement. The rotor iron and magnet losses are neglected as these losses are expected to be small for the motor designs under consideration [58].

5.2.1. Mechanical Motor Losses

The modelled mechanical losses are due to the resistance to motion and are included as a reduction in motor output torque. There are three main mechanical loss mechanisms in a motor: windage, bearing rolling resistance, and seal drag. The combination of losses is dependent on the torque and speed of the motor.

Windage loss is the power absorbed by the medium surrounding the rotor due to the relative motion between the rotor and stator. The power loss of a smooth rotating cylinder inside a stationary motor housing is given by Vrancik [133]. This loss is converted to a torque loss and given below:

$$T_{l,wind} = \pi C_{frotor} \rho r_{rotor}^4 \omega^2 l_{rotor} \tag{5.5}$$

Where C_{frotor} is the skin friction coefficient.

$$\frac{1}{\sqrt{C_{frotor}}} = 2.04 + 1.768\, ln\left(Re\sqrt{C_{frotor}}\right) \tag{5.6}$$

Here 'ρ' is density, 'r_{rotor}' is rotor radius, 'l_{rotor}' is rotor length, 'ω' the rotational speed and 'Re' the Reynolds number.

Seal losses '$T_{l,seal}$' arise from frictional losses where the seal contacts the rotor shaft. Seals are commonly used to seal the rotor airgap and bearing internals from

contaminants. The resultant torque loss is a constant dependent on the seal design and interface diameter [134].

The torque loss due to the frictional moment of the rotor bearings, independent of the final drive, can be determined using the principle relationships outlined in the SKF frictional moment model [134]. Here the bearing torque loss '$T_{l,br}$' has four contributing factors:

$$T_{l,br} = T_{l,rr} + T_{l,sl} + T_{l,brseal} + T_{l,drag} \tag{5.7}$$

These factors are '$T_{l,rr}$' – torque loss due to bearing rolling resistance; '$T_{l,sl}$' – torque loss due to sliding friction; '$T_{l,brseal}$' – torque loss due to bearing seals; and '$T_{l,drag}$' – torque loss due to bearing drag in an oil bath. The behaviour of the losses with respect to shaft speed is all that is required here. The following relationships are therefore employed, $T_{l,drag} \propto \omega^2$, $T_{l,rr} \propto \omega^{0.6}$, $T_{l,sl}$ and $T_{l,brseal}$ are constant.

As the chain drive is mounted directly to the motor output shaft in the UoN motorcycle the ability to model the additional bearing losses due to chain tension is required. The increased loss is approximated simply as a static friction increase due to the normal load with a μ_{frict} value of 0.0012 [135]. This was compared with the value generated by the SKF bearing analysis tool and found to be in good agreement except at low rpm due to the increased starting torque [134]. As the motorcycle spends very little time at low rpm and the difference is of the order of 0.5 Nm at full load this can be ignored for simplicity.

The resulting torque loss due to chain tension $T_{l,ch}$ is, therefore, a function of the motor torque T_{mot}, bearing inner diameter D_{IDb} and the radius of the motor output sprocket R_{msproc}.

$$T_{l,ch} = \frac{\mu_{frict}\, T_{mot} D_{IDb}}{R_{msproc}} \tag{5.8}$$

The total torque loss due to the resistance to motion of the rotor is therefore given as follows:

$$T_{l,rot} = T_{l,wind} + T_{l,br} + T_{l,seal} + T_{l,ch} \tag{5.9}$$

This can be further simplified by combining the respective coefficients as appropriate to:

$$T_{l,rot} = k_1\omega^2 + k_2\omega^{0.6} + k_3 + \frac{\mu_{frict}T_{mot}D_{IDb}}{R_{msproc}} \quad (5.10)$$

An example plot of the resulting mechanical loss model for the Parker GVM 210–150 in the UoN superbike with and without the increased loss due to chain tension is shown in Figure 5.11.

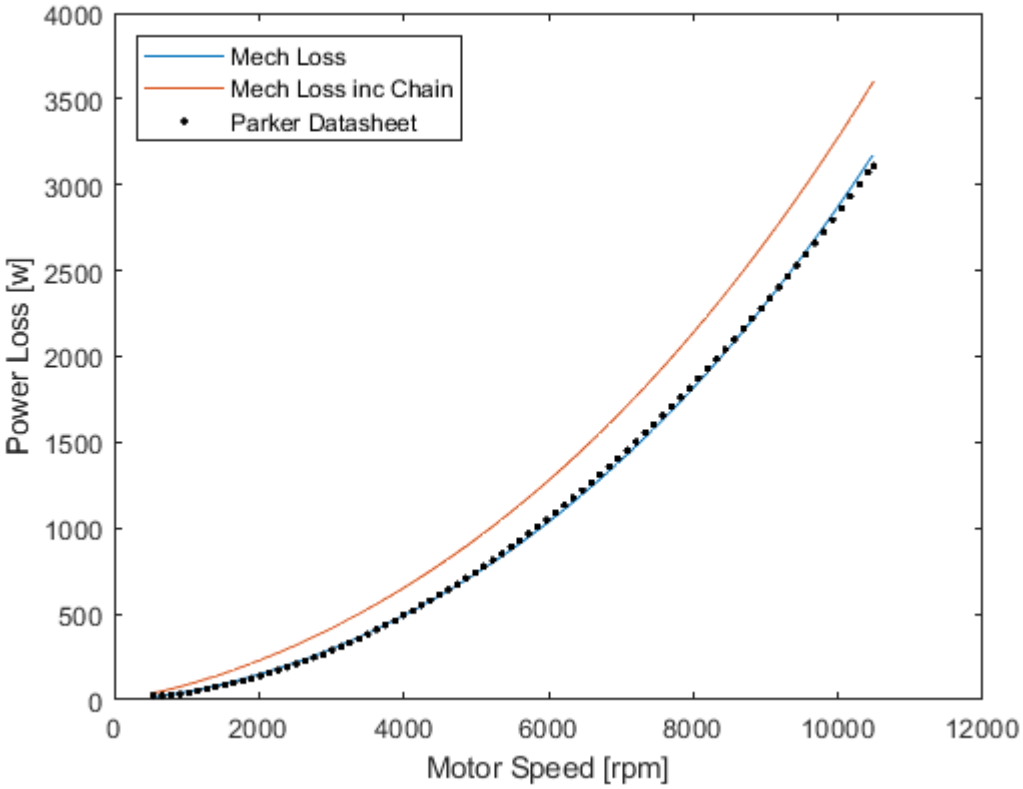

Figure 5.11 - Mechanical loss model for Parker GVM210-150P6 with directly mounted chain drive

5.2.2. Motor Winding Losses

Winding losses and core losses generally form the bulk of the motor losses [65]. The winding losses are the losses generated within the motor windings. A component of these losses relates to the resistive heating losses from the bulk current flow. This is frequency independent. Within an electric motor there are also frequency-dependent components to the current flow. These arise primarily from the generation of eddy currents within the conductors. The main contributions here are the skin and proximity effects.

The skin effect is where the current distribution within a wire is non-uniform. The current flows primarily in a band stretching from the outer surface to a depth known as the skin depth. The skin depth relates to the frequency of the current with higher frequencies causing shallower depths. The non-uniform distribution increases losses by effectively limiting the conductor cross-sectional area. This can be mitigated by choosing a conductor where the diameter is smaller than the skin depth [65].

Proximity losses are caused by the field generated in one conductor inducing eddy currents in surrounding conductors, causing additional losses. This can be partially mitigated by optimisation of the size, number of and distribution of conductors [136].

A common solution to the problem of large high-frequency losses is the use of 'Litz' wire, which makes use of multiple conductors in parallel insulated from each other to reduce the skin effect and twisted in such a way as ensure even current distribution between conductors [137]. However, this still serves to reduce copper fill of the stator slot due to increased insulation increasing DC losses. 'Litz' wire is also expensive [65].

This thesis is not a motor design thesis and therefore it is not appropriate to implement complex subroutines to analytically model the various individual components of the frequency dependant losses. The goal is to understand the magnitude and behaviour of the losses within the separate components as a tool for focusing development. As the DC resistance value was the only value provided for the motor in question this value was used here but further work should include the effect of high-frequency losses as described above.

The winding resistance varies with temperature. This variation can be captured through the following standard formula. Here '$T_{stat,ref}$' is the reference temperature, 'R_{s0}' is the resistance measured the reference temperature, 'α_{rs}' a coefficient that describes the change in resistance with the change in temperature and 'T_{stat}' is the stator temperature.

$$R_s = R_{s0}\left(1 + \alpha_{rs}\left(T_{stat} - T_{stat,ref}\right)\right) \tag{5.11}$$

The final expression for the power lost due to winding losses '$P_{l,rs}$' is shown below. This thesis uses the peak values by convention and the loss relates to the RMS value for 'i_s', hence the division by two in the power loss formula.

$$P_{l,rs} = \frac{3R_s i_s^2}{2} \tag{5.12}$$

5.2.3. Stator Core Losses

Core losses are primarily due to two causes, hysteresis and eddy-currents. Hysteresis losses '$P_{l,hyst}$' result from the steel 'resisting' changing its magnetic state. The energy loss per cycle can be described by the area enclosed on a B/H diagram where the steel undergoes a full cycle, the power loss is therefore proportional to the frequency of cycling. The hysteresis losses are given by the following, where 'B' is the magnetic flux density and 'β' is the Steinmetz constant.

$$P_{l,hyst} = K_{hyst} B^{\beta} \omega_e \tag{5.13}$$

Eddy-current losses are caused by variations in flux density which itself is a function of the frequency and peak flux density. The power loss due to eddy currents '$P_{\mathrm{l,eddy}}$' is, therefore, a function of the frequency squared [66] and is given below.

$$P_{l,eddy} = K_{eddy} B^2 \omega_e^2 \tag{5.14}$$

The power loss due to core losses can be approximated by the following formula[67]:

$$P_{l,iron} = P_{l,hyst} + P_{l,eddy} = K_{hyst} B^{\beta} \omega_e + K_{eddy} B^2 \omega_e^2 \tag{5.15}$$

5.2.4. Motor Model Correlation

The iron losses are omitted in the Parker motor datasheet but are expected to be significant due to the motor frequency and lamination thickness used. The manufacturer did not provide data on its material properties so the lamination thickness of 0.35mm was measured and data [138] for a common grade, M235-35A, was used to approximate the losses.

The mass of a stator was measured as 19.6kg. This includes the casing, potting compound and copper wire. Without knowing the specific design of the core the iron mass was estimated as 10kg.

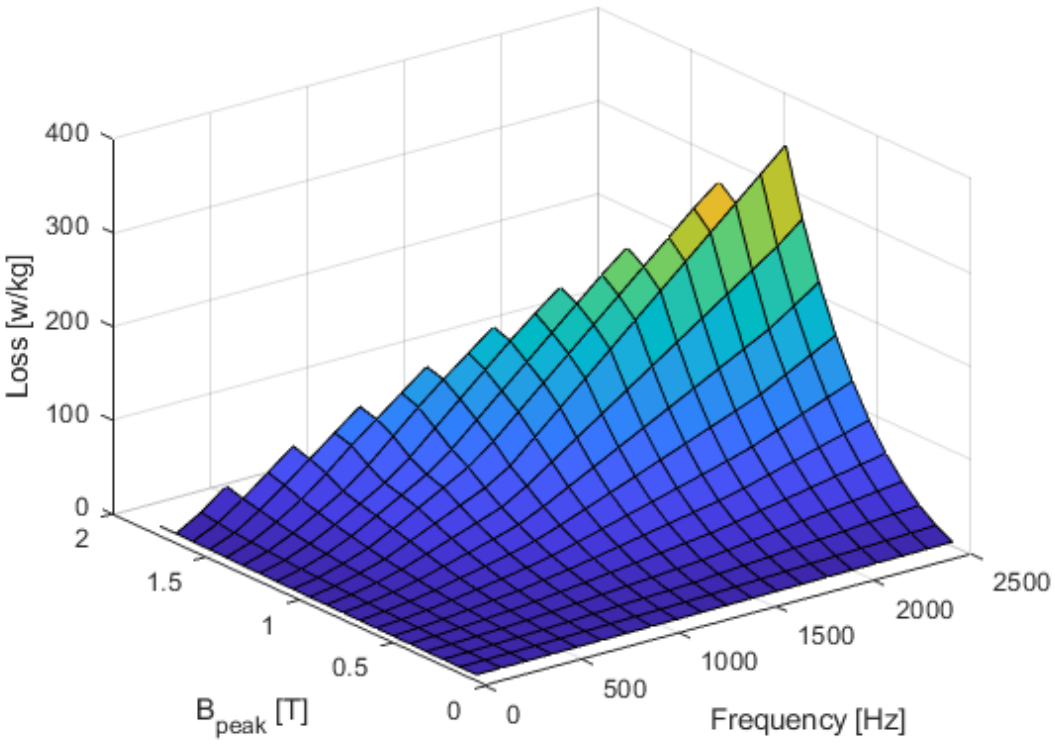

Figure 5.12 - Plot of M235-35A iron losses with respect to flux linkage and frequency [138]

It is extremely difficult to model iron losses from datasheet values without the use of FEM. Even then, Iron loss deviations between the manufacturers' Epstein frame results and the final assembled stator core measurements can deviate by more than 50% [139]. This is in part due to residual stresses and alterations in heat treatments due to the manufacturing processes used. An additional loss contribution as a result of higher frequency harmonics from the drive switching frequency can increase losses by up to 18% and 30% for SiFe and NiFe stator cores [139]. A combination of these additional losses can lead to total loss deviations up to twice the datasheet values.

For this thesis, a baseline performance is measured, and a reference material is used to give a representation of the performance throughout the operating range. This material specification can then be exchanged for another material and a relative performance benefit approximated. As this is not a motor design thesis this assumption is appropriate for the work in hand. However, further work to fully integrate this iron loss determination with FEM would be a worthwhile enhancement.

To determine the motor losses at no-load, data captured during a spin down test of the GVM210-150-P6 motor by Blissett [16] was used. By measuring motor losses this way, it is possible to isolate the moving losses from the copper losses as there is no current flowing in the motor. Here the motor is accelerated to a high speed and

allowed to coast down to zero. As there is no power input to the system the change in rotor speed depends on the rotor inertia and losses. As the rotor inertia is known it is possible to determine the power losses. Having performed this test Blissett [16] notes that the manufacturer's published data is a poor approximation of the measured results and that it is likely that a loss component is missing. Through refitting the data using the bearing and seal friction model developed earlier and including the iron loss model it is possible to improve this fit. The measured no-load losses, modelled no-load losses, and manufacturer's datasheet values are compared in Figure 5.13.

As the flux density will vary with i_s the variation was modelled as a linear progression with a peak B=1.8 T (the maximum datasheet value) at the motor rated stall current and a no-load value of B =1.4 T (chosen to best approximate the loss magnitude seen in the spin-down data). Motor operation near the maximum datasheet value is confirmed by the saturation evident in the torque vs current test shown in Figure 5.10.

Iron losses are interpolated from the M235-35A data sheet with a scaling factor of 1.5 applied to account for the manufacturing and drive switching frequency losses as outlined in [139]. To simplify and speed up the simulation the core loss approximation formula was implemented. Here the hysteresis and eddy current coefficients are fitted to the material data at 1.4 T. There are several assumptions here beginning with the stator core mass assumption, the additional loss scaling factor and the no-load flux density. These have been taken with reference to literature and measured as far as possible, however, an improvement here would be to use FEM or direct measurement of the stator core, but this is outside the scope of this thesis. It is important to point out the goal is to approximate the underlying physics and ensure a good representation of the loss mechanisms at play. The intention is not to develop a motor design thesis but to better understand the impact of design changes from a whole vehicle standpoint and develop a useful tool capable of respecting the impact of these design changes.

A comparison of datasheet values to the modelled values is shown in Figure 5.14. There is a difference between the datasheet and model values with the datasheet values representing a better approximation of reality. This discrepancy is due to the simplicity of the core loss approximation formula. However, both models will have

discrepancies when compared to the real core due to manufacturing processes and geometric considerations. As the goal here is to capture the relative magnitude of design changes, the simplified model is deemed appropriate. It captures the underlying trend without consuming significant computational resources.

To verify the full powertrain model performance the motorcycle was run on a rolling road dynamometer. This provides a measured reference point that includes all aspects of the motorcycle powertrain including the transmission and tyre response as well as the motor, drive, and battery. The model should match this well to ensure the longitudinal acceleration computed by the model will match reality. Testing was performed at SPR Racing using a Dynojet 250i rolling road dynamometer. The outputs from the dynamometer are a power speed plot. The motor drive parameters are logged separately using the onboard data logger and used in conjunction with the dynamometer output. The resulting torque speed plot is shown in Figure 5.15. It is worth noting that the power speed response differs at low speed due to the need to limit the wheel power at the beginning of the run and avoid wheel spin against the dyno roller at low speed.

The field weakening response is very similar to the measured response with minor discrepancies at higher speeds due to differences between the ideal field weakening used in the simulation and the multitude of de-rate parameters used in the commercial drive. The data shows i_s dropping at high rpm in the drive. This is possibly due to a pre-programmed thermal de-rate within the proprietary drive software or an incorrect motor drive setup. Figure 5.16 shows good agreement between the wheel output power model and dynamometer measurements.

The UoN motorcycle currently uses an IPM machine that has similar L_d and L_q values. The model described in Blissett [16] uses SPM motor current control for simplicity and Blisset believed it to be sufficient as L_d and L_q are similar for this motor. Closer investigation, shown in Figure 5.17, reveals that proper IPM control has a noticeable impact on motor torque production and the inclusion of improved motor control algorithms is a worthwhile enhancement. While the difference between L_d and L_q is negligible at 200 A*rms* (Figure 5.6) the saturation at high current alters the ratio of L_d and L_q noticeably leading to the differences in torque generation shown in Figure 5.17.

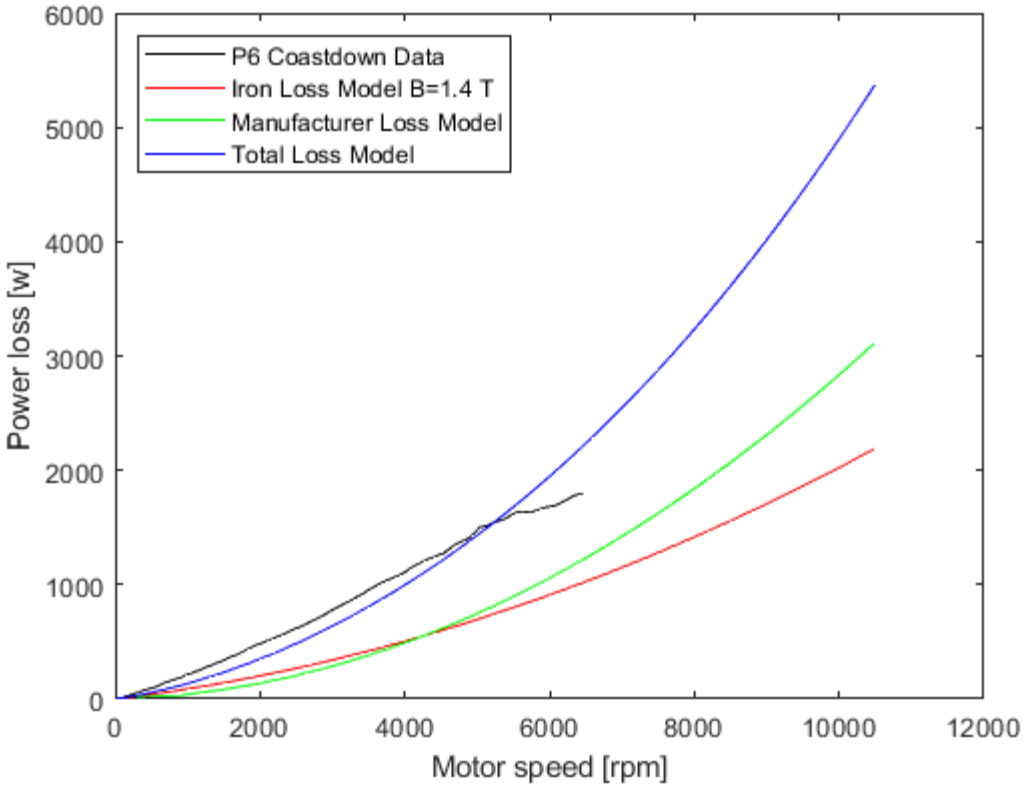

Figure 5.13- No-load motor losses, comparison of measured and modelled losses

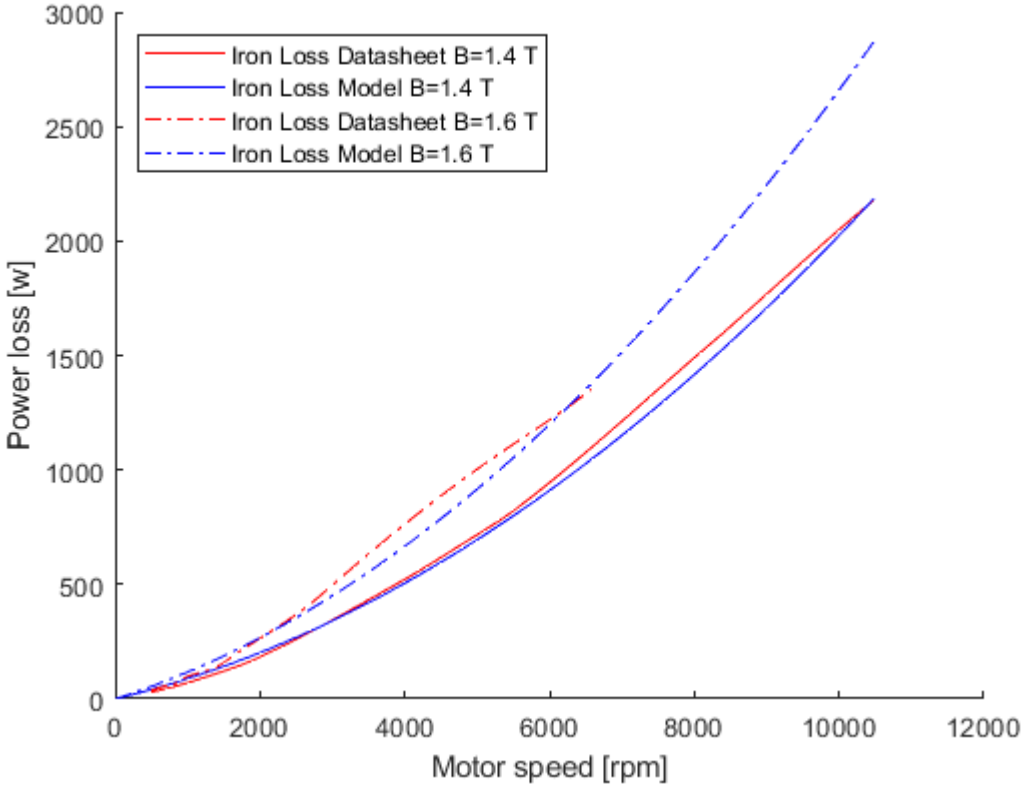

Figure 5.14 - Plot of Iron datasheet loss values and model approximation

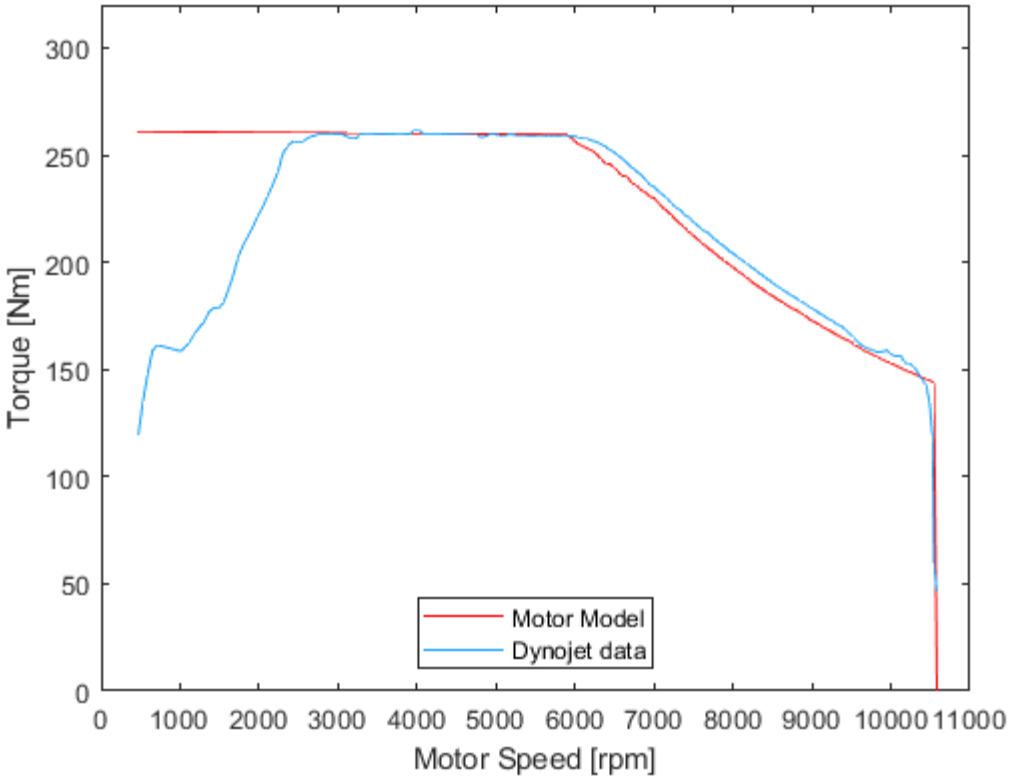

Figure 5.15 - Motor torque for the Parker GVM210-150P6 as modelled compared to measured data.

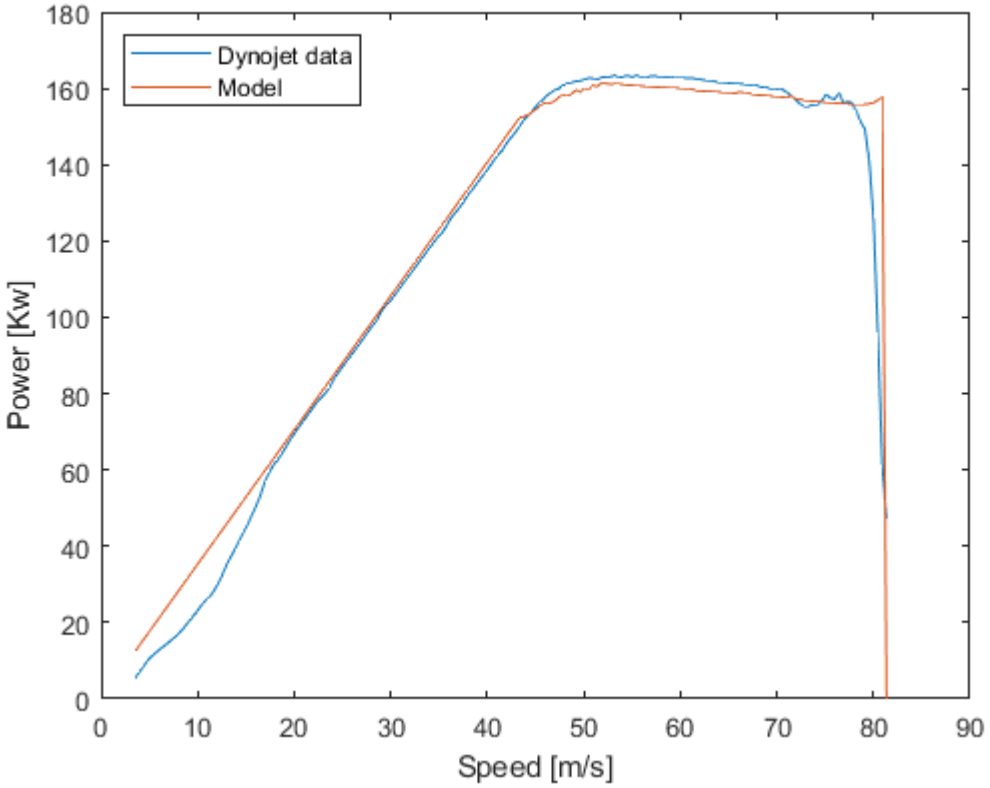

Figure 5.16 – Wheel output power for the motorcycle on the rolling road dynamometer and as modelled.

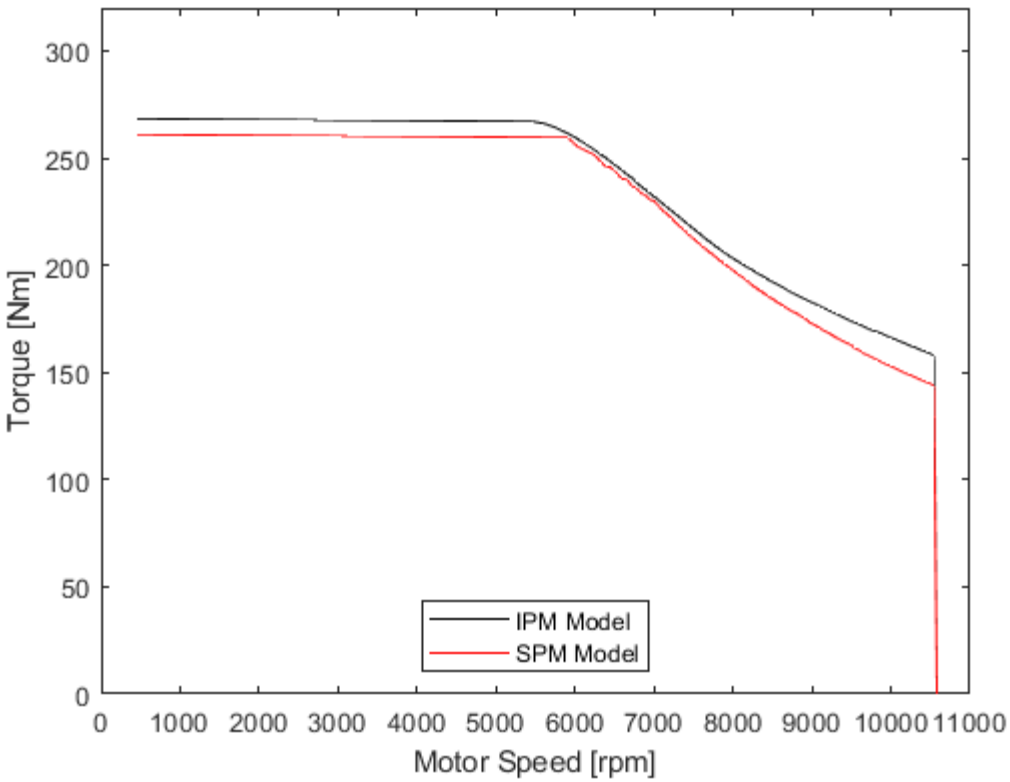

Figure 5.17 - Simulated motor plot showing performance increase from the use of IPM control.

5.3. Motor Drive

The effect of motor drive losses on the full system efficiency is important from both the thermal analysis standpoint and for the full vehicle efficiency. Further powertrain losses such as the IGBT switching losses and DC link capacitor losses are evaluated as follows.

There is a large body of research into the differing number of phases and topologies offering a varying array of small advantages and disadvantages, but these are generally complex, difficult to obtain, and outside the scope of this thesis.

The most common motor drive employed is a 3-phase inverter consisting of six IGBTs and antiparallel diodes. The drive is constructed as shown in Figure 5.18. This is consistent with most motor drives available on the market and the drives used by the Nottingham team and competitors. One notable difference is that the drive in the UoN machine has two IGBTs in parallel to satisfy the phase current requirement.

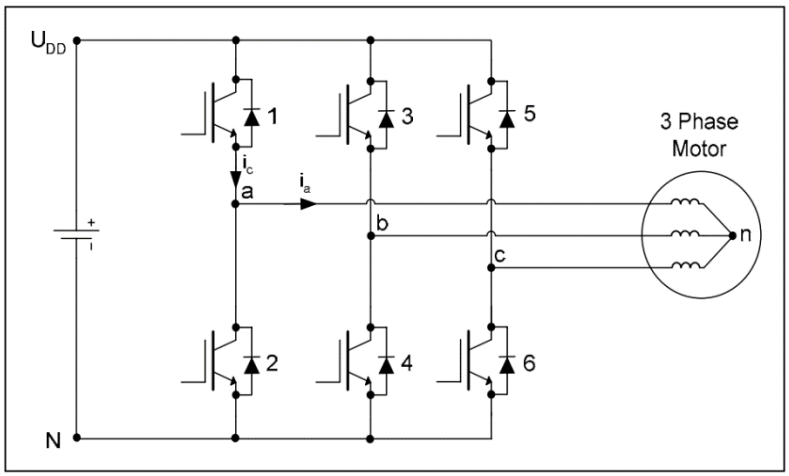

Figure 5.18 - 3 Phase motor drive connection schematic from Graovac

5.3.1. Switching Device Losses

IGBT and Diode power losses are commonly divided into three components: conduction losses; switching losses; and blocking (leakage) losses. Blocking losses and diode switch-off losses are commonly small and neglected [68]. The phase voltages and currents are determined for a single IGBT at the motor operating point, assuming the system is balanced between phases. The losses are then easily scaled to account for the entire drive. The method for modelling the IGBT losses is the same as that described by Graovac [68]. An overview is provided in Appendix D – IGBT Loss Calculations.

The method is simply the summation of the individual loss components '$P_{l,sw}$' - switching loss, '$P_{l,CD}$' – diode conduction losses and '$P_{l,CT}$' – IGBT conduction loss. Of these loss components, the switching energy is a function of the change in current and voltage of the device as it switches. This can be roughly approximated to a linear relationship within the normal operating region of the drive. This relationship can be seen in [140].

$$P_{l,sw} = \frac{\left(E_{on}I_{on} + E_{off}I_{off} + E_{Don}I_D\right)f_{sw}V_{batt}}{I_{ref}V_{ref}} \qquad (5.16)$$

Here the remaining terms are as follows: 'E_{on}' – IGBT switch-on energy; 'E_{off}' – IGBT switch-off energy; 'E_{Don}' – Diode switch-on energy; 'I_D' – is the equivalent direct current in the diode; 'I_{on}' – is the equivalent direct current in the IGBT minus half the current ripple magnitude; 'I_{off}' – is the equivalent direct current in the IGBT

plus half the current ripple magnitude; and 'V_{ref}' and 'I_{ref}' are the datasheet reference values.

The total power loss in the switching devices and diodes is given by the equation:

$$P_{l,drive} = 6\left(P_{l,sw} + P_{l,CD} + P_{l,CT}\right) \times N_{parallel} \quad (5.17)$$

$N_{parallel}$ is the number of IGBTs in parallel. This is particularly relevant as the Sevcon G4S10 in the UoN motorcycle uses two Infineon FS450R12 power modules [140] in parallel per phase. The resulting drive is simply modelled as two drives operating separately at half the total current each. This method scales for a higher number of devices in parallel. The power loss is included in the powertrain losses as a motor input power loss.

Silicon carbide devices are becoming increasingly popular in motor drives due to the potential efficiency gain resulting from the reduction in switching energies. As these switching energy losses are very low it is also possible to increase the switching frequency with resulting efficiency benefits through finer motor control, without the penalty of significantly increased switching losses associated with IGBTs.

The evaluation of Silicon Carbide MOSFET switching devices is also possible using a modified version of this method outlined by Graovac [70]. Comparison between the methods reveals the only change required being the setting of the 'u_{CE0}' term - IGBT on-state zero-current collector-emitter voltage, to zero. This is understandable as the main loss mechanism for Silicon Carbide MOSFETs is resistive and is captured by the remaining terms. See Appendix D – IGBT Loss Calculations for more details.

5.3.2. DC-Link Capacitor Loss

Another significant component in a motor drive is the DC link capacitor. This does not usually require active cooling and it is expected that its losses are comparatively small. A quick approximation of the capacitor losses is used here to determine if they are significant in terms of overall powertrain losses. Capacitor losses can be loosely approximated to the losses derived from the product of the square of the RMS ripple current in the DC-link and the equivalent series resistance of the capacitor (ESR).

As an example, the ESR (Equivalent Series Resistance) of the capacitor taken from the Infineon hybrid kit [141] was chosen. This drive is similar to that used in the UoN motorcycle, but its capacitor data is freely available. This capacitor has an ESR of

approximately 0.7 mΩ [142, 143]. To determine the capacitor ripple current ($I_{C,rms}$) the following formula can be used [144]. Here the modulation index is $Mod = V_s/0.5V_{batt}$, the RMS phase current $I_{N,rms} = i_s/\sqrt{2}$ and the angle 'ϕ_e' is the angle between the voltage and current vectors in the 'dq' frame as shown in Figure 5.2.

$$I_{C,rms} = I_{N,rms}\sqrt{2Mod\left(\frac{\sqrt{3}}{4\pi} + \cos^2\phi_e\left(\frac{\sqrt{3}}{\pi} - \frac{9}{16}Mod\right)\right)} \qquad (5.18)$$

A plot of the normalised ripple current with respect to modulation index and vector separation angle is shown in Figure 5.19.

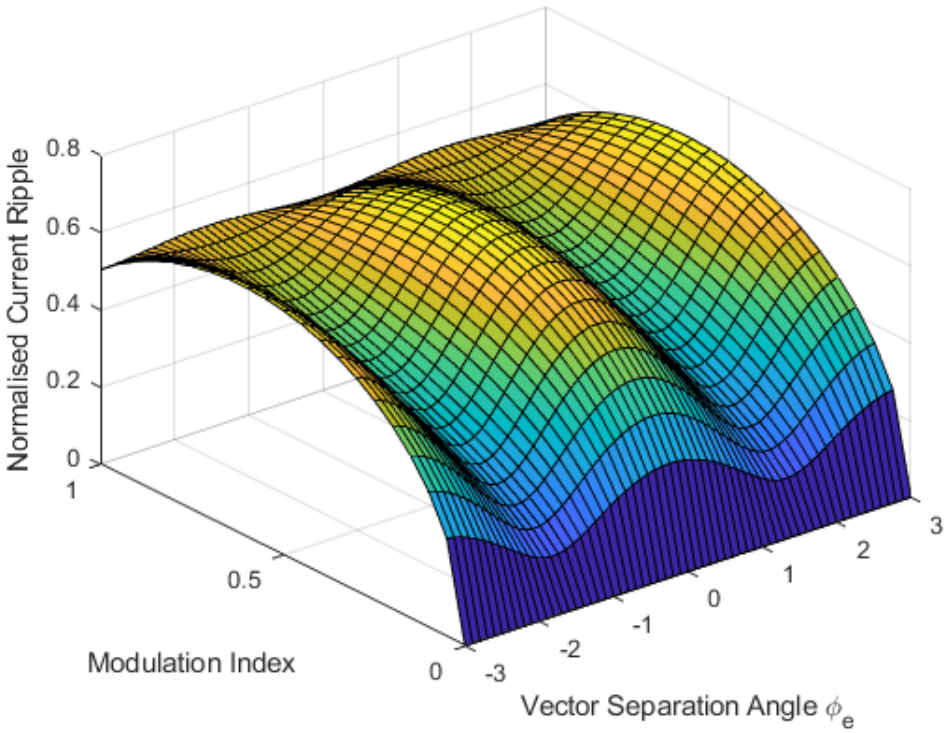

Figure 5.19 - Plot of Normalised capacitor ripple current variation with modulation index and vector separation angle.

Taking the worst-case peak normalised value of 0.65 and an estimated maximum peak phase current of 700A for the Infineon hybrid kit, the capacitor loss is ~140w and scales with the drive current. This drive is capable of 150kw [141]. As a result, this loss is deemed insignificant except at extremely high torque and low speed, an area only seen at the start line in a racing machine. The capacitor losses are therefore neglected for simplicity.

5.4. Transmission

The transmission model described here follows that developed by Burgess and Lodge for chain transmissions [145] and a contemporary 600cc racing machine [146]. There are limited references dealing with the efficiency of motorcycle chain drives.

The dominant chain losses are due to friction at the pin joints. The effect of impact and adhesion losses with the sprocket is ignored as these losses are small in comparison to chain drives under significant tension [145-147]. The chain tension due to torque on the input sprocket (F_{ch}) is given by the following, where $T_{ch,inp}$ is the input torque and $r_{ch,inp}$ is the input sprocket pitch circle radius.

$$F_{ch} = \frac{T_{ch,inp}}{r_{ch,inp}} \tag{5.19}$$

The other contribution to chain tension arises from the centripetal acceleration of the chain around the sprockets. This is written as $F_{cf} = m_{cl}{r_{ch}}^2\omega^2$ by [146] but should read as follows, where m_{cl} is the mass of an individual chain link, r_{sproc} the pitch circle radius of the sprocket in question and ω_{sproc} that sprocket's angular velocity.

$$F_{cf} = m_{cl}r_{sproc}{\omega_{sproc}}^2 \tag{5.20}$$

There are four major points of articulation, located where the chain enters and leaves the respective sprockets. There are also two types of chain articulation, one where the pin rotates within the bushing and two where the bush rotates around the pin and beneath the roller. A diagrammatic explanation is given by Wragge-Morley *et al.* [148]. These different articulations will alternate as the pin is rigidly attached to the outer plates so can only rotate when the outer plate angle changes.

As the materials are the same at the pin bush and roller bush interface the friction coefficient μ_p can be assumed to be the same [147, 148]. The only difference between the articulations is therefore the radius at which they occur. The alternating nature means that an average value can be taken, this is given as r_b.

The work done, $W_{articulate}$ is given by the following equation where the articulation angle of the pin joint is α_{pin}. The power dissipated by the chain is then calculated from the sum of these losses and the frequency at which they occur, $N_{inp}\omega_{inp}\sum W_{articulate}$.

$$W = \frac{F_{ch} + F_{cf}}{\sqrt{1 + \mu_p^2}} \mu_p r_b \alpha_{pin} \tag{5.21}$$

The chain force in the return side (slack side) chain is assumed to be only due to the centripetal component. This neglects tension due to gravity and preload. Motorcycle chains are usually installed so that there is an amount of chain slack remaining, so this return side or slack side tension is assumed to be small in comparison to the driven-side chain tension.

There has been difficulty recreating the published results by Burgess and Lodge [146]. The paper publishes efficiency results against velocity but does not give a conversion between rpm and velocity. To approximate this conversion data for a 600 cc sports motorcycle from the early 2000s with approximately the same output power as the motorcycle in the paper is used. This was a GSXR600, the standard rear-wheel having a rolling radius of 315mm. Taking the data up to 150 mph and the sprocket ratio of 15:47 from the paper gives a maximum gearbox output rpm of 6370.

Taking the example given in [146], the pin dimensions, and the mass per link given for contemporary 530 motorcycle chain [149] the efficiency of the chain in question throughout the motorcycle's speed range can be determined. Comparing the calculated result with the results given in [146] give a poor match at high speed, Figure 5.20

Modern motorcycle transmissions commonly use an 'X-ring' chain where rubber sealing washers seal lubricant into the pin bush gap. This ensures the chain maintains its lubrication over time however adds additional friction between the seals and the chain plates under articulation. This additional friction can be determined through the measurement of the chain-link friction [148]. The additional friction will be constant as the load on the seals does not vary with tension. However, the data is not widely available and such a test rig is outside the scope of this thesis, so this has been ignored here.

As a quick sensibility check, a 110 link chain equates to 1.85 kg of chain, primarily steel. Using 0.49kj/kgK as the specific heat capacity of steel and the power loss of 5.2kW at 150mph gives a chain temperature increase of 4.7Ks. Therefore, without cooling the chain lubrication would be destroyed due to temperature (~180°C) [150] after approximately 25 seconds at 150mph. Given that more powerful machines travel

faster than this with higher chain tensions it is difficult to believe that this level of loss is correct.

Renold roller chain guide states an efficiency between 98.4% and 98.9% [151], which is more likely. By including the r_{sproc}^2 error in F_{cf} and multiplying the chain mass by 1000 it was possible to match the results given by Burgess and Lodge [146], see Figure 5.21. It has therefore been determined that an error lies in the original paper.

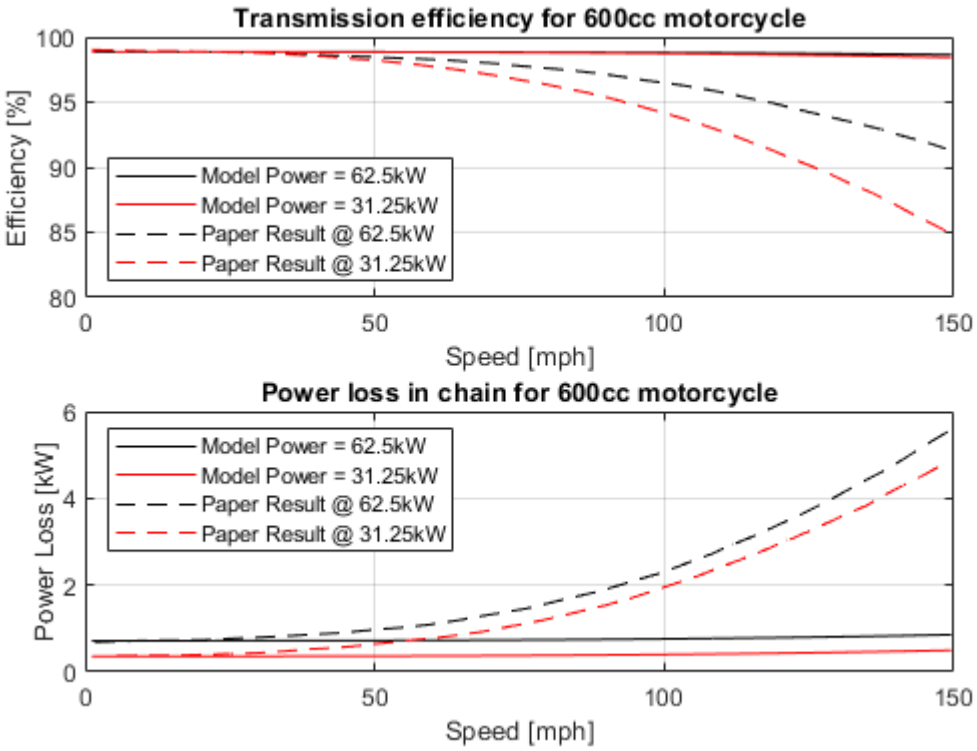

Figure 5.20 - Comparison of the modelled chain efficiency and the published results showing poor agreement at high speed

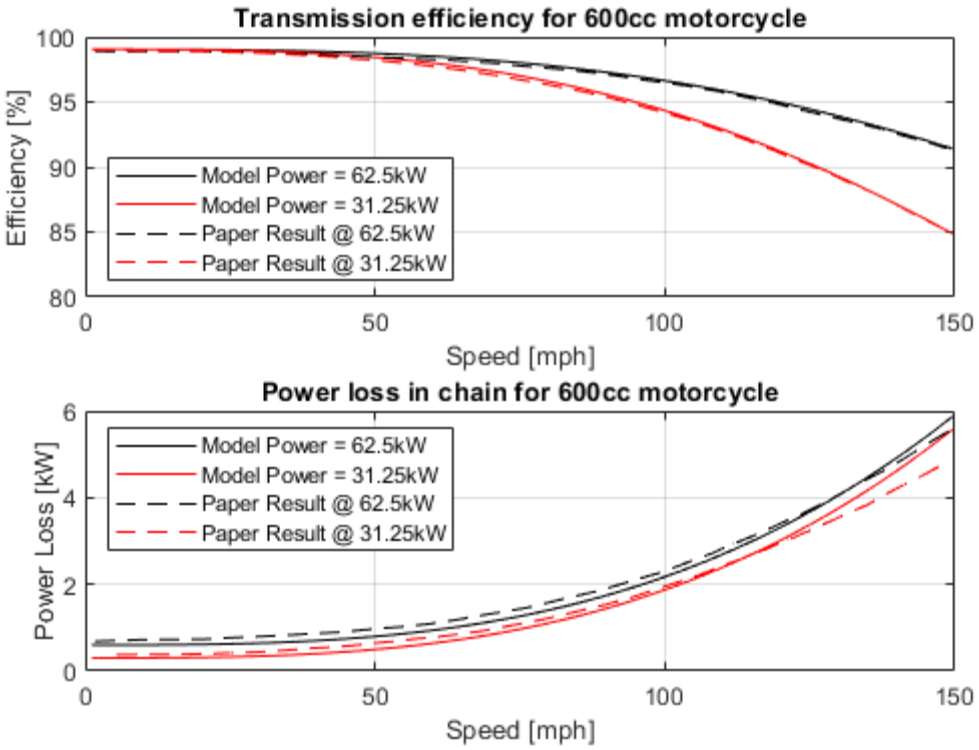

Figure 5.21 - Plot showing the alignment between the modified model and the published results.

5.5. Cumulative Loss Breakdown

Powertrain losses are highly dependent on the operation point of the motor. These losses contribute to increased battery consumption as well as increased cooling requirements and reduced power delivery. Figure 5.22 shows a cumulative loss plot of the UoN parker motor model at full torque operation. It is interesting to highlight the iron losses. These are omitted from the datasheet provided by the manufacturer but are significant at higher RPM.

Another point to highlight is the knee point at just over 6000 rpm. This is the point at which the motor enters the field weakening region. Here the motor frequency continues to increase resulting in increases in the iron and mechanical losses. However as the peak phase current, battery voltage and switching frequency remain constant the motor drive losses remain constant. This is until MTPV control serves to reduce the peak phase current. This slightly reduces the drive losses but also reduces the corresponding copper losses.

The ability to break down the significant system losses in this manner allows the use of a targeted development process for the full powertrain. This reduces the effort wasted chasing minor gains and streamlines the development process.

This model can be used to understand the effect of operating the motor at different maximal current, voltage and motor speeds. The effect of increased losses due to the use of a gearbox or the effect of increased chain loads from smaller sprockets on the motor bearing losses can also be evaluated here.

One example of the information shown in Figure 5.22 is how cumulative losses increase with motor speed. This highlights how the targeting of iron losses is beneficial for continued high-speed operation. An example upgrade here would be a switch in core material from M235 to a material with thinner laminations, which will reduce the eddy current losses. Similarly, when cost is of lower concern, cobalt iron could be used to further reduce losses. However, the higher density of this material should be accounted for.

Further examples include Inverter losses. These are influenced by switching frequency and switching module choice. Here a switch to Silicon Carbide MOSFETs, which have lower switching energies, will have lower losses, especially when switching at higher frequencies.

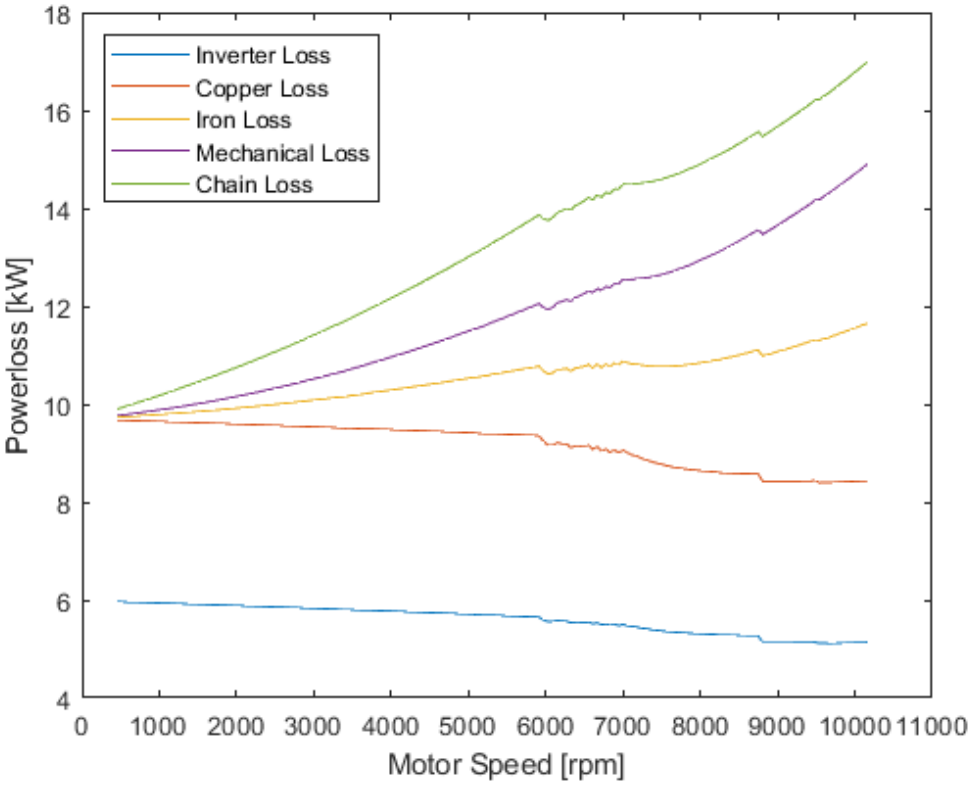

Figure 5.22 – A cumulative stacked plot of powertrain power losses at peak torque.

However, the simplified nature of the motor model does have some limitations. As the motor drive switching losses are proportional to the switching frequency reducing the

switching frequency will also reduce the inverter losses. The drawback with this approach is the effect of lowering drive switching frequencies increases the harmonic current distortion. This distortion serves to increase the motor losses. This is specific to the iron used and design of the motor and is not included in this analysis. The switching frequency has been kept constant in this thesis for this reason. Determination of these losses is usually performed using FEM and is outside the scope of this thesis.

Copper losses again can be reduced by reducing the lengths of end windings which do not contribute to torque generation but do contribute to motor losses. Additional improvements include increasing copper fill and reducing the effect of high-frequency content by using Litz wire [137]. These enhancements can be explored through FEM based updates to the loss coefficients included in this model.

5.6. Battery Modelling

The battery provides all the energy to propel the vehicle and its associated losses as well as store any regenerated energy. In a high-performance machine, it must do so efficiently for the minimum mass possible. A battery is a reversible electrochemical reaction and as such its performance is governed by the chemical processes and diffusion rates within the cell as well as the external electrical demands placed on it. A battery's response is dependent on several factors including its construction, temperature and state of charge [72].

There are many battery models of varying complexity, some attempts at electrochemical modelling and some purely empirical models. Typically, physical models are much more complex and used primarily for the development of the cell itself as they give greater insight into the mechanics of cell performance [72].

Here battery modelling is focused on areas that have a significant influence on the wider vehicle performance. It is necessary to consider only what is required for the vehicle system to respond appropriately. The factors that heavily influence the vehicle design are the voltage response under load, the total mass and stored energy of the battery, and the degree to which its temperature rises due to the discharge profile (to avoid exceeding design limits). The chemical interactions within the cell itself while of significant interest to a cell designer are not the focus of this thesis.

The temperature is important from a battery standpoint as the cell will degrade internally at high temperatures leading to cell failure at the extreme. Less extreme effects are accelerated ageing, of high importance to the automotive industry, but not as relevant when considering pure performance. Interestingly, the effect of increased temperature has some performance benefits through lowering cell internal resistance and associated losses.

The limits to be aware of are the point at which the electrode coating material begins to degrade [73] leading to internal short circuits and thermal runaway. This typically begins at around 80 ˚C. It is worth noting different cell constructions have differing self-ignition temperatures [74]. If runaway becomes self-sustaining (in the case of a full separator failure) the electrolyte itself can begin to combust and the cell fails rapidly, often with catastrophic consequences. Ensuring that every cell in the pack remains below this temperature is paramount, and an important limitation on performance.

The demand on the battery is not known before simulation and different events have differing demands. Therefore, it is important to be able to generate a representative model from a standard suite of tests whilst retaining sufficient accuracy for all events. To determine the definition of ‘sufficient accuracy’ it is worthwhile referring to the wider vehicle model to ensure that modelling assumptions do not have a significant effect on the wider system performance.

To quantify the effect of battery model voltage error for the full powertrain power output, the powertrain model was utilised in nominal 2018 TT specification and the effect of differing DC link voltages was investigated. It was found that 6 V DC-link error equates to a 1% power output error under these conditions. A 171s pack was used so this equates to an individual cell voltage error of approximately 35 mV. Figure 5.23 illustrates this difference in torque-speed response of the UoN motorcycle when fully charged and when the battery is discharged illustrating the effect of supply voltage on power output.

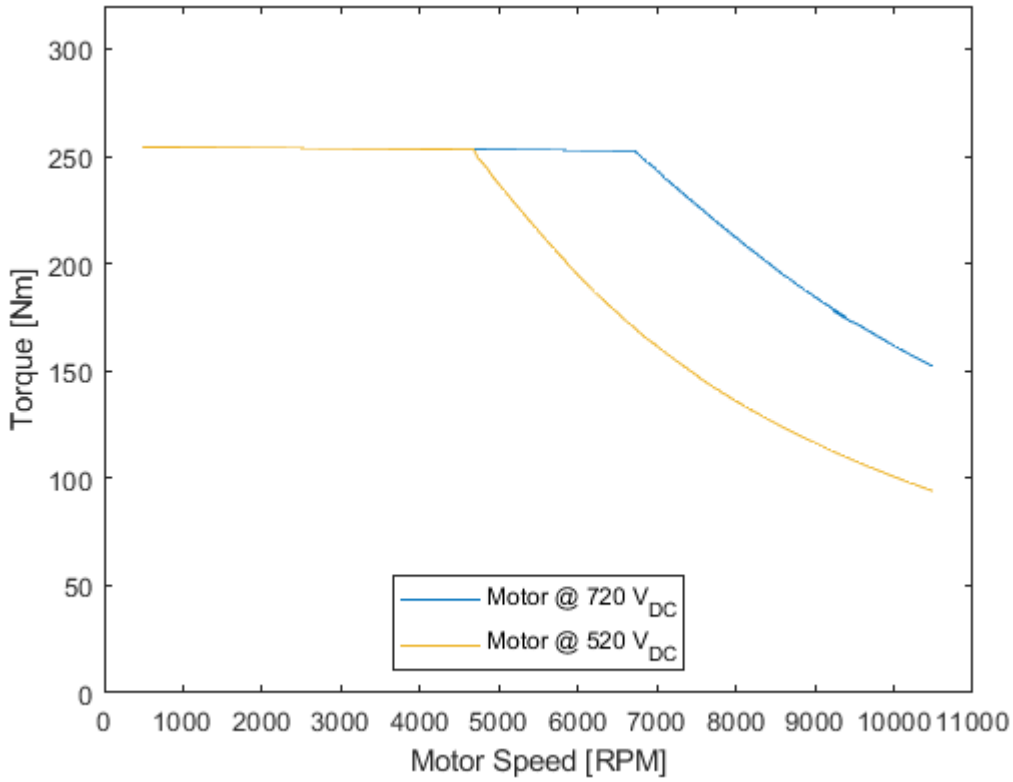

Figure 5.23 - Development of the limit torque response throughout the TT Zero lap

There are many equivalent circuit models available and most of them display high performance for the limited scenarios that the respective tests used to develop them undergo. However, in the case of the racing motorcycle, or any other high-performance electric vehicle, the demand profile is far removed from simple lab pulse tests. Previous electric motorcycle models [16, 17] have assumed that a fixed internal resistance model is appropriate with little justification. One example [17] also ignores the significant nonlinearity of Open Circuit Voltage (OCV) evolution with respect to State of Charge (SOC), resulting in even more significant voltage differentials even after parameter fitting to the data subsequently used for evaluation.

To determine the most appropriate choice of model, five varieties of equivalent circuit model are implemented, and parameters extracted from laboratory tests. The goal is to identify a suite of tests and procedures that allows for the rapid evaluation of a cell for the target application and has good predictive capabilities in terms of runtime, output voltage and temperature.

To investigate this, cell testing apparatus is required. A forced 7-month hiatus due to the closure of university laboratories due to the COVID 19 pandemic delayed this testing considerably. Due to difficulties in obtaining the expensive purpose-built

battery testing suites, the low-cost version described herein was constructed and found to give acceptable results for a fraction of the cost.

The setup is as follows: a Chroma 63206 DC load and a Picolog USB TC-08 temperature logger with ‘K’ type thermocouples taped to the surface of the test cell. The test cell was connected to the load using a four-wire ‘Kelvin’ connection to remove the resistance of the load wires from the test data. A laboratory power supply was included to allow full automation and bidirectional cycling. The test was controlled via MATLAB script and serial interface. Single cells were placed in a steel container with heating and cooling fans connected to a thermocouple and a relay that engaged the respective fan at a deviation of over 1 degree from the set point. This rudimentary temperature control method managed to keep the cell surface temperatures within ±2.5 degrees of the target temperature. The test enclosure setup can be seen in the following image, Figure 5.24.

Figure 5.24 - Battery testing enclosure and bidirectional load testing setup.

Initially, the approach described in Blissett’s thesis [16], discharging at a low discharge rate, was used to determine the relationship between OCV and SOC. However, it is widely known that the internal resistance varies with a multitude of

factors and removing the effect of this from the result is non-trivial, requiring further testing or large assumptions to be made. In response to this a pulsed discharge test at 0.2C, similar to the process used Birkl *et al.* [77], was trialled with the cell permitted to relax to a steady-state between pulses. This allowed for the resting voltage to be determined directly as well as the internal resistance approximated.

Both Plett and Birkl *et al.* [76, 77] highlight a potential hysteresis effect that was overlooked by this singular directional approach and by other contemporary electric motorcycle models. This is particularly important for high-performance vehicles. Due to regenerative braking, the battery current will be bidirectional resulting in increased voltage prediction errors if not accounted for.

Low discharge rate cycle tests at 0.5C were performed to differing states of charge. By overlaying the voltage response of these tests, it can be seen if the cell voltage response immediately returns to the steady-state performance of the other tests or if there is a hysteresis effect that delays this progression after a charge/discharge reversal. A delay was found in the UoN example cell and an example of this can be seen in the following cycle response, Figure 5.25.

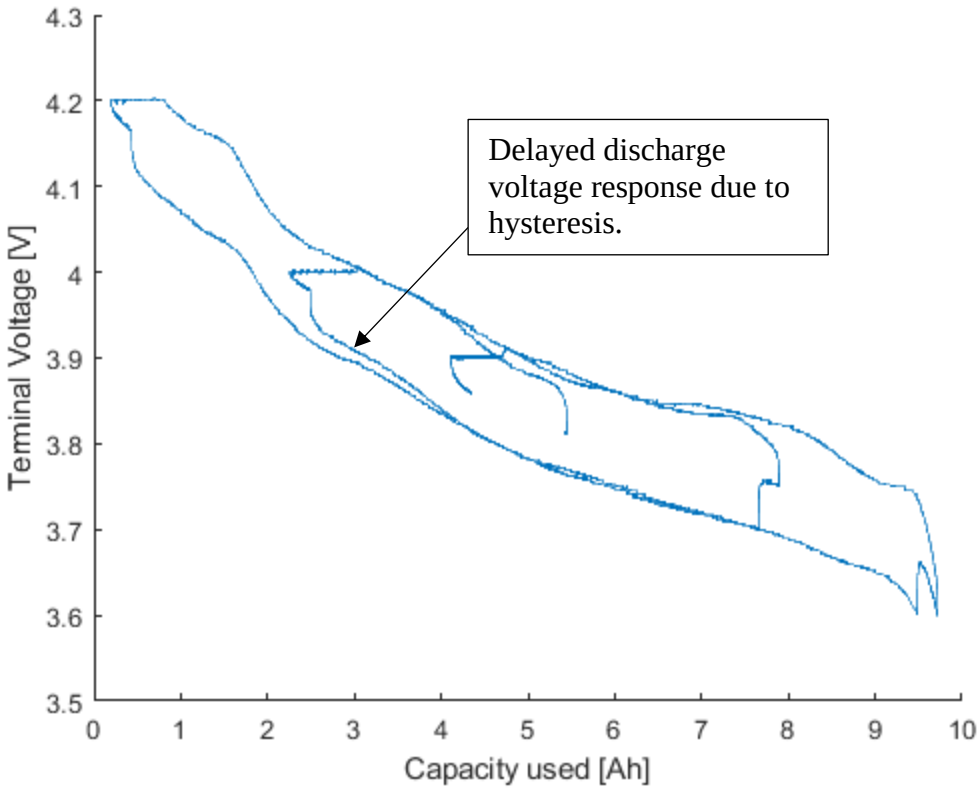

Figure 5.25 - Battery terminal voltage response to 0.5C cycling test to different voltage levels.

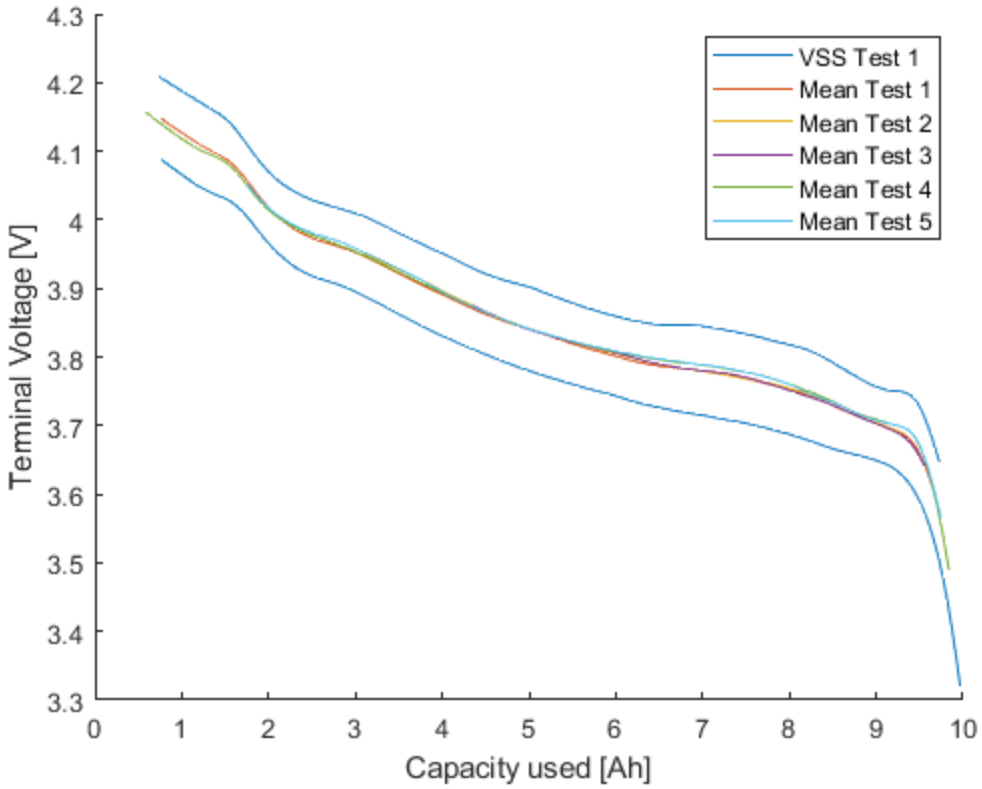

Figure 5.26 - Open circuit voltage approximation using the means of constant current regions.

The next step is to determine the magnitude of this effect. This is achieved by removing the variable current regions, relating to the charge current profile tapering off at the end of charge. This is done to avoid regions dominated by the hysteresis response. It is then possible to approximate the mean voltage at similar states of charge. An example of this approximation for multiple tests can be seen in Figure 5.26.

To determine the magnitude of the hysteresis, the voltage differential between the constant current regions and the mean voltage is obtained. The discharge current is known from the test data. By assuming the voltage drop is a combination of ohmic resistance and a fixed hysteresis offset, both the offset and internal resistance can be approximated from the difference between tests at differing discharge rates.

This hysteresis effect and a simple model that approximates the effect on cell terminal voltage is described by G.Plett [76]. The coefficients, M_0 – Instantaneous hysteresis voltage, M_1 – exponential hysteresis voltage, γ_{hyst} - Hysteresis decay constant, can be fitted to the cell cycling data and the hysteresis voltage V_{hyst} given as follows.

$$V_{hyst} = M_0 h_0 + M_1 h_1 \tag{5.22}$$

Here 'i_{cell}' is the cell current, 'h_0' is the instantaneous hysteresis state, $h_0 = sign(i_{cell})$, h_1 is the unitless hysteresis state $-1 \leq h_1 \leq 1$. The discrete-time hysteresis state is given by the following equation [76], where Q_{cell} – is the cell capacity in ampere hours and η_c – the coulombic efficiency of the cell.

$$h_1[k+1] = e^{-\left|\frac{\eta_c[k]\, i_{cell}[k]\gamma_{hyst}\Delta t}{Q_{cell}}\right|} h_1[k] - \left(1 - e^{-\left|\frac{\eta_c[k]\, i_{cell}[k]\gamma_{hyst}\Delta t}{Q_{cell}}\right|}\right) sign(\, i_{cell}[k]) \quad (5.23)$$

η_c – is neglected for simplicity as it is typically around 0.99 for charging and 1 for discharging [76]. The error associated with this simplification surrounding regenerative charging is assumed to be small for the single discharge race event.

The next task is determining the SOC to OCV relationship. The battery energy used with reference to a zero-loss discharge is used as the measure of SOC. This allows easier conversion of heat energy and lost energy due to ohmic heating. The open-circuit voltage is taken from the mean voltage, and the energy obtained by combining this with the current delivered in ampere-hours [Ah]. Cycling was performed at both 0.5C and 0.25C to determine the hysteresis magnitude and the same data is reused here. Low discharge rates are used to reduce the energy loss due to ohmic heating and therefore the error of the OCV to usable energy remaining relationship.

To illustrate the impact of discharge rates on the accuracy of the SOC to OCV relationship the example of a 10Ah cell used in the UoN 2018TT bike is taken. The cell has a capacity of ~37Wh. When discharged at 0.25C the energy lost to resistive heating is just under 0.2Wh or around 0.5%. The difference in energy usage due to inaccuracies in the approximation of internal resistances of up to 25%, is in the region of 0.1% of the total capacity. It is therefore appropriate to use an approximate fixed internal resistance value, taken from the hysteresis magnitude analysis, for this determination of the OCV to SOC relationship. This simplifies the parameter extraction process. The resulting relationship is shown in Figure 5.27, illustrating the non-linear nature of this relationship and the drawbacks of the linear relationship between the state of charge and open-circuit voltage used by Dal Bianco and Lot [17]. This may account in part for the voltage differential between measured and simulated battery voltage in that paper.

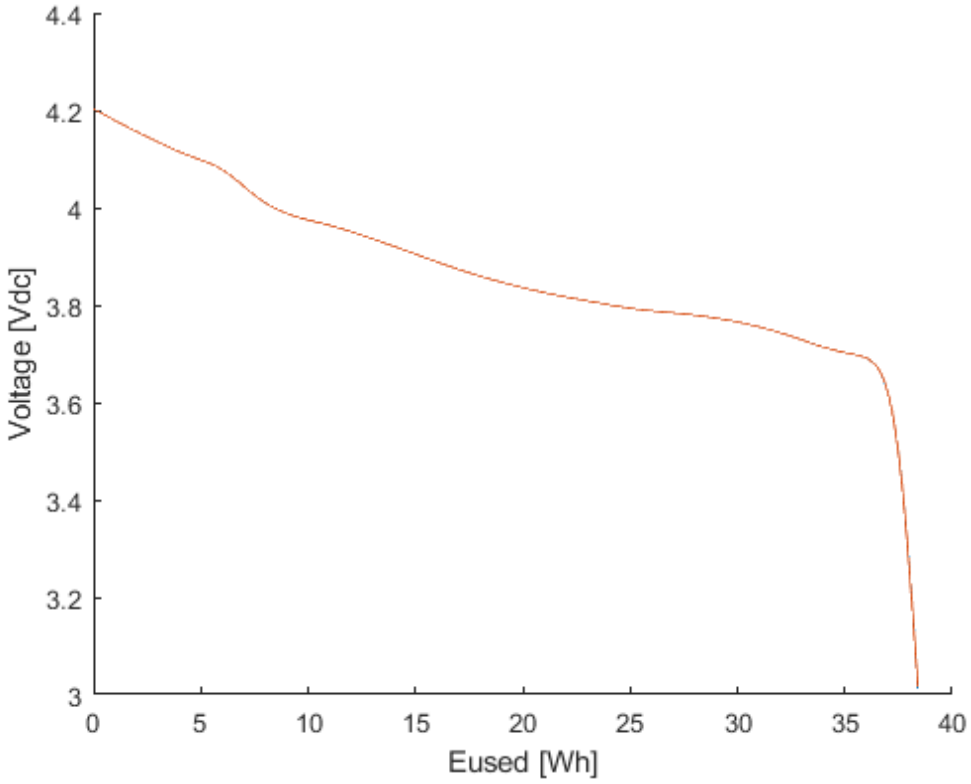

Figure 5.27 - Plot of cell open-circuit voltage with energy usage between manufacturers voltage limits

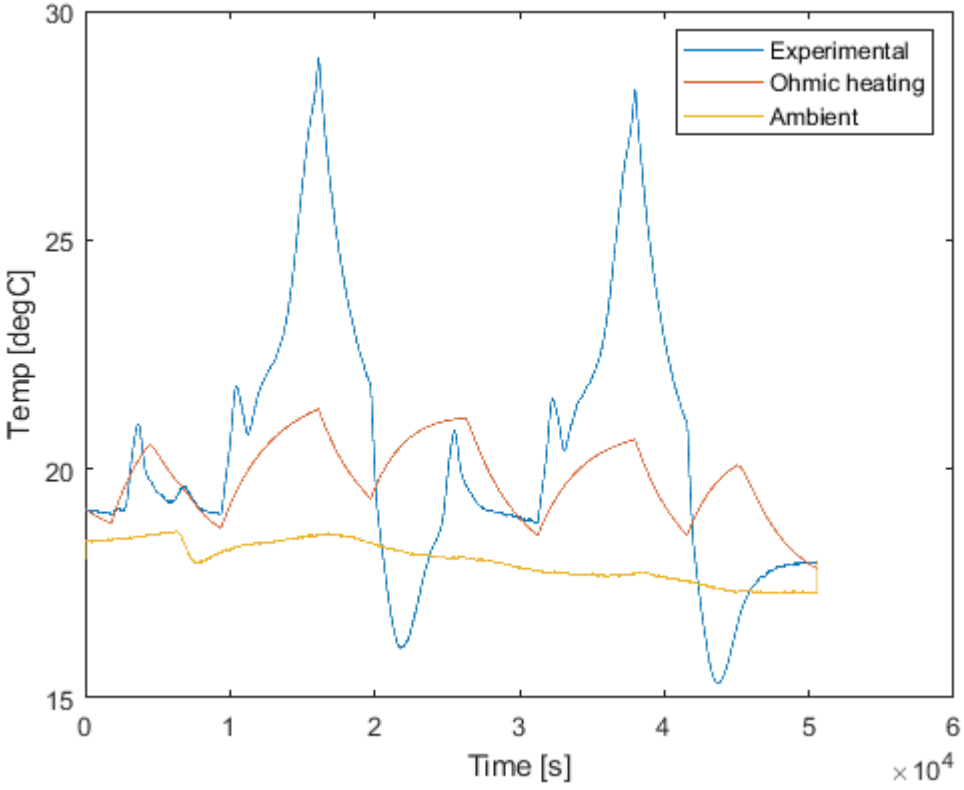

Figure 5.28 - Plot of cell temperature during 0.5C cycle testing

The next piece of information that can be extracted from the low discharge cycle response is the cell temperature variation with state of charge and cooling performance of the experimental setup. The cell heating is not purely ohmic as can be seen in Figure 5.28.

The cause of this deviation is largely due to entropy variation within the cell. This is due to the change in state of the cell components during discharge. A common method to determine this relationship is the potentiometric method [78]. However, this method takes many days and requires equipment not available to the author. A faster calorimetric method is proposed in [78] and claims similar levels of accuracy. A modified and improved version of this method is used here.

The caloric method is simply an energy balance method. Thomas and Newman [79] derive an expression for the heat sources in a lithium-ion cell. The heat sources considered are resistive or ohmic heating, entropic heating, and the heat of mixing. The heat of mixing is negative during the creation of concentration gradients and positive as these gradients disappear but is generally neglected as insignificant in a properly designed cell [79]. A simplified version of this equation neglecting the heat of mixing is given below [80].

$$\dot{Q_{heat}} = i_{cell}\left(V_{cell} - V_{oc,cell} + T_{cell}\frac{\partial V_{oc,cell}}{\partial T_{cell}}\right) \tag{5.24}$$

Here '$\dot{Q_{heat}}$' is the change in heat energy, V_{cell} the cell output voltage, $V_{oc,cell}$ the cell equilibrium or open-circuit voltage and T_{cell} the temperature. It is not possible to prevent heat flow to the surroundings in the test enclosure. Therefore, terms for conductive and convective cooling as well as radiation are included. The respective cooling rates are simply a function of the temperature differential between the cell and its environment. The change in temperature of the cell is a result of its mass, specific heat capacity and change in heat energy. An expression combining these elements is as follows.

$$dT_{cell} = \frac{i_{cell}\left(V_{cell} - V_{oc,cell} + T_{cell}\frac{\partial V_{oc,cell}}{\partial T_{cell}}\right) + \left(h_{conv}A_{SA,cell} + \frac{kA_{CSA,wire}}{l_{wire}}\right)(T_{cell} - T_{air}) + \sigma_{bm}\varepsilon A_{SA,cell}(T_{cell}^4 - T_{air}^4)}{M_{cell}C_p} \tag{5.25}$$

Here: 'T_{air}' is the ambient air temperature; 'h_{conv}' is the heat transfer coefficient for convection; '$A_{SA,cell}$' is the surface area of the cell; 'k_{wire}' is the thermal conductivity of the load wires; '$A_{CSA,wire}$' is the cross-sectional area of the wires; 'l_{wire}' the length of the load wire to the exit of insulation; 'σ_{bm}' the Stefan Boltzmann constant; 'ε' the emissivity; 'C_p' the specific heat capacity of the cell; and 'M_{cell}' the mass of the cell.

The method outlined by Damay *et al.* [78] calls for the determination of the cooling parameters purely from the rest period of the cycle test. However, when cycled multiple times any inaccuracies result in a cumulative error that quickly renders the test meaningless. The cause of these inaccuracies is likely due to the simplified cooling model used.

Damay *et al.* [80] determine the specific heat capacity by evaluating the change in temperature due to a 20s pulse cycle at 1C. This is performed at close to ambient temperature to reduce heat transfer. This method also suffers from the same issue as described previously, the temperature change is small (2 ˚C) and can easily result in extrapolation errors causing a cumulative error and inaccurate results. The method also assumes a fixed ohmic heating value, neglecting any variations. This has a low impact on the testing performed in the paper but is not necessarily true for all cells. These methods were replaced by the following improved methods.

Using the SOC to OCV relationship determined earlier the $V_{oc,cell}$ term can be determined. i_{cell}, V_{cell}, T_{cell} and T_{amb} have all been measured. This means that the ohmic heating $i_{cell}(V_{cell} - V_{oc,cell})$ is easily determined. The three elements outstanding are then cooling parameters, cell-specific heat capacity and entropic heat change. By starting and ending the test at a steady state with the same temperature and state of charge there should be no net heat gain to the cell. Therefore, total Joule heating will equate to total cooling. This is used to determine the cell cooling coefficients.

By comparing the sum of the heat transfers into and out of the cell from ohmic heating and various cooling pathways, with the measured temperature change, it is possible to determine the excess energy required to achieve the measured temperatures. As ohmic heating is dependent on the rate of charge and discharge, but the entropic energy change is not, performing this test at multiple discharge rates results in different heat energy inputs and correspondingly different temperature

ranges. It is then possible to use this data to determine the specific heat capacity of the test setup. This is done by determining a value for specific heat capacity that gives the same calculated entropic energy change for different cycle rates. Low rate, 0.5C and 0.75C, cycles were used in this thesis to ensure the entropic heating was significant and easily determined.

The measured energy differential between ohmic heating, cooling and the measured temperature rise with respect to the state of charge is shown in Figure 5.29. There appears to be a hysteresis effect in this data. This is likely due to the heat model not modelling the temperature gradient within the cell. This is ignored for this thesis as the goal is to capture the total heat generation. The output of this test is a lookup table of internal energy differential with respect to the state of charge, seen in Figure 5.29.

The inclusion of entropic heating into the cell temperature model results in an improved temperature fit for the cell cycle tests when compared to the simple ohmic model commonly used. This can be seen in Figure 5.30. The inclusion of this effect has reduced the maximum temperature prediction error from approximately 12 ˚C to 2 ˚C, a significant improvement. The effect is less marked for a higher discharge rate test as ohmic heating dominates but it is still significant.

The temperature prediction performance for the model over the test TT Zero cycle using both the ohmic heating and combined ohmic/entropic heating model is shown in Figure 5.31. For this test, the cell cooling model is re-calibrated using 5C constant discharge test data. This is used to calibrate the cooling model at higher temperatures more representative of operation. Note different thermal calibration coefficients are obtained for the ohmic heating model and the combined ohmic and entropic heating models which are expected due to the differing energy contributions from both methods. The ohmic heating used here is determined from the modelled voltage drop provided by the Thevenin model described later in this chapter.

As can be seen, the inclusion of entropic variation into the temperature model reduces the error when compared to experimental data by approximately 50%. The temperature evolution profile is also a markedly better fit. This could be further improved by re-calibrating the model parameters to fit the experimental data, but this defeats the goal of using a standard suite of tests for prediction over multiple events.

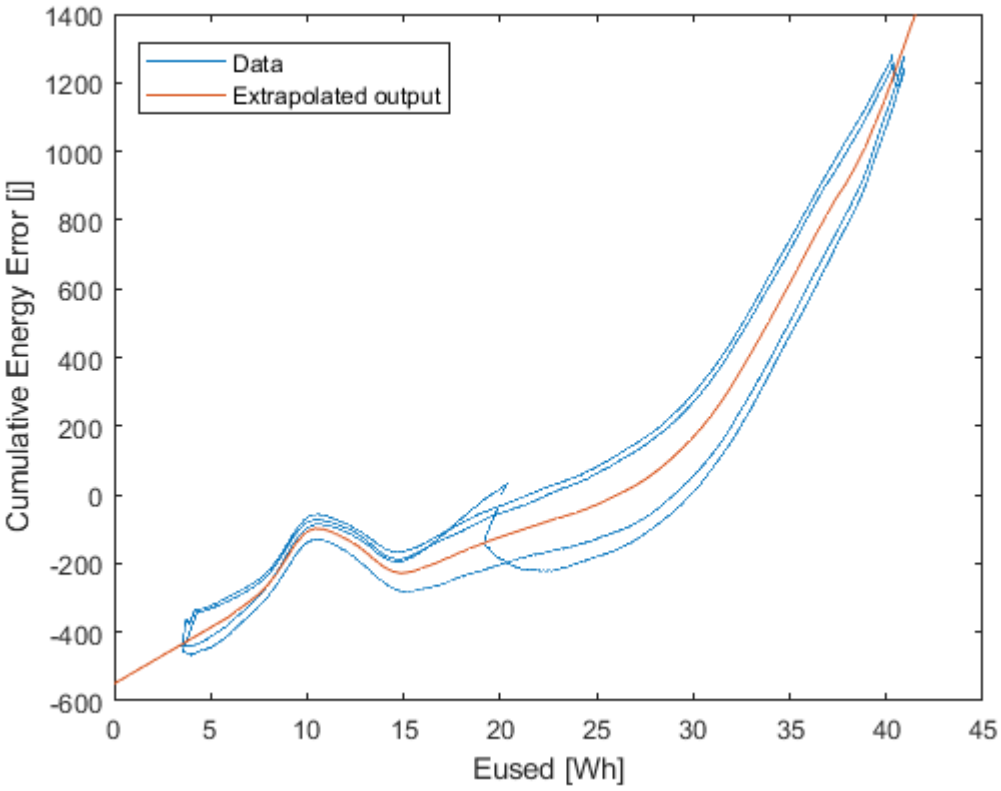

Figure 5.29 - Measured energy differential between ohmic heating and cooling plotted against state of charge. The mean extrapolated output curve is used in further simulations.

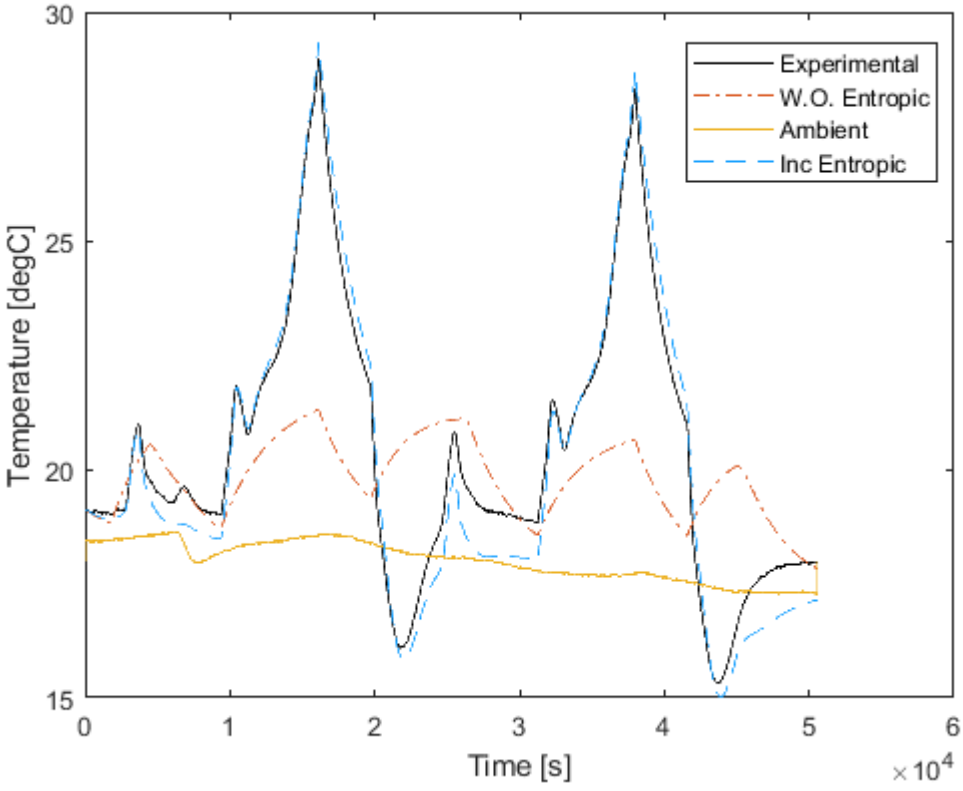

Figure 5.30 - Comparison of cell temperature models with and without the inclusion of entropic heating for a 0.5C cycle test.

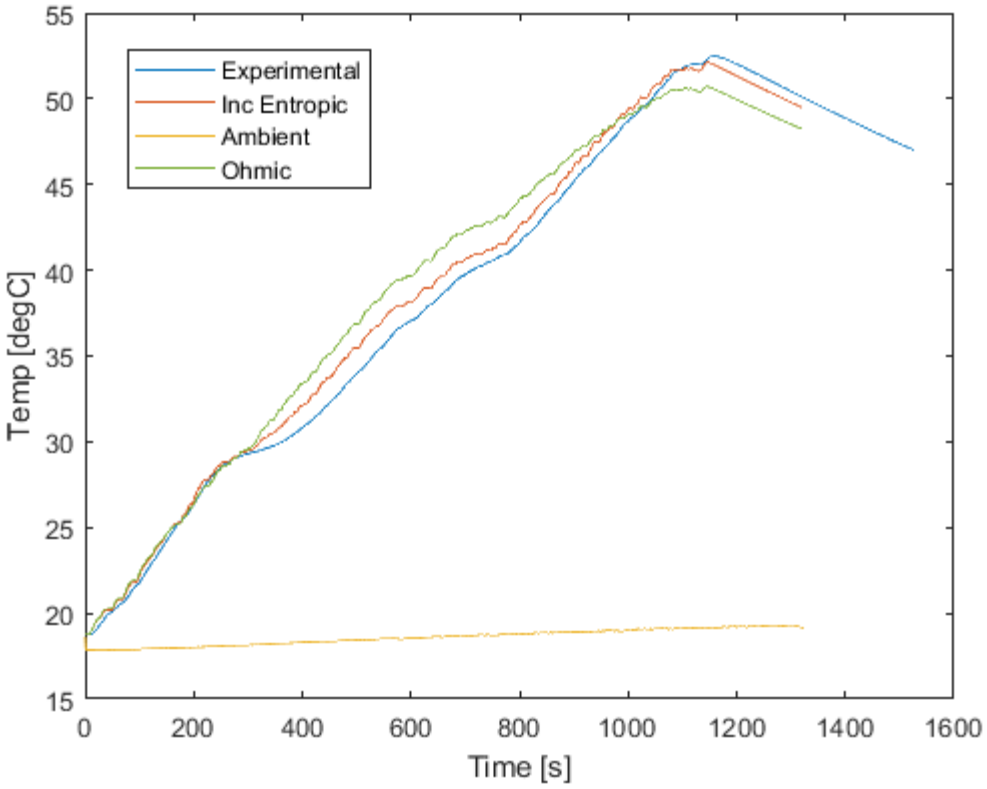

Figure 5.31 - Comparison of cell temperature prediction models for a TT lap cycle.

Having determined the underlying reference data describing the OCV to SOC relationship as well as the hysteresis response it is time to determine the load dependant response. Many differing cell models promise benefits from simplicity to high accuracy in different areas. A summary of the current state of some of these models and their respective benefits has recently been published [152] with the general recommendation that equivalent circuit models are the most appropriate for the application in this thesis. This is due to the combination of accuracy, flexibility and ease of implementation and data collection when compared to other model types such as the full electrochemical models. It would not be an efficient use of space to delve further into this here.

Within the equivalent circuit model approach, there are several different models available but most are based around the same principle. A fixed resistor is used to model the ohmic resistance of the electrolyte, separator, and electrode. A variable number of RC circuits in series are used to model the time dependant response resulting from the slower processes such as charge transfer and lithium-ion diffusion.

To determine the best equivalent circuit model choice for use in a high-performance electric motorcycle simulation, a quantitative analysis of both the current methods

used for electric motorcycle simulation [16, 17, 98] and other equivalent circuit models with varying levels of complexity is required.

Several different testing methods can be used to determine cell internal resistance. The most common of these are electrochemical impedance spectroscopy (EIS) and pulsed DC. EIS applies a full spectrum of perturbation frequencies to the cell in the order of 100 kHz to 10 mHz and determines the cell response across this spectrum. The Pulsed DC technique simply applies a DC load or charge pulse to the cell and determines the cell resistance according to ohms law [153]. Due to equipment availability, the DC pulse technique is used in this thesis. A standard suite of pulsed DC tests was devised capable of highlighting discharge rate dependant, state of charge dependant and temperature dependant behaviour of the cells in question.

The respective model coefficients are then determined from this discharge data. The performance of these models in terms of temperature prediction, runtime prediction and maximum voltage error is evaluated against a further bidirectional discharge test representative of a competitive lap of the Isle of Man TT course.

The pulsed discharge testing procedure is as follows: The cell was placed into the environmental chamber. Desired test temperature between 10 and 55 degrees is set. The cell is charged to the manufacturer specified fully charged voltage of 4.2 Vdc by the CCV method with a charge cut-off current of C/50. The cell was then left for 1-hour post charge to stabilise at the desired temperature. The cell is then subjected to 20s duration alternating 10C, 8C and 5C discharge pulses with a 30min rest period between pulses to determine the cell recovery. This rest period was chosen as a balance between test runtime, cell heating and allowing the voltage response to decay. The discharge test continued cycling the pulses until the cut-off voltage of 2.9 Vdc under load was reached. This test was repeated at different temperatures and tested in a random order with multiple cells to prevent the influence of cell ageing manifesting as a systematic error.

Testing is time-consuming with each test taking approximately 12 hrs to complete. To speed up the process and reduce the temperature rise per pulse, 7 s pulses with 120 s rest were trialled. The result of this test is discussed later.

Some models highlight the fact that the response under charge and discharge differ and this is the rationale behind the hybrid pulse power characterisation (HPPC) test

procedure [154]. However, as the limit performance of the powertrain is dictated by the voltage under discharge the addition of a duplicate set of charge parameters and associated extra testing is deemed unnecessary and detrimental to simulation speed.

Before attempting to extract parameters from pulsed discharge data it is worth identifying the different parts of the voltage response. An example discharge pulse is shown below. As can be seen, the voltage recovery is far from instantaneous. Also shown is the change in resting voltage due to the discharge pulse. It is common to extract parameters from the recovery period as this is at a constant state of charge. The instantaneous change in voltage dV_0 and the total recovery voltage change dV_{tot} are illustrated in Figure 5.32 below.

The first model to be evaluated is a fixed internal resistance model as used by both [16, 17]. Obtaining this value is simply the total voltage change over the pulse current, $R_{0-RC0fixed} = dV_{tot}/di_{cell}$. The fixed internal resistance model is the mean of these resistance values for all tests. The model is now referred to as the '0RCfixed' model.

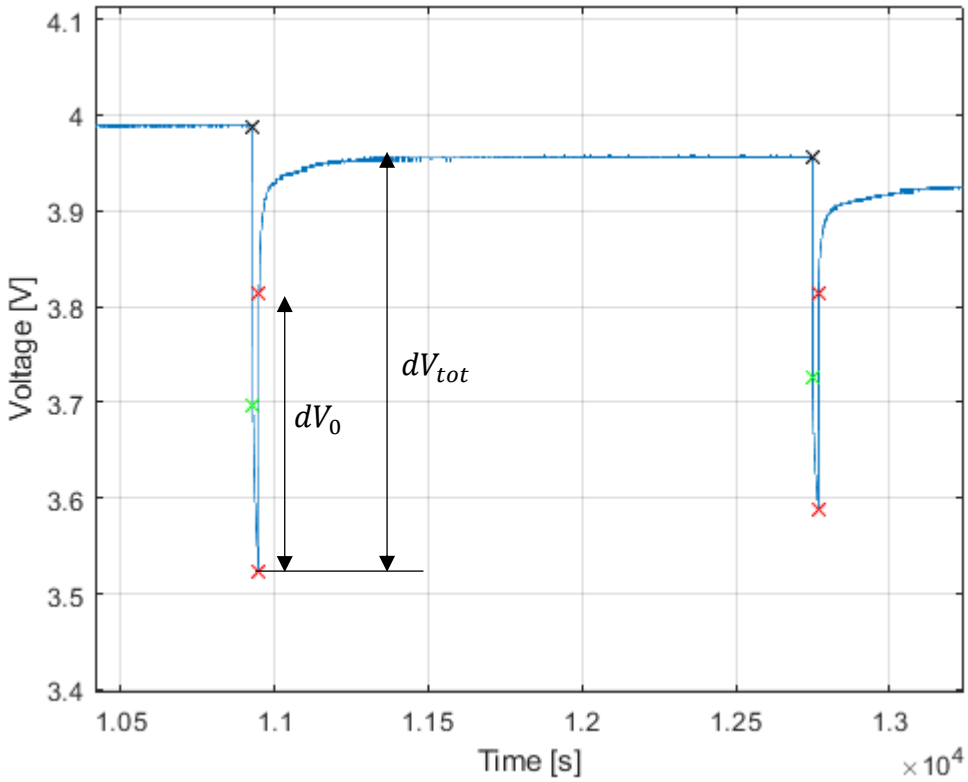

Figure 5.32 - Example discharge pulse.

It is widely known that internal resistance values vary with temperature and state of charge. The internal resistance value reduces nonlinearly with increasing temperature and tends to increase at the extremes of state of charge. To capture this the variation due to temperature is approximated to an exponential decay and a second-order polynomial is used to approximate the state of charge dependant variation. Simple coupling terms are included to capture interdependencies and the following equation is used to fit the output data. Note, 'a_{1-8}' are fitted coefficients.

$$R_{0-RC0} = a_1 e^{-a_2 T_{cell}} + (a_3 T_{cell} + a_4)\left(a_5\left(V_{oc,cell} + a_8\right)^2 + a_6\left(V_{oc,cell} + a_8\right) + a_7\right) \quad (5.26)$$

The resulting response surface is illustrated in Figure 5.33, capturing the major trends of reduction in internal resistance with battery temperature as well as the increased internal resistance at the limits of the state of charge. The use of a custom equation improves the fit and makes the fitting process more robust than simply using the inbuilt 'polyfit' functions available in MATLAB. The interpolation of experimental data was disregarded here as the captured data is noisy. This is the second internal resistance model selected for evaluation and will now be referred to as '*RC-0'*.

As can be seen in Figure 5.32 the change in voltage is not instantaneous as approximated by the two previous models. The time-dependent voltage response can be approximated by resistor-capacitor (RC) pairs. Multiple RC pairs can be used in series to fine-tune the response. This is commonly known as an equivalent circuit or Thevenin model, an example of which is illustrated in Figure 5.34. The final models under evaluation are the single and double RC pair models. These models also include temperature and state of charge variation for their parameters.

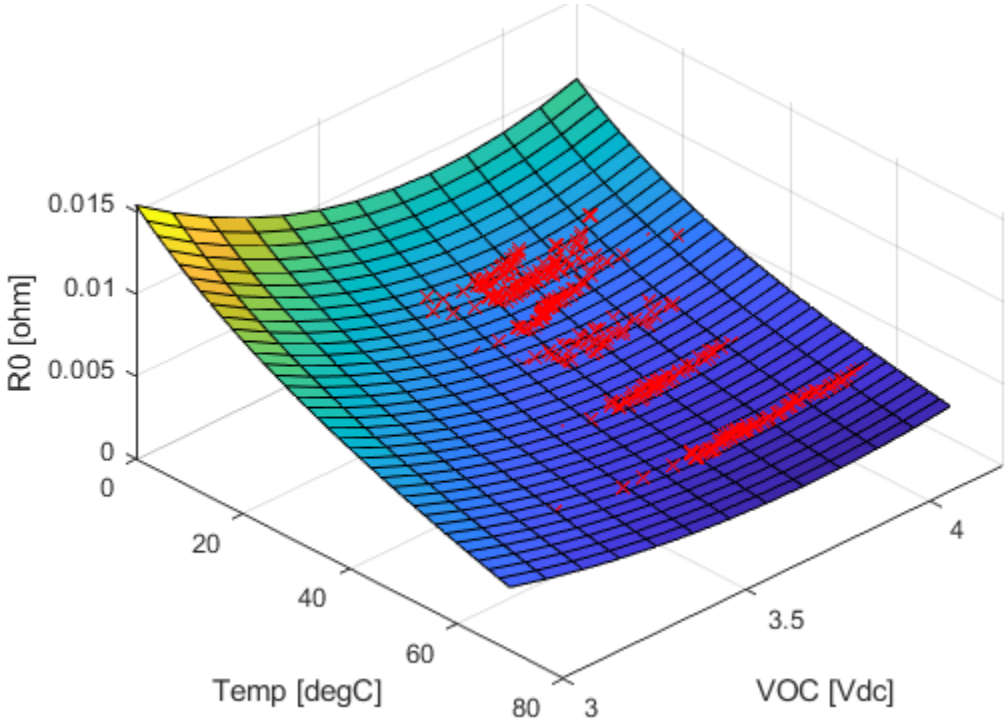

Figure 5.33 - Plot showing test data and resulting fitted surface for 'RC-0' battery model.

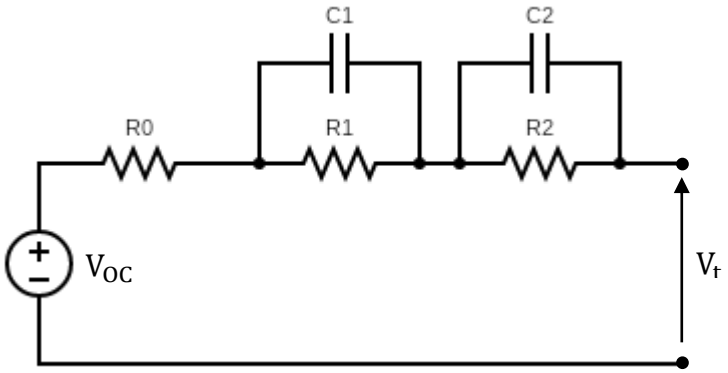

Figure 5.34 - Second-order Thevenin model

The discrete-time equation for the terminal voltage V_{cell} using two RC pairs (second-order Thevenin) is given by Plett [76] and is as follows:

$$V_{cell} = V_{oc,cell} - i_{cell}R_0 - i_{R1}R_1 - i_{R2}R_2 \tag{5.27}$$

Where i_{R1} and i_{R2} are as follows:

$$i_{R1}[k+1] = e^{\left(-\frac{\Delta t}{R_1 C_1}\right)} i_{R1}[k] + \left(1 - e^{\left(-\frac{\Delta t}{R_1 C_1}\right)}\right) i_{cell}[k] \tag{5.28}$$

$$i_{R2}[k+1] = e^{\left(-\frac{\Delta t}{R_2 C_2}\right)} i_{R1}[k] + \left(1 - e^{\left(-\frac{\Delta t}{R_2 C_2}\right)}\right) i_{cell}[k] \qquad (5.29)$$

Note, for the single RC pair model the terms relating to the second resistor-capacitor pair are ignored.

To determine the parameter values for the single RC circuit subscript 'RC1' the fixed ohmic resistance is extracted from the instantaneous voltage response $R_{0-RC0} = dV_0/di$. The time-dependent decay is then approximated as an exponential decay to the resting voltage. Here the remainder of the voltage change is due to R_1 therefore $R_{1-RC1} = (dV_{tot}/di) - R_{0-RC1}$. The final parameter to extract is the time constant of the response, τ_1. This is determined as the time taken to achieve 63% of the voltage change between dV_0 and dV_{tot}. The relationship between capacitance, resistance, and the time constant of an RC pair is then used to determine the capacitance: $C_1 = \tau_1/R_1$. This model is referred to as the '*RC-1*' model.

To determine the parameters used in the second-order model the analytical approach outlined by Hu *et al.* [155] and the layered estimation approach as outlined by Jackley *et al.* [156] were both trialled. The analytical approach is significantly faster but includes the assumption that the state of charge does not change within a discharge pulse and focuses on the fitting of the relatively short discharge pulse ignoring the recovery phase. Additional issues include the fact that occasionally complex numbers are generated. However, the calculated values can be filtered and fitted to the temperature and SOC variation model. This model is now referred to as the '*RC-2 ana*' model. And is further used as the initial starting point for the layered estimation approach.

An outline of the layered estimation technique is as follows. Here the test is discretised into individual pulses. Parameter estimation is performed on these individual pulses and some overlap is included with previous and following pulses. This overlap is required to include sufficient data points to account for the parameter variation during discharge. This parameter variation is due to the state of charge changing during a discharge pulse and thus requiring parameter interpolation between regions of constant state of charge. The constant state of charge regions being the recovery phase.

To include the effects of hysteresis and non-decayed voltage response the output values of I_{R1}, I_{R2}, h_1, h_0 from the previous pulse are used as the initial conditions for the following pulse. This restricts the use of parallel optimisation to full test profiles making the parameter estimation a time-consuming process. This could be improved by neglecting hysteresis and assuming that the voltage response has reached a steady state at the end of a pulse. The attempt to use a 120s rest period and substantially speed up the test data acquisition makes the steady-state assumption difficult to justify as well as the inclusion of the hysteresis model. This model is now referred to as '*RC-2 opt*'.

The final test is to perform a TT lap discharge on the test cell and compare the test model predictions to the measured data. Note as mentioned previously the temperature coefficients for the test cell are obtained by fitting to a 5C constant current discharge, this calibration was repeated for each test model individually. The RMS and peak errors for voltage and temperature during discharge are then computed as well as the state of charge error from the final resting voltages. The response was evaluated for all 5 models, as well as the effect of including hysteresis and entropy variation. A comparison was also performed for the differing rest periods in the test data.

As can be seen in Figure 5.35 and Figure 5.36 the inclusion of the entropy model reduces the peak temperature prediction error by approximately 1.5 degrees and the RMS temperature error by 1 degree, which is 30-50% of the total temperature error.

Figure 5.37 shows a noticeable reduction in peak voltage error using the higher-order models. Visual inspection of the predicted and measured responses indicates this is most likely due to the improvement in the modelling of dynamic behaviour.

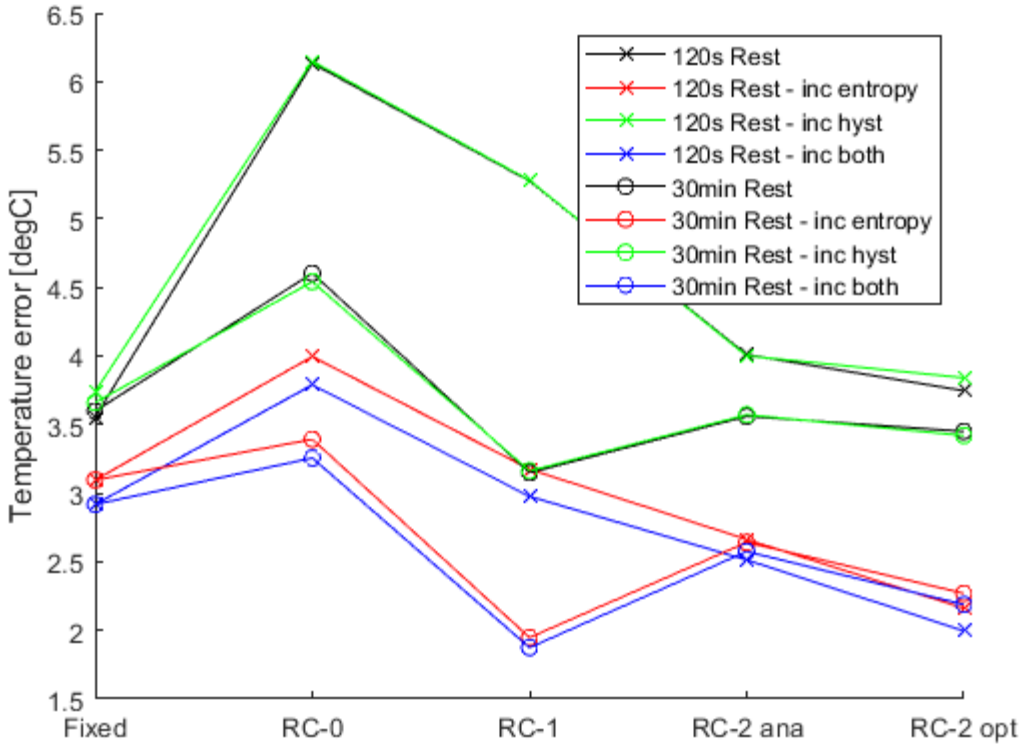

Figure 5.35 - Maximum temperature prediction error for TT lap vs test cell response.

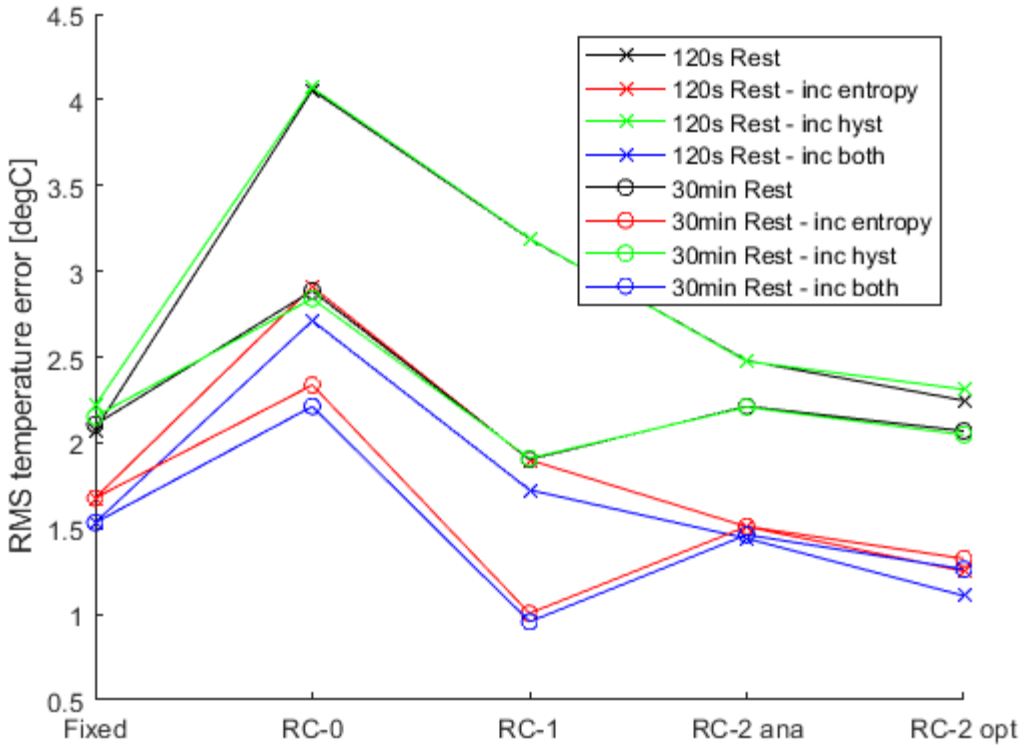

Figure 5.36 - RMS temperature prediction error for TT lap vs test cell response.

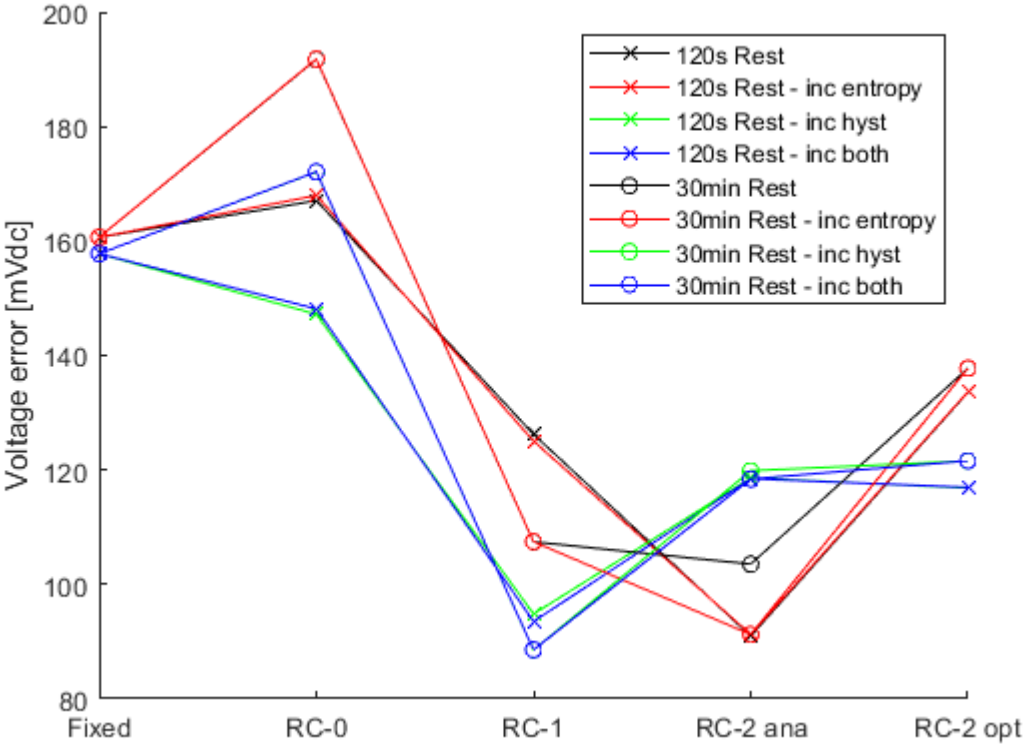

Figure 5.37 - Maximum voltage prediction error for TT lap vs test cell response.

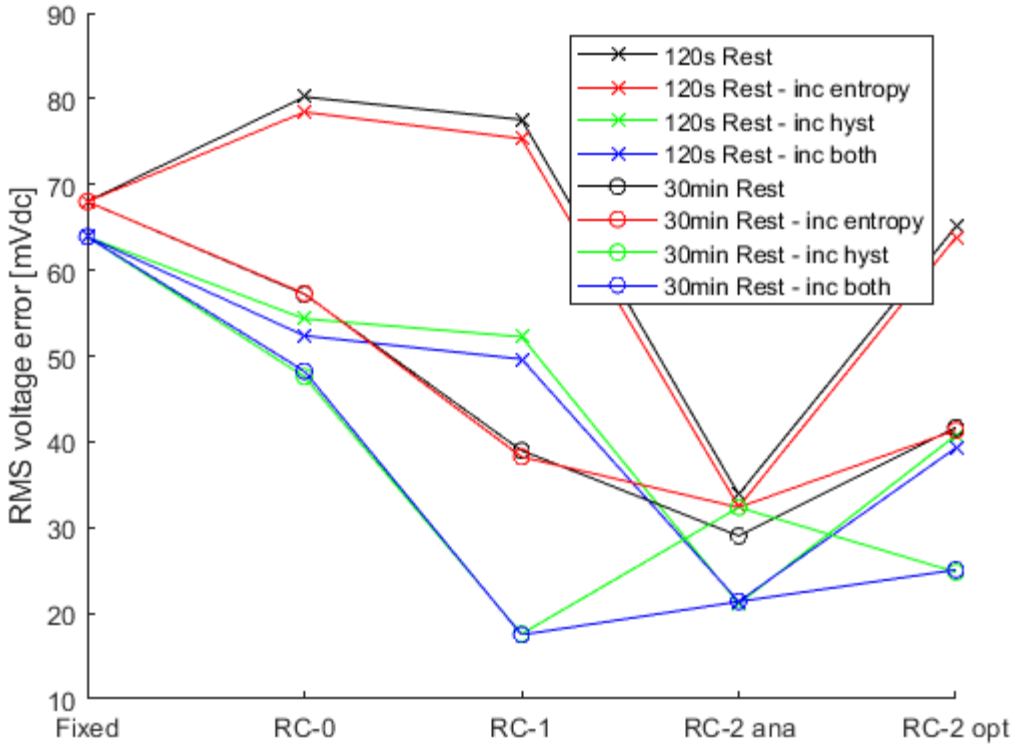

Figure 5.38 - RMS voltage prediction error for TT lap vs test cell data.

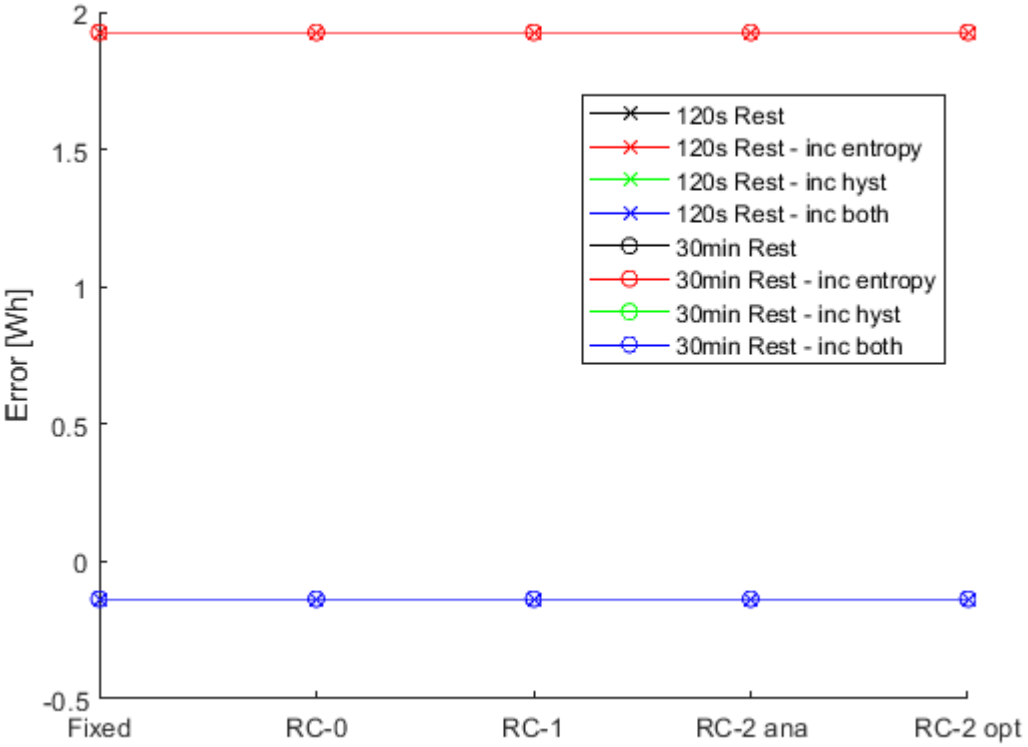

Figure 5.39 - State of charge error computed from OCV at end of test vs test cell response.

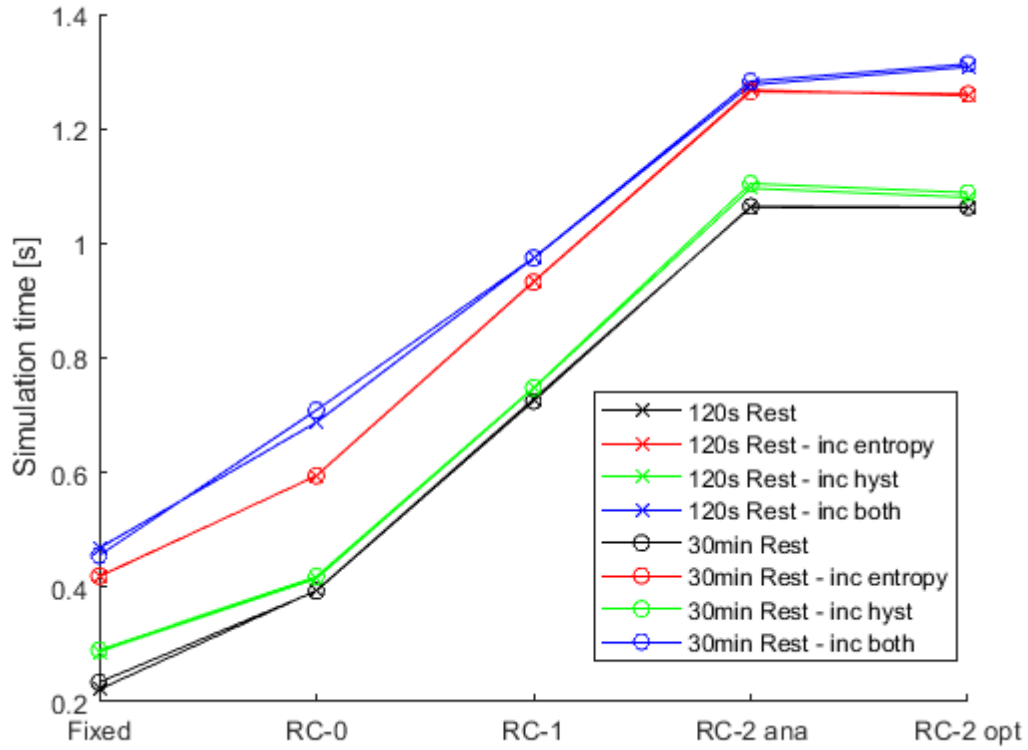

Figure 5.40 - Battery model simulation time comparison for a single TT lap with 1s timestep.

The optimisation procedure appears to have little benefit over the analytical solution. This is possibly due to poor optimisation setup as other authors have reported RMS tracking errors below 10mV [156]. However, the paper in question only utilises a pules discharge test for comparison and when exposed to a simplified approximation of a drive cycle in [157] the error grows to 2% of battery voltage or 80mV peak. This lends weight to the possibility that the voltage tracking error could be due to difficulties in the equivalent circuit model accurately modelling cell behaviour for highly dynamic loads due to simplifications inherent to its construction. Some research indicates the existence of a current dependency to the response that is not included here. However, a full investigation and/or the use of electrochemical models is far outside the scope of this thesis and the response of the models already included is more than adequate when considered in the context of the full vehicle response.

The shortened testing rest period is significantly detrimental to the RMS voltage error for lower-order models. This can be easily explained as the simple parameter extraction techniques rely on the rest period reaching a steady state. It appears possible to mitigate some of this using '*RC-2*' models due to the differing parameter fitting procedures. The issue then becomes, as expected, that simulation time increases with model complexity, Figure 5.40.

The state of charge error is shown in Figure 5.39. The influence of the hysteresis model on the state of charge error is significant as it is effectively an offset to the initial open-circuit voltage value. Ignoring this effect overestimates the charge available which is a costly mistake in the design process. One factor ignored in this investigation is the effect of battery degradation, as this is not required for a single discharge pure performance analysis. However, due to the realities of testing, multiple tests will be performed on the same cell resulting in different levels of degradation between tests. Further testing with more cells would provide a more satisfactory answer to this question however this is beyond the scope of the thesis.

The model chosen for inclusion into the powertrain model is the '*RC-1*' model using the 30min rest data as well as the hysteresis and entropy variation models as it offers a reduction in error of approximately 50% to both the temperature and voltage prediction when compared to the fixed method, as used in [16, 17]. It also has a smaller computational burden than the '*RC-2*' models which offer a debatable

improvement for the highly dynamic drive cycle under evaluation. The temperature prediction benefit is explored previously but the voltage prediction benefit equates to a reduction in powertrain power output prediction error of approximately 2% peak and 1% RMS.

The pack is constructed by combining individual cells in series and in parallel to get the voltage and capacity required. In a large battery pack, there can be 100s of individual cells and the battery pack response is simply a scaled-up version of the single-cell response. The cells are connected using busbars which are not included in the cell testing detailed previously. To keep track of the battery internal resistance the DC-link resistance is split into two parts, cell internal resistance and fixed internal resistance coming from the remaining DC components such as the DC-link cables and busbars. The resulting pack's internal resistance is simply determined as a combination of parallel and series resistors matching the battery configuration.

5.7. Conclusions

This chapter aims to develop a robust high-fidelity model of a modern high-performance electric motorcycle powertrain. This has been achieved by combining several previously published component models from different sources and validating this full model using real world data. There have been previous attempts to accomplish this however the powertrain model described within this chapter is more capable than any previously published works on electric motorcycle powertrain modelling [16, 17, 24, 91, 97], particularly concerning battery modelling, the inclusion of a wider variety of applicable motor constructions and improved loss modelling.

Notable attempts at electric motorcycle powertrain modelling are Dal Bianco *et al.* [17] and the Blissett model [16]. Dal Bianco *et al.* modelled the original Brunel University motorcycle. This motorcycle featured outdated low powered DC motor technology and therefore so did the model. The powertrain in question had an output of 50 kW, a 10.3 kWh battery pack and an optimal lap speed of 81.4 mph. In contrast, modern electric superbikes can produce over 170 kW using AC motors and drives, with 25 to 30 kWh battery packs and an average lap speed of 120 mph or more. A further issue involves the battery response, particularly the use of linear fits and lack of battery temperature modelling, a key performance differentiator. The model

described within this thesis overcomes all these issues and is superior in its accuracy, scope, and relevance to the current state of the art.

The Blissett model described in [16] has some similarities to the model described within this chapter but notable improvements have been made. These are the inclusion of IPM motor control in addition to SPM motor control. The inclusion of saturation models for L_d L_q and ψ and the improvement of motor mechanical and electrical loss modelling. Extensive advancements have been made in battery modelling concerning temperature and parameter variation. These inclusions have been verified using track and lab data and used to good effect to combat the difference in powertrain performance between reality and simulation.

Additionally, the chain loss model used by Blissett [16] has been investigated and found to have issues that have been addressed here. The motor mechanical loss modelling has been expanded to include the contribution from direct chain tension, an issue pertinent to chain drive vehicles such as motorcycles.

The final contribution comes in the form of a comprehensive evaluation of several different battery modelling techniques including the development of novel test procedures for the fast determination of cell entropic heating using low-cost equipment. The model prediction errors due to these techniques are evaluated and a short cell test procedure for the determination of relevant battery parameters is also described. This allows the rapid low-cost testing of many potential cell choices useful for the wider dissemination of battery testing.

There is a large interdependency between the powertrain and vehicle capabilities, especially with electric vehicles. For example, in the case of the UoN motorcycle, powertrain mass comprises over 65% of the vehicle mass. Following in Chapter 6, this powertrain model is combined with the vehicle model developed in Chapter 4 and used to develop a lap simulation for the isle of Man TT Zero amongst other competition events.

Cell choice, switching device choice and motor construction compromises can now be explored in the context of a full powertrain. Multiple motor construction methods can now be evaluated allowing both the optimisation of racing machines and for developing cost-effective compromises in mass-market offerings.

6. Full Vehicle Lap simulation

Having developed and validated a model of both the powertrain and the motorcycle performance envelope in Chapters 4 and 5 the next step is to use these models to predict the full vehicle performance over a target operating cycle. As the target operating cycle depends on the machine parameters it is important capture this interaction.

The battery, electric motor design, aerodynamic design and chassis design are all highly interdependent and simulation is key to understanding the inherent design trade-offs before arriving at a race event. To this end, it is important to be able to determine parameter sensitivities using a lap simulation that accurately covers a wide operational envelope. This is especially useful concerning long lead time decisions, for example, the centre of gravity location, battery, electric motor, and inverter choices.

This chapter starts by outlining the lap simulation approach chosen in Section 6.1. A more detailed description of the rationale behind the choices included in the associated sub-sections. The process for filtering and defining the racing line from raw GPS data is covered in Section 6.2. Section 6.3 contains the method for determining performance over the target course and the implementation of energy management strategies. The validation of this approach, using lap data collected at various events by the University of Nottingham motorcycle, is tackled in 6.4. Section 6.5 contains a comparison of the model to other electric motorcycle modelling methods.

6.1. Lap Simulation Approach

The most common approach used to assess the performance of racing vehicles is the time taken to complete a lap of a pre-defined course. This course can be defined in several ways, and the objective is to complete the course in the minimum time for the given vehicle constraints.

As with all simulation approaches, there is a trade-off between accuracy, simulation time, and setup time. As the design freedom is extremely broad for electric motorcycles due to the lack of regulation and the relative novelty of the modern design work, it was deemed appropriate to develop a relatively simple simulation capable of rapid changes for evaluating the relative sensitivity of design choices. This

can then be followed by further work to improve modelling in areas that show high sensitivity.

The lap simulation technique employed here uses the GGV surface as developed in Chapter 4 and the powertrain model developed in Chapter 5. The term GGV corresponds to the three axes of the plot, lateral acceleration ‘G’, longitudinal acceleration ‘G’ and velocity ‘V’. The GGV response structure also contains the lateral and longitudinal tyre forces associated with each limiting point. The lap simulation assumes a point mass motorcycle and begins by apex finding similar to the approach outlined by Hausner and Saccon [18]. Here, the road curvature is determined from the path definition and the maximum speed at each point is determined from the lateral force limit of the GGV response and the vehicle mass.

An overview of the lap simulation procedure is given below with further details on the specific areas given in the following sub-sections:

1. A vehicle path is determined. The model used in this thesis is commonly referred to as a fixed trajectory model. Here, the vehicle path is determined from a previous lap of the same course. The GPS data points associated with the lap are filtered and converted into x, y, z coordinates. The vehicle must achieve these positions, see Section 6.2.1
2. The x, y curvature at each point in the track is then determined from this data. This is handled in Section 6.2.3.
3. The vehicle performance envelope is determined for the motorcycle and the powertrain and battery initial conditions set. This consists of the limiting GGV performance envelope developed in Chapter 4 and the starting battery open-circuit voltage, hysteresis state and temperature, as described in Chapter 5.
4. Through determining the path curvature and limiting lateral performance of the machine, the maximum speed at all points, from a lateral force perspective, can now be obtained. This procedure is detailed in Section 6.3.1.
5. The next task is to include the braking limitations for the vehicle. As the braking phase will end with a minimum speed, set by the limiting lateral force determined previously, this is handled by iterating the track in reverse. Starting at the end of the lap, if the next point closer to the start is of a higher velocity than the current point the maximal braking force at the current point

is determined. This force is utilised in conjunction with the vehicle's effective mass to determine the resultant change in velocity over the spatial step. If this velocity is lower than that obtained from the lateral force constraint, the velocity is retained and the simulation moves to the next point. The regeneration power developed during this timestep is also captured. This process is detailed in Section 6.3.2.

6. Having determined the velocity trace due to the lateral and deceleration limits the influence of the longitudinal acceleration limits and battery needs to be determined. This is handled starting at the beginning of the course. If the velocity of the subsequent point is higher than the current then the acceleration limits are determined at the current point, accounting for powertrain and chassis limit performance, and the resulting velocity at the next spatial step determined. This velocity and distance are used to determine a resultant time-step which is used to determine the change in battery state. This process is detailed in Section 6.3.3.
7. The inclusion of deployment strategy involves setting an index of maximum motor torque limits corresponding to each spatial step. As the powertrain evaluation occurs, this additional torque limit must be respected. This process is outlined in Section 6.3.4.

6.2. Vehicle Path

There are many options for path definition ranging from the use of optimal control theory to determine ‘ideal’ vehicle paths given road constraints [17, 23, 49, 51, 158], to the idealisation of the course as a series of constant radius arcs and straight lines, as per the 1950’s Mercedes F1 cars [159].

Some electric motorcycle simulations have ignored the path curvature and simply taken previously recorded cornering speeds [24], while some have described the track boundaries and allowed the simulation to generate its path [17, 158]. This has its benefits and drawbacks. Allowing the vehicle path to be optimised for the vehicle setup can result in greater sensitivity to major setup changes, as these can affect the optimum racing line. However, the path generation procedure is non-trivial and dependent on vehicle model tuning. This can therefore result in the potential to generate slower or non-feasible solutions for human pilots if not managed correctly.

In this thesis, the path is defined from a filtered GPS trace of a racing lap of the course on a similar powered machine. This was chosen as it is a significantly more appropriate solution than the use of pre-recorded corner speeds avoiding the additional computational expense of determining the vehicle path. Also, the need to accurately define course boundaries and checkpoints with their associated errors and issues is avoided. The GPS data required is readily available for multiple tracks due to the widespread use of GPS-based data logging on race vehicles.

The use of fixed-point input data leads to working in the spatial domain. It also constrains any optimisation as it prevents variations in racing lines. However, a rider will attempt similar lines for the electric machine as they are accustomed to using with their IC machine, especially for high-risk road racing. Evidence for this can be seen in the UoN 2018 race data, illustrated in Figure 6.1. This data set contains three racing laps taken from an IC machine and the race lap from the electric machine. Both machines were ridden by the Nottingham rider at the same TT event in 2018. The origin of this dataset is detailed in section 6.3.1. Here, there are several instances of the rider unexpectedly reducing the throttle in anticipation of a corner that requires deceleration using a higher speed IC machine but not for the electric machine.

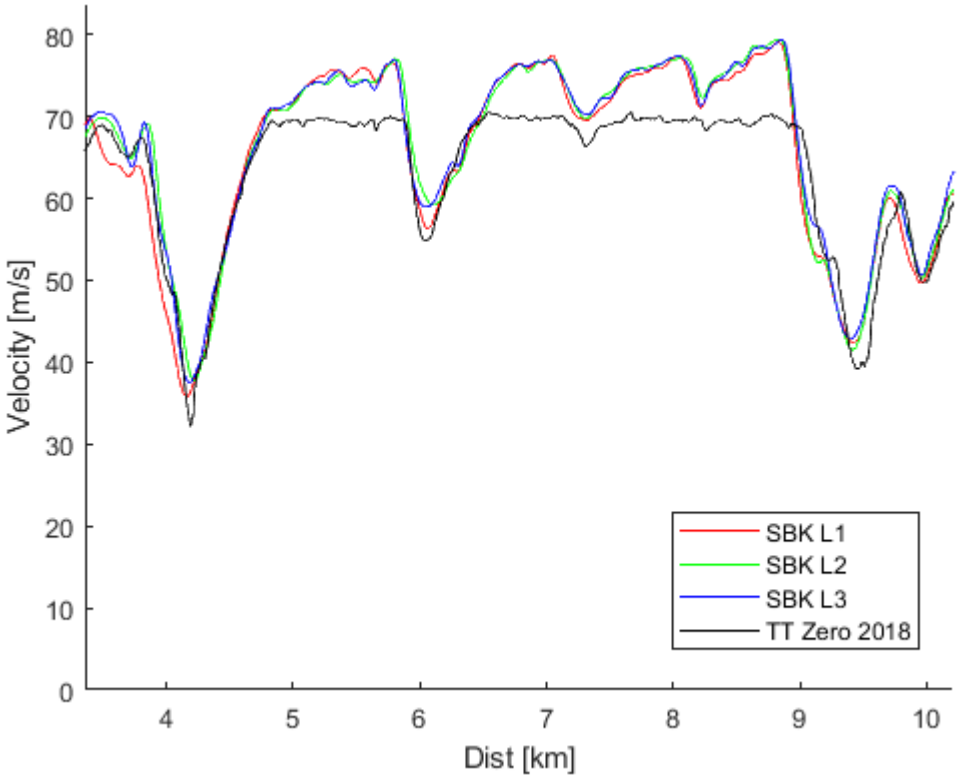

Figure 6.1 - Lap velocity overlay showing instances of phantom braking using the electric machine.

6.2.1. Path Generation

As GPS data is simply a collection of reference points on the surface of a globe the raw GPS data is converted into X-Y coordinates using an azimuthal equidistant projection. Of the many differing projection methods available [160], the azimuthal projection method is chosen as the GPS data for a racetrack can be reasonably assumed to be centred around a single point. This point is used as the point of tangency. The area to be projected is also small (in comparison to the globe) and localised to the point of tangency minimising the shape distortion. The flexibility to input any track around the globe and repeatably ensure minimal distortion is key. A MATLAB script is also available in the public domain to automate the conversion to planar coordinates [161]. The projection method involves idealising the globe as a sphere and projecting from the point of tangency to the point of interest. The distance from the projection point to the points collected for the track map is the true distance and direction over the idealised sphere [162].

As an example of the process, the 2018 TT track data is utilised as follows. The lap data is sampled at 200 Hz and is discontinuous due to numerical truncations. Additionally, the GPS position updates at a slower rate than this sampling frequency. To resolve these issues, and avoid large discontinuous lateral accelerations, the input data is smoothed and re-sampled. An example of the effect of path smoothing is illustrated in Figure 6.2.

Track data is first smoothed using a Savitzky-Golay (SG) filter [126]. The filter employs a moving window with a least-squares polynomial fit. The resulting X-Y coordinates are first graphically compared to the original data. The goal of the filtering is to remove the discontinuities but avoid over smoothing as this results in artificially high lap times due to smoothing of corners.

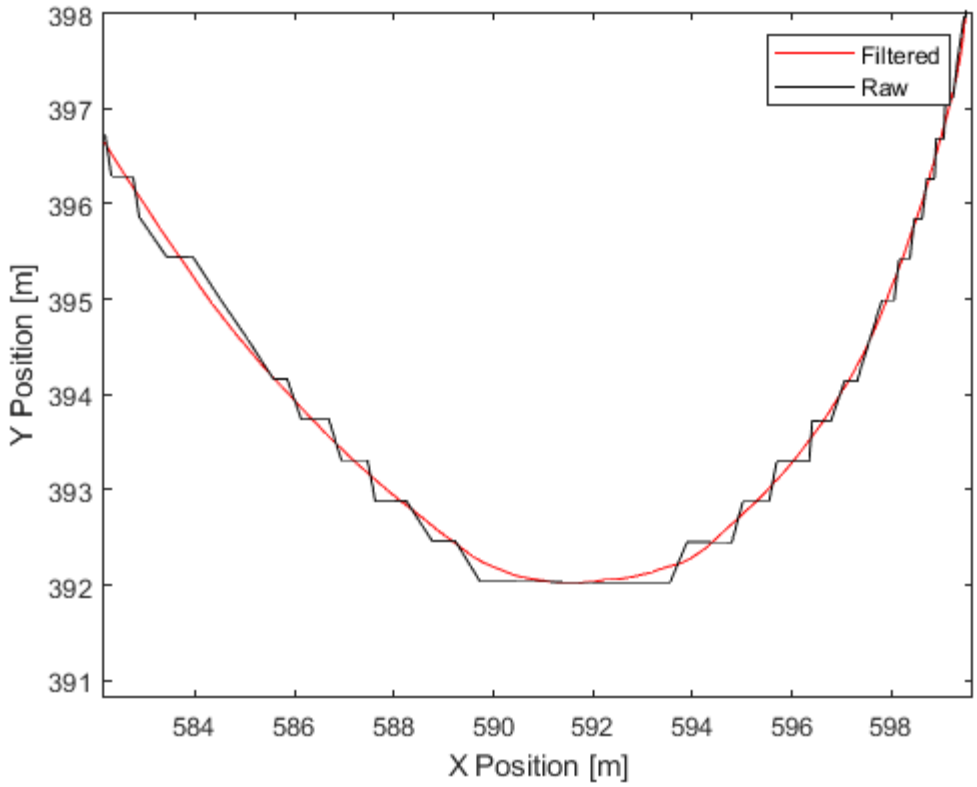

Figure 6.2 - Comparison of Raw and Filtered Path Data for the Isle of Man TT Mountain Course

The path is further checked for over-smoothing by comparing the raw path trace to the smoothed path at the tightest radius turns. For the TT mountain course, 'Ramsey hairpin' and 'Governor's Bridge' were singled out for further inspection.

This is accomplished by first determining the distance from the input data to the filtered data point, the 'residual displacement vector magnitude'. To obtain an expression for which side of the filtered path the unfiltered point lies, the sign of the determinant of the cross product of the unfiltered path vector and the displacement vector to the filtered path is obtained.

By multiplying these two values together it is possible to obtain the residual displacements and their direction from the filtered path. This residual displacement is shown in Figure 6.3 and should consist of only noise. It is possible to verify this simply by inspection. To perform a more rigorous evaluation a 'lowess' fit, locally weighted linear regression [126], is applied to the residual displacement error for the section under investigation. This is to attempt to identify any underlying trends indicative of over smoothing. Such an error would appear as long periods of single-sided residual displacement error. This would be highlighted by a deviation in the lowess fit from zero.

The example of this process using a 3rd order, 349-point window, Savitzky-Golay filter on the TT lap input data at 200 Hz sample frequency is shown in Figure 6.3 for the two tightest corners. This clearly shows that there is no significant systematic deviation of the filtered path from the input path and therefore this input path has not been over smoothed. These filter settings were retained for this lap profile.

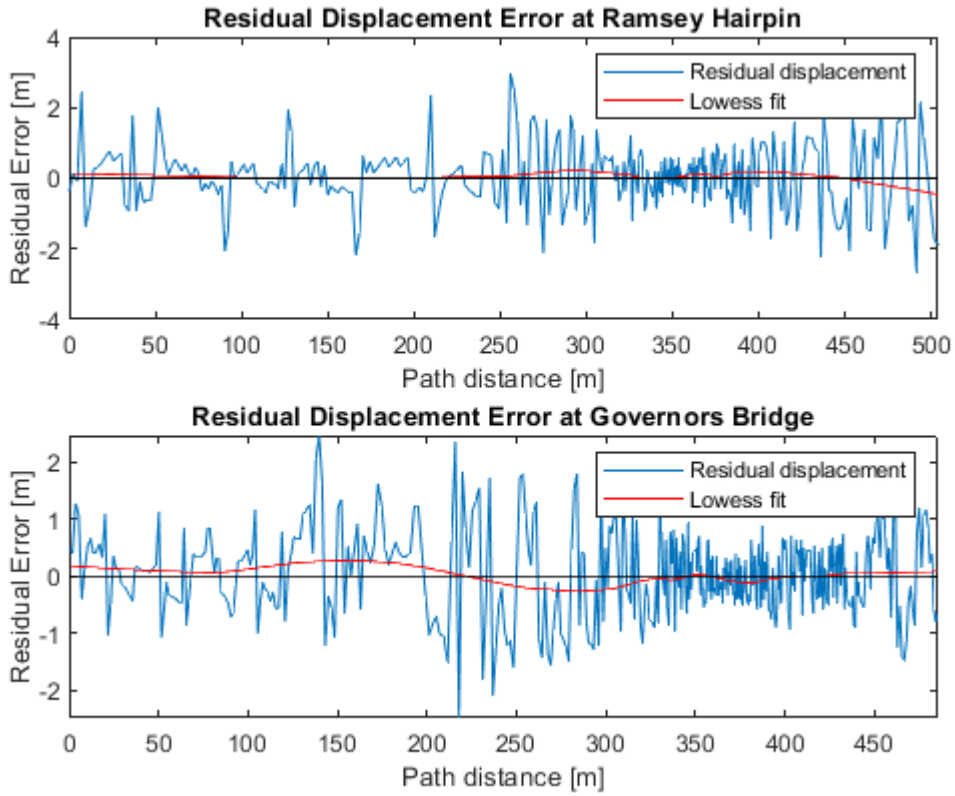

Figure 6.3 – Comparison of raw path data to smoothed path data at check points.

6.2.2. Path Length

There are multiple methods of computing the path length ranging from spline length estimation using Gaussian quadrature [163] to the simple Euclidian method taking the straight-line distance between fixed points. The distance 'dl_{euc}' is given by the equation below for points in an x, y, z axis system but will always be an underestimate of a circular path:

$$dl_{euc} = \sqrt{dx^2 + dy^2 + dz^2}$$

A further method is the fitting of a circular arc in 3D between 3 points and calculating the distance between the points 'dl_{arc}' as arc lengths. This is performed on every consecutive point, giving two values of arc length for every segment bar the first and

last. The mean of these values is taken as the segment length. The method for obtaining these arc lengths is as follows. First, a plane is described by the three $x_0y_0z_0$ coordinate vectors (U, V, W) The unit normal vector to this plane '$\widehat{N}$' is used to determine two orthogonal unit vectors. These are used to generate the 3x2 rotation matrix 'R' that maps the 3D coordinates onto the 2D plane $x_{arc}y_{arc}$. Using these 2D coordinate vectors (u, v, w), the 2D circle centre 'o_{arc}', segment angles 'θ_1, θ_2' and radius '$r_{arcpath}$' are obtained and used to calculate the sector arc lengths:

$$\widehat{N} = \widehat{UV} \times \widehat{VW} \tag{6.1}$$

$$R = \left[\widehat{UV}, \widehat{VW} \times \widehat{N}\right] \tag{6.2}$$

$$u = R^T U, \qquad v = R^T V, \qquad w = R^T W \tag{6.3}$$

$$o = \begin{bmatrix} v_x - u_x & v_y - u_y \\ w_x - u_x & w_y - u_y \end{bmatrix}^{-1} \begin{bmatrix} \left(\left(v_x^2 + v_y^2\right) - \left(u_x^2 + u_y^2\right)\right)/2 \\ \left(\left(w_x^2 + w_y^2\right) - \left(u_x^2 + u_y^2\right)\right)/2 \end{bmatrix} \tag{6.4}$$

$$r_{arcpath} = |u - o_{arc}| \tag{6.5}$$

$$\theta_1 = \cos^{-1}\left(\frac{\overrightarrow{o_{arc}u} \cdot \overrightarrow{o_{arc}v}}{|o_{arc}u| \times |o_{arc}v|}\right) \tag{6.6}$$

$$dl_{arc} = \theta_1 r_{arcpath} \tag{6.7}$$

A comparison of the effect of down sampling the input data on path length for both the Euclidian and arc-length approaches is given in Figure 6.4. This results in a total path discrepancy of only 3.6 m for the arc fitting versus 46.6 m for the Euclidian when down sampling 250 times. The arc fitting method is selected. When compared to the original data over the 60 km track with an average speed of circa 120 mph this is a potential error of 0.06s or ~0.005% and is insignificant. Further mesh sensitivity work is undertaken in 6.2.3.

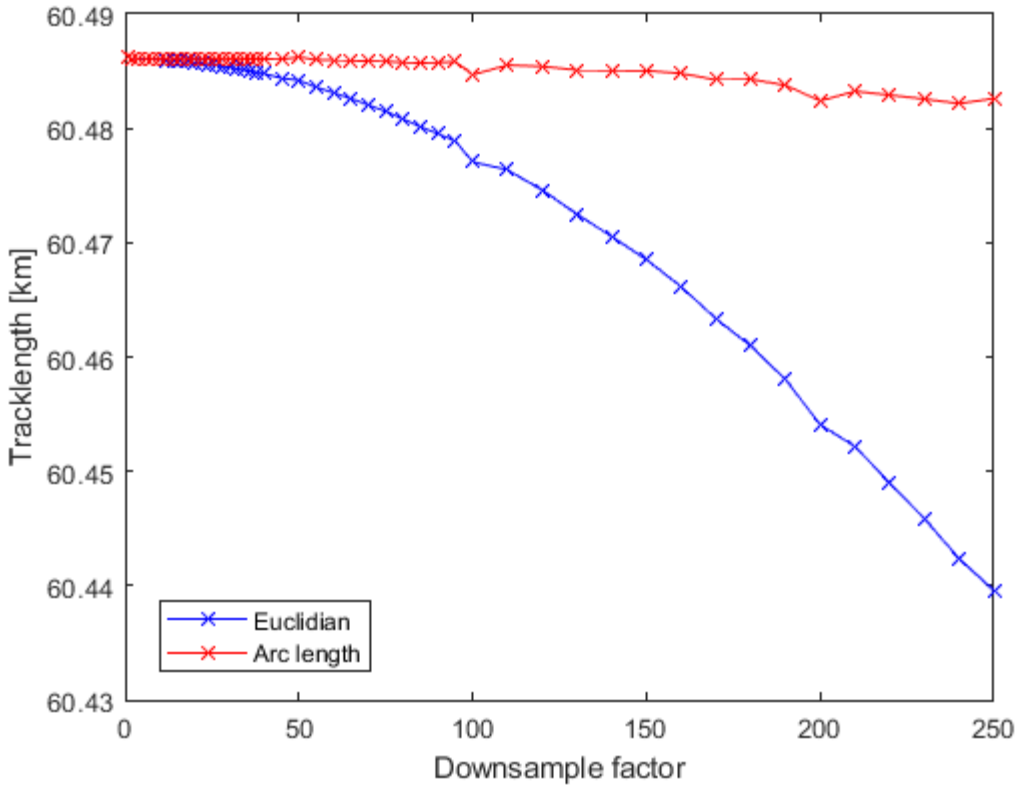

Figure 6.4 - Comparison of track length calculation methods and down sampling rates.

6.2.3. Path Curvature

To determine the maximal cornering velocity, the path curvature is required. The path curvature can be easily obtained similarly to the previous section, but utilising xy coordinates only. Curvature magnitude is $1/r_{2Dpath}$ and its sign is taken from the sign of the determinant of the cross product of the xy path vectors. However, this process generates a noisy discontinuous signal. This noise is commonly addressed using a 1 Hz lowpass filter [164]. To attempt to improve on this, a spline fitting technique was used to impose a continuous curvature constraint for the path. The method used is described as follows.

For a plane curve given by the equations $y = y(s)$ and $x = x(s)$ the curvature 'κ' at a given point can be determined from the following standard formula by taking the first and second derivatives of the functions $x(s)$ and $y(s)$, where dots denote the derivative with respect to distance 's'.

$$\kappa = \frac{\dot{x}\ddot{y} - \dot{y}\ddot{x}}{(\dot{x}^2 + \dot{y}^2)^{3/2}} \tag{6.8}$$

A smoothing spline is fitted to a 'window' of data, and it is this spline that is then differentiated at its central points. The derivatives at these central points are then stored and the process repeated. As this is computationally expensive, a stepping procedure is used to move the window by multiple points (its step size).

To ensure that the spline fitting is stable the 'window' only moves a fraction of the step size, and the resulting overlapping steps are compared to the values for those in earlier and later 'windows'. A mean of these derivatives can then be taken. The comparison of the error between these derivatives indicates the stability of the path fitting. An outline of this overlapping spline differentiation method is illustrated below:

$$\begin{bmatrix} \frac{dx_a}{ds_a} \\ \frac{dx_b}{ds_b} \\ \frac{dx_c}{ds_c} \end{bmatrix} = \begin{bmatrix} \frac{dx_{1a}}{ds_{1a}} & \frac{dx_{2a}}{ds_{2a}} & \frac{dx_{3a}}{ds_{3a}} & \cdots & \cdots \\ \cdots & \frac{dx_{2b}}{ds_{2b}} & \frac{dx_{3b}}{ds_{3b}} & \frac{dx_{4b}}{ds_{4b}} & \cdots \\ \cdots & \cdots & \frac{dx_{3c}}{ds_{3c}} & \frac{dx_{4c}}{ds_{4c}} & \frac{dx_{5c}}{ds_{5c}} \end{bmatrix} \tag{6.9}$$

$$\frac{dx_3}{ds_3} = mean\left(\frac{dx_{3a}}{ds_{3a}}, \frac{dx_{3b}}{ds_{3b}}, \frac{dx_{3\ldots}}{ds_{3\ldots}}, etc\right) \tag{6.10}$$

For an initial comparison, a window of 70 points was used for the spline fit with a step size of 11 points, and an average over 3 steps was taken.

The effectiveness of these path curvature determination methods is shown in Figure 6.5. Here the TT lap curvature data was computed by the spline method, the 2D arc fitting method and the filtered 2D arc method. This data is also compared to an extract of 'optimal' curvature data for a TT electric motorcycle published by Dal Bianco *et al.* [17].

A comparison of spline and arc fitting at this point indicates the spline fitting method is effective at peak 'shaving' when compared to the unfiltered arc procedure. It is however still severely affected by noise at the down-sample rate (10) used for this plot. Manual adjustment of smoothing spline parameters can improve this markedly but is not a feasible solution as the adjustment varies with the down-sample factor.

The comparison to Dal Bianco *et al.* [17] is interesting as the 'Optimal lap' method appears to suggest a route with higher curvature for a shorter period. This contrasts with the measured route which represents a rider attempting to smooth their path as

much as possible to maintain the highest velocity through a corner. This could be an interesting path variation but highlights an issue with the optimal path method whereby the path chosen is dependent on the accurate modelling of the underlying system, and therefore an additional source of variation to understand and control.

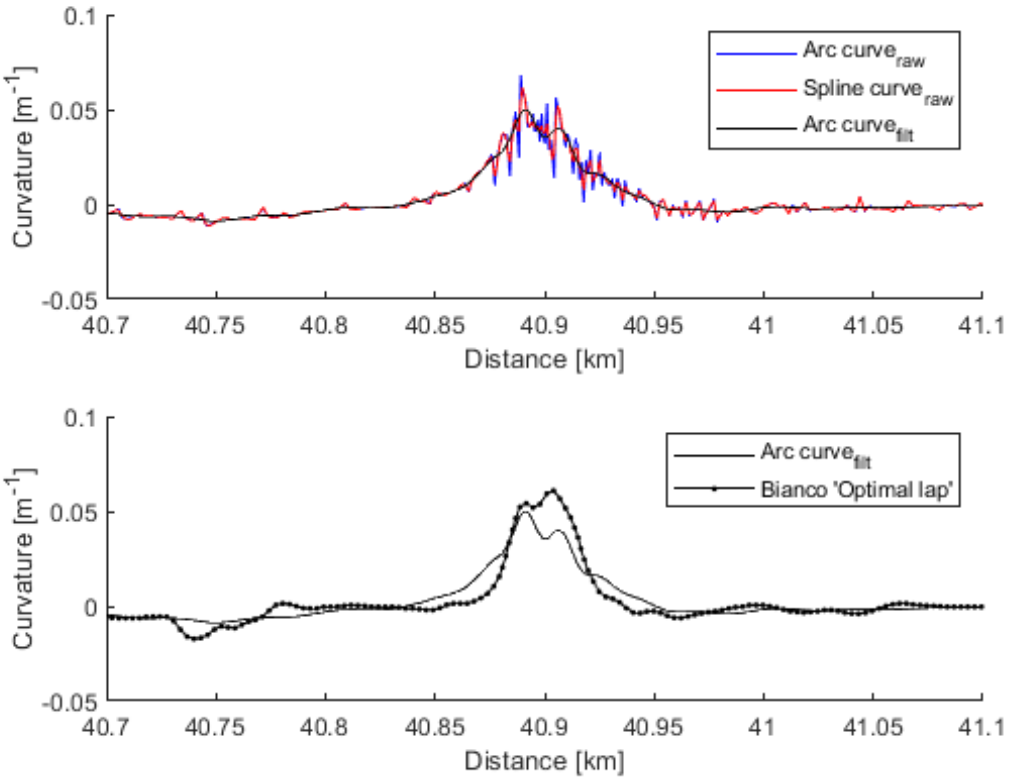

Figure 6.5 - TT course curvature taken shortly after Ramsey hairpin.

This comparison is only part of the consideration required to choose a curvature determination method. It is also important to balance computational efficiency and accuracy. To investigate this, the effect on the computational time of further down-sampling of the input GPS points and the associated lap time variation is compared. Note that all optimisations for a particular track are completed using the same down-sample factor and path smoothing parameters to avoid the introduction of additional sources of variation.

The only data available for direct comparison here is the 2018 UoN TT Zero race lap. However, as the effects of noise and over-smoothing will be most noticeable for the highest performance machines an additional rough data point can be generated using the ‘perfect lap’ of fastest sector times for the Senior TT [165]. This combination of sectors gives a flying lap time of 995.7 s and a standing start lap time of 1001.7 s,

generated by taking the approximately 6 s difference in first sector times between flying laps and standing start laps from published 2015 senior TT sector times [166].

The Senior TT utilises modified road bikes, therefore approximate specifications for these machines are publicly available. For example, the BMW HP4 Race, similar to that used by P. Hickman in the 2018 TT, gives a peak power of 160 kW and a bike mass of 171 kg [167]. A second example is the British Superbike specification Ducati Panigale V4 R built for M. Dunlop in 2020. This has a reported 171 kW and bike mass of 166 kg [168]. A rider weight of 85 kg has been assumed.

To investigate the effects of path smoothing the electric motorcycle simulation was used here with the vehicle mass and CoG position set to best approximate the publicly available data. In addition, the powertrain torque and battery limitations are removed leaving just a maximum power limit, which was set to match the IC machine's maximum output. This is an extremely rough approximation that ignores several factors such as gear changing, validated drag values for the machines in question amongst several other simplifications. As a result, this is not used for validation purposes but is used here to magnify the effects of path curvature variations. The lap times generated for the S1000RR and the V4R are 991 s and 989 s, respectively, when down-sampled 10 times (20 Hz) and 988 s and 986 s, respectively, when down-sampled 50 times (4 Hz). Both times are within 1.5% of the estimated best lap.

Figure 6.6 gives a summary of this investigation. At high down-sample rates, a decrease in lap time is found due to over smoothing and a reduction in lap distance. Conversely, at low down-sample rates with minimal filtering, there is an increase in noise, generating artificially high curvatures and resultingly higher lap times. The generation of artificially high lap times can be seen in the comparison of the filtered and unfiltered arc-fitting methods.

The filtered arc method was trialled using a Butterworth filter and MATLAB ‘filtfilt’ function to ensure zero phase shift [126]. Cut-off frequencies of 1, 1.25, 1.5 and 2 Hz were trialled. Closer inspection of the velocity trace generated revealed evidence of noise influencing some corner speeds using the 2 Hz filter. The 1, 1.25, and 1.5 Hz performed similarly with slight variations due to relative levels of smoothing.

With the spline-fitting technique, some promising results can be seen reducing peak values without losing the underlying detail. However, it still suffers significantly from

noise. This can be reduced with down-sampling and with manual adjustment of spline-smoothing parameters. Ultimately attempts to further filter this signal were unsatisfactory and defeated the purpose of using the spline technique. As can be seen in Figure 6.6, both methods give similar lap time results with down sample factors between 50 and 100 (representing 4 and 2 Hz input signals). Minor variations between lap speed traces can still be seen, with the spline method typically reporting higher lap times and lower apex speeds.

The benefit to computational time of down-sampling is also clear. A down-sample factor of 50 (4 Hz) was chosen as this represents a lap time variation of only ~0.3% (2.85s) but a 630% computational time reduction when compared to a down sample factor of 10 (20 Hz).

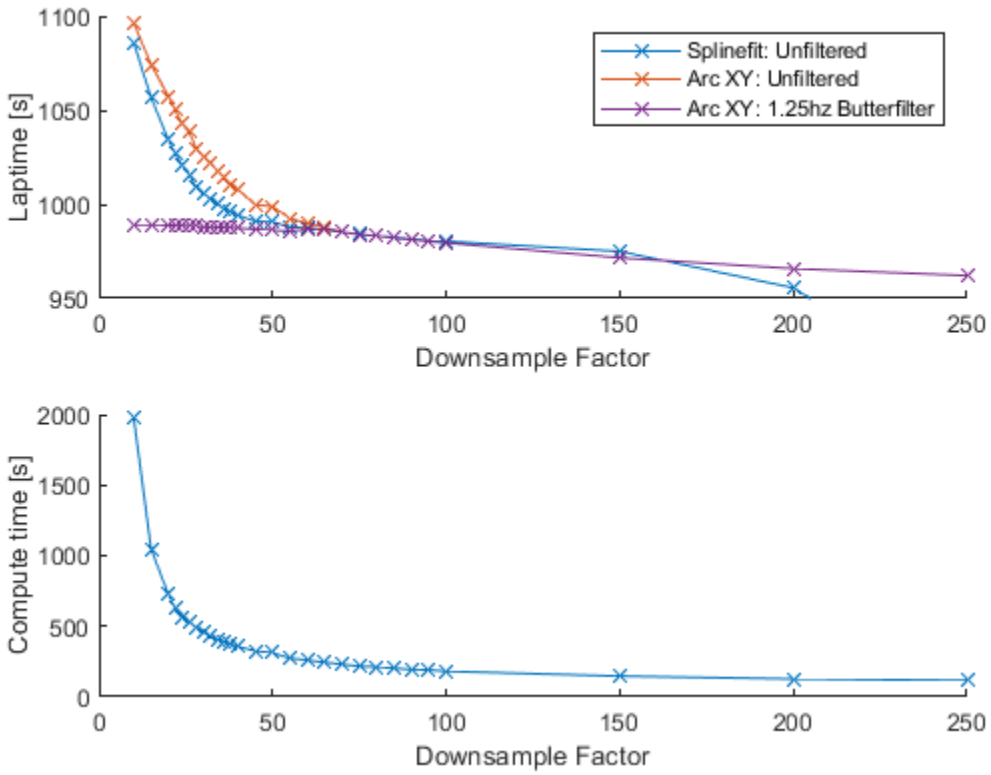

Figure 6.6 - Effect of down sampling on TT Superbike lap time and computational time

Due to the large variations with the spline technique and the desire to avoid repeated adjustment of spline smoothing parameters for each down-sample level, the simpler more conventional filtered arc technique with a Butterworth filter was selected for use in the remainder of this thesis.

To select the cut-off filter frequency for this filter, simulations using the 2018 TT path data and the UoN machine parameters (given in Appendix B – Nottingham Electric Motorcycle Parameters) were graphically compared to laps generated using the UoN 2018 machine. The effect of the 1, 1.25 and 1.5 Hz filters was compared, the variation between these was small and the 1.25 Hz was selected as the best compromise. Further investigation is not appropriate here, as due to issues with data collection only one complete dataset for the TT is available. With only one complete lap for the 2018 TT, it is difficult to distinguish measurement errors from rider errors or simulation errors. In future work, multiple datasets should be used to improve accuracy and confidence. The resulting fit is shown and explored in more detail in Section 6.4.3.

6.3. Path following

Having defined the target path, the next task is to determine how the vehicle follows this path with the maximum performance possible. Due to the significant compromises in terms of vehicle mass and battery sizing, the fastest lap time is not necessarily maximal acceleration at all points. Therefore, the inclusion of energy management strategies is also important.

6.3.1. Lateral Acceleration

The lateral acceleration required for the motorcycle to follow the given path is dependent on the motorcycle velocity and path curvature. The instantaneous path radius is obtained from the curvature as outlined in the previous section. By combining this radius with the GGV performance envelope developed in earlier chapters and the equation for steady-state circular motion ($a = v^2/r$), it is possible to obtain a steady-state velocity limit for every point on the track.

To compare cornering speeds from the same rider with the same tyres on his IC machine and the UoN electric machine a graphical data-trace was obtained from the rider (the rider was unable to share the underlying data file). Due to the graphical data output, the lap data was then extracted from these plots using a pixel identification process [169]. The data from three laps was converted and overlaid to identify conversion errors and rider lap variations. Sadly, it was not able to be determined if the speed trace provided was based on wheel speed or GPS speed. The reconstructed lap distance was shorter than the distance obtained using the 2018 TT GPS trace and the published lap distance. To better align the data traces, a distance scaling factor of

1.027 was used for the superbike data. This uncertainty reduces the usefulness of the data but does allow for some qualitative evaluation.

Figure 6.7 contains an extract of the data showing the comparison using the scaled speed and distance trace. This is taken from a part of the lap where the electric machine's top speed restriction has minimal interference. From this evaluation, it is evident that the corner speeds of the IC superbike slightly exceed those of the electric superbike. This discrepancy is of the order of 1-2 m/s when the speed trace is unscaled but increases to 2-4 m/s if the speed trace is scaled in conjunction with the distance trace. The electric machine is approximately 120 kg heavier. This difference is likely due to both the load sensitivity of the tyres and the rider's familiarity with the respective machines.

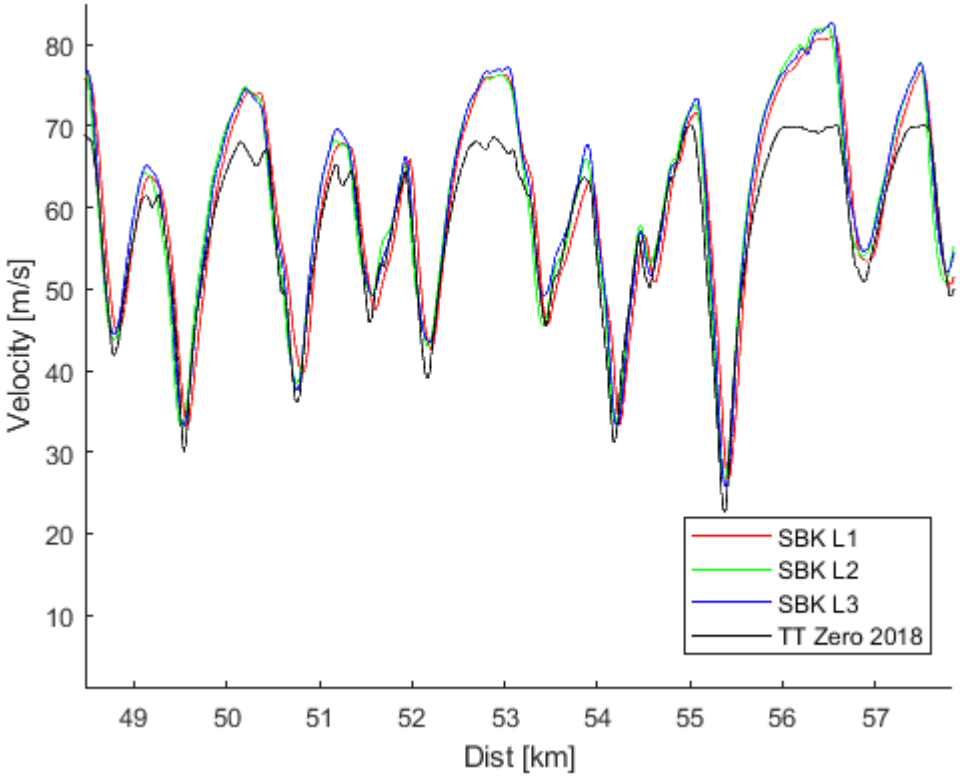

Figure 6.7 - Extract of velocity data comparison between EV and IC superbikes ridden by the same rider at the TT 2018.

As the maximal apex speed the motorcycle can achieve is important to the performance of the machine over the lap, it is important to test the model sensitivity to this parameter. To demonstrate the model sensitivity to lateral friction coefficient variation Figure 6.8 shows two plots. The first is the direct effect of scaling vehicle mass on the minimum radius of curvature at specific velocities using the UON2018

TT motorcycle and the tyre parameters from De Vries and Pacejka [15]. The second plot directly scales the lateral friction parameter to highlight the vehicle model sensitivity to lateral friction coefficient variation possible with other tyre data sets.

This plot performs two functions. Firstly, it outlines the effect of the restrictions in the tyre data set used as highlighted in Chapter 4. This data set is retained due to its availability in the public domain, but future work would ideally include a data set utilising sensitivity to this parameter. In response to this future need, the second plot is used to demonstrate the underlying model retains sensitivity to this parameter if the tyre model is altered.

As can be seen in the second plot the velocity achieved at a given radius of curvature correlates directly with the tyre lateral friction coefficient. This is expected and has implications for the lap time response as if a motorcycle can traverse the corner apex at a higher speed it can brake later at the end of the previous straight and begins the following straight at a higher speed. It is therefore concluded that the developed model retains the required sensitivity even though the underlying data set does not.

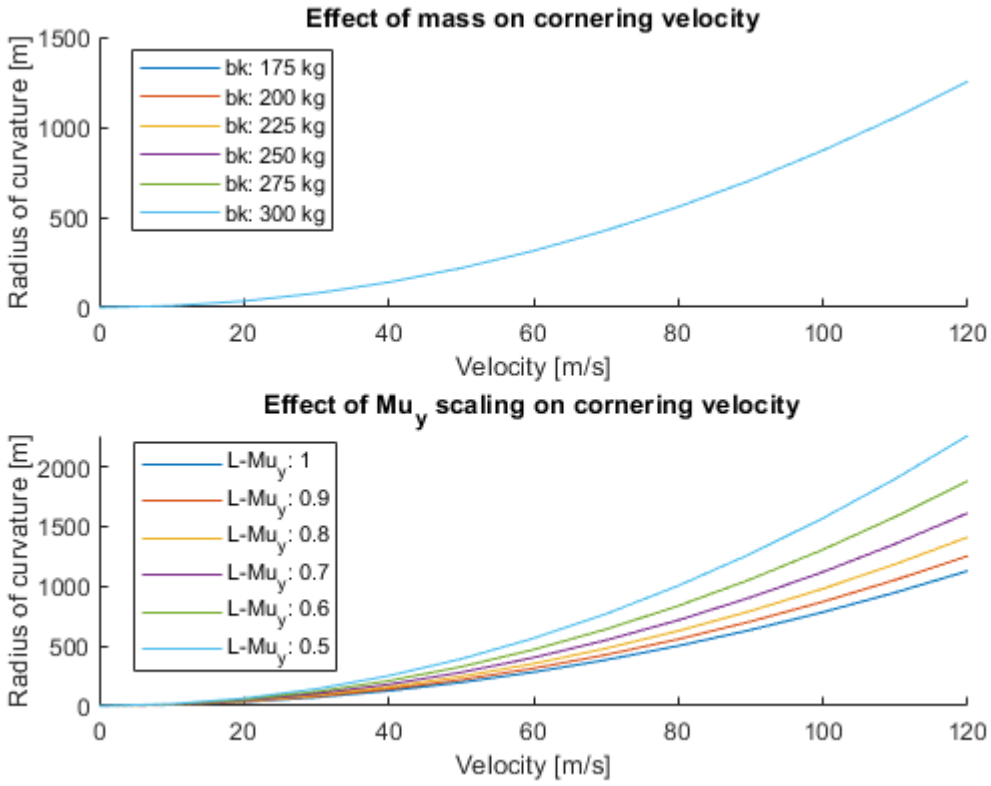

Figure 6.8 - Effect of mass and lateral friction coefficient on cornering velocity

6.3.2. Longitudinal Deceleration

A racing vehicle seeks to reduce its lap time by maximising the velocity at each point along the path. Thus it follows that the motorcycle will either be applying maximal acceleration or deceleration unless instructed otherwise by energy deployment strategy.

The motorcycle velocity limitations due to lateral force limits, and the corresponding radius of curvature at each point have already been determined. This phase is concerned with the approach to these minimums. To obtain a unique solution for the braking phase, backwards integration is required from the local minimums identified by the lateral acceleration limits.

Here, if the velocity of the point closer to the start of the lap is higher than that of the current point then the longitudinal force limit needs to be computed. Limiting braking performance is independent of the powertrain state as the mechanical brakes are sufficient to lock both wheels. Therefore, the maximal lateral and longitudinal tyre forces at each tyre and the corresponding vehicle deceleration rate can be found by interpolating the GGV performance envelope computed in Chapter 4.

Using this maximal tyre force, plus the drag and rolling resistance contributions, the road inclination angle and the vehicle equivalent mass a longitudinal acceleration can be computed. This acceleration is assumed fixed over the spatial step and the velocity at the previous point determined. This continues to the beginning of the lap.

The deceleration force is taken from the sum of the available longitudinal tyre forces 'F_{fx}'and 'F_{rx}', the aerodynamic drag 'F_{bx}', the rolling resistance 'F_{rr}' and the longitudinal component of gravity in the motorcycle frame caused by the pitch angle required to negotiate the change in height between the two points 'F_{hill}'. Additional coefficients used include '$C_{db}A$' and '$C_{dw}A$' representing combined terms for the coefficient of drag combined with respective effective area terms for the motorcycle body and winglet.

$$F_{hill} = m_{mc} g sin\theta \tag{6.11}$$

$$F_{bx} = \frac{1}{2} \rho_{air} v^2 C_{db} A \tag{6.12}$$

$$F_{wx} = \frac{1}{2}\rho_{air} v^2 C_{dw} A \tag{6.13}$$

$$a_x = -\left(\frac{F_{fx} + F_{rx} + F_{bx} + \mathrm{F_{wx}} + F_{rr} + F_{hill}}{m_{eq}}\right) \tag{6.14}$$

The resultant acceleration and distance between the two points give a minimum velocity value. This is compared to the value given by the lateral path generation. The minimum value of these two is taken to ensure that the lateral constraint is not violated. The process is then repeated for the remainder of the full path. An illustration of this process of building up the limiting speed profile from the lateral and longitudinal constraints is shown in Figure 6.9. As can be seen, this is an effective method for building a velocity trace. A discussion of the correlation of the full velocity profile is undertaken in Section 6.4.3.

As significant computational effort is spent on powertrain simulation, reducing the number of powertrain simulations is helpful. When braking, the maximum regeneration torque can be affected by the battery voltage at speed. However, in rear-wheel-drive UoN TT Zero configuration, the effect of weight transfer dictates the maximal regeneration torque is only 20% of the forward torque. In this scenario, the powertrain is not voltage limited and can achieve the maximal regeneration torque throughout the full speed range. This allows us to simplify the powertrain torque response and loss models to a lookup table for these periods. This also simplifies the calculation of the battery response as now the response can be determined later during the following forwards iteration phase to capture the full lap history.

6.3.3. Longitudinal Acceleration

The longitudinal acceleration profile starts with the velocity profile generated by the lateral and deceleration limits. The process is similar to the deceleration profile generation but iterates forwards from the start of the lap. At any point where the motorcycle is accelerating ($v_{i+1} > v_i$) the lateral force required to satisfy the curvature constraint at 'v_i' is determined and this lateral force is used to determine the motorcycle steady-state camber angle. The maximum longitudinal tyre force available given the lateral force constraint is determined using interpolation of the GGV response.

The battery model is used to determine the internal resistance 'R_0' utilising the lap history. The instantaneous voltage response due to the powertrain state is determined as part of the powertrain evaluation step. Having determined the battery state, maximum tyre force limitations and camber angle these limitations are passed to the powertrain model (developed in Chapter 5).

The method by which the powertrain model determines this steady-state output is as follows:

1. The steady-state weight transfer is computed to determine the front and rear tyre loads. The maximal longitudinal acceleration and camber angle determined by the GGV surface are used for this.
2. These forces are then used to determine the longitudinal tyre slip and tyre deformation at that operating point for the tyre in question.
3. These slips and forces are used to derive the required electric motor torque and motor speed required to satisfy the limit of the performance envelope.
4. The electric motor maximal output torque is determined at this operating speed using the motor model developed in Chapter 5.
5. If the motor can supply this torque, then this operational point is selected.
6. If not, then the maximal motor torque is selected and used to recalculate the associated steady-state weight transfer and resulting tyre slip.

Having determined the tyre force due to the electric powertrain the additional forces are determined. These include the force representing the longitudinal component of gravity due to road inclination 'F_{hill}', rolling resistance 'F_{rr}', and aerodynamic drags 'F_{bx}' and 'F_{wx}'

The calculation of the longitudinal tyre slip allows the calculation of the effect of rear-wheel inertia. Gear ratio, front and rear wheel as well as the electric motor rotor inertia are accounted for as an 'effective mass' and the forward acceleration calculated.

$$T_{mot} = f(i_s, V_s, \omega_m) \tag{6.15}$$

$$F_{rx} = \frac{T_{mot}}{r_{rw}} \frac{N_2}{N_1} \tag{6.16}$$

$$m_{eq} = m_{bk} + \frac{I_{fw}}{r_{fw}^2} + \frac{I_{pt}(1 + \kappa_r)}{r_{rw}^2} \tag{6.17}$$

$$I_{pt} = I_{rw} + I_{mot}\left(\frac{N_2}{N_1}\right)^2 \quad (6.18)$$

$$a_x = \frac{F_{rx} - F_{bx} - F_{rr} - F_{hill}}{m_{eq}} \quad (6.19)$$

This forward acceleration allows the calculation of the velocity achieved at the following spatial step. Again, the minimum of this velocity and the previous braking and later force limits is taken.

At the intersection of the limiting velocity traces, there is a point where the calculated longitudinal acceleration will determine a velocity above the lateral or deceleration limits. At this point, the force required to achieve the lower velocity constraint is determined and the motor model re-simulated with this as a limit to capture this lower torque output.

The time taken to achieve this spatial step is then determined from the velocity and distance between points. This is then used to determine the battery response. Here of interest is the energy consumption of the powertrain, heat generation with the battery and heat energy transfer out of the battery due to cooling. This is used to determine the battery state and thus time dependant voltage response.

The resulting acceleration trace evolution from lateral limit to deceleration limit and then acceleration limit is shown below in Figure 6.9.

A simplification that can be made for some events is the use of an interpolated powertrain lookup table. This only covers the motor, motor drive and transmission. The battery response is always simulated in full.

To create this performance map, the battery nominal voltage and instantaneous voltage drop at a battery temperature of 40 ˚C are taken as inputs to the motor model. The choice of 40 ˚C approximates the mean expected battery temperature. The GGV response surface is used to determine the input maximum tyre forces to the powertrain model. The resulting powertrain performance is determined using the same process outlined above. As this powertrain performance map also contains the motor input power requirements interpolation of these variables allows the calculation of the battery demands and thus the simulation of the full battery.

This simplification speeds up the simulation considerably but does ignore the variation in powertrain performance resulting from battery voltage decay with discharge. The significance of this is simplification varies with the event being simulated and is explored in more detail in Section 6.4.

An illustration of the assembly of these three velocity limitations for a section of the TT lap using the UoN TT 2018 parameters is given in Figure 6.9 below. The resulting velocity trace is named ‘Acceleration trace’ as this is the final limit to be included. As can be seen, the velocity trace satisfies all limitations at all points. The effect of the motor speed limitation is also neatly shown at 65 m/s when the acceleration trace reaches a limit. Also seen in this plot is how all the velocity limitations are respected. A simple and robust method for determining the maximal velocity profile of the motorcycle has thus been implemented. The validation of this method is examined in more detail in Section 6.4.

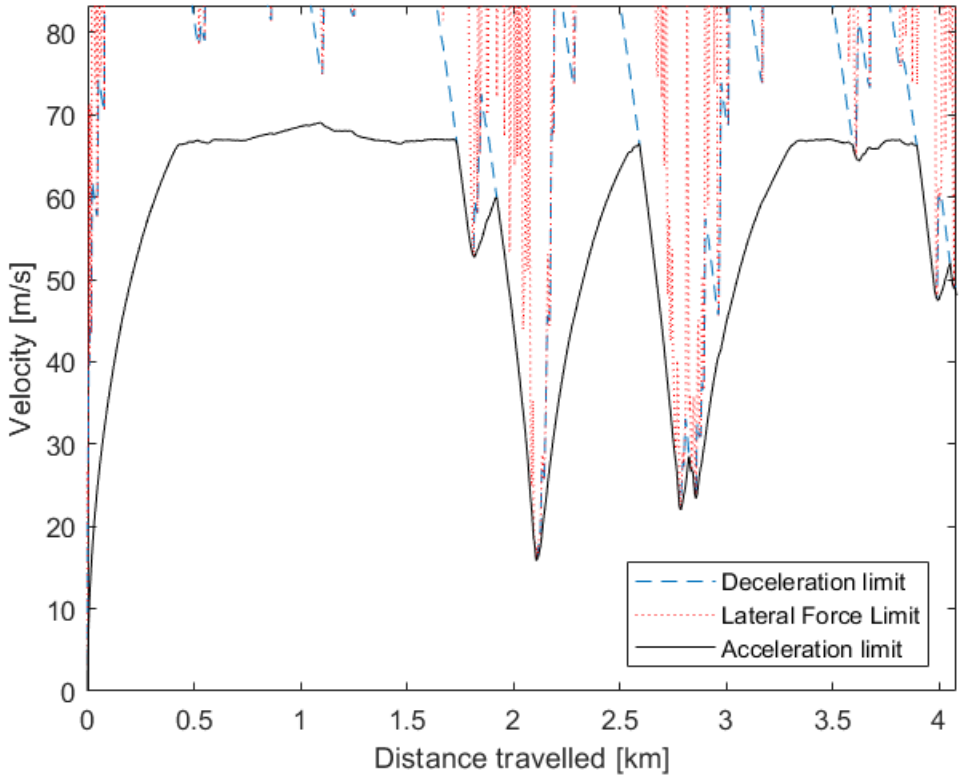

Figure 6.9 - Vehicle velocity trace evolution for example TT simulation

6.3.4. Deployment Strategy

Due to the energy storage requirements and the 300 kg mass limit for the motorcycle, the rider can't complete the full TT lap at full chassis limit power. Therefore, energy

management strategies need to be evaluated. A simple energy management strategy, used in 2018 and 2019, is to restrict the maximum velocity of the machine. This is simple to implement and effective as power is proportional to velocity cubed ($P \propto v^3$). This is easily implemented as a motor speed-dependent torque map in both the simulation and on the vehicle.

More advanced strategies involving varying energy deployment, with varying lift and coast periods based on the lap time-sensitivity per straight, have been explored by Sheard [82]. Here, the lap is broken into individual straights with those with higher deployment sensitivity prioritised. It can be seen that it is generally more efficient to deploy the maximum available energy early and coast to the end of the straight, before braking to achieve the required apex speed at the following corner [82]. It is also apparent that different straights have different sensitivities with it being preferable to deploy a larger proportion of energy on longer straights. The vehicle model used by Sheard [82] is basic, ignoring battery state, tyres, braking and lateral performance entirely.

The deployment strategy by Sheard [82] requires lap-position based electric motor torque limit variation. This is incorporated as a position-based torque limit that is pre-set before the lap. The trade-off for limit performance for the motorcycle is found where the lap time sensitivity for increased deployment is outweighed by the lap time penalty for increased battery mass.

As an example, three energy management strategies, power limit, speed limit and powertrain ‘clipping’ are compared in Figure 6.10. Powertrain clipping is achieved by allowing the machine to accelerate at full power, followed by the ‘clip’ where the power is removed and the machine coasts and only the forces due to drag and rolling resistance are present, the machine then brakes and regenerates at the end of the coasting period to achieve the required minimum speed for the following corner. Here all three velocity traces represent the same total energy consumption from the battery, inclusive of powertrain losses. It is clear powertrain ‘clipping’ results in the minimum lap time for the example straight. This result is only valid for the example straight shown here (Elvington Airfield, land speed record attempt specification machine) but this does demonstrate the need for further investigation of deployment strategy.

The other major factor to consider in deployment strategy is temperature, notably battery temperature. This is dominated by ohmic losses that increase with the square of the current and are extremely sensitive to periods of high deployment. For a comparison, a similar exercise comparing the effect of the three energy management strategies for equal battery temperature rise with no cooling is shown in Figure 6.11. It is worth noting that temperatures can be managed during the lap through the introduction of cooling systems, however, energy capacity cannot.

As these more advanced energy management strategies are not implemented in the race data they are not used for the remainder of this chapter. However, they are explored in more detail and included in the following Chapter 7.

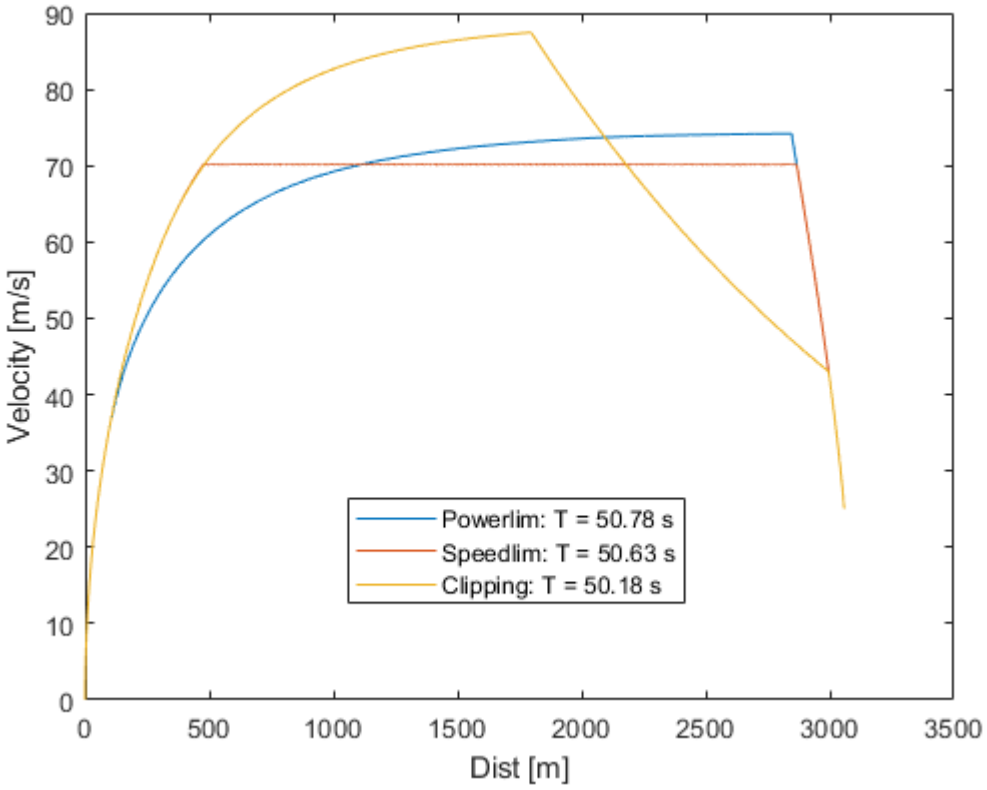

Figure 6.10 - Energy management strategy comparison for Elvington

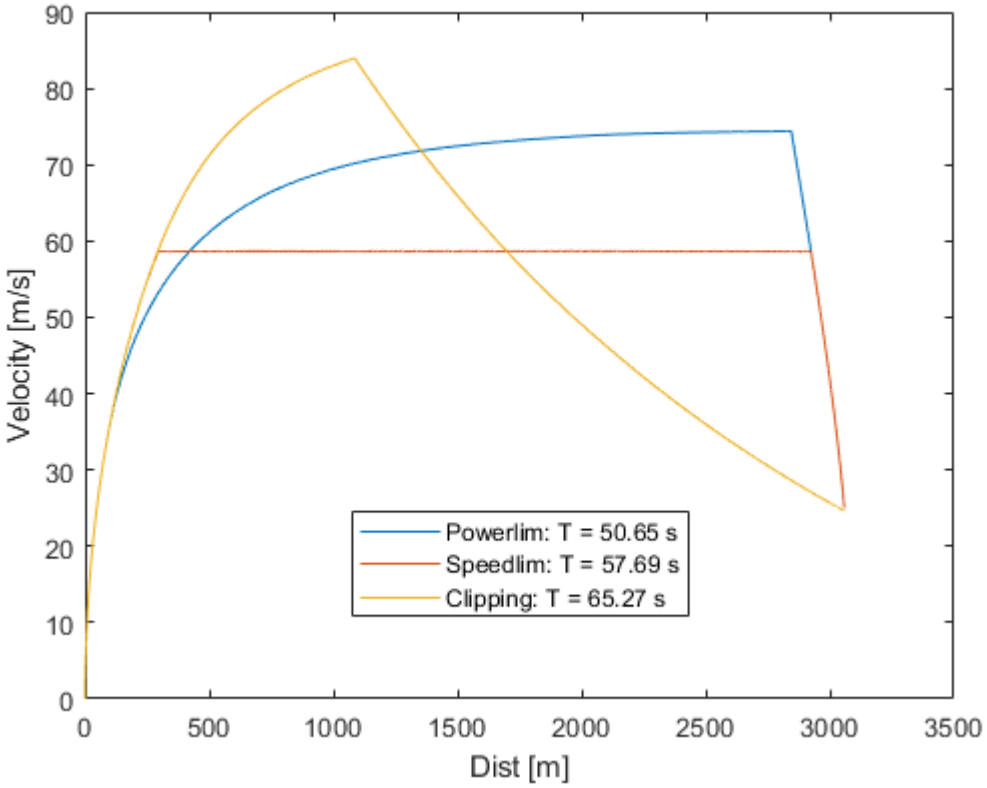

Figure 6.11 – Temperature management strategy for Elvington

6.4. Validation

Having developed this model, it is important to validate its performance using representative data. This is achieved through comparison to data collected during the 2018 Isle of Man TT Zero, 2019 Pikes Peak International Hillclimb (PPHIC), and the 2019 Elvington Land Speed record attempt. These are significantly different in terms of vehicle configuration and setup representing the extremes of electric motorcycle setups. An outline of the respective benefits for variations to the simulation for each type of event is also given. For example, the inclusion of battery voltage drop on powertrain performance is important at Elvington but less so at Pikes Peak, allowing the powertrain evaluation at each step to be reduced to a nominal torque map evaluated at a fixed voltage.

6.4.1. Comparison with Elvington Land Speed Record Data

The UoN motorcycle attempted and achieved multiple FIM World speed records at Elvington Airfield in 2019. Here the simulation is compared to the Elvington data-trace in Figure 6.12. Unfortunately only the vehicle speed and acceleration parameters logged by the AIM Evo 5 data logger [127] are available as the motor drive logging

system failed. Luckily the powertrain used was identical to the 2018 TT specification, so this is validated through other means. Note rear wheel diameter has been fitted to the data as the tyre choice was altered and data for this tyre size was missing.

To investigate the requirement for evaluating the full battery and motor model at every spatial step, a model with fixed powertrain performance evaluated at a predefined voltage is included. GGV_{Vmax} represents the fixed performance with a fully charged battery (4.2 Vdc per cell). The same starting cell voltage was used in the full powertrain simulation. GGV_{Vmin} represents a fixed voltage evaluation at 3.70 Vdc per cell, with a corresponding full simulation at the same starting voltage. 3.70 Vdc is chosen as for this case it represents low charge remaining.

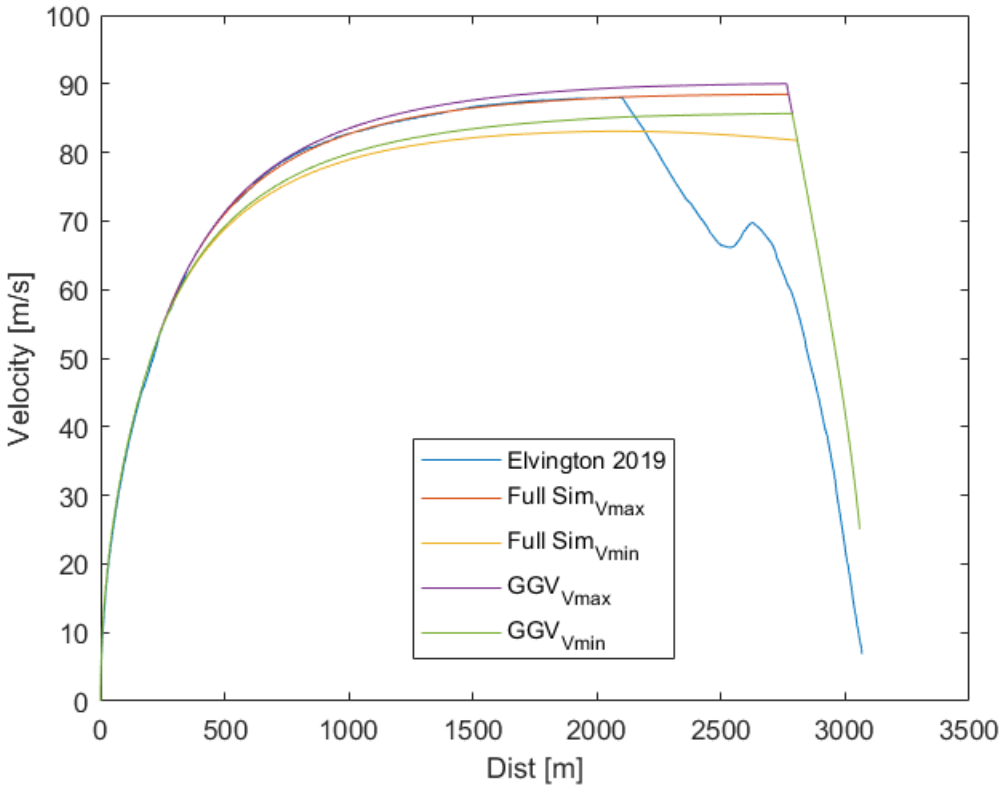

Figure 6.12 - Comparison of fixed voltage model and full battery model at top and bottom of charge

As can be seen, there is a good match between the simulated data and the lap trace with the real rider backing off the throttle earlier than the limit predicted by the road curvature. This is expected having passed the timing gates and slowing down to return to the pits. Also, it shows that in a power-sensitive scenario the battery model inclusion is important. Here, voltage drops due to the state of charge depletion and internal resistance variation have a noticeable effect on the powertrain performance at

high speed. This underlines the importance of tracking battery voltage on long high-power runs that make use of the field weakening region.

Also shown is that powertrain performance is unaffected by battery voltage in the constant torque region, as expected. This finding is important for deciding when to use the full powertrain evaluation at every spatial step and when an interpolated response is appropriate. Here it is clearly shown that the interpolated response would not be appropriate and so the full response evaluation is retained for this event.

Before the event, this simulation was used to determine the optimum gear ratio for the attempts at maximum speed and the standing mile time. A comparison of the available gear ratios can be seen in Figure 6.13 and Figure 6.14. The conclusion from these plots is that to achieve a maximal speed a 20T:79T sprocket ratio is selected, and a 20T:83T ratio for the standing mile time. Here 'T' refers to the number of teeth on the respective sprocket and the motor sprocket value is given first.

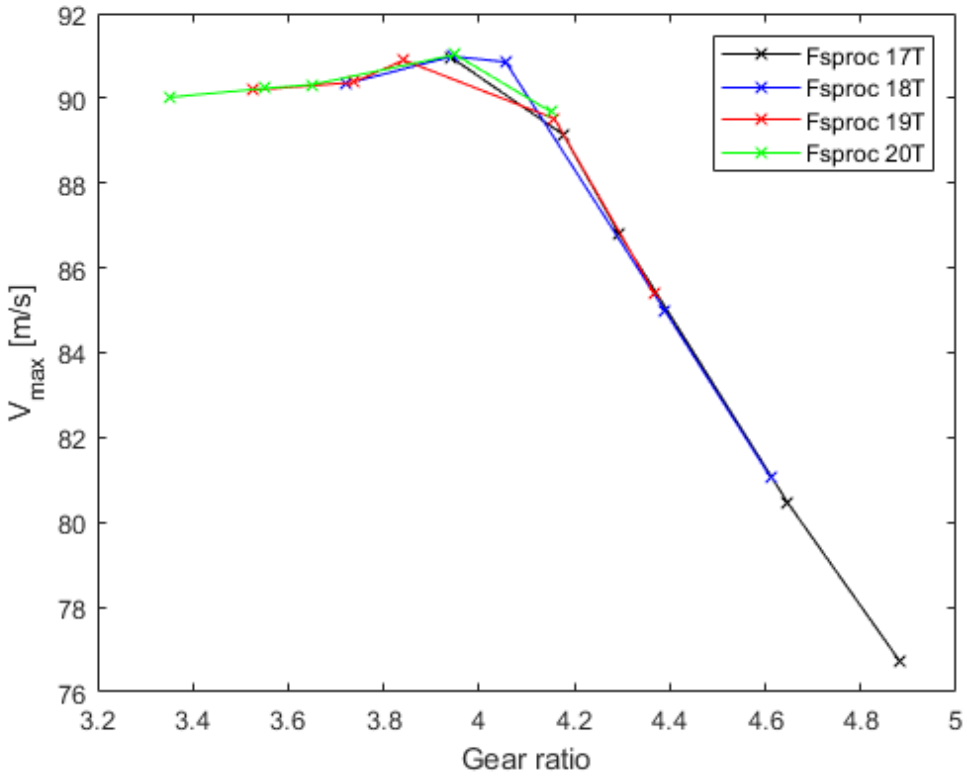

Figure 6.13 - Effect of gear ratio on maximum velocity using full powertrain simulation

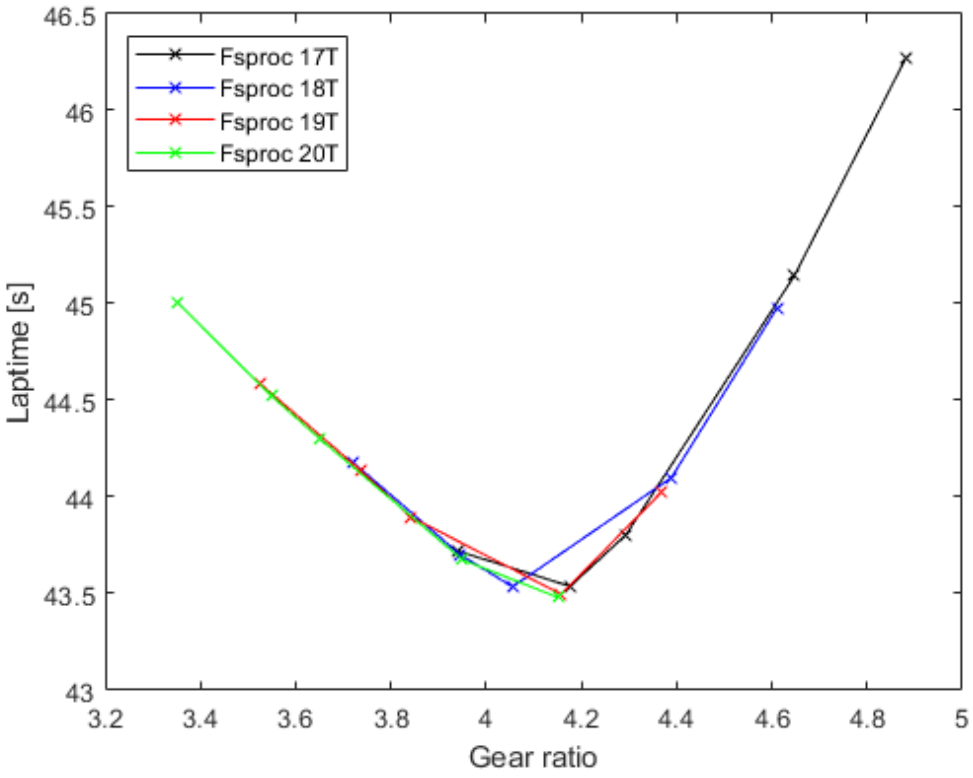

Figure 6.14 - Effect of gear ratio on standing mile time using full powertrain simulation.

6.4.2. 2019 Pikes Peak International Hillclimb

Again only the vehicle speed and acceleration parameters logged by the AIM Evo 5 data logger [127] are available as the motor drive logging system failed, and there is only one attempt per year at this event. This is unfortunate but the comparison of GPS speeds is still useful.

A note here is that after the race the rider admitted that his fitness and lack of familiarity with the course and machine had contributed to a lack of pace. And that there were still significant lap-time gains to be had. This can be seen clearly in Figure 6.15 and it is another reason to abandon the previous fixed corner speed approach taken by Blissett [16]. The idealised lap time at (566 s) was 53 s faster than the time achieved at the race (619 s), a significant decrease and 18s faster than the current lap record. However, this lap record would have been reduced to an estimated 572 s in 2019 by an IC machine ridden by Carlin Dunne had it not been for the tragic outcome.

It is not unreasonable to assume that the ultimate performance of the UoN machine could exceed this. Electric vehicles have an advantage over their internal combustion counterparts due to the altitude negatively affecting combustion power output, no

requirement to change gear, and the short low-speed nature of the course, requiring only a relatively small battery, giving similar IC and electric vehicle masses.

This lap discrepancy is still worth investigating and there are several contributory factors. Inspection of Figure 6.15 reveals that initially the data and the model show good alignment, particularly with regards to the slope of the acceleration and deceleration periods. There is also good alignment with minimum corner speeds after approximately 3 km of the course. As the track was colder than expected and there are no warm-up laps, the rider reported taking a cautious approach initially. This is likely the cause of the corner speed discrepancy before the 3 km point.

Another notable discrepancy comes with the rider lifting off earlier and initially braking more gently than would otherwise be optimal. It should be mentioned that the rider had recently recovered from a serious crash requiring hospitalisation and a long rehabilitation. This crash was caused by his brakes failing on a competitor's machine at the same event a year previously, so a cautious approach was taken.

For further comparison Figure 6.16 shows how the correlation deteriorates further as the race progresses. This can also be explained by a lack of race fitness coupled with extreme altitude (the course is a hill climb to 14,000 ft). Add to this the fact that the track becomes a mountainous hairpin trail with no guard rails (with fatal consequences if an error was made), and the discrepancy becomes more understandable.

In summary, there are multiple reasons why the rider was not able to exploit the ultimate performance of the machine, and this can largely explain the perceived differences between simulation and reality. There is also only one opportunity per year to make a full run on the course so there are no second chances for data collection. This analysis also illustrates why it is useful to be able to separate rider and machine performance and avoid wasted development effort. Further work involving track grip measurement could be undertaken to further resolve these differences but as this continuously evolves it would likely be a large effort for little gain, and is outside the scope of this thesis.

The Pikes Peak International Hillclimb course is much shorter and of lower speed than the Isle of Man TT course. As a result the battery pack mass was approximately 75 kg less. This reduction coupled with low top speeds significantly reduces the

influence of powertrain limitations. For comparison, the use of an interpolated lookup table with nominal powertrain performance was trialled. This resulted in a computational time of 15% of the time required for the full simulation. The effect of this change for this race was minimal, a lap time change of 0.2s. Inspection of Figure 6.15 and Figure 6.16 confirms this as the interpolated lap trace is almost entirely concealed by the overlaid full simulation trace. This simplified simulation is therefore a useful tool for exploring powertrain insensitive configurations.

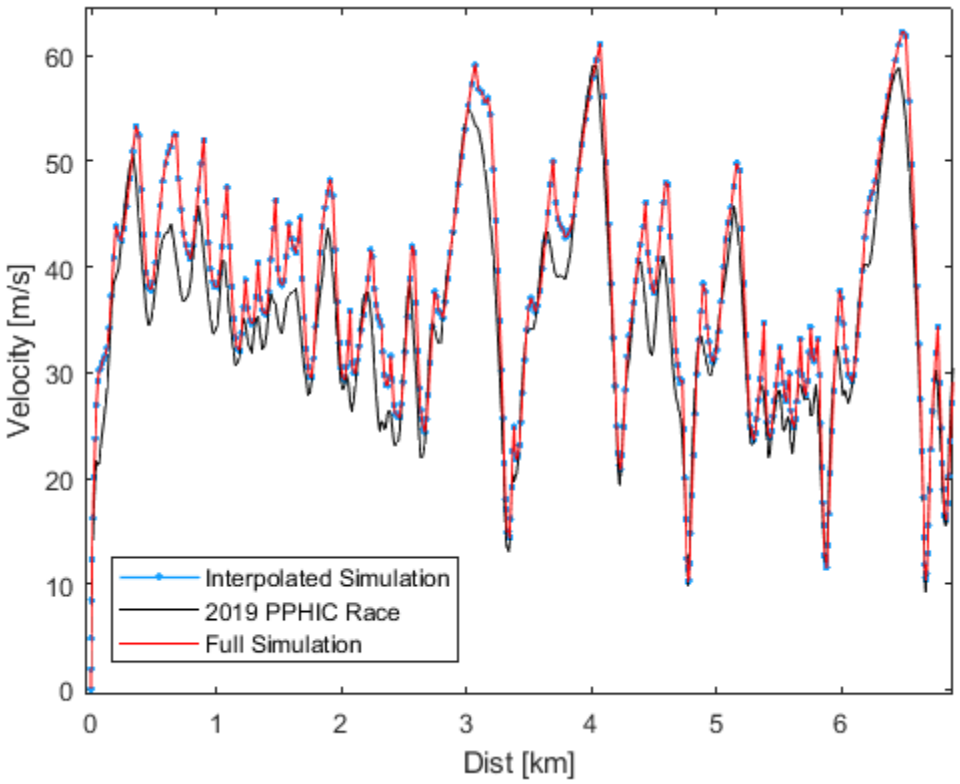

Figure 6.15 – Pikes Peak lap beginning speed comparison, Race data compared to Full and Interpolated simulations.

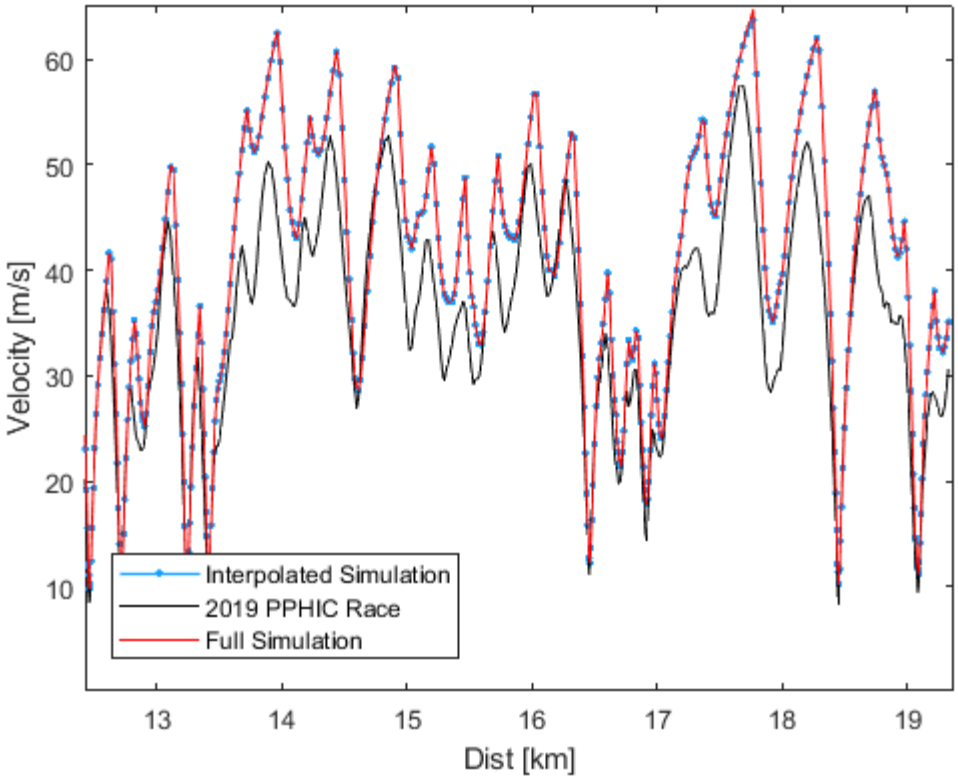

Figure 6.16 - Pikes Peak lap end speed comparison, Race data compared to Full and interpolated simulations.

6.4.3. 2018 TT Race Data Comparison

Much of the work correlating the motor model and the powertrain has been handled in previous chapters, but it is worth revisiting a few lap-dependent elements here.

As has been mentioned, one of the areas of improvement is the inclusion of a full tyre model. This has the benefit of improving the correlation between the electric motor torque speed curve and the vehicle acceleration profile. The impact of tyre slip can change the motor speed to motorcycle velocity relationship by up to 10 m/s, or 1000 rpm, depending on the axis used, and it is important to include especially in regions where motor torque varies. This effect as well as the correlation between the measured and simulated data can be seen in Figure 6.17.

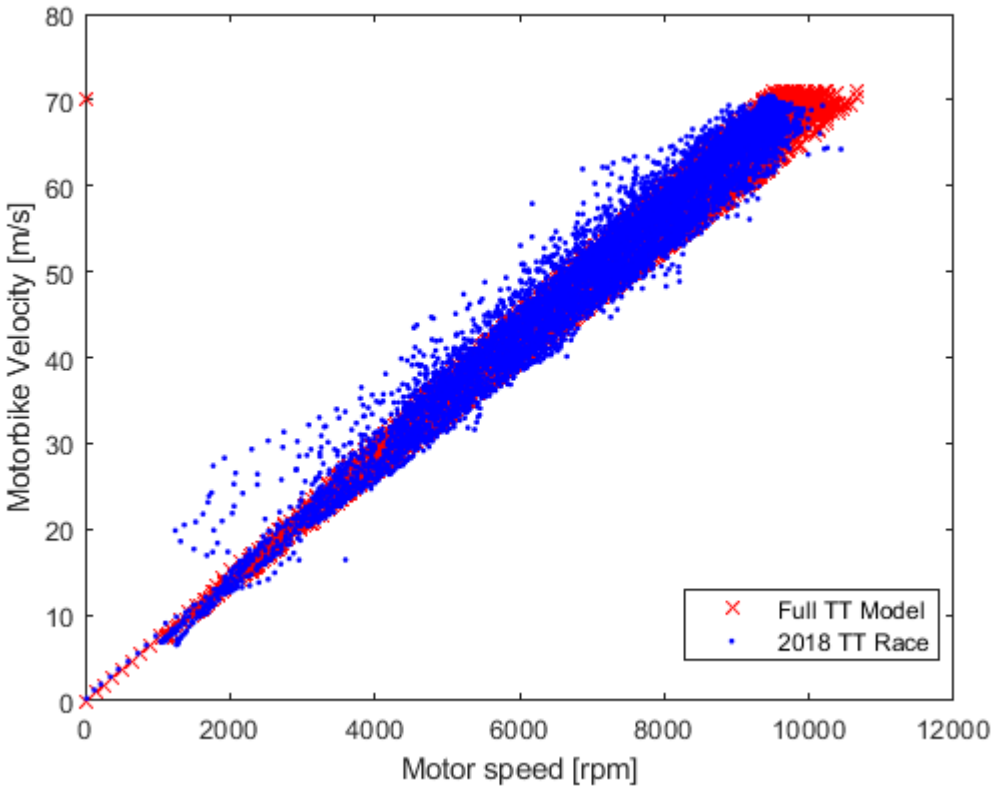

Figure 6.17 - Overlay of measured and simulated motor speeds and vehicle velocities illustrating the impact of tyre slip

It is also worth noting that the rear tyre is frequently under rotating during braking. This suggests that the fixed regeneration level used in the race was set slightly too high. The increased incidence of this at low speed suggests there is a speed-dependent element to the optimum braking level. This could be improved by allowing the rider full control over the regenerative braking levels using an imitation brake pedal or implementing a form of slip control to extract maximum torque and therefore maximum energy from the rear wheel.

The battery temperature is an extremely important parameter to monitor. Above a critical temperature, batteries can become unstable, burst, and ignite, resulting in the loss of the vehicle. As can be seen in Figure 6.18, there is a good match between the simulation and measured track data. It is worth highlighting here that all cell data was obtained in the previously mentioned lab tests and did not require fitting to lap data. This demonstrates the predictive capability of the lab testing methods used for predicting battery performance.

One area of concern for this data set is the variability within the thermistor readings. There are several potential reasons for this ranging from manufacturer quality control, assembly issues (there are other incidences of poor assembly procedure leading to ruptured cells), the reuse of old cells (the cells in this pack had competed in two previous TT events), or simply measurement error. As none of the equipment remains it is not possible to determine the exact cause of the variation. But its use as a predictive tool is reinforced and is an improvement over existing methods as will be shown in Section 6.5 from a comparison with the model developed by Blisset [16].

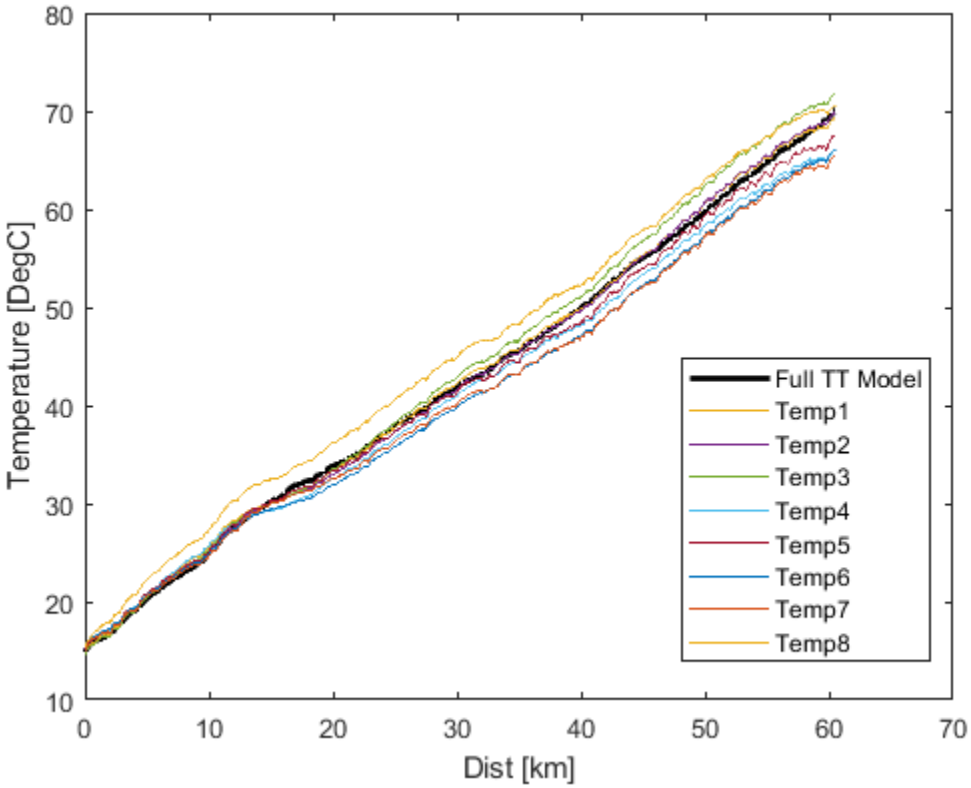

Figure 6.18 - Comparison of model temperature prediction and measured 2018 Race Data

The velocity trace comparison shown in Figure 6.19 shows the close correlation between the simulation and the race data. However, the lap time generated by the full simulation is 1081.1 s. This is faster than the 1138.6 s recorded in the 2018 TT Zero and represents a ~5% error. For comparison, the winning time in 2018 was a 1115.0 s lap recorded by the Honda Mugen ridden by the multiple TT winner Michael Rutter.

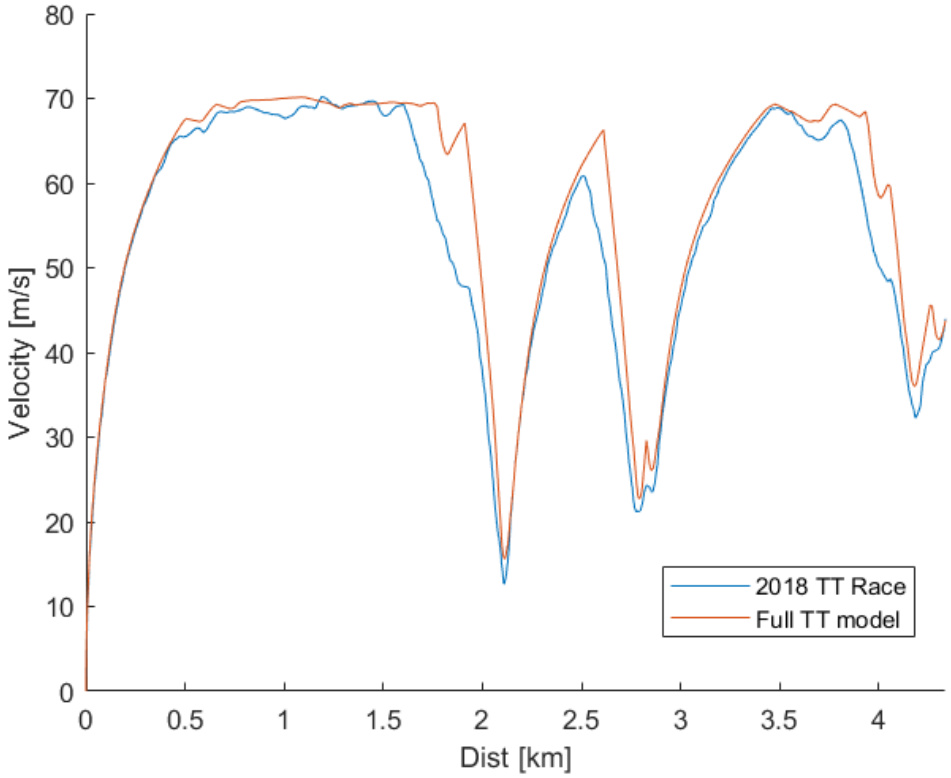

Figure 6.19 - Comparison of velocity traces from simulation and 2018 Race data

This variation has several sources. Firstly, the simulation assumes a perfect lap. This is very difficult to achieve especially at the TT, given the length and danger of the course. It is not feasible to include the entire 60 km velocity trace here, but as illustrated in Figure 6.19 and Figure 6.23, there are a few areas where it is theoretically possible to either increase the apex speed, get on the power earlier or brake later. This feedback can be given to the rider resulting in lap time gains. These improvements would naturally come with increasing rider confidence in the track and their machine. Interestingly a comparison with the lap profile achieved on his more familiar IC machine shows that some of these improvements have already been achieved. The Nottingham rider, Daley Mathison, only had one or two practice sessions on the electric machine in its most recent configuration before the event and likely would have improved further if given more time.

The second source of error was an unexpected motor temperature derate near the end of the lap. This was caused by using the incorrect thermistor settings in the motor drive and was uncovered post-race but resulted in reduced motor power, particularly towards the end of the actual lap.

Another point worth noting is that the lateral friction coefficient was modified with a 0.9 scaling factor to better represent the lap, particularly concerning apex speeds. This could be due to the track surface, poor setup, or the tyre vertical load sensitivity not being sufficient in the tyre dataset. Despite much help from the suspension manufacturers, K-Tech, with vehicle setup, there will have still been performance to unlock with increased testing and setup time.

Variations in grip levels due to differing road surfaces throughout the lap will also influence the performance. This has anecdotally been reported to equate to grip level variations of up to 20%, which again, can account for some of the speed profile variations. This variation could be measured using a grip testing machine, but this is outside the scope of this project.

The final sources of variance will be due to the nature of the simulation used. The approach used here assumes instantaneous load transfer which will have the effect of causing artificially low lap times. This error could be reduced by building a more sophisticated multibody model including suspension compliance and vehicle inertias. But as the simulation already represents a significant improvement over existing models, allowing the combined evaluation of both mechanical and electrical design choices, the extra work and computational effort were deemed unnecessary at this stage.

For comparison, the interpolated lookup table with nominal powertrain performance model with a set open-circuit battery voltage of 3.85 Vdc (representing the middle of discharge) was trialled for the TT using the same vehicle parameters. The performance map was interpolated in 10 m/s increments and the lap time generated was 1091.9 s, representing a 9.1 s (~0.8%) increase over the full model's lap time. The computational time was 22% of that required for the full simulation. The velocity discrepancies are greatest at high speed, with the nominal performance model typically not reaching the same peak velocities. This is illustrated in Figure 6.20.

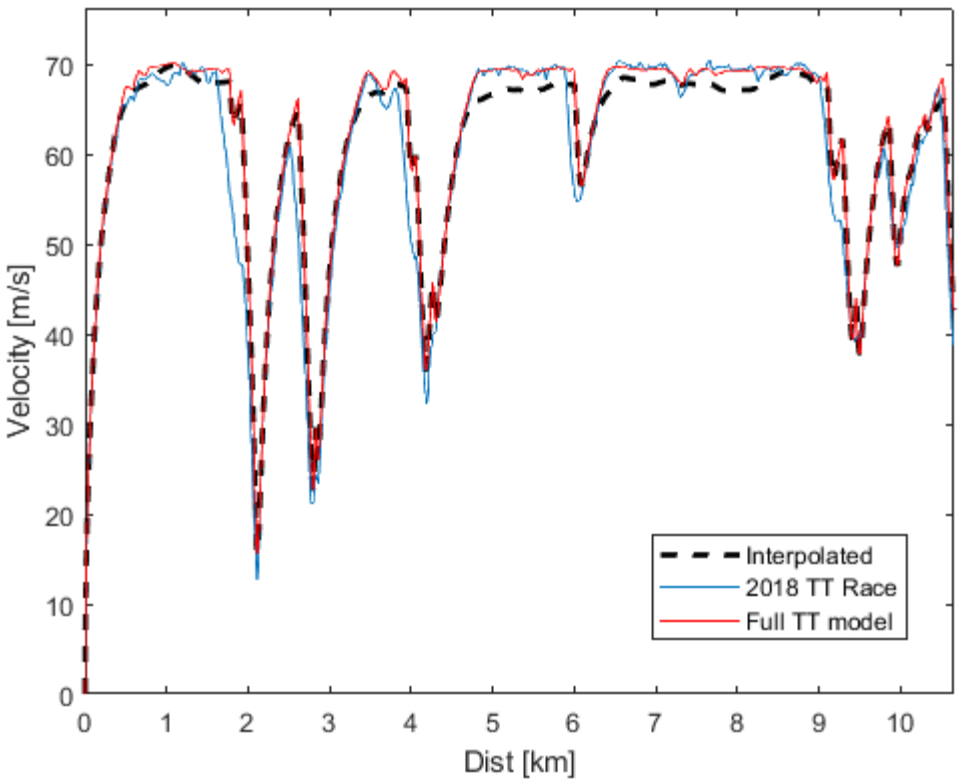

Figure 6.20 – Velocity traces for measured, full simulation and interpolated nominal performance map.

The use of an overly coarse interpolated vehicle performance map in a dynamic region with powertrain speed limiters and changing torque response leads was the cause of this. This is addressed by increasing the interpolation mesh density in the field weakening region. Having reduced the field weakening region velocity step size to 2.5 m/s, the lap time deficit is only 0.4s. This comes with a doubling of computational 'setup' time but is still only 43% of the time for the full simulation.

It is worth noting that this is again a situation where the powertrain performance is constrained, by torque and speed limitations set for energy management purposes. A lap velocity trace showing the improved fit is shown below in Figure 6.21. The shifting of computational time to the setup phase is extremely useful when performing multiple lap simulations with the same vehicle setup, i.e. when investigating energy deployment strategies.

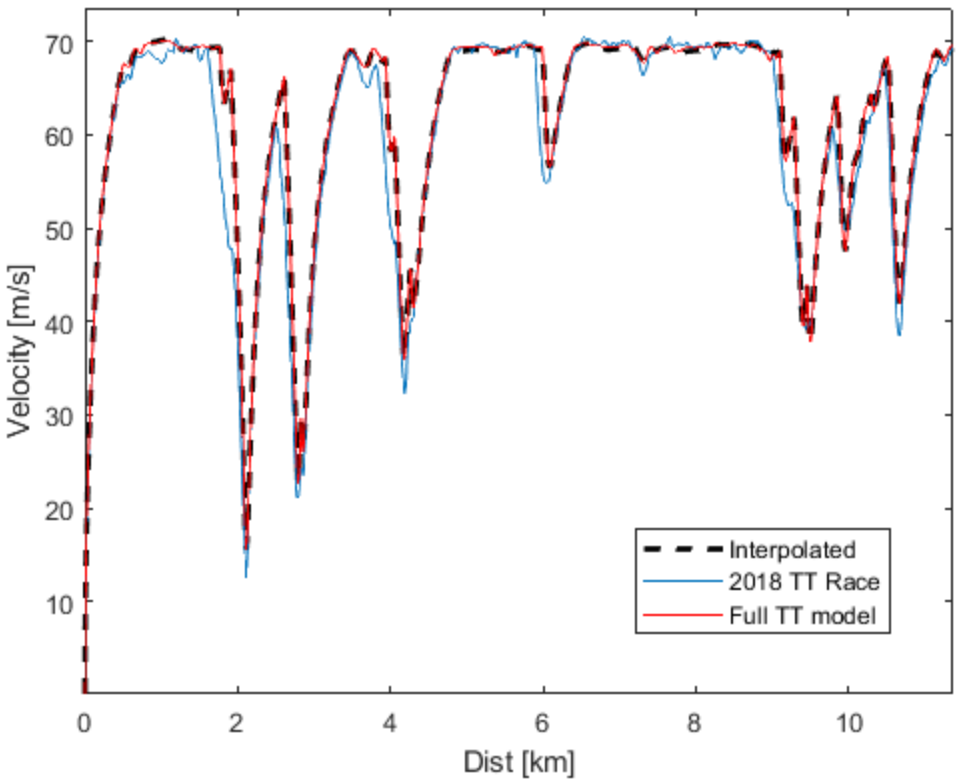

Figure 6.21 - Velocity trace for refined interpolated powertrain, 2018 measured race data, and the full simulation.

6.5. Comparison with the Blissett Model

The approach used in Blissett [16] is focused on using pre-recorded lap data to fix the cornering speeds and simulate a drag race between corner points. The addition of 'smoothing' parameters is an attempt to allow for corner entry and exit effects not captured in the model, like trail braking and feeding in power on corner exit. The model ignores the effect of tyres and lateral acceleration instead focusing on the powertrain response. This simplifies the model construction considerably. However, it results in infeasible speeds and a poor match to reality at points where a mixture of lateral and longitudinal acceleration is required.

Examples can be seen in a comparison with the Blissett simulation (using 2017 lap data), the 2018 TT measured lap data, and the simulation described in this thesis. Examples discrepancies are highlighted in Figure 6.22. The Bissett simulation continues past the braking point and a spurious artefact captured in the previous year's data is repeated despite being unrelated to the physical limits of the machine.

An area where the rider is still optimising his corner speed and the new simulation can be used to guide improvement as shown in Figure 6.23.

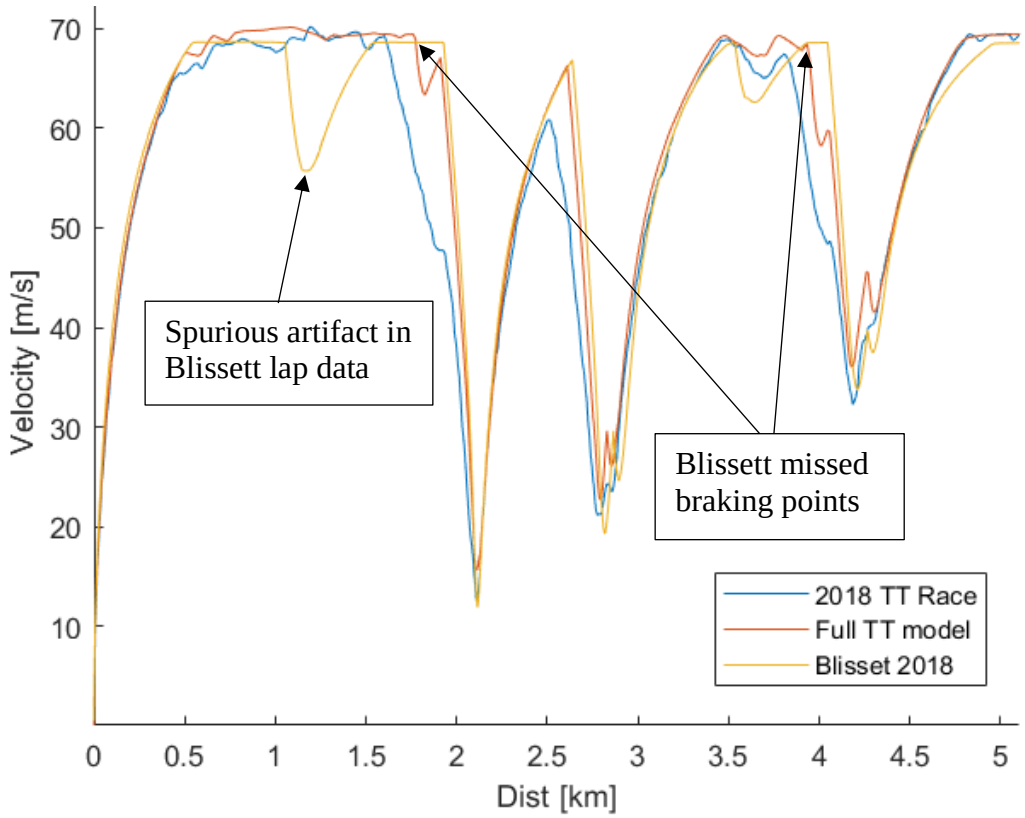

Figure 6.22 – 2018 Lap trace comparison illustrating the issues apparent when not considering combined acceleration

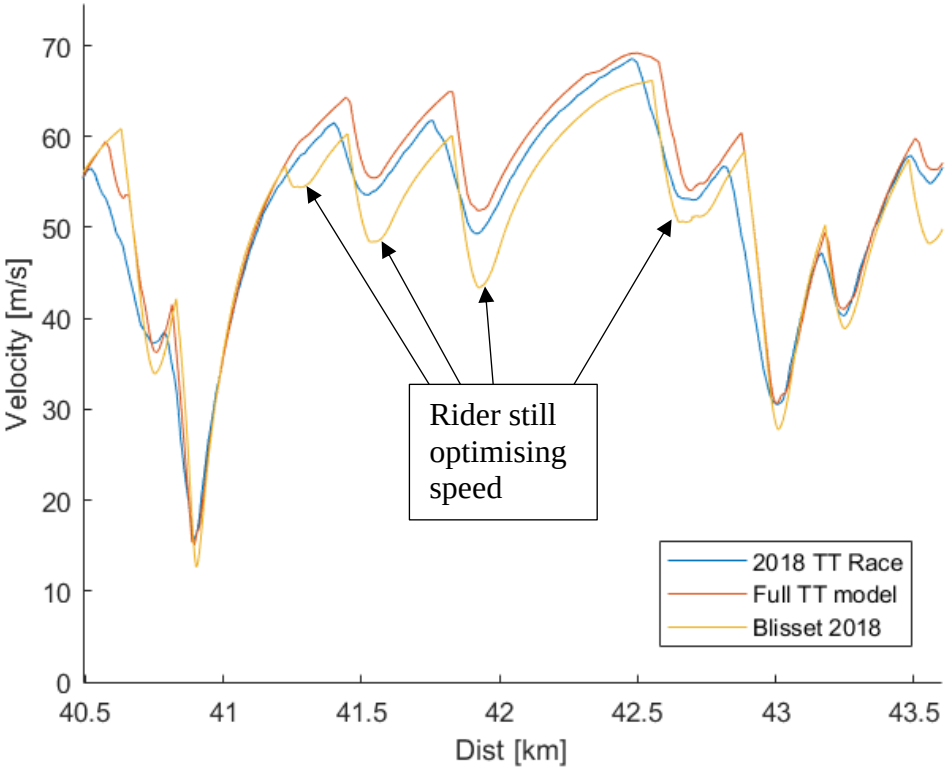

Figure 6.23 – 2018 lap comparison illustrating riders improving cornering speed and physical limit identified by simulation

Figure 6.22 and Figure 6.23 neatly illustrate the benefits of using the upgraded methodology. By respecting the physical limits of the machine, the match to real-world data is improved, and the new simulation has the added benefit of being able to inform the rider where in the track better performance is to be found. There are some minor discrepancies in apex speed in some corners, but these can be easily explained by friction coefficient variations in the road surface, especially around a 60 km street circuit, or additional effects neglected by the simplification of the model. To improve this match further, measuring the road friction coefficient with dedicated apparatus (typically a specially designed trailer), and scaling the tyre response appropriately could help. This is of no benefit to this thesis.

Blissett [16] handles each apex-to-apex speed profile as a single event with parameters such as battery voltage fixed for the duration of the event. The machine parameters are then updated at each apex. Issues with this approach are most keenly felt on long high-speed straights and are clearly illustrated in Figure 6.12 which highlights the impact of this on the land speed record run at Elvington Airfield.

However, this is a trade-off that needs to be balanced with the event being simulated as with a constrained powertrain, e.g. torque/speed map limitations for the 2018 TT. The powertrain performance is almost invariant to battery voltage, as can be seen in Figure 6.21.

The Blissett model was developed with a firm grasp of the requirements and capabilities of the modern electric powertrain. However, several important vehicle response elements are omitted. The most notable omissions are tyre slip and tyre deflection under load, as well as the lack of consideration for cornering performance. The impact of tyre slip is illustrated in Figure 6.24. Here it is clear that the inclusion of a tyre model greatly improves the correlation between electric motor speed and motorcycle velocity where differences of up to 10 m/s or 1000 rpm can be seen between the measured results and the Blissett model depending on the axis used for comparison.

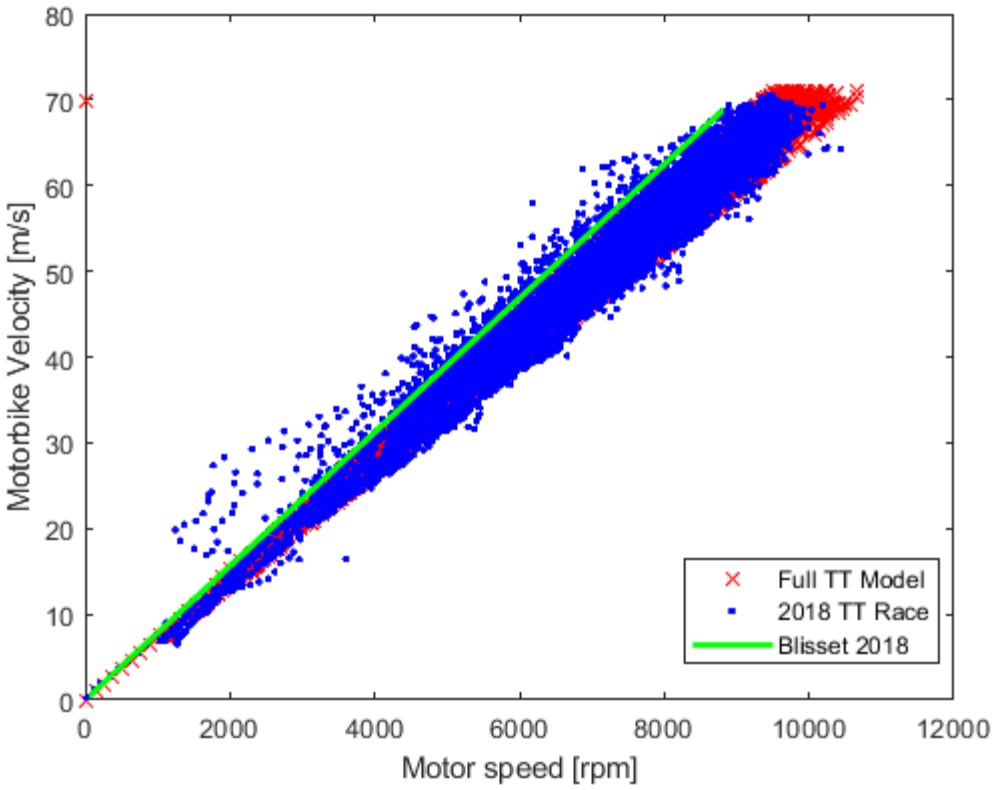

Figure 6.24 - Plot of recorded and simulated 2018 motorcycle velocity and motor speed.

Another important area of comparison is battery temperature prediction. As mentioned in Blissett [16] the lab test ohmic heating value obtained did not correlate well with measured track data at the Jurby test track. To improve this fit (post lap test) Blissett increased the internal resistance value by 35% to increase the level of cell heating in the model and simulations were rerun. The resulting battery temperature fit is shown in Figure 6.25. As can be seen despite the refitting the shape of the curve is still a poor match to the data. An issue with this approach is the lack of confidence in its predictive ability and the fact that a different track may require a different adjustment factor. The battery is one of the longest lead time components and is critical to machine performance. Once the pack is built and tested on track it is too late to make any radical improvements to the design. The approach described in this thesis is far more useful as it not only has a significantly improved fit in both shape and magnitude it is better suited to being used as a predictive tool based on lab testing alone.

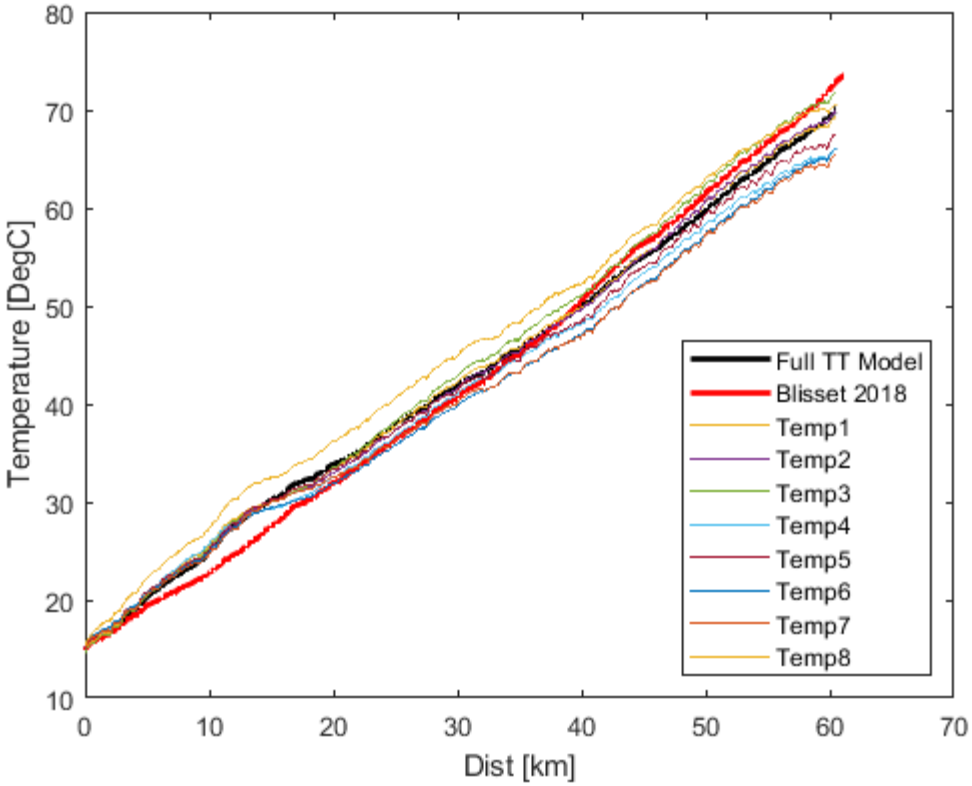

Figure 6.25 - Comparison of Blissett fitted Ohmic resistance model to predictive battery temperature model used in this thesis.

Other notable omissions can be found in the idealisation of an IPM motor as an SPM machine using SPM control. There are further issues surrounding the chain efficiency model and the effect of direct chain tension on motor bearing efficiency. A more detailed explanation of these is included in earlier chapters.

The effect of these inaccuracies has the potential to mask areas for development and the large approximations lead to the restricting of the validity of optimisations to a narrow window around the pre-recorded lap data. These issues have been addressed in the new model and the benefits of the improved approach outlined.

6.6. Conclusion

The goal of the current chapter and Chapters 4 and 5, has been to develop and validate a model capable of determining lap time sensitivities for a wide range of high-performance electric motorcycles. This goal has been achieved and the superior performance of the approach taken here in terms of wide-ranging correlation has been demonstrated with multiple examples with differing setups.

Comparison with the Blissett model [16] has identified several areas where the new approach shows significant benefit. The switch to GPS-based lap definition and the use of tyre models has removed artificial constraints and improved the ability to differentiate between machine limitations and rider limitations. Notable improvements can be seen particularly with regards to the correlation between electric motor speed and road speed due to the inclusion of a tyre model, with resulting improvements in the modelling of high-speed high-power vehicle behaviour. The evaluation of the powertrain state at each acceleration point is important in some cases but not necessary for all.

This coupled with the improvements outlined in Chapters 4 and 5 has resulted in a substantial improvement in both the ability to predict lap behaviour using laboratory test data and the ability to determine the effects of more substantial changes to machine setup such as the movement of the centre of gravity and addition of downforce.

The next step in this investigation is to determine the influence of parameter variations and uncover the main lap time sensitivities including energy management strategy. This is handled in the following Chapter 7.

7. Lap Time Sensitivities

Having developed and validated vehicle (Chapter 4), powertrain (Chapter 5) and lap time models (Chapter 6), the next stage is to use this model to determine the main performance drivers for high-performance electric motorcycles. The goal here is to identify the sensitivities to design parameters and quantify their effect from a full vehicle perspective. This can then be used to guide the trade-offs and development pathways required for a full vehicle design optimisation

As the energy deployment strategy has a large influence on ultimate performance, it is important to ensure the drive cycle reflects the efficient use of stored energy. Therefore, the first section of this chapter, Section 7.1, develops simple deployment strategies that can target battery deployment to reduce energy consumption or battery heating as required. This includes the investigation of direct air cooling on the battery temperature and additional motorcycle drag.

Section 7.2 then delves further into the lap time sensitivities of a high-performance electric motorcycle at the TT Zero race. As the battery is a significant performance differentiator, the mass sensitivity and energy sensitivity are determined, the resulting trade-off is then calculated when considering the TT drive cycle with the energy deployment strategy used in this thesis. Further sensitivities including the minimum viable winglet lift to drag ratio, gearbox efficiency, electric motor construction choices, as well as switching module choices, are evaluated in the context of the TT Zero race.

As the design trade-offs can differ between events Section 7.3 contains a summary of a similar activity undertaken for the Pikes Peak International Hillclimb (PPHIC). Here areas of significant difference are investigated such as the need for an energy deployment strategy and the optimal winglet lift to drag ratio.

7.1. Deployment Strategy

7.1.1. Energy Limited Deployment Strategy

Due to the energy storage requirements and the 300 kg mass limit for the motorcycle, the rider can't complete the full TT lap at full chassis limit power. Therefore, energy management strategies need to be evaluated. A simple energy management strategy, used in 2018 and 2019, is to cap the peak power and restrict the maximum velocity of

the machine. This is simple to implement as a motor speed-dependant limit torque map in both the simulation and on the vehicle, and effective as power is proportional to velocity cubed.

More strategies involving varying energy deployment with varying lift and coast periods, based on the lap time-sensitivity per straight, have been explored by Sheard [82], albeit without consideration for battery heating, lateral force requirements, or corner entry speeds. This is shown to be a significant over-simplification. In [82], the lap is broken down into individual straights with those with higher deployment sensitivity prioritised. The initial findings suggested this strategy would provide significant benefits. To evaluate this properly using the full model developed in Chapters 4, 5 and 6 the following process was followed. This process begins by identifying the points at which energy deployment can be used. This problem is tackled as follows:

1. An index of points corresponding to the start of individual straights is created by:
    i. Removing battery energy and temperature limits, the lap is then simulated to create an upper performance bound.
    ii. This data-trace is then inspected to find points where the rear tyre longitudinal force is near zero. This is used as an indicator that the motorcycle is near the apex of a corner.
    iii. This index of cornering points is then filtered to contain only those points separated by a set distance of full acceleration and braking. For the TT and PPHIC, 50 m was chosen for both.
    iv. This index is then further filtered to remove points above a set velocity to avoid constraining the strategy to achieve high-velocity target points. In this case, the velocity boundary selected was 60 m/s for the TT. 50 m/s was selected for the PPHIC race owing to its lower speed profile.
2. The lower deployment bound is then generated. Here, battery limits are reintroduced, and the simulation is run without brakes and with a target end velocity of 10 m/s. Special consideration involves permitting braking for downhill sections leading into a corner, where the velocity

generated by the slope exceeds the maximum of the corner. Here, the minimum braking required to achieve the corner is permitted.

3. All deployment points required to achieve the minimum lap are fixed.
4. The deployment profiles of both runs are compared, this allows the determination of the amount of energy available for targeted deployment.

A comparison of the maximum and minimum deployment profiles is shown in Figure 7.1. As can be seen typically the fixed minimum deployment points involve corner exit. This fixing has two functions. Firstly, it allows the analysis to avoid infeasible solutions, and secondly, it provides the rider with a machine that behaves predictably on the corner exit.

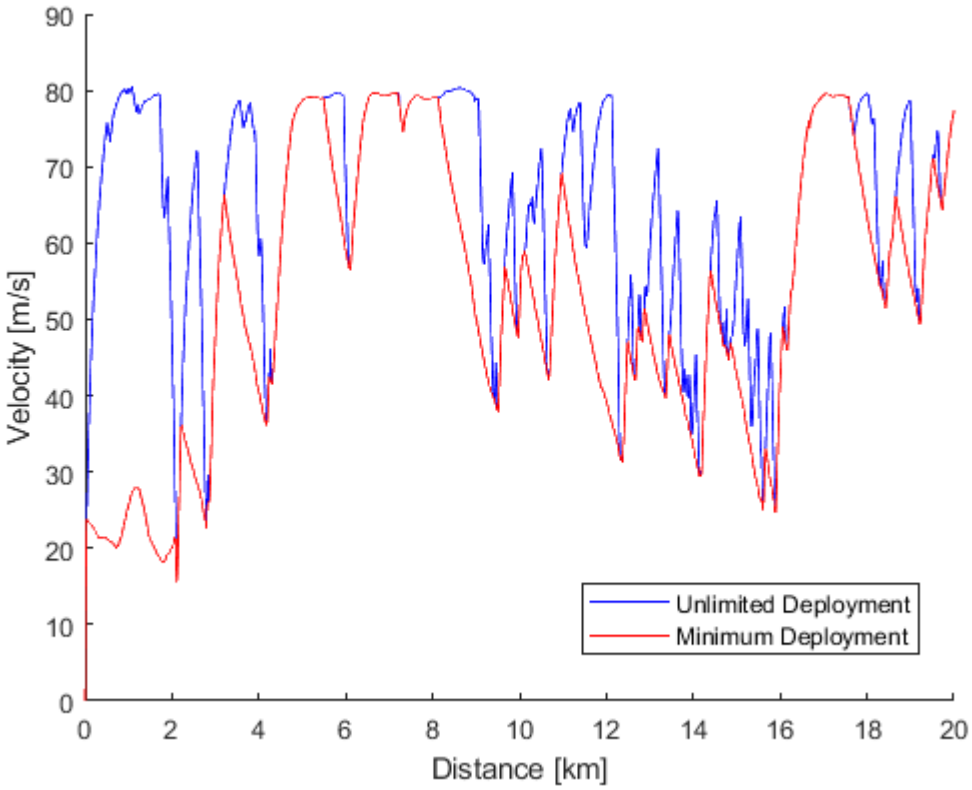

Figure 7.1 - Speed trace comparison for unlimited and minimum deployment energy bounds for the start of the TT Zero lap

As can also be seen in Figure 7.1 there is significant scope to vary the deployment strategy between the upper and lower bounds. The next task then becomes the determination of how to best use this deployment freedom. This is achieved by ranking the index of points valid for deployment. These are ranked in terms of lap

time-sensitivity per unit energy deployment. As the lap time gain per unit of energy use generally decreases with distance from the start of the straight, the relative ranking of each point on the straight can be approximated by its distance along it.

Figure 7.2 contains a plot of the energy consumed per straight against the corresponding lap time gain for the Isle of Man TT Zero using the UoN 2018 specification machine. This shows that the lap time sensitivity to energy deployment generally decreases along a straight. This is simply the gradient of the plotted line. This underpins the approximation that the relative ranking of each point on the straight can be approximated by its distance along it.

This approximation, however, ignores the influence of small high-speed kinks in the road which can slightly disturb this ranking and leads to some noise when determining energy sensitivity. This can also be seen in Figure 7.2. However, this is a useful simplification for the following reasons. Firstly, the rider requires a predictable machine, cutting the power in and out multiple times down a straight is not acceptable, and secondly, the number of evaluations required is significantly reduced. The TT includes 1800 points for ranking but only 68 straights.

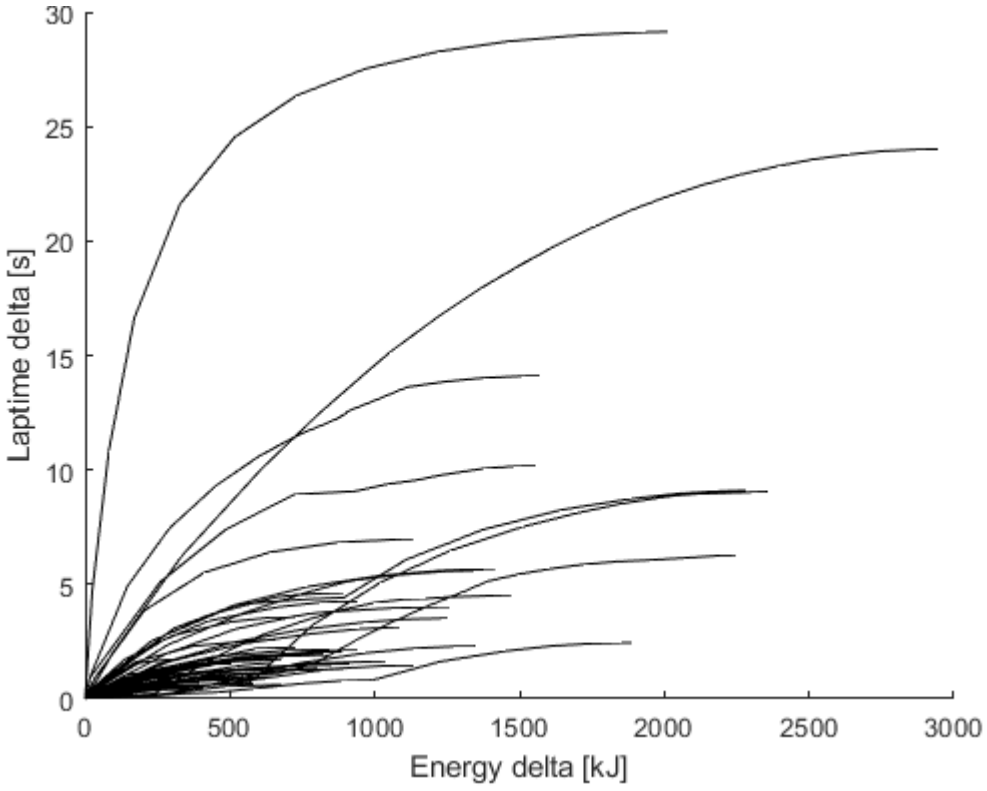

Figure 7.2 - Energy delta between minimum and maximum deployments and resulting lap time delta per straight for TT Zero

To rank the deployment points and determine the resulting deployment the following process is used:

1. The simulated lap is broken into individual straights and the energy consumption and lap time delta are sampled at several points down the straight. Each straight is treated as an independent event saving significant further computational time through parallel processing.
2. The response for the entire straight is then interpolated from these points.
3. The sensitivity of each point can then be determined and ranked with its associated energy consumption.
4. A map of sensitivity threshold values and cumulative energy use for the entire lap, using the deployment strategy, is interpolated from this data.
5. A sensitivity cut-off point corresponding to the target energy use (typically full battery deployment) is determined from this interpolated map. The corresponding deployment points are identified and then the full lap simulated to confirm the interpolated values when including the full lap history.

To ensure robustness a penalty function is included within the lap simulation, whereby if the battery becomes exhausted or exceeds its maximum temperature, it is shut off. The machine then coasts down to a 5 m/s speed and continues the lap to the end at that speed. This approximates a rider attempting to run to the line. This penalty function adds robustness and allows for the inclusion of strategies where the battery may fail just before it crosses the line, but the race would still be completed while including an appropriate penalty for doing so. This penalty function is the cause of the otherwise unintuitive increases in lap time with additional attempted deployment in Figure 7.3.

Figure 7.3 shows a comparison of the interpolated and simulated lap times. There is an obvious difference that can be traced to battery overheating, a process not captured by Sheard [82]. To highlight this discrepancy, the motorcycle is modelled with a battery internal resistance scaling factor (IR Scale), to represent different battery heating rates. The effect on lap time and maximal attainable deployment is neatly

shown. Here, the battery maximum temperature is set to match the maximum temperature generated by the global speed and power constraint method used by Blissett [16]. A post-search of the minimum lap time is verified using MATLAB function ‘fmincon’ [126]. The minimum time found during previous evaluations is used as the starting point with the two surrounding points used as search bounds.

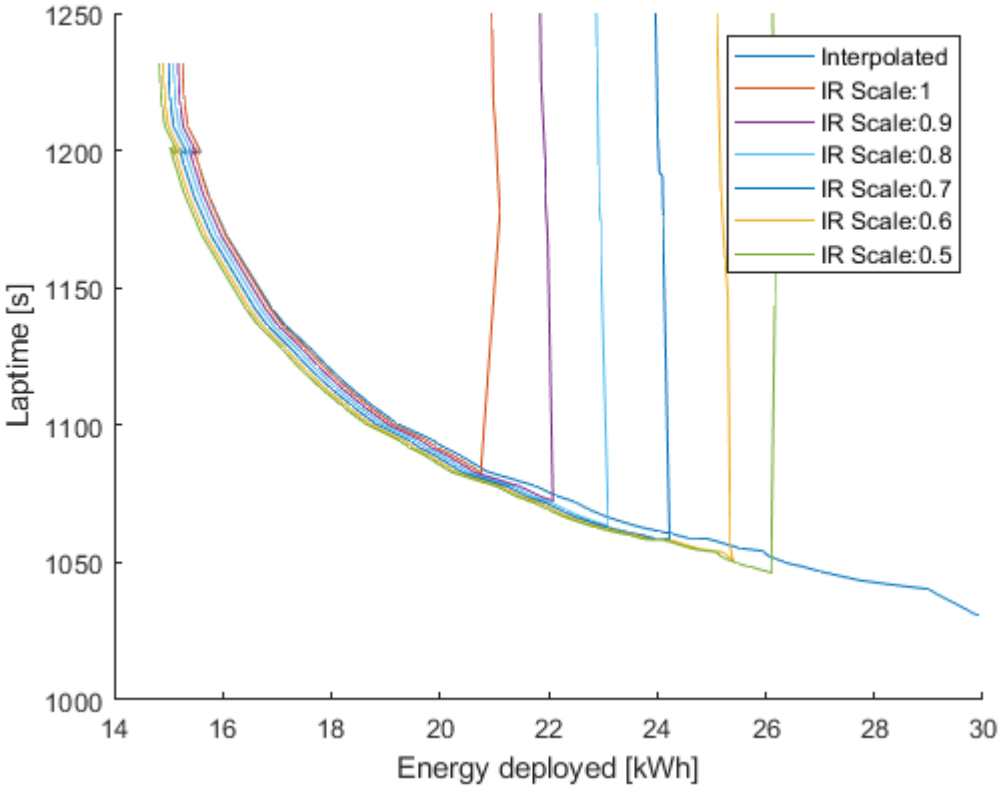

Figure 7.3 - Plot of energy deployment and resulting lap time for a sweep of deployment thresholds

Without any temperature management, it is clear the battery overheats after only 19.45 kWh of deployment using this strategy. Interestingly, despite this constraint, the lap time generated (1082 s) is similar to the global power and speed limitation strategy (1081 s) while using significantly less energy (19.45 kWh vs 22.54 kWh). In addition, battery internal resistance reduction reduces energy loss to cell heating and therefore lowers respective lap times per energy used, as can be seen by the curve shifts in Figure 7.3. This highlights the importance of proper cell selection from a full system standpoint as well as accurate battery modelling.

7.1.2. Temperature Limited Deployment Strategy

It is possible to reformulate the energy management sensitivity approach to apply temperature management to an existing design. Here, the limiting factor is

temperature therefore the sensitivity is defined as lap time gain per degree battery temperature rise.

However, as battery internal resistance varies with temperature so does the sensitivity of the following straight. Therefore, the parallel processing of independent straights needs to be abandoned. Instead, the maximum sensitivity is determined with a trial full lap run and the search space is defined between zero and the maximum sensitivity found in this run. Several equally spaced search points corresponding to the number of available CPU cores on the machine used are identified. Full laps are then run at these search points in parallel. This step is used to bisect the search space as efficiently as possible to reduce overall simulation time.

After these parallel runs have been completed, the temperature response is interpolated from their results to find the best approximation of the target point. This interpolated target point is run and compared to the target temperature (Pack maximum temperature). If the points lie outside the maximum error bound the process is rerun with the search bounds set to the points bisecting the target temperature.

As before the lap is broken down into individual straights, however, this time the variable to be controlled is the per-straight velocity limit. Previously for the energy management strategy, this was the deployment ‘clipping’ point. The use of a global power limit was chosen to simplify the search and provide the rider with a machine that has predictable performance as far as possible.

The effect of this strategy on lap time both with and without the inclusion of regenerative braking is shown in Figure 7.4. The performance of this approach can be compared to the Blissett approach of global power and speed limits, this is shown by the ‘x’ below. This plot shows that the revised strategy results in a 7s lap time reduction when compared to the previous strategy. This is a useful margin considering it is just a control strategy change, requiring only integration to a vehicle controller. Additionally, the plot shows that regenerative braking is still required to achieve the best lap time, even when thermally limited.

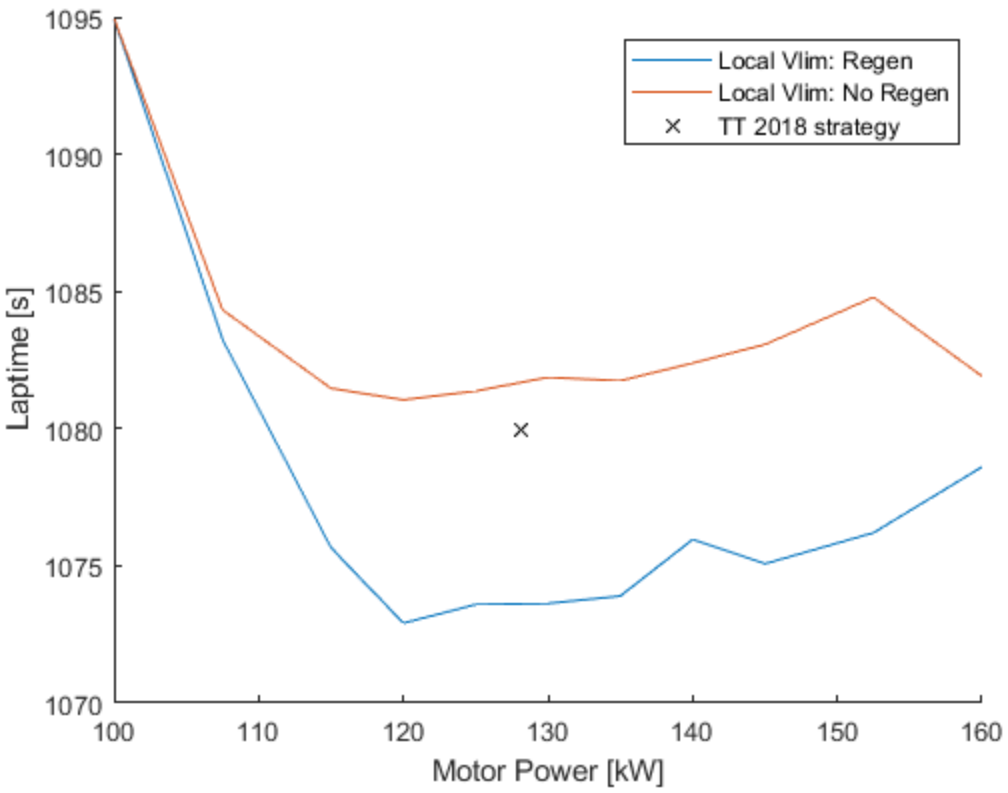

Figure 7.4 - Comparison of temperature management strategies. Per straight velocity limits with global power limits compared to global power and velocity limits as per TT 2018

An illustration of the parallel section search process outlined earlier using a quad-core machine is shown in Figure 7.5. For this search a maximum temperature of 73 degrees was targeted around the TT lap with a power limit of 120 kW, using the UoN 2018 specification machine.

The resulting lap velocity trace using this velocity limitation strategy and a 120 kW power limit is shown in Figure 7.6. Here it is evident that longer duration straights are prioritised, and short durations peaks are sacrificed.

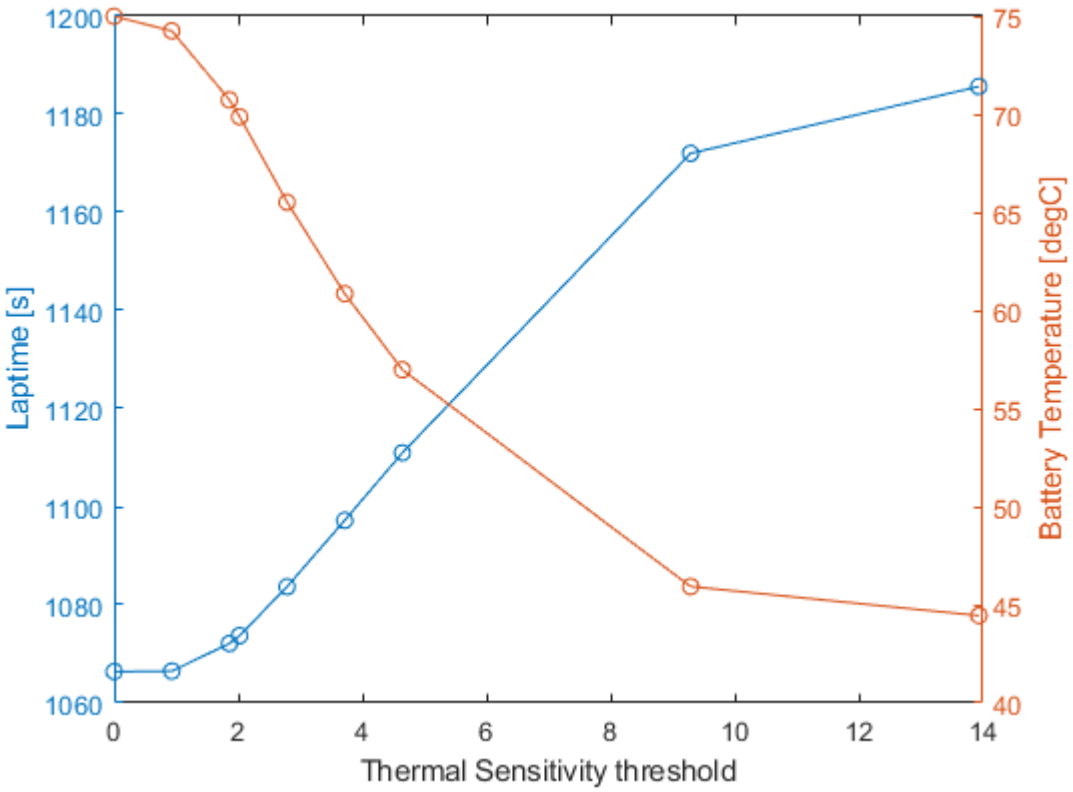

Figure 7.5 - Plot of thermal sensitivity threshold showing lap time and battery temperature trade-off

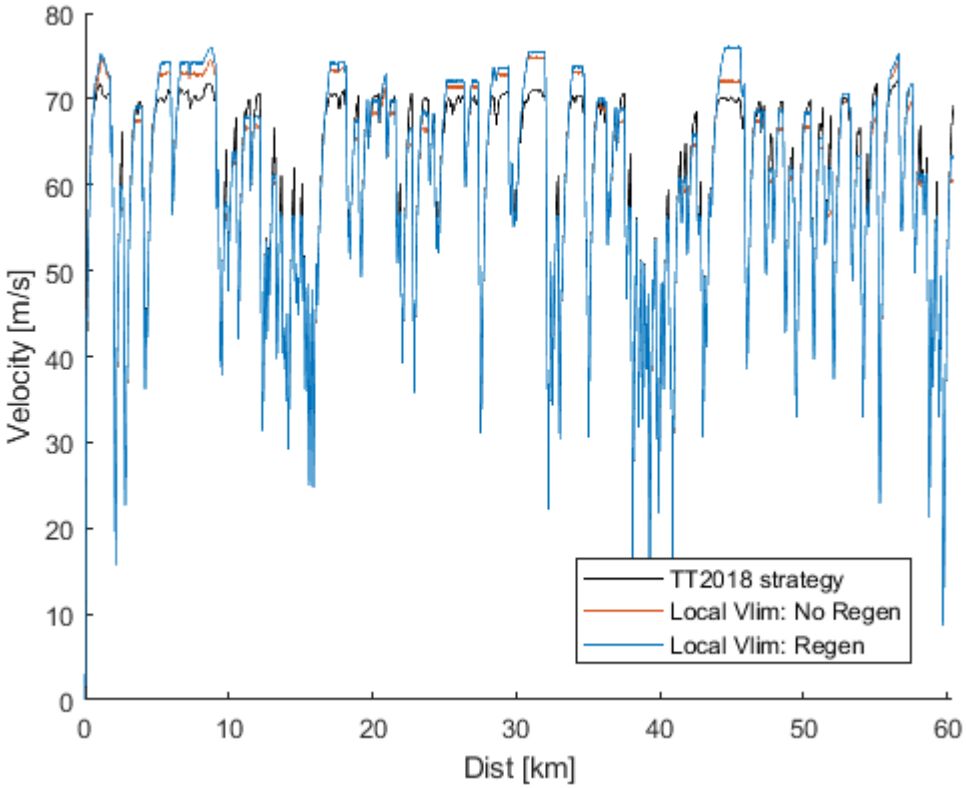

Figure 7.6 - Velocity trace comparison, 2018 TT global power and speed limitations vs straight specific velocity limitations with and without regenerative rear-wheel braking.

7.1.3. Battery Temperature Management with Energy Deployment Strategy

Temperature management can be incorporated through battery cooling. The simplest and possibly lightest implementation of this is air cooling. Given the high-speed nature of the race, this is likely to be effective. A common trade-off with increased cooling is increased drag. A simple cooling method, as used on the University of Bath electric motorcycle from 2016, is to allow airflow over the edges of the pouch cells [170].

To approximate the effectiveness of this method forced convection through rectangular ducts, with a heat transfer area equal to the combined area of all pouch cell side edges, was modelled. The duct is modelled as having two walls of constant temperature. The assumption that the non-circular duct performance can be approximated using circular duct equations and the hydraulic diameter instead of the pipe diameter [171], allows the calculation of the Nusselt number 'Nu' using the Gnielinski correlation for $Re > 2300$, and Nusselt-Graetz for lower Re values. The duct width '$W_{duct}{}'$ is the edge separation between the cells and is combined with the channel height 'H_{duct}' to give the hydraulic diameter 'D_{hyd}'. 'Pr' is the Prandtl number, 'Pe' the Peclet number. The heat transfer coefficient 'h_{cool}' is calculated using this and the thermal conductivity of dry air, as follows:

$$Nu_{turb} = 0.0214(Re^{0.8} - 100)Pr^{0.4} \tag{7.1}$$

$$Nu_{lam} = 1.61\left(\frac{PeD_{hyd}}{L_{duct}}\right)^{\frac{1}{3}} \tag{7.2}$$

The drag force for an extremely rough channel (due to the rough edges of battery cells) is approximated using a Darcy friction factor $f_{dcy} = 0.075$ for $Re > 2300$ and $f_{dcy} = 64/Re$ for lower Re values. In the following equations, 'ρ' is air density and 'v_{duct}' the fluid velocity in the duct.

$$F_{d,duct} = \frac{f_{dcy}H_{duct}W_{duct}L_{duct}\rho v_{duct}^2}{2D_{hyd}} \tag{7.3}$$

$$Q_{cool} = 2h_{cool}H_{duct}L_{duct}(T_{air} - T_{batt}) \tag{7.4}$$

The duct air velocity is set as a fixed ratio of the forward velocity, with an upper bound of 100 m/s is placed on this duct velocity value. These are assumptions for the initial evaluation of the potential significance of direct air cooling of cell edges.

The effect of this heat transfer is included in the lap simulation as a heat energy transfer out of the battery at each timestep and the duct drag force '$F_{d,duct}$' included as an increase to the motorcycle body drag force 'F_{bx}'. The following approximations are used for this simulation. The velocity ratio is fixed to 1, the channel width is fixed to 6 mm, and the channel height varied. This gives a minimum lap time of 1051.2 s and a final temperature of 73 ˚C with a 40x6 mm cooling channel. A lap time surface plot resulting from this grid search is shown in Figure 7.7. This was confirmed by a short optimisation of cooling channel height and deployment sensitivity threshold value using MATLAB 'fmincon'. This point is indicated by the red circle in Figure 7.7. This is a significant lap-time improvement of 29 s.

Inspection of the lap time surface, Figure 7.7, shows that a deviation from the modelled behaviour will not result in a significant lap time penalty and therefore this is a sensible development avenue to pursue for stable lap-time gain.

Figure 7.8 shows the lap time reduces until the battery capacity limit is reached and the heating constraint is no longer violated. It is also evident that the drag increase has a non-negligible effect on the response. This is illustrated by the shift of the lap time energy curve in Figure 7.8. This suggests further lap time reduction could come from optimisation of the cooling channel. As $F_{d,duct} \propto v_{duct}^{2}$ and $Q_{cool} \propto v_{duct}^{\sim 1}$ it appears best to reduce duct velocity. However, the transition to laminar flow reduces the Nusselt number, and the cooling efficiency is reduced. Further optimisation would be best undertaken using CFD to better understand a reasonable approximation of these coefficients, but this is outside the scope of this thesis.

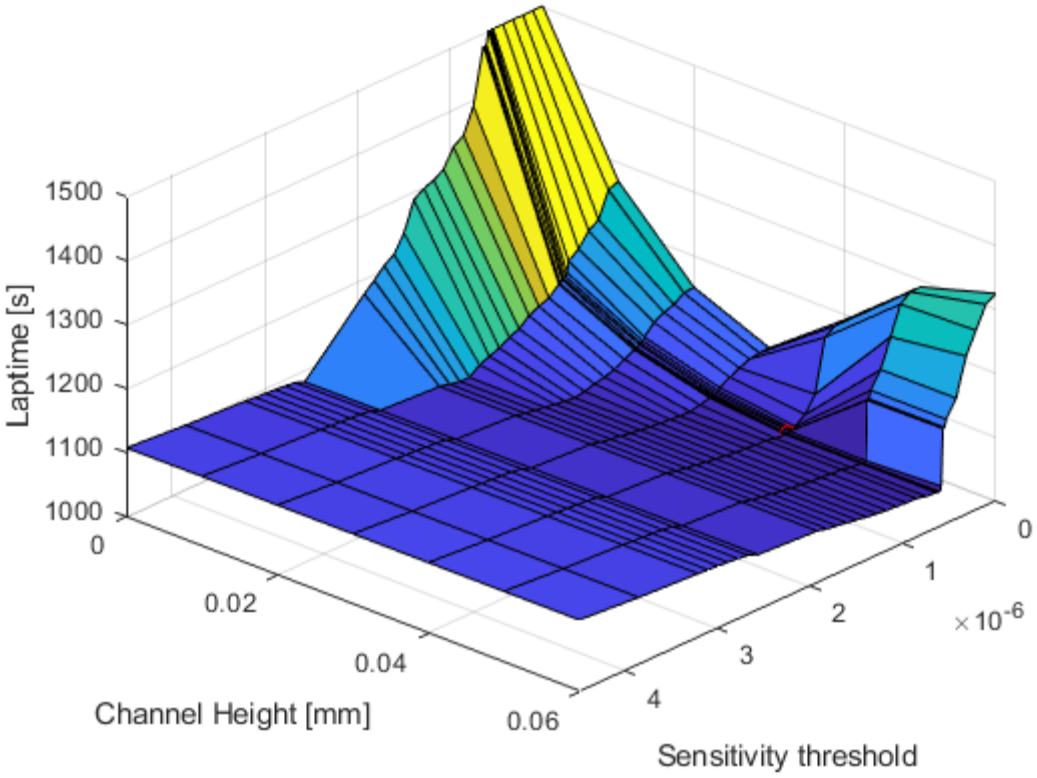

Figure 7.7 - Lap time surface plot for cooling channel height and Energy deployment sensitivity threshold value

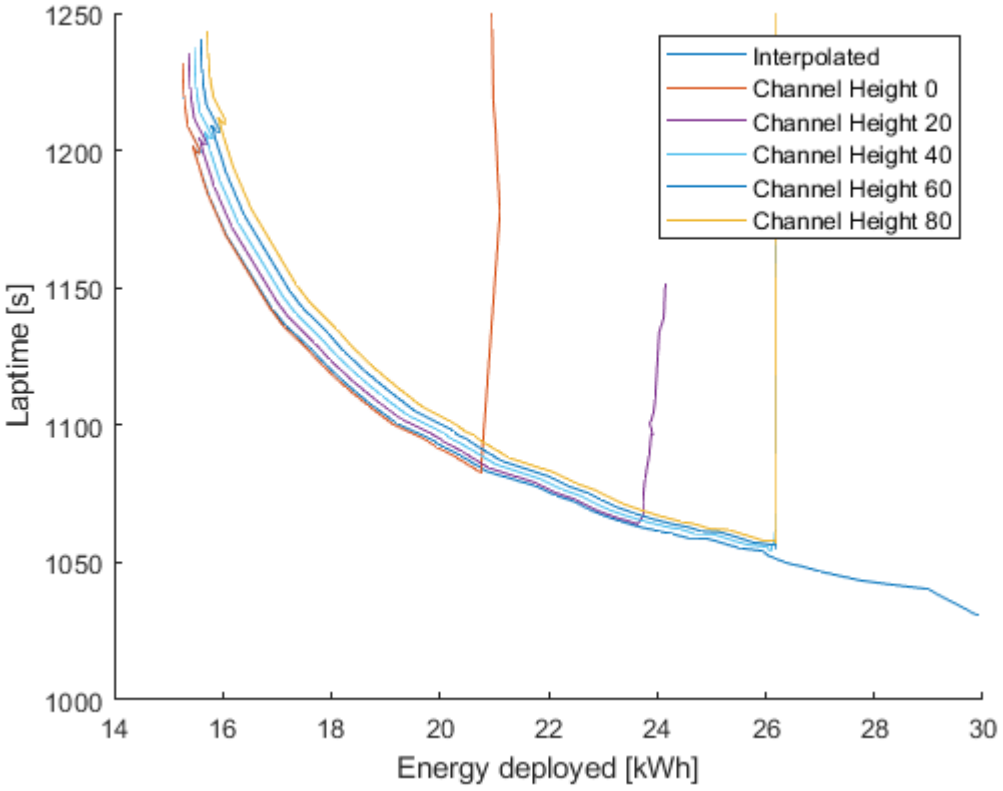

Figure 7.8 - Energy deployment vs lap time curve for differing cooling channel configurations.

As the cooling rate varies with battery temperature, there may be a lap position dependency to the optimal deployment. To investigate this the deployment sensitivity value was adapted to include a linearly varying lap position dependency in addition to the fixed value. This investigation was performed using a grid search, followed by a local optimisation using MATLAB 'fmincon', with constraints used to ensure the threshold values did not generate a negative sensitivity target. This was used to determine if a lap time improvement was possible. This process was trialled for three different cooling channel sizes. The best lap times achieved are as follows, Table 7.1:

Lap Time Achieved	*Fixed energy sensitivity*	*Linearly variable sensitivity*
No Cooling Channel	1081.9 s	1078.8 s
20 mm Cooling Channel	1062.8 s	1061.6 s
40 mm Cooling Channel	1051.2 s	1051.1 s

Table 7.1 – Lap time achieved with differing cooling channel sizes and differing energy managements strategies

While this does show that improvements can be achieved utilising a more intelligent threshold, the gain is small and the linear variation coefficients optimised close to zero. This is a computationally expensive exercise to undertake for each design variable change and will have a limited effect on design variable selection with properly designed cooling. Therefore, it was decided to forgo this additional level of complexity for the design variable sensitivity investigations. However, this should be reintroduced when determining race strategy.

To better visualise the lap time response to these variations, a lap time response surface for the UoN2018 TT specification machine with a 20 mm cooling channel to fixed and linearly varying sensitivity threshold coefficients is shown in Figure 7.9. This also neatly illustrates the significant lap time penalty for over-heating or over-discharging a battery pack.

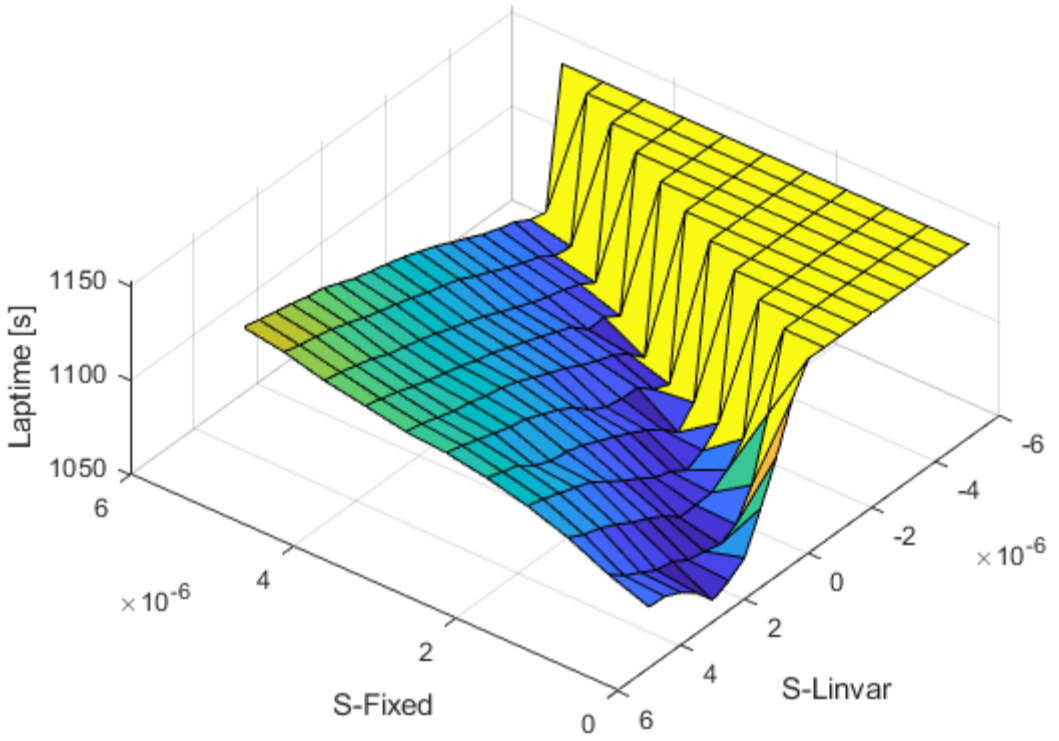

Figure 7.9 - Lap time response surface showing the combined effect of fixed and varying sensitivity threshold coefficients

7.1.4. Combined Management Strategy

The potential for a combination of these strategies to yield further improvements is also investigated. Here, fixed sensitivity thresholds are used for both energy and temperature sensitivity, and a grid search is performed for no cooling channel and 40 mm channel. Combined sensitivity shows an improvement for the case with no cooling to 1065.1 s. This is better than either temperature management or energy management alone. However, when sufficient cooling is introduced (40 mm channel) the best lap time is achieved when the temperature sensitivity coefficient drops to zero, and the energy sensitivity method is selected. Therefore, the energy management method, combined with sufficient cooling, is selected for the following design sensitivity investigation.

7.1.5. Electric Motor Scaling

Using the electric motor model developed in Chapter 5 it is possible to scale a motor torque output by scaling the motor core length. This has the effect of altering the torque output and mass of the motor. Further scaling of the number of winding turns allows the retuning of the motor torque-speed response for a given motor drive and battery configuration.

The plot in Figure 7.10 illustrates the effect of scaling motor turns and core length on lap time at the Isle of Man TT Zero. This shows that there is a significant effect on lap time. However, as the gear ratio is not reoptimized for each motor configuration this is purely illustrative of the process and used here to demonstrate model parameter sensitivity.

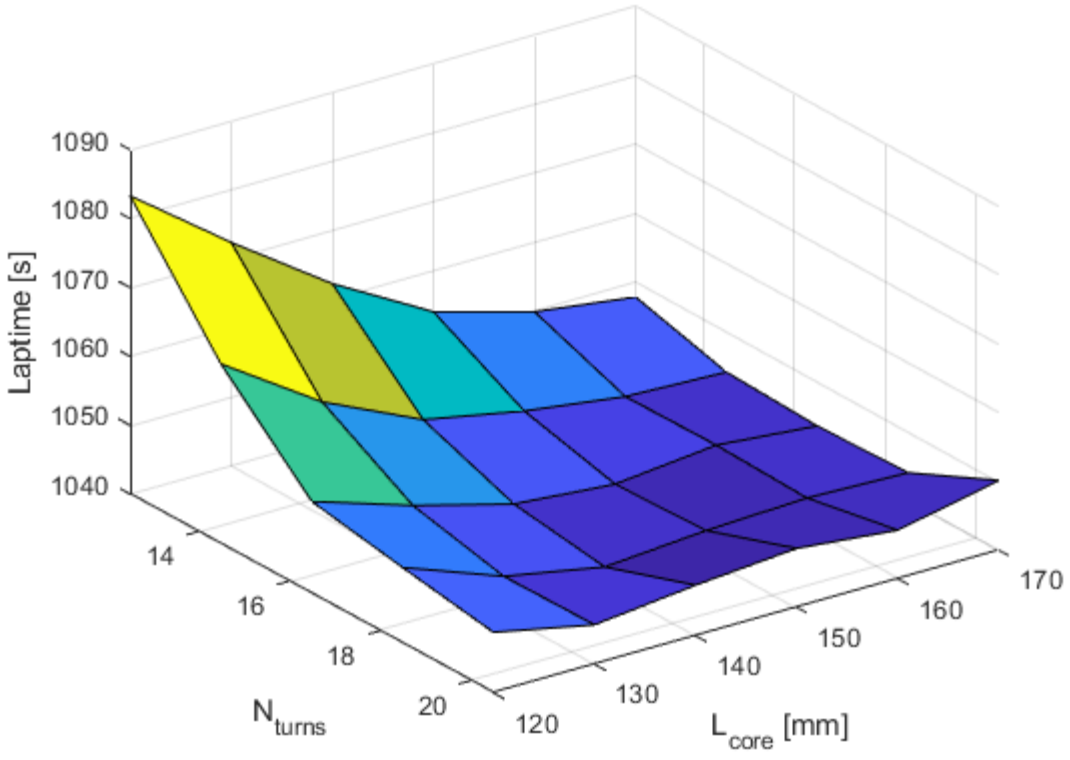

Figure 7.10 - Plot of motor core length and number of winding turns the effect on lap time.

7.2. Isle of Man TT Zero Design Sensitivities

To properly evaluate the effect of design decisions, it is useful to have a view on the sensitivity of the design to the proposed changes. This is usually performed using parameter sweeps. For the following section, the UoN TT 2018 machine has been used as a reference. Up to this point, only the management strategy has been varied. To ensure that the sensitivities determined are representative of the ultimate performance of the machine it is important to first re-optimise the gear ratio with energy management and battery cooling included, and then to determine the sensitivities to other design parameters. This has led to an additional 8 s lap time improvement and therefore a shift in baseline lap time.

To speed up the parameter sweep process and ensure no hidden bias, the final optimisation step for the energy management determination was removed, instead of

relying on the best values from the grid search. This has led to some noise in the data, but, as the goal is to determine the design sensitivity, a linear fit through multiple points is used to robustly capture the required sensitivity.

By determining the sensitivity of a design parameter such as mass, and another competing requirement, such as battery capacity it is possible to determine an optimum design point while respecting both constraints. For the racing use case, the performance metric is lap time. Other potential commercial uses will have different metrics such as vehicle range.

To this end, several sensitivity studies have been performed to investigate different common design trade-offs inherent with an electric motorcycle. These include battery sizing, the introduction of a reduction gearbox, the impact of motor rotor inertia, the optimum lift to drag ratio and the potential benefit of a motor drive featuring silicon carbide MOSFETs.

7.2.1. Mass Sensitivity

Mass sensitivity is defined as the lap time change for each kilo of mass added to the machine. Here the mass sensitivity sweep is performed for both the 2018 TT specification machine as ran in 2018 with fixed speed and power limit, see Figure 7.11. The same mass sweep is then performed for the same baseline setup but with energy management and battery cooling, Figure 7.12.

As can be seen the mass sensitivity changes significantly in differing operational regimes. With a value of 0.139 s/kg for the original deployment strategy and 0.261 s/kg for the upgraded deployment strategy. The introduction of the need to accelerate hard and then coast has altered the vehicle design requirements. This has implications for the entire machine design process and highlights the importance of building a simulation that encompasses the entire machine performance in an integrated manner.

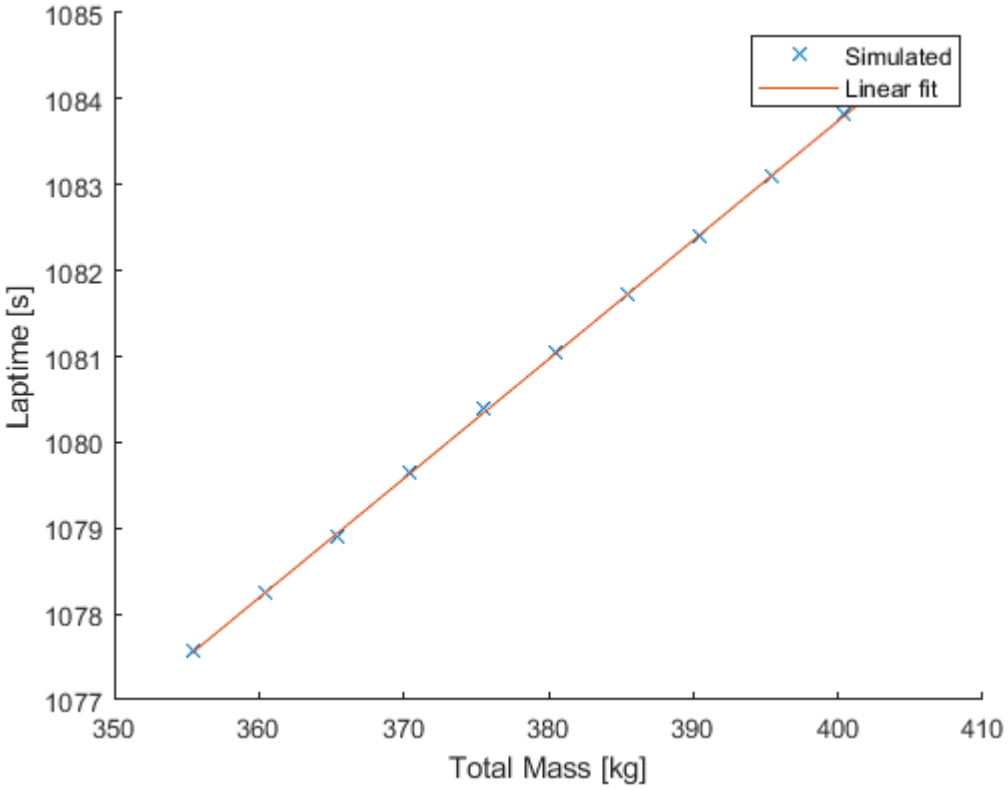

Figure 7.11 - Mass sweep for UoN 2018 TT Zero motorcycle. Fixed speed limit, power limit, and gear ratio: 0.139 s/kg

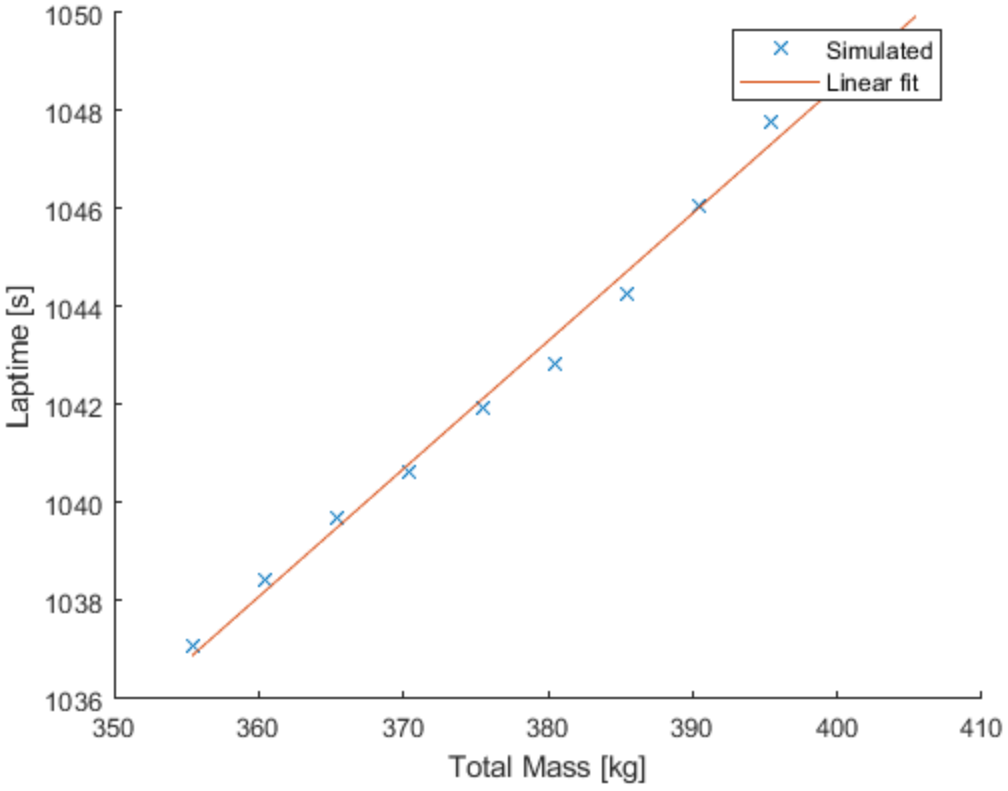

Figure 7.12 - Mass sensitivity sweep with energy management and battery cooling: 0.261 s/kg

7.2.2. Battery Sizing

An important factor to determine is the effect of additional battery capacity on lap time achieved. This can be obtained by differentiating the lap-time gain/energy use plot, Figure 7.8. An example of this using the UoN TT2018 machine as a reference is shown below in Figure 7.13. The data is noisy but a value of 4.32 s/kWh at 26 kWh capacity can be obtained.

To determine if more battery will be beneficial to the lap time, the energy density of the battery is required. In the case of the UoN machine, this is can be approximated as 184 Wh/kg at 5C. ‘C’ here refers to the discharge rate of a battery cell compared to its capacity; a 10 Ah cell discharged at 50 A is undergoing a 5C discharge. This value is used as the energy density varies with discharge rate and the 5C discharge is similar to the RMS discharge current for the TT lap.

By taking the change in lap time for a change in energy usage, at the current pack capacity of 26kwh, the lap time gain for an additional kilo of battery is 0.795 s/kg. This can then be compared to the lap time mass sensitivity of 0.261 s/kg. The evaluation of these two sensitivities determines that each additional kilogram of battery mass will improve lap time by 0.534 s, for the TT race with the UoN 2018 setup, using proper battery cooling and energy management strategy. Practical limitations such as the regulation upper mass limit of 300 kg can prevent the optimum value from being reached for this race.

As this line of investigation progresses a theoretical 31 kWh is required for an unrestricted deployment with the motor and drive limitations unchanged. However, as additional capacity is added the energy sensitivity drops to 0.847 s/kWh or 0.156 s/kg. This is below the mass sensitivity threshold. The optimum is reached where the energy sensitivity and mass sensitivity achieve equilibrium. This is at 1.418 s/kWh which corresponds to a pack size between 30.5 and 31 kWh. A small mass and therefore lap time saving could be possible here. However, due to the presence of battery degradation, it is always wise to slightly over-specify the battery capacity where sensible. It is therefore recommended that any capacity reduction be done with caution.

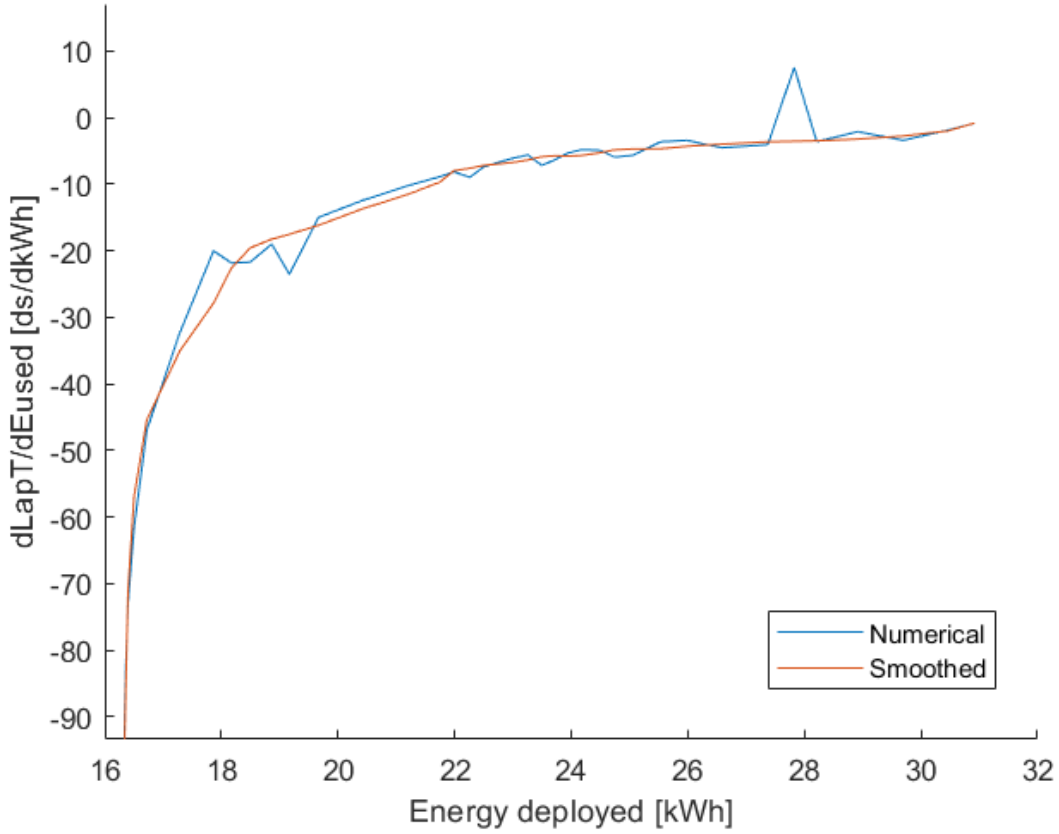

Figure 7.13 - Lap time energy sensitivity plot for UoN TT 2018 specification machine.

7.2.3. Driveline Efficiency

To get a better understanding of the design trade-off inherent with gearbox use it is important to quantify the lap time penalty from reductions in torque efficiency. Torque efficiency is given as a percentage value. Here torque efficiency is defined as the gearbox input torque minus the torque lost divided by the input torque. This sweep is performed on a UoN TT 2018 specification machine with energy management and a 40 mm battery cooling channel, the results of which can be seen plotted in Figure 7.14.

This sensitivity value of 1.92 s/% can then be combined with the mass sensitivity to show that a 98.5% efficient gearbox would have to save over 11 kg in powertrain mass to be a worthwhile investment assuming no motor efficiency changes. This is potentially an over-estimate as the mass saving can be used to incorporate a larger battery pack but also potentially an underestimate as the inertial sensitivity is omitted in this evaluation, and gearbox efficiency is more complex than a fixed percentage torque loss.

This is an important result that reinforces the decision to utilise the direct to chain drive electric motor setup, as used on the UoN machine, but also quantifies inherent trade-off allowing for the evaluation of technologies that can overcome this compromise.

To properly evaluate the effect of a gearbox, a design study should be undertaken that will identify the approximate sizing and appropriate loss modelling. The vehicle model can then properly investigate the appropriate design space, but this is again not a useful addition to this thesis.

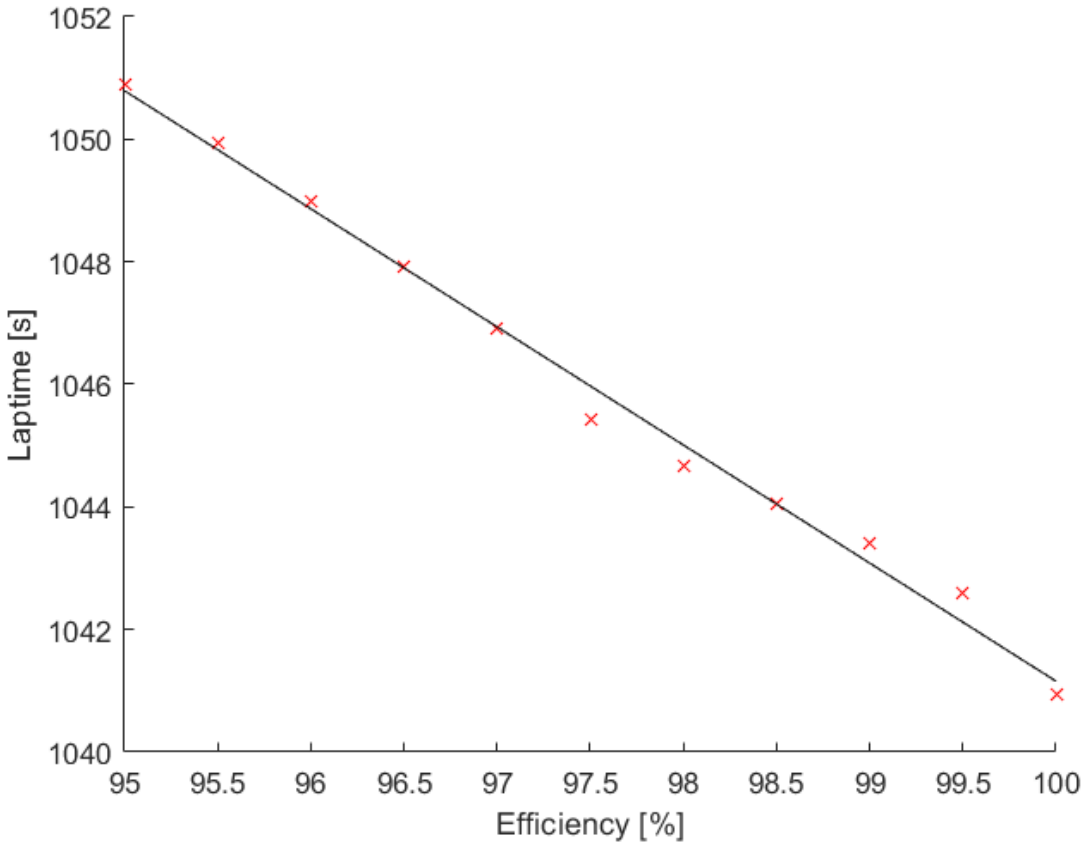

Figure 7.14 - Effect of electric motor to chain drive torque efficiency on lap time: 1.92 s/%

7.2.4. Motor Inertia Sensitivity

Motor inertia is included as an equivalent mass, and it is important to understand the impact of motor inertia itself on full vehicle performance. The result of this parameter sweep can be seen in Figure 7.15, with a motor inertial sensitivity of 48.8 s/kgm^2. This makes reductions to the motor rotor inertia appear an attractive prospect. However, the rotor inertia is comparatively small and a 10% reduction in this (0.0023 kgm^2) results in only a 0.11 s lap reduction. Therefore, although rotor inertia should

be reduced where possible it is likely that there are bigger gains to be had focusing elsewhere.

It is also worth remembering the effect of the transmission ratio here. The sprocket ratio 18:81 was used for the inertial sweep and therefore the effective inertial sensitivity is 2.41 s/kgm^2 when referred to the rear wheel. This rear-wheel referenced value can now be used to evaluate the effect of different motors that operate at different speeds with different rotor inertias.

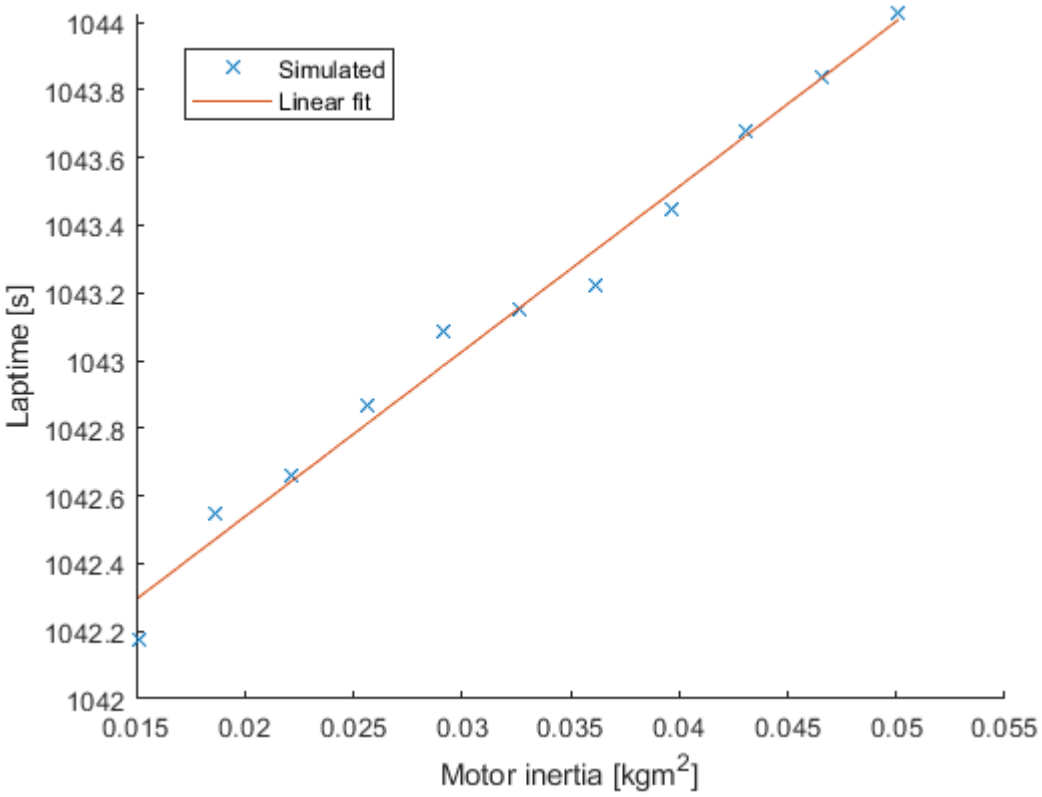

Figure 7.15 - Motor inertia sensitivity for Parker GVM210-150: 48.8 s/kgm^2

7.2.5. Electric Motor Choice

Of the motors available for direct drive applications, the three most common options are the Parker GVM210-150 [117] as used on the UoN motorcycle, the EMRAX 268 [172], and the motor developed by Blissett [16].

Here, the change in lap time in comparison to the reference motor (GVM210-150) is determined. The gear ratio is set so that the same peak rear-wheel torque is reached for each motor. It is assumed that freedom over winding configuration allows similar torque-speed responses with respect to the rear wheel to be obtained. This allows

direct comparison of equivalent rear-wheel inertial contributions; a summary of these values is given in Table 7.2 below.

Motor	*Motor Mass*	*Mass time*	*Motor Inertia*	*Effective Inertia*	*Inertial time*	*Total time*
Parker GVM210	42 kg	0	0.0233	0.472	0	0
EMRAX 268	21.5 kg	-5.61 s	0.0922	0.505	0.08s	-5.53 s
Blissett Motor	28 kg	-3.65 s	0.0373	0.567	0.29s	-3.36 s

Table 7.2 – Effect of differing motor choices on lap time when comparing mass and rotor inertia

This initially suggests the EMRAX 268 motor will outperform the Blissett motor, however, a key metric missing here is the cycle efficiency. A 1% full cycle efficiency gain will overturn this deficit. It can be seen that 1% drive cycle torque efficiency is worth 7.36kg of motor mass for the TT Zero race. This reinforces the need to properly evaluate the full powertrain efficiency. As the required measured motor parameters are not available for all motors it would be unfair to compare datasheet and measured values, so this is curtailed here.

7.2.6. Silicon Carbide MOSFET switches

Silicon Carbide MOSFETs have lower switching energies and are currently used in some high-performance electric racing cars as a result. To evaluate the potential lap time gain from efficiency improvements, resulting from implementing a motor drive containing Silicon Carbide MOSFETs, the appropriate loss coefficients are transposed. The losses from the six Infineon FS450R12 IGBTs [140] in the Sevcon Gen4 Size 10 used by the UoN TT2018 machine are replaced by the loss coefficients associated with CREE CAS325M12HM2 and CREE CAS480M12HM3 ‘All Silicon Carbide’ switches [173, 174].

For further comparison, the BAMOCAR D3 motor drive loss coefficients are included [175]. This was the motor drive used by UoN before the Sevcon Gen4 Size10 and contained three FF600RME12 IGBTs. Also included is the effect of combining several devices in parallel to reduce the current per module. CAS325M12HM2 has not been evaluated as a single module as the motor requires higher phase currents than a single module can supply. The results of this investigation are set out in Table 7.3.

Switching Module	*Loss contribution*	*Additional Mass*	*Total Lap time*
FS450R12-6of	0	0	0
FF600R12-3of	+0.1 s	-0.22 s	-0.12 s
FF600R12-6of	-0.6 s	+0.05 s	-0.55 s
CAS325M12HM2-6of	-3.7 s	-0.26 s	-3.96 s
CAS480M12HM3-3of	-3.8 s	-0.34 s	-4.14 s
CAS480M12HM3-6of	-3.8 s	-0.20 s	-4.00 s

Table 7.3 – Effect of differing switching module choices and number in parallel on lap time

This clearly shows that the implementation of Silicone Carbide MOSFETs is of appreciable benefit and that the best benefit will be obtained with 3 CAS480M12HM3. These lap time gains are a useful performance differentiator. This analysis does however ignore other benefits such as drive volume reduction and the ability to implement higher switching frequencies. Both are additional benefits to using the Silicon Carbide MOSFETs. Higher switching frequencies can reduce motor losses and are useful for controlling motors with a high electrical frequency. To properly realise these benefits a full redesign of motor and drive would be required.

7.2.7. Aerodynamic Drag

An important metric representing the overall aerodynamic efficiency of the machine is the motorcycle drag coefficient multiplied by the cross-sectional area, C_dA. This is referred to as the drag sensitivity. As the change in C_dA is generally small, of the order of 0.01 C_dA, and the effect of a change is high, sensitivity here is calculated in 'points', or 0.001 C_dA. In the case of the UoN motorcycle at the TT Zero, the drag sensitivity can be found in Figure 7.16 as 0.22 s/pointC_dA. For reference motorcycle side mirrors can add between 0.012 and 0.025 to the C_dA figure for a road going motorcycle [19]. This equates to 2.6 to 5.5 s of lap time. This means that there are significant gains to be found through drag reduction.

The author's rearrangement of the motorcycle's battery layout to allow the movement of the rider's knees 75mm towards the centre of the machine on both sides will have saved an estimated 75 mm by 400 mm of frontal area. This equates to 6.6 s of lap time (ignoring any changes to the drag coefficient itself). This is more than that gained from designing a Silicon Carbide MOSFET based inverter. This sensitivity is not a surprising result given the emphasis on efficiency due to the restrictions in energy

capacity and is one of the reasons that a significant UoN development effort was focused on drag coefficient and frontal area reduction, despite the many protestations about ‘looks’.

Another area of significant interest on modern racing motorcycles is the addition of downforce generating winglets. When evaluating the performance benefit of downforce generating devices it is important to understand what level of performance provides a benefit to the machine. The downforce sensitivity is in this case given in terms of 0.001 $C_{lw}A$ for similar reasons to the above for C_dA. Figure 7.17 contains the results of this investigation and gives a downforce sensitivity of 0.0078 s/point Cl.

The generation of downforce is usually associated with a corresponding drag penalty. The combination of these factors is known as the downforce to drag ratio or lift to drag ratio, depending on context. By determining the minimum downforce to drag ratio that provides benefit, designs can be immediately characterised as useful or not useful. If the performance exceeds the cut off ratio, then the part is useful. If it does not, then it is scrapped or retained for a race with a different sensitivity.

In the case of the UoN motorcycle, at the TT Zero, by taking the drag sensitivity of 0.22 s/pointC_dA from Figure 7.16, and the downforce sensitivity of 0.0078 s/point Cl from Figure 7.17, a target ratio of 25.6 is obtained. This is extremely unlikely to be obtained with a motorcycle winglet and drag reduction is the preferred course of action for the TT.

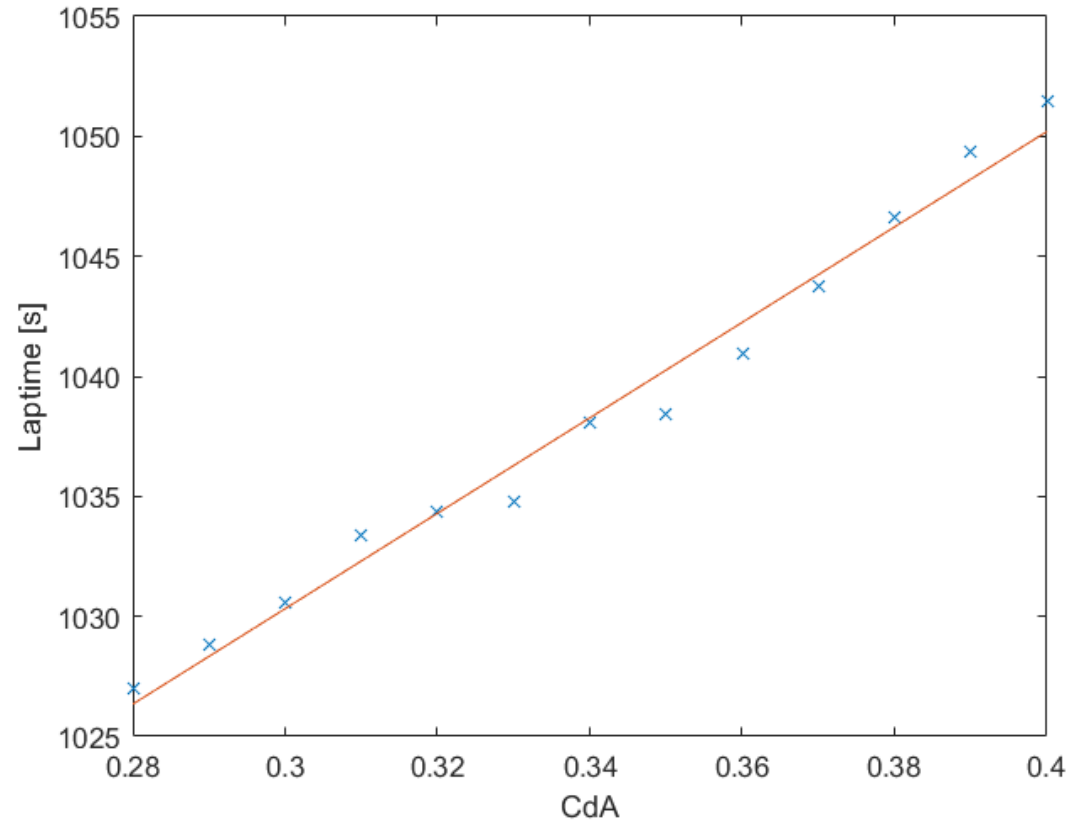

Figure 7.16 - Plot of lap time with varying CdA values, resulting sensitivity is -0.22 s/pointC_dA

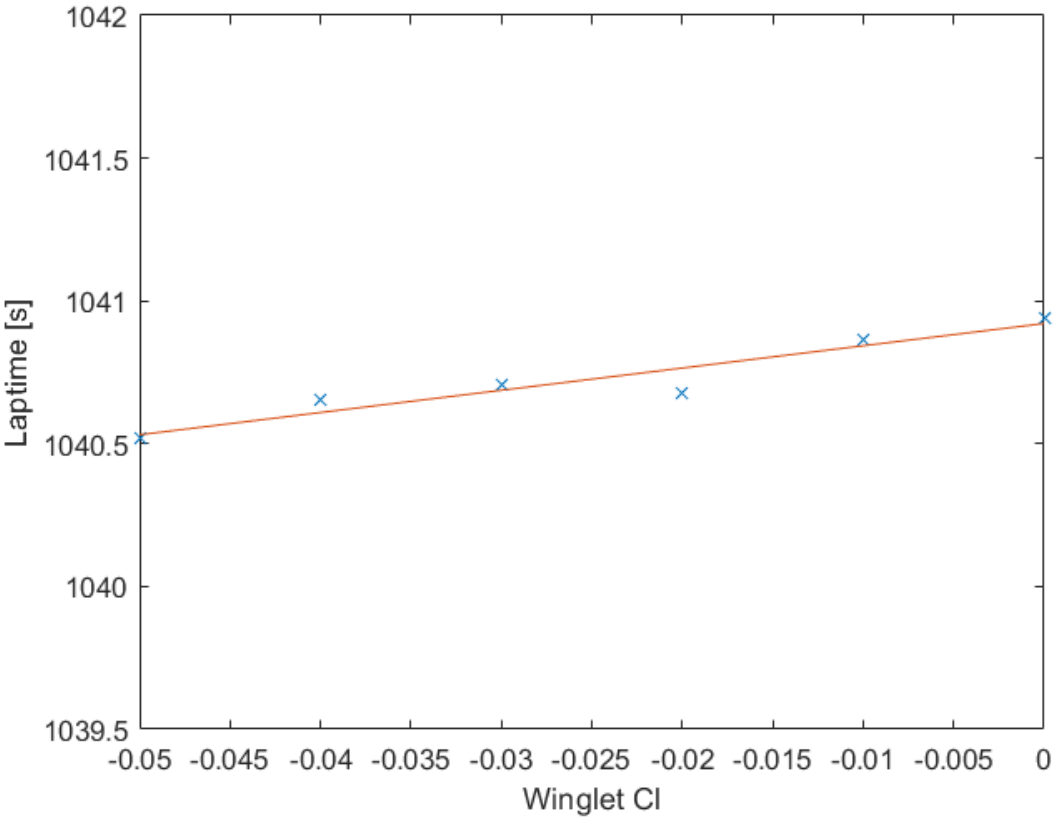

Figure 7.17 - Effect of Winglet Cl on lap time. -0.0078 s/point $C_{lw}A$

7.3. Pikes Peak International Hill Climb Sensitivities

It is worth pointing out here that the total lap time at Pikes Peak International Hillclimb (PPHIC) is just over half that of the TT, therefore the magnitude of the sensitivities will be scaled by a similar amount.

7.3.1. Pikes Peak Battery Sizing

There is no mass limit at PPHIC. The track is short, and the track is comparatively low speed so it is possible to include sufficient energy for a full race without requiring energy management. The question is then, is it preferable to reduce the battery size, save mass, and include energy management, or is it better to design the battery to allow ultimate deployment? To answer this question the sensitivity to additional energy as well as the mass sensitivity is required. Figure 7.18 is used to determine the mass sensitivity as 0.021 s/kg and Figure 7.19 is used to determine the energy sensitivity as 6.42 s/kWh. A similar process to that used for TT battery sizing is then followed.

The cells used at PPHIC have a higher peak power rating due to the shorter discharge time than those used at the TT and are correspondingly less energy-dense. The individual cell mass was similar to that of the TT cell but the capacity available was only 80% of the TT cell. This leads to a representative energy density in the region of 150 Wh/kg when cell connections and packaging are included. This could be improved through better cell selection but is representative of the performance level and will be used here.

This results in 0.963 s/kg for additional energy at the end of discharge which is significantly higher than the mass sensitivity. This means that energy management is not beneficial for a suitably sized designed PPHIC battery pack and is therefore not required for further PPHIC performance investigations. This is a useful finding both in terms of battery design and the fact that this knowledge can be used to reduce simulation time by eliminating the need to determine deployment strategy.

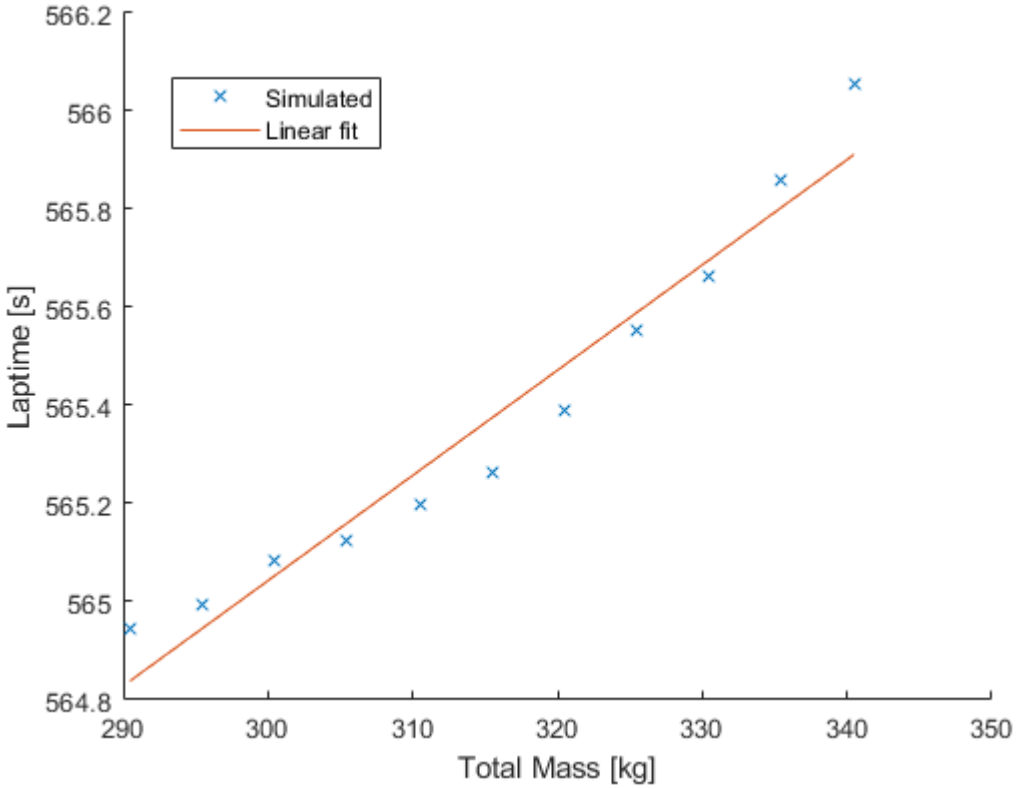

Figure 7.18 - PPHIC Mass sensitivity: 0.021s/kg

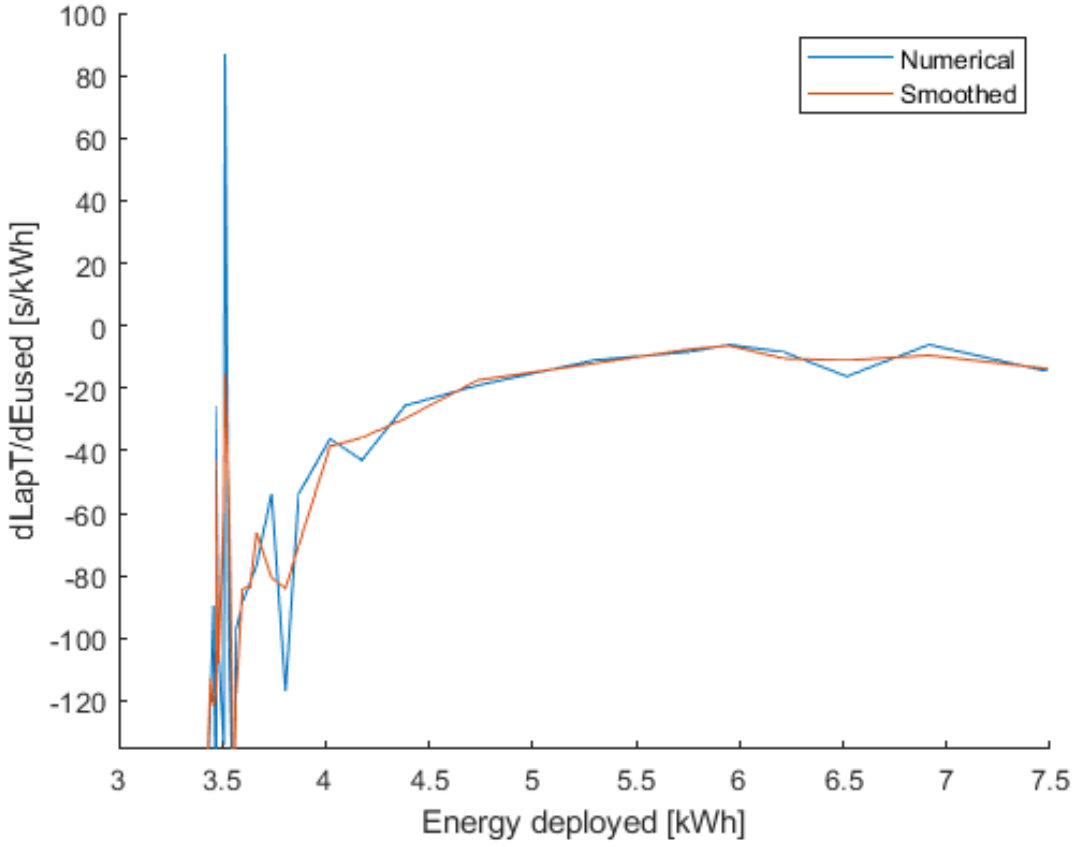

Figure 7.19 - Energy lap time sensitivity with increasing energy use. Minimum value 6.42 [s/kWh]

7.3.2. Winglet Sensitivity

The PPHIC course is significantly different to the TT with lower maximum speeds and more emphasis on acceleration out of low-speed corners. As a result, the aerodynamic compromise is extremely different to that of the TT.

The process used for the IoM TT is again repeated here to determine the cut-off lift to drag ratio. This involves taking the drag sensitivity of 0.0153 s/pointC_dA from Figure 7.20 and 0.00873 s/pointC_lA from Figure 7.21. Therefore, the minimum lift to drag ratio for an effective winglet is now 1.75:1. This figure is a significantly more achievable figure than the previous TT figure and should be pursued.

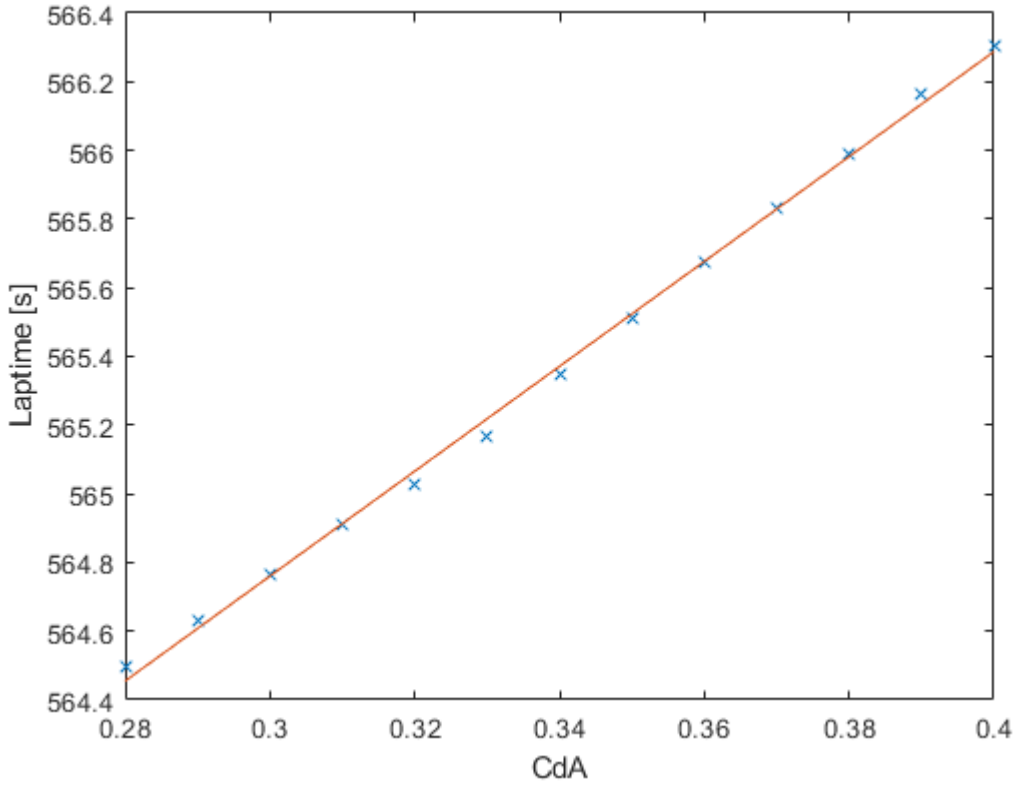

Figure 7.20 - Drag sensitivity plot for PPHIC: 0.0153 [s/pointC_dA]

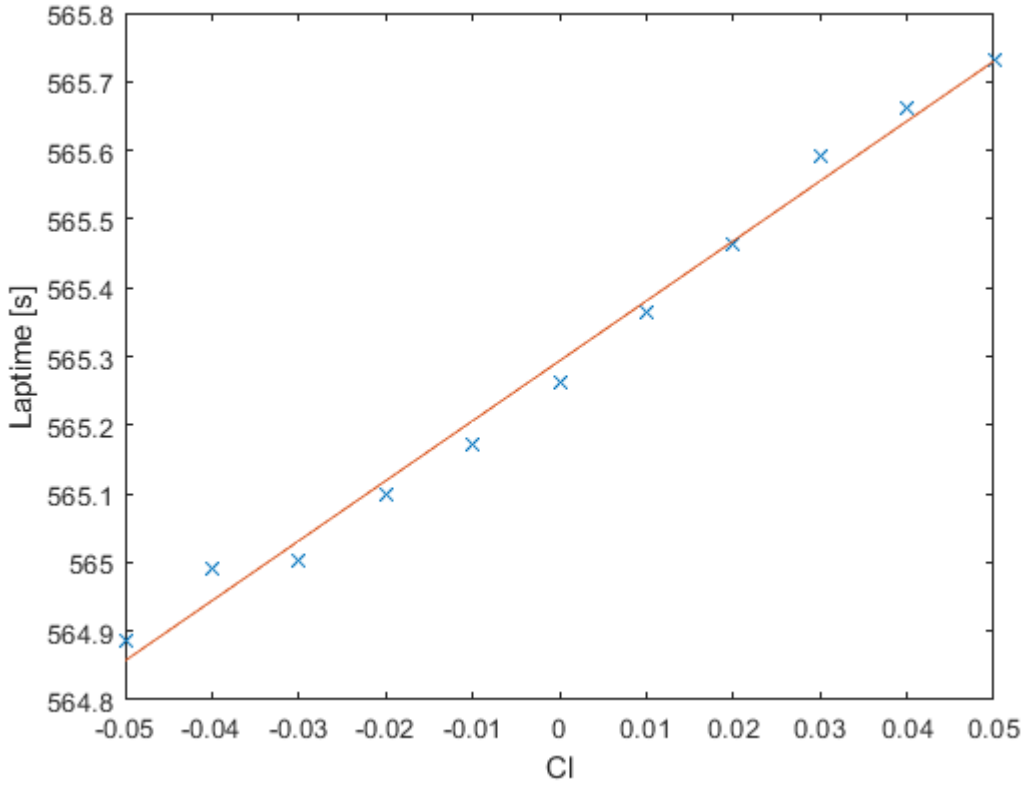

Figure 7.21 - Lift coefficient sensitivity for winglet at PPHIC: 0.00873 [s/point]

7.4. Conclusion

A lap simulation tool for high-performance electric superbike evaluation has been developed, and a simplified energy and temperature management methodology implemented. This tool has been used to identify the fact that the UoN 2018 TT Zero contender was severely compromised by its choice to forgo battery cooling as well as by the lack of energy deployment strategy.

Methods to overcome these issues have been outlined through design changes and/or deployment strategy changes. The use of targeted velocity and power limitations without design changes results in 7 s of lap time improvement when compared to the global power and velocity limitation strategy employed by Blissett [16] as well as only requiring a peak power of 120 kW. The inclusion of battery air cooling however results in a 30 s lap time reduction and the full deployment of the stored energy. This lap time reduction is further improved by an additional 8 s by re-optimising the gear ratio for this higher deployment level.

By equating the relative lap time sensitivities to mass and additional energy it is shown that in most circumstances it is beneficial to increase the battery size up to a point where no energy management is required. However, in some scenarios even

with unlimited battery choice, it can be advantageous to include some energy management as the mass sensitivity exceeds that of the energy sensitivity. Although caution is recommended here, as battery degradation will serve to reduce the available battery energy with multiple battery cycles.

Further investigations of design trade-offs reveal that the lap time penalty for efficiency is particularly restrictive for the TT. In addition, it reveals that practical downforce generating winglets will not be an advantage for the TT. The integration of a primary reduction gearbox is also shown to be unlikely to be beneficial for this race unless this results in significant motor mass savings.

PPHIC is an entirely different race and the findings are also entirely different. Lap simulation recommends the inclusion of winglets for PPHIC and finds that energy management strategy is not beneficial. Instead, the design should focus on full deployment at all points.

The evaluation of several commonly used motors for electric superbikes reveals that the mass and efficiency are more significant performance differentiators than the rotor inertia, although rotor inertia should still be included for accuracy of vehicle performance determination. With a 1% drive cycle torque efficiency increase being worth 7.36 kg of motor mass it is very important to optimise motor efficiency for the target operating cycle.

In summary, the lap simulation tool is shown to be extremely useful for the design and development of high-performance electric superbikes, with sensitivity to many pertinent design parameters, from switching module choice to winglet target aerodynamic efficiencies. Further work to utilising multivariate optimisation would automate this performance discovery effort and lead to an accelerated and more refined design process but is beyond the scope of this thesis.

8. Conclusion

The aim of this thesis was to perform an integrated performance analysis of high-powered electric motorcycles. For the integrated analysis, it is important to first understand the underlying differences between internal combustion motorcycles and their electric counterparts, then to expand this investigation to determine if current modelling techniques fully capture the electric powertrain specific compromises.

Initial work to understand the available literature determined that although there have been some previous attempts to build a fully integrated electric motorcycle model, they fell short of fully capturing the response of a modern high-performance electric motorcycle. The most notable attempts are those by Blissett [24] and Dal Bianco *et al.* [17]. Further investigations also revealed that there have been no investigations into the stability and control of high-performance electric motorcycles and that this could be an interesting avenue for further research given the significantly higher mass of the contemporary machine.

This led to the development of two primary objectives. The first was to investigate whether the current state of motorcycle stability and control analysis is capable of handling certain high-performance electric motorcycle-specific compromises, such as the higher mass and differing chain drive setups required. This is answered in Section 8.1.1.

The second objective was to perform an integrated performance analysis of the modern high-performance electric motorcycle. This was to include significant elements of both mechanical and electrical design to properly understand vehicle design trade-offs to allow targeted development and resultingly significant performance improvements. This is handled in Sections 8.1.2, 8.1.3 and 8.1.4. The conclusions of this thesis including recommendations for further work are detailed in section 8.2.

8.1. Review of Aims and Objectives

In this section, the aims and objectives set in Section 1.2 are reviewed and it is determined how they have been met during this investigation. The following four sections directly address the initial objectives.

8.1.1. Investigation into the performance of existing IC modelling techniques when applied to a contemporary high-performance electric motorcycle.

To satisfy this objective, investigations into gearing, squat response and contemporary high-performance motorcycle stability were performed. A modern high-performance electric racing motorcycle was available for research purposes, and therefore work to characterise it was undertaken. This characterisation involved the measurement of the motorcycle geometry and electrical setup.

An investigation into electric motorcycle gearing underlined the need to retain a single-stage reduction. This leads to a situation where an abnormally large rear chain drive sprocket is desired. As an abnormally large rear sprocket will affect the squat response of the motorcycle, an investigation was performed to see if it was possible to restore a conventional response. This was achieved through the repositioning of the motor and swingarm mounting points. The analysis was performed while respecting practical constraints on chain length variation and packaging. The task was found to be possible using existing techniques.

The second area that required investigation was the stability of the machine itself. To this end measured geometry and rear frame inertias were used as inputs into an extremely well-known motorcycle stability analysis tool: the Sharp 71 model. It was found that the capsize and weave responses were broadly similar, albeit with slightly higher damping, for the higher mass electric machine. The weave response was found to have differences in terms of both shape and magnitude, however, when the front frame mass and geometry settings are altered to be common across both machines, the weave response shape regained similarity with the original reference Sharp model. This determines that existing stability analysis techniques remain appropriate and simply require updating with new parameter values.

In summary, the objective has been satisfactorily achieved and the contribution here is the provision of reference high-performance electric motorcycle data. This investigation concluded that although there are some differences between the stability of the high-performance electric motorcycle and reference internal combustion designs, the differences could be easily accounted for and rectified as required using existing modelling techniques. This is an understandable conclusion as there are major similarities from a mechanical standpoint between both designs.

8.1.2. Investigation into and implementation of appropriate vehicle performance modelling techniques for high-performance electric motorcycles.

This objective was approached by initially studying the existing literature surrounding high-performance electric motorcycle modelling. This investigation identified the two most relevant existing contributions to the field and analysed their suitability for the task. A summary of the findings is included here.

Of the previous works on the subject the most notable are those by Blissett [24] who focused on permanent magnet motor development and Dal Bianco *et al.* [17] who analysed the lap time response of an early competitor in this race. The major limitations with each respecting approach are summarised here but greater detail is contained in Chapters 4 and 5. Both have their merits but neither manages to fully capture the holistic vehicle response of a modern high-performance electric motorcycle.

The model developed by Blissett [24] utilises an advanced motor model but is noticeably lacking in terms of battery modelling as well as full vehicle response. This is particularly with regards to tyre response and the effect of lateral force on vehicle speed profile. The effect of tyre slip is ignored as is the effect of a tyre friction circle on longitudinal response. This leads to a poor determination of overall vehicle performance and is masked by the fitting of the model to lap data. Additionally, by altering battery internal resistance values and fitting of other parameters, such as gear ratio to track data, this fitting approach reduces the ability to predict machine performance in advance of arrival at an event.

The second work by Dal Bianco *et al.* [17] utilises a more advanced approach to the machine lateral and longitudinal dynamics through the use of a vehicle and tyre model and electric motor model, which is then solved for the race event using the optimal control approach. The drawbacks with this model primarily surround powertrain modelling and component selection, as well as the solve time required particularly for a more advanced model. This approach used highly simplified battery and motor modelling, including a fixed battery internal resistance similar to Blissett [16]. The powertrain modelled consisted of two 25 kW DC motors and recommended a maximum battery capacity of 10.3 kWh would result in a lap average speed of 85.7

mph if updated to include 3 Agni DC motors. This is no longer representative of a modern electric motorcycle powertrain.

To address these shortcomings and properly understand the performance of the modern machine, a new model was developed. It was decided to use the fixed trajectory quasi-steady-state (QSS) approach to lap simulation. This decision is made with reference to Massaro and Limebeer [48]. A useful rule of thumb detailed within this paper is that a free trajectory full dynamic model approach solved as an optimal control problem will take two orders of magnitude more time than a fixed trajectory QSS approach. The development of the QSS model is broken down into three steps, the development of the mechanical model, the electrical model, and the lap simulation technique.

8.1.2.1. Mechanical modelling

For the purposes of the full vehicle, the mechanical model must properly include tyre response to both vertical load variation and lateral force requirements. This allows for accurate powertrain to road speed and load dependant response modelling. The motor operating point also must consider the geometric variation due to the camber of the motorcycle and the tyre's toroidal shape. Both are included using the Pacejka tyre model and a geometric approximation of the tyre rolling radius.

The vehicle is approximated as a simple and effective rigid body chassis model. This model has been developed and validated using experimental data. The model developed responds to the effects of acceleration, braking, and aerodynamic load distribution as well as the tyre load sensitivity of separate front and rear tyres. The ability to capture the effect of two-wheel-drive is also included and is important for electric motorcycles. This is particularly useful for determining the correct traction limits and the effect on regenerative braking levels. This is an enhancement over the rigid body dynamics model described by Biral and Lot [22] which ignores the effects of downforce, assumes that front and rear tyres are identical and does not account for the possibility of a front-wheel-drive machine. This model is also a significant enhancement over both previous electric motorcycle performance modelling attempts. The development of this model is detailed in Chapter 4.

8.1.2.2. Electrical powertrain model

The electrical system comprises a battery, electric motor, motor drive and transmission model. The model developed here has been achieved by combining several previously published component models from different sources and validating this full model using real-world data. The motor, drive and transmission model developed here is based loosely on the model developed by Blissett [16] but with some notable improvements to expand both the scope and accuracy of the model, particularly with regards to electric motor control and mechanical loss elements. Extensive improvements have been made to the battery modelling.

The single fixed-resistance battery model used in previous models is shown to be a source of inaccuracy particularly for cell temperature prediction. Cell temperature prediction is key to extracting the ultimate performance from the powertrain as battery cells have an upper cell temperature limit that cannot be exceeded as well as performance benefits to be realised through running at elevated temperatures. The management of these competing factors is key to designing a high-performing battery pack and therefore a high-performance electric vehicle.

To resolve this issue lab testing of battery cells was performed in conjunction with an evaluation of several candidate models. It was found that a Thevenin 1RC equivalent circuit model is a good balance of performance and voltage predictive accuracy. In addition, it was found that both the entropic heating and battery voltage hysteresis should be included to properly capture the battery response voltage and temperature.

This enhanced battery model response was evaluated and shown to be superior to that achieved by previous electric motorcycle performance evaluations. In addition to this, novel modifications to established battery testing procedures have been developed and described that are more applicable to the fast estimation of battery parameters with low-cost equipment. This improved model was then successfully integrated into the full powertrain model. The development of this powertrain model is detailed in Chapter 5.

In conclusion, the objective has been met. Existing modelling techniques are found to be lacking in important areas. These shortcomings have been rectified through the development of an appropriate vehicle model that allows the effective evaluation of many design parameter variations. These vary from battery construction to electric

motor winding configuration, electric motor core length variation and switching module choices amongst other parameters in the context of the full vehicle response. This vehicle model applies to both the optimisation of racing machines and for developing cost-effective compromises in mass-market offerings.

8.1.3. Validation of models developed, using data collected using a contemporary high-performance electric motorcycle.

To satisfy this objective a method of evaluating the model performance against real-world data was required. A common method of evaluating a high-performance vehicle is through racing and lap simulation. The high-performance electric motorcycle developed by the University of Nottingham competed at the Isle of Man TT Zero, Pikes Peak International Hillclimb, and in a land speed record attempt at Elvington airfield. This generated data suitable for validation. To use this data and validate the developed vehicle model, as well as providing a tool for performance analysis, a lap simulation model was developed and validated in Chapter 6.

This was achieved through the implementation of a full lap simulation based on GPS coordinates of the racing line. Input data filtering and path curvature determination procedures are evaluated. A common lap simulation method involving apex finding and the forwards and backwards simulation from these points [18] is expanded to incorporate electric vehicle-specific areas, such as powertrain evolution and regenerative braking, as well as rider deployment strategies.

The performance of this assembled model is compared to lap data recorded at both the Isle of Man TT Zero, an extremely long high-speed race, and the Pikes Peak International Hillclimb, an extremely short low speed, high acceleration event. These events are chosen as they are representative of entirely different vehicle trade-offs at the opposite ends of the high-performance electric motorcycle design spectrum and competition data was available. The modelling approach is shown to be effective and able to provide a good correlation between simulation and reality.

Comparison with the Blissett model [16] has identified several areas where the new approach shows significant benefits. The switch to GPS-based lap definition and the use of tyre models has removed artificial constraints and improved the ability to differentiate between machine limitations and rider limitations. Notable improvements can be seen particularly with regards to the correlation between motor

speed and road speed due to the inclusion of a tyre model, with resulting improvements in the modelling of high-speed high-power vehicle behaviour. This has resulted in a substantial improvement in both the ability to predict lap behaviour using laboratory test data and the capability to determine the effects of more substantial changes to machine setup across a wide range of track demands.

In summary, the objective to validate the full vehicle has been met with the performance validated against real-world vehicle and subsystem performance data.

8.1.4. Investigation of potential performance development pathways using validated model.

To achieve this objective, the lap simulation tool developed in Chapter 6 is enhanced in Chapter 7 to include the effect of energy deployment strategies on vehicle performance. This has been possible through developing algorithms to determine the energy and temperature sensitivity of different parts of the lap and alter the deployment accordingly to achieve minimum lap time.

The enhanced lap simulation is applied to a retrospective analysis of the Nottingham TT Zero machine. This determined that the UoN 2018 TT Zero contender was severely compromised by its choice to forgo battery cooling, as well as the lack of energy deployment strategy. The Pikes Peak contender did not require these strategies as it was not energy or temperature limited in its deployment.

The investigation into battery sizing was achieved by equating the relative lap time sensitivities to mass and additional energy. It is shown that in most circumstances it is beneficial to increase the battery size up to a point near that where no energy management is required. However, in some scenarios, even with unlimited battery choice, it can be advantageous to include some minor energy management. This is because the mass sensitivity exceeds that of the energy sensitivity. Although, caution is recommended here as this effect is small and battery degradation will serve to reduce the available battery energy with multiple battery cycles.

Further investigations of powertrain design trade-offs reveal that the lap time penalty for efficiency is particularly restrictive for the TT. This leads to the conclusion that the integration of a primary reduction gearbox is unlikely to be beneficial for this race unless this results in significant motor mass savings.

The evaluation of several commonly used motors for electric superbikes reveals that mass and efficiency are more significant performance differentiators than the rotor inertia with a preference for high-efficiency designs, although rotor inertia should still be included in a vehicle model for accuracy of vehicle performance determination.

A final evaluation into lift-to-drag ratio is undertaken and reveals that downforce generating winglets are not likely to provide benefit at the TT Zero, however, they are likely to be beneficial at PPHIC. This highlights the ability of the model to identify event-specific performance differentiators.

In conclusion, the objective to investigate the main performance differentiators and provide recommendations on performance development pathways has been achieved.

8.2. Conclusions

The main conclusions and recommendations for the design and analysis of high-performance electric motorcycles are as follows:

It was quickly determined that to better understand the full high-powered electric motorcycle performance, it is important to understand both the electrical and mechanical response of the system. It is only by understanding the interactions between these two elements that a truly optimised solution can be found.

Existing literature was examined and found to be unable to provide the required level of detail while respecting both the electrical and mechanical domains. In response to this great effort was put into building and validating a holistic vehicle model at both a subsystem and full vehicle level using both laboratory testing and track testing data.

The new model was developed for the fast evaluation of modern high-performance motorcycles, and this was coupled with an electric powertrain model that properly included measured battery dynamics, motor saturation and loss modelling, as well as motor drive loss modelling. The performance of the model developed here was found to be superior when compared to that of previous attempts, particularly with regards to battery response as well as improvements concerning vehicle response and electric motor modelling.

The benefit of this enhanced modelling was then explored with the inclusion of energy and temperature management strategies, and it was found that the performance of the reference machine was severely compromised by both the poor thermal

management of the battery pack, developed using exiting modelling techniques. In addition, it was found that the lack of intelligent onboard energy deployment strategies was a severe performance deficit. The recommendation is that both elements should be addressed in any future high-performance electric motorcycle designs.

Further work using this model identified that it is important to optimise the vehicle holistically for the event in question, using a tool such as that developed in this thesis. This is because many design trade-offs, such as battery pack size and optimum downforce to drag ratios, vary significantly for each event.

8.3. Contributions

This section summarises the contributions of this thesis to the knowledge in high-performance electric motorcycle performance analysis. The main contributions are:

- The determination that existing stability analysis and motorcycle squat response methodologies developed for use on internal combustion machines remain appropriate for use on high-performance electric motorcycles. This has been examined using a case study on a representative modern example of a high-performance electric motorcycle.
- The development and validation of an integrated system model for the performance simulation of the modern high-performance electric motorcycle. This model properly combines the elements important to the accurate performance prediction of the high-performance electric motorcycle into a single tool. It is the first to do so while incorporating a modern powertrain consisting of an inverter-fed permanent magnet alternating current motor, an advanced battery model and tyre-based performance limitations. This holistic vehicle view has not been previously undertaken on a machine representative of modern high-performance machines to the level of detail used in this thesis. This allows the rapid determination of development pathways and design trade-offs. Contributions to each area are as follows:
    - A motorcycle rigid body dynamics model is developed that includes the effects of differing front and rear tyres as well as a downforce generating winglet. This is useful for improved performance envelope

predictions representative of the modern high-performance machine using a rigid body approach.

- A battery model capable of accurately transferring laboratory test data to lap predictions is integrated into this vehicle model. Previous models have used a fixed resistance approach. This is shown to be a poor choice, particularly with regards to temperature prediction, a key performance differentiator. This model is validated using laboratory test data. Additionally the battery test procedures and fitted battery coefficients are made available for future work.
- Provision of a full data set representing an example of the modern high-performance electric motorcycle, including motor saturation effects and non-linear battery behaviour.

- Development of a GPS based lap simulation with integrated strategies to determine the optimal energy and battery temperature limited deployment strategies for a target operating cycle allows the following additional contributions:
  - It is determined that the energy deployment strategy is a significant performance differentiator, and this strategy should be included within the design process to ensure that the entire system is optimised to fully utilise this strategy, especially with regards to cooling and component peak performance levels.
  - It is discovered that there is a design cut-off point for some drive cycles where the machine's lap time sensitivity to additional stored energy is lower than that of increasing the mass to accommodate this additional energy. This is a novel contribution only made possible by the development of the integrated approach within this thesis, as previous strategies to determine the energy storage requirement simply aim to achieve the target cycle demand and ignore the potential gain outlined above.

8.4. Recommendations for Further Work

The initial objectives have been achieved and an advanced integrated electric motorcycle performance analysis tool built and validated. The use of this tool has helped to identify areas of a significant performance benefit to the reference machine

and has the flexibility to be applied to multiple configurations. However, there are benefits to be found with further work which was not possible to include here due to time constraints.

In particular, the model would benefit from its expansion to include automated optimisation procedures and further refinement through more detailed investigations into the modelling of battery cooling techniques, gearbox design, and tyre modelling.

- Battery cooling was shown to be a substantial performance differentiator and the underlying thermal transfer to vehicle drag trade-off included using a one-dimensional heat transfer model. However, this can be improved significantly through expanded heat transfer modelling, and this improvement will better inform battery pack design decisions.
- The implementation of a primary reduction gearbox has several compromises associated with it but primarily it boils down to an efficiency versus mass trade-off. The underlying trade-off has been explored in the full vehicle context. Again, this area would benefit from a more detailed study to properly include the gearbox efficiency variation across the full operational envelope.
- Tyre modelling would benefit from the availability of a tyre data set with lateral force sensitivity to vertical load. Additionally, one area not investigated here is the thermal effects of increased tyre loading on tyre performance. The inclusion of a tyre thermal model would help shed light on this, particularly for races such as the TT with significant vehicle mass increases.
- Finally, the current model requires manual intervention to select the next point for simulation. This allows a good understanding of the effect of different design changes. This seems to be an inefficient use of an engineer’s time, and it would be beneficial to develop an automated optimisation procedure to undertake this exercise without manual intervention.

Overall, the fully integrated design approach has been undertaken for a high-performance electric motorcycle and shown to be an important and effective design analysis tool. It is hoped that the modelling and data acquisition techniques developed in this thesis will provide a strong baseline for further work, to ultimately ensure that electric motorcycles can thoroughly explore their performance envelope.

References

[1] M. Xylia *et al.*, "Impact of bus electrification on carbon emissions: The case of Stockholm," *Journal of Cleaner Production,* vol. 209, pp. 74-87, 2019/02/01/ 2019, doi: https://doi.org/10.1016/j.jclepro.2018.10.085.

[2] U. Nations, "COP26: Together for our planet," ed. un.org, 2021, p. https://www.un.org/en/climatechange/cop26.

[3] U. N. C. Change, "The Paris Agreement," ed, pp. https://unfccc.int/process-and-meetings/the-paris-agreement/the-paris-agreement.

[4] Department for Transport. (2016). *National Travel Survey Motorcycle use in England*.

[5] *Veh 0170*. [Online]. Available: https://www.gov.uk/government/statistical-data-sets/all-vehicles-veh01

[6] *Veh 0153*. [Online]. Available: https://www.gov.uk/government/statistical-data-sets/all-vehicles-veh01

[7] K. Zamasz, J. Stęchły, A. Komorowska, and P. Kaszyński, "The Impact of Fleet Electrification on Carbon Emissions: A Case Study from Poland," *Energies,* vol. 14, no. 20, p. 6595, 2021. [Online]. Available: https://www.mdpi.com/1996-1073/14/20/6595.

[8] Mercedes-Benz. "INSIGHT: Five examples why F1 is accelerating the future." https://www.mercedesamgf1.com/en/news/2018/10/insight-five-examples-why-f1-is-accelerating-the-future/ (accessed 18/01, 2022).

[9] iomtt.com, "ISLE OF MAN TT RACES: The ultimate 'must see it' event for motorsport fans," ed, p. https://www.iomtt.com/.

[10] pphic.org, "THE RACE: WHAT IS THE PPIHC?," ed, p. https://ppihc.org/about/.

[11] C. Teague, "Racer Zef Eisenberg Sets Electric Motorcycle Land Speed World Record With 194-MPH Run." [Online]. Available: https://www.thedrive.com/news/30021/speed-demon-zef-eisenberg-sets-electric-motorcycle-land-speed-world-record-with-194-mph-run

[12] iomtt.com, "TT Map Tea Towel: Isle of Man TT Shop," ed, p. https://shop.iomtt.com/images/productimages/1/13TTOWEL.jpg?width=720.

[13] "TT Zero regulations available to download," in *Isle of Man TT Races*, ed, 2010.

[14] R. S. Sharp, "The Stability and Control of Motorcycles," *Journal of Mechanical Engineering Science,* vol. 13, no. 5, pp. 316-329, 1971, doi: 10.1243/jmes_jour_1971_013_051_02.

[15] E. J. H. De Vries and H. B. Pacejka, "Motorcycle Tyre Measurements and Models," *Vehicle System Dynamics,* vol. 29, no. sup1, pp. 280-298, 1998/01/01 1998, doi: 10.1080/00423119808969565.

[16] J. Blissett, "A wholistic motor design philosophy for electric motorcycles in motorsport," PhD, Power Electronics Machines and Control, University of Nottingham, 2019.

[17] N. Dal Bianco, R. Lot, and K. Matthys, "Lap time simulation and design optimisation of a brushed DC electric motorcycle for the Isle of Man TT Zero Challenge," *Vehicle System Dynamics,* Article in Press pp. 1-28, 2017, doi: 10.1080/00423114.2017.1342847.

[18] J. Hauser and A. Saccon, "Motorcycle modeling for high-performance maneuvering," *Control Systems, IEEE,* vol. 26, pp. 89-105, 11/01 2006, doi: 10.1109/MCS.2006.1700047.

[19] V. Cossalter, *Motorcycle Dynamics*, Second Edition ed. Lexington, KY: Lulu, 2006.

[20] R. Lot and J. Sadauckas, *Motorcycle Design: Vehicle Dynamics Concepts and Applications*. Lulu, 2021.

[21] T. Foale, *Motorcycle handling and chassis design : the art and the science*. Benidoleig, Spain: Tony Foale Designs (in English), 2006.

[22] F. Biral and R. Lot, "An interpretative model of g-g diagrams of racing motorcycle," in *International Conference on Mechanical Engineering and Mechanics*, Beijing, P. R. China, 01/01 2009.

[23] V. Cossalter, M. Da Lio, F. Biral, and L. Fabbri, "Evaluation of Motorcycle Maneuverability With the Optimal Maneuver Method," presented at the Motorsports Engineering Conference & Exposition, 1998.

[24] J. Blissett, M. Degano, M. Gimeno-Fabra, and P. Wheeler, "Design of electrical system for racing electric motorcycles," in *2016 International Conference on Electrical Systems for Aircraft, Railway, Ship Propulsion and Road Vehicles and International Transportation Electrification Conference, ESARS-ITEC 2016*, 2017, doi: 10.1109/ESARS-ITEC.2016.7841419.

[25] F. J. W. Whipple, "The Stability of the Motion of the Bicycle," *Quarterly of Applied Mathematics,* vol. 30, pp. 312-385, 1901.

[26] S. Evangelou and D. Limebeer. I. C. o. S. T. a. Medicine. Lisp programming of the 'Sharp 1971' motorcycle model. Available: http://www2.ee.ic.ac.uk/cap/cappp/projects/2/files/bk_71.pdf

[27] S. Rowell, "Modelling the control strategies for riding a motorcycle / Stuart Rowell," Thesis (PhD)--University of Nottingham, 2007.

[28] V. Cossalter, R. Lot, and F. Maggio, "The Modal Analysis of a Motorcycle in Straight Running and on a Curve," *Meccanica,* Article vol. 39, no. 1, pp. 1-16, 2004, doi: 10.1023/A:1026269926222.

[29] K. A. Seffen, G. T. Parks, and P. J. Clarkson, "Observations on the controllability of motion of two-wheelers," *Proceedings of the Institution of Mechanical Engineers. Part I: Journal of Systems and Control Engineering,* Article vol. 215, no. 2, pp. 143-156, 2001, doi: 10.1243/0959651011540932.

[30] R. Lot and M. Da Lio. "The Sharp '71 motorcycle model." http://www.multibody.net/mbsymba/vehicles/sharp-motorcycle/ (accessed 01/01, 2022).

[31] J. W. Griffin and A. A. Popov, "Multibody dynamics simulation of an all-wheel-drive motorcycle for handling and energy efficiency investigations," *Vehicle System Dynamics,* Article in Press pp. 1-19, 2017, doi: 10.1080/00423114.2017.1296962.

[32] L. Hsien-Chung, L. Jing-Sin, D. T. Lee, and W. Li-Sheng, "Finding battery locations of electrical motorcycles for better perception of riding comfort," in *Proceedings of the 2002 American Control Conference (IEEE Cat. No.CH37301)*, 8-10 May 2002 2002, vol. 2, pp. 915-920 vol.2, doi: 10.1109/ACC.2002.1023134.

[33] J. P. Meijaard and A. A. Popov, "Multi-body modelling and analysis into the non-linear behaviour of modern motorcycles," *Proceedings of the Institution of Mechanical Engineers, Part K: Journal of Multi-body Dynamics,* vol. 221, no. 1, pp. 63-76, 2007, doi: 10.1243/1464419jmbd49.

[34] R. S. Sharp, "The Influence of Frame Flexibility on the Lateral Stability of Motorcycles," *Archive: Journal of Mechanical Engineering Science 1959-1982 (vols 1-23),* vol. 16, pp. 117-120, 1974.

[35] R. S. Sharp, "The Influence of the Suspension System on Motorcycle Weave-mode Oscillations," *Vehicle System Dynamics,* vol. 5, no. 3, pp. 147-154, 1976/10/01 1976, doi: 10.1080/00423117608968410.

[36] R. S. Sharp and D. J. N. Limebeer, "A Motorcycle Model for Stability and Control Analysis," *Multibody System Dynamics,* vol. 6, no. 2, pp. 123-142, 2001/09/01 2001, doi: 10.1023/A:1017508214101.

[37] R. S. Sharp, S. Evangelou, and D. J. N. Limebeer, "Advances in the Modelling of Motorcycle Dynamics," *Multibody System Dynamics,* vol. 12, pp. 251-283, 10/01 2004, doi: 10.1023/B:MUBO.0000049195.60868.a2.

[38] V. Cossalter, A. Doria, and R. Lot, "Steady Turning of Two-Wheeled Vehicles," *Vehicle System Dynamics - VEH SYST DYN,* vol. 31, pp. 157-181, 03/01 1999, doi: 10.1076/vesd.31.3.157.2013.

[39] V. Cossalter and R. Lot, "A Motorcycle Multi-Body Model for Real Time Simulations Based on the Natural Coordinates Approach," *Vehicle System Dynamics,* vol. 37, no. 6, pp. 423-447, 2002/06/01 2002, doi: 10.1076/vesd.37.6.423.3523.

[40] A. A. Popov, S. Rowell, and J. P. Meijaard, "A review on motorcycle and rider modelling for steering control," *Vehicle System Dynamics,* vol. 48, no. 6, pp. 775-792, 2010/06/01 2010, doi: 10.1080/00423110903033393.

[41] A. Schmeitz, I. Besselink, J. Hoogh, and H. Nijmeijer, "Extending the Magic Formula and SWIFT tyre models for inflation pressure changes," 01/01 2005.

[42] G. Mavros, "A thermo-frictional tyre model including the effect of flash temperature," *Vehicle System Dynamics,* vol. 57, no. 5, pp. 721-751, 2019/05/04 2019, doi: 10.1080/00423114.2018.1484147.

[43] F. Farroni, D. Giordano, M. Russo, and F. Timpone, "TRT: Thermo racing tyre a physical model to predict the tyre temperature distribution," *Meccanica,* vol. 49, 10/31 2013, doi: 10.1007/s11012-013-9821-9.

[44] H. B. Pacejka, *Tyre and Vehicle Dynamics*, 2 ed. Butterworth-Heinemann, 2006.

[45] V. Cossalter, A. Doria, R. Lot, N. Ruffo, and M. Salvador, "Dynamic Properties of Motorcycle and Scooter Tires: Measurement and Comparison," *Vehicle System Dynamics - VEH SYST DYN,* vol. 39, pp. 329-352, 06/01 2003, doi: 10.1076/vesd.39.5.329.14145.

[46] T. Automotive, "MF-TYRE & MF-SWIFT 6.1 USER MANUAL 2008."

[47] J. P. Meijaard and A. A. Popov, "Tyre modelling for motorcycle dynamics," *Vehicle System Dynamics,* vol. 43, no. sup1, pp. 187-198, 2005/01/01 2005, doi: 10.1080/00423110500140682.

[48] M. Massaro and D. Limebeer, "Minimum-lap-time optimisation and simulation," *Vehicle System Dynamics,* vol. 59, pp. 1-45, 04/05 2021, doi: 10.1080/00423114.2021.1910718.

[49] M. Veneri and M. Massaro, "A free-trajectory quasi-steady-state optimal-control method for minimum lap-time of race vehicles," *Vehicle System Dynamics,* pp. 1-22, 04/24 2019, doi: 10.1080/00423114.2019.1608364.

[50] W. F. Milliken and D. L. Milliken, *Race car vehicle dynamics*. Warrendale, Pa: Society of Automotive Engineers (in English), 1995.

[51] V. Cossalter, R. Lot, and D. Tavernini, "Optimization of the centre of mass position of a racing motorcycle in dry and wet track by means of the "Optimal Maneuver Method"," in *2013 IEEE International Conference on Mechatronics, ICM 2013*, 2013, pp. 412-417, doi: 10.1109/ICMECH.2013.6518572.

[52] V. Cossalter, M. Peretto, and S. Bobbo, "Investigation of the influences of tyre-road friction and engine power on motorcycle racing performance by means of the optimal manoeuvre method," *Proceedings of the Institution of Mechanical Engineers, Part D: Journal of Automobile Engineering,* Article vol. 224, no. 4, pp. 503-519, 2010, doi: 10.1243/09544070JAUTO1312.

[53] F. Biral, E. Bertolazzi, and P. Bosetti. "Test Suite for Optimal Control Software." https://github.com/pins-ocs/TS-OCS (accessed 2018).

[54] L. Leonelli and D. J. N. Limebeer, "Optimal control of a road racing motorcycle on a three-dimensional closed track," *Vehicle System Dynamics,* vol. 58, no. 8, pp. 1285-1309, 2020/08/02 2020, doi: 10.1080/00423114.2019.1617886.

[55] "The history of Porche begins electronically." VW Group Media. https://newsroom.porsche.com/en/products/taycan/history-18563.html (accessed 29/12, 2021).

[56] C. Simon, "OFFICIAL TTXGP RESULTS RELEASED." [Online]. Available: https://www.iomtt.com/news/2009/06/12/official-ttxgp-results-released

[57] T. Finken, M. Felden, and K. Hameyer, "Comparison and design of different electrical machine types regarding their applicability in hybrid electrical vehicles," in *2008 18th International Conference on Electrical Machines*, 6-9 Sept. 2008 2008, pp. 1-5, doi: 10.1109/ICELMACH.2008.4800044.

[58] J. F. Gieras, *Permanent Magnet Motor Technology: Design and Applications*, 3 ed. CRC Press, 2009.

[59] *Global Vehicle Motors GVM Series Technical Manual: PVD 3668_GB*. [Online]. Available: parker.com/literature/SSD%20Drives/Mobile%20Electrification/PVD3668_GB%20GVM.pdf

[60] LORD, "Thermally Conductive Potting for Electric Motors: Accelerated Endurance Tests Prove Efficacy of Potted Motors." [Online]. Available: https://www.lord.com/products-and-solutions/electronic-materials/thermal-management-materials/efficacy-potted-motors

[61] D. Golovanov, A. Galassini, L. Flanagan, D. Gerada, Z. Xu, and C. Gerada, "Dual-Rotor Permanent Magnet Motor for Electric Superbike," in *2019 IEEE International Electric Machines & Drives Conference (IEMDC)*, 12-15 May 2019 2019, pp. 951-956, doi: 10.1109/IEMDC.2019.8785287.

[62] J. Lemmens, P. Vanassche, and J. Driesen, "PMSM Drive Current and Voltage Limiting as a Constraint Optimal Control Problem," *IEEE Journal of Emerging and Selected Topics in Power Electronics,* vol. 3, pp. 1-1, 01/01 2014, doi: 10.1109/JESTPE.2014.2321111.

[63] W. A. Khan, "Torque Maximising and Flux Weakening Control of Synchronous Machines," MSc, School of Electrical Engineering, Aalto University, 2016.

[64] M. Fadel, L. Sepulchre, and M. Pietrzak-David, "Deep Flux-Weakening Strategy with MTPV for High-Speed IPMSM for Vehicle Application," *IFAC-PapersOnLine,* vol. 51, no. 28, pp. 616-621, 2018.

[65] A. Al-Timimy, P. Giangrande, M. Degano, M. Galea, and C. Gerada, *Investigation of AC Copper and Iron Losses in High-Speed High-Power Density PMSM*. 2018, pp. 263-269.

[66] J. R. J. Hendershot and T. Miller, *Design of Brushless Permanent-Magnet Motors* 1ed. Oxford University Press, 1994.

[67] C. Mi, G. R. Slemon, and R. Bonert, "Modeling of iron losses of permanent-magnet synchronous motors," *IEEE Transactions on Industry Applications,* Article vol. 39, no. 3, pp. 734-742, 2003, doi: 10.1109/TIA.2003.810635.

[68] D. D. Graovac, "IGBT Power Losses Calculation Using the Data-Sheet Parameters," in *Application Note, V 1.1*, M. Pürschel, Ed., ed: Infineon, 2009.

[69] A. K. Ferkingstad, "Design and testing of a voltage source inverter and three-phase motor controller system for use in a race car.," Masters in Electrical Engineering, Department of Electrical Engineering and Computer Science, University of Stavanger, 2017.

[70] D. D. Graovac, "Mosfet Power Losses Calculation Using the Data-Sheet Parameters," in *Application Note, V 1.1*, M. Pürschel, Ed., ed: Infineon, 2006.

[71] Y. Miao, P. Hynan, A. von Jouanne, and A. Yokochi, "Current Li-Ion Battery Technologies in Electric Vehicles and Opportunities for Advancements," *Energies,* vol. 12, no. 6, p. 1074, 2019.

[72] N. A. Chaturvedi, R. Klein, J. Christensen, J. Ahmed, and A. Kojic, "Algorithms for Advanced Battery-Management Systems," *IEEE Control Systems Magazine,* vol. 30, no. 3, pp. 49-68, 2010, doi: 10.1109/MCS.2010.936293.

[73] A. Hammami, N. Raymond, and M. Armand, "Lithium-ion batteries: runaway risk of forming toxic compounds," (in eng), *Nature,* vol. 424, no. 6949, pp. 635-6, Aug 7 2003, doi: 10.1038/424635b.

[74] Q. Wang, P. Ping, X. Zhao, G. Chu, J. Sun, and C. Chen, "Thermal runaway caused fire and explosion of lithium ion battery," *Journal of Power Sources,* vol. 208, pp. 210-224, 2012.

[75] R. Lot and S. Evangelou, "Lap Time Optimization of a Sports Series Hybrid Electric Vehicle," in *Proceedings of the World Congress on Engineering 2013*, London, U.K, 2013, doi: 10.13140/2.1.2166.3522.

[76] G. Plett. "ECE4710/5710: Modeling, Simulation, and Identification of Battery Dynamics - Equivalent-Circuit Cell Models." University of Colorado Springs. http://mocha-java.uccs.edu/ECE5710/ECE5710-Notes02.pdf (accessed 10/10, 2020).

[77] C. R. Birkl, E. McTurk, M. R. Roberts, P. G. Bruce, and D. A. Howey, "A Parametric Open Circuit Voltage Model for Lithium Ion Batteries," *Journal of The Electrochemical Society,* vol. 162, no. 12, pp. A2271-A2280, 2015, doi: 10.1149/2.0331512jes.

[78] N. Damay, C. Forgez, M.-P. Bichat, and G. Friedrich, "A method for the fast estimation of a battery entropy-variation high-resolution curve – Application on a commercial LiFePO4/graphite cell," *Journal of Power Sources,* vol. 332, pp. 149-153, 2016.

[79] K. E. Thomas and J. Newman, "Thermal Modeling of Porous Insertion Electrodes," *Journal of The Electrochemical Society,* vol. 150, no. 2, p. A176, 2003, doi: 10.1149/1.1531194.

[80] N. Damay, C. Forgez, M.-P. Bichat, and G. Friedrich, "Thermal modeling of large prismatic LiFePO4/graphite battery. Coupled thermal and heat generation models for characterization and simulation," *Journal of Power Sources,* vol. 283, pp. 37-45, 2015.

[81] T. Herrmann, F. Christ, J. Betz, and M. Lienkamp, "Energy Management Strategy for an Autonomous Electric Racecar using Optimal Control," in *2019 IEEE Intelligent Transportation Systems Conference (ITSC)*, 27-30 Oct. 2019 2019, pp. 720-725, doi: 10.1109/ITSC.2019.8917154.

[82] B. Sheard, "Vehicle Control of an Electric Racing Motorcycle for the Isle of Man TT," University of Nottingham, Masters Thesis, 2019.

[83] *FIA Formula E World Championship Technical Regulations,* F. I. d. l'Automobile, 2021.

[84] "Agni Motors." Agni Motors. http://www.agnimotors.com/ (accessed 2021).

[85] "Agni: Is this the future of electric bike racing?" Adrian Flux. https://www.adrianflux.co.uk/influx/features/agni-the-future-of-bike-racing/ (accessed 02/02, 2022).

[86] H. Staff. "Team Agni wins inaugural TTXGP." https://www.rideapart.com/news/260182/team-agni-wins-inaugural-ttxgp/ (accessed 02/02, 2022).

[87] J. Beeler. "Mission Motors providing Mugen with Electric Powertrain." Asphalt & Rubber. https://www.asphaltandrubber.com/racing/mission-motors-team-mugen-shinden-san/ (accessed 2021).

[88] iomtt.com. "TT 2014 SES TT Zero Results." https://www.iomtt.com/tt-database/events/races?meet_code=TT2014&race_seq=5 (accessed 02/02, 2022).

[89] F. Tibu. "All-Naked Mugen Shinden-San Electric Superbike." Autoevolution. https://www.autoevolution.com/news/all-naked-mugen-shinden-san-electric-superbike-photo-gallery-79550.html (accessed 02/02, 2022).

[90] "About Saietta Racing." http://saiettaracing.com/about/ (accessed 2019).

[91] L. Rodgers *et al.*, "Designing an electric motorcycle for the Isle of Man TT Zero race, and how electric vehicle racing could be used to spur innovation," in *26th Electric Vehicle Symposium 2012, EVS 2012*, 2012, vol. 4, pp. 2862-2873.

[92] D. G. Dorrell and M. Popescu, "Drive motor designs for electric motorcycles," in *2012 IEEE Energy Conversion Congress and Exposition, ECCE 2012*, 2012, pp. 4354-4361, doi: 10.1109/ECCE.2012.6342230.

[93] "Shinden Roku unveiled for 2017 TT Zero." http://www.mugen-power.com/english/news/detail/id=416 (accessed 2020).

[94] "Manx7." Sarolea. http://www.sarolea.com/manx7 (accessed 2020).

[95] "Isle of Man TT Zero Results 2017." [Online]. Available: https://www.iomtt.com/~/media/Files/2017/Downloads/Results/09-June-17/Zero%20result.pdf

[96] M. Gardiner. "Why did the Isle of Man halt the TT Zero?" Revzilla. https://www.revzilla.com/common-tread/why-did-the-isle-of-man-halt-the-tt-zero (accessed 12/12, 2021).

[97] A. Bonnell-Kangas, P. Brodsky, J. Cline, N. Lord, and M. Canova, "System design and optimization of The Ohio State University Electric Motorcycle for the 2014 Isle of Man TT Zero Race," in *15. Internationales Stuttgarter Symposium: Automobil- und Motorentechnik*, M. Bargende, H.-C. Reuss, and J. Wiedemann Eds. Wiesbaden: Springer Fachmedien Wiesbaden, 2015, pp. 1107-1125.

[98] P. Brodsky, G. Fan, and M. Canova, "Battery pack design and optimization for the OSU Buckeye current 2016 electric racing motorcycle," in *2016 International Conference on Electrical Systems for Aircraft, Railway, Ship Propulsion and Road Vehicles & International Transportation Electrification Conference (ESARS-ITEC)*, 2-4 Nov. 2016 2016, pp. 1-6, doi: 10.1109/ESARS-ITEC.2016.7841436.

[99] B. Möller, R. Biffard, K. Matthys, E. Wu, L. Rodgers, and M. Jeunnette, "Analyzing the Limitations of the Rider and Electric Motorcycle at the Pikes Peak International Hill Climb Race," 2019.

[100] M. Baumann, T. Bächle, M. Buchholz, and K. Dietmayer, "Model-based Corner Braking Control for Electric Motorcycles," *IFAC-PapersOnLine,* vol. 49, no. 11, pp. 291-296, 2016, doi: https://doi.org/10.1016/j.ifacol.2016.08.044.

[101] M. Baumann, M. Buchholz, and K. Dietmayer, "A two-wheel driven power train for improved safety and efficiency in electric motorbikes," *World Electric Vehicle Journal,* Article vol. 8, no. 1, pp. 102-111, 2016.

[102] J. Robinson and T. Singh, "eABS: Regenerative Anti-Lock Braking for Electric Motorcycles," *SAE International Journal of Passenger Cars - Mechanical Systems,* Article vol. 6, no. 3, 2013, doi: 10.4271/2013-01-2064.

[103] C. L. Lin and L. Weng-Ching, "ABS control design for two-wheel drive electric vehicles," in *2011 Second International Conference on Mechanic Automation and Control Engineering*, 15-17 July 2011 2011, pp. 1011-1014, doi: 10.1109/MACE.2011.5987104.

[104] T. Abumi and T. Murakami, "Posture stabilization of two-wheel drive electric motorcycle by slip ratio control considering camber angle," in *2015 IEEE International Conference on Mechatronics (ICM)*, 6-8 March 2015 2015, pp. 353-358, doi: 10.1109/ICMECH.2015.7084001.

[105] T. Abumi and T. Murakami, "Posture stabilization control of two-wheel drive electric motorcycle with assistant pendulum for rider motion," in *Fifth Asia International*

Symposium on Mechatronics (AISM 2015), 7-10 Oct. 2015 2015, pp. 1-6, doi: 10.1049/cp.2015.1526.

[106] "2WD – the complete story." Öhlins Racing AB. http://ohlins.episerverhotell.net/Checkpoint-Ohlins/2WD---The-Complete-Story/ (accessed 2019).

[107] B. C. Chen, C. H. Chu, and S. J. Huang, "Fuzzy sliding mode control of traction control system for electric scooter," in *2010 Seventh International Conference on Fuzzy Systems and Knowledge Discovery*, 10-12 Aug. 2010 2010, vol. 2, pp. 691-695, doi: 10.1109/FSKD.2010.5569400.

[108] "The basics of AWD." Christini Technologies Inc. http://www.christini.com/awd-technology/about-the-technology (accessed 2019).

[109] Y. Luo and D. Tan, "Study on the Dynamics of the In-Wheel Motor System," *IEEE Transactions on Vehicular Technology,* vol. 61, no. 8, pp. 3510-3518, 2012, doi: 10.1109/TVT.2012.2207414.

[110] A. A. A. Omar and B. Özkan, "Analysis of effect of in-wheel electric motors mass on passive and active suspension systems," *ARPN Journal of Engineering and Applied Sciences,* Article vol. 10, no. 14, pp. 5924-5928, 2015.

[111] W. Tong and Z. Hou, "Vertical vibration analysis on electric vehicle with suspended in-wheel motor drives," in *2013 World Electric Vehicle Symposium and Exhibition (EVS27)*, 17-20 Nov. 2013 2013, pp. 1-9, doi: 10.1109/EVS.2013.6914998.

[112] *273 QS Spoke Hub Motor 50H 72V/96V 12000W - 16000W V3 Type*, e-smartway.com. [Online]. Available: https://e-smartway.com/products/273-qs-spoke-hub-motor-50h-72v-96v-12000w-16000w-v3-type. Accessed: 02/02/2022.

[113] T. H. Pham, J. Jacob, S. Wilkins, C. Lauwerys, and M. Dhaens, "Integrated model for battery Electric Vehicles with energy harvesting active suspension system," in *2017 12th International Conference on Ecological Vehicles and Renewable Energies, EVER 2017*, 2017, doi: 10.1109/EVER.2017.7935863.

[114] N. Amati, A. Festini, and A. Tonoli, "Design of electromagnetic shock absorbers for automotive suspensions," *Vehicle System Dynamics,* Article vol. 49, no. 12, pp. 1913-1928, 2011, doi: 10.1080/00423114.2011.554560.

[115] L. ZHUHAI HANGE BATTERY CO., "Specification Approval Sheet(Cell) Model: HGB8665155-10C."

[116] L. Balamurugan and J. Jancirani, "An investigation on semi-active suspension damper and control strategies for vehicle ride comfort and road holding," *Proceedings of the Institution of Mechanical Engineers. Part I: Journal of Systems and Control Engineering,* Review vol. 226, no. 8, pp. 1119-1129, 2012, doi: 10.1177/0959651812447520.

[117] K. Holloway, "Combined Motor and Amplifier Specification Sheet: GVM210-150P6," ed: Parker, 2017.

[118] "AC Motor Controller Gen4 (size10)." BorgWarner. (accessed 02/01, 2021).

[119] L. ZHUHAI HANGE BATTERY CO., "Specification Approval Sheet(Cell) Model: HGB8665155-20C."

[120] A. Irimescu, L. Mihon, and G. Pãdure, "Automotive transmission efficiency measurement using a chassis dynamometer," *International Journal of Automotive Technology,* journal article vol. 12, no. 4, pp. 555-559, August 01 2011, doi: 10.1007/s12239-011-0065-1.

[121] P. A. Veenhuizen, B. Bonsen, T. W. G. L. Klaassen, P. H. W. M. Albers, C. Changenet, and S. Poncy, "Pushbelt CVT Efficiency Improvement Potential of Servo-electromechanical Actuation and Slip Control," 2004.

[122] F. C. Moon, *Applied Dynamics. With applications to Multibody and Mechantronic Systems*, Second edition ed. Darmstadt: WILEY-VCH Verlag GmbH & Co., 2008.

[123] R. A. Mattey, "Bifilar pendulum technique for determining mass properties of Discos packages," July 01, 1974 1974, vol. 75.
[124] S. Timoshenko and D. H. Young, *Engineering Mechanics*, Fourth Edition ed. London: McGraw-Hill book company, inc.
[125] J. Bradley, *The racing motorcycle : a technical guide for constructors. Vol 1 Vol 1*. York: Broadland Leisure (in English), 1996.
[126] MathWorks. Help Center: Documentation [Online] Available: https://uk.mathworks.com/help/index.html?s_tid=CRUX_lftnav
[127] A. technologies, "EVO 5: The professional datalogger." [Online]. Available: https://www.aim-sportline.com/en/products/evo5/index.htm.
[128] V. Klein and E. A. Morelli, "Aircraft system identification : theory and practice," (in English), 2006.
[129] S. Chattopadhyay, M. Mitra, and S. Sengupta, "Clarke and Park Transform," in *Electric Power Quality*. Dordrecht: Springer Netherlands, 2011, pp. 89-96.
[130] S. Huard, "GVM210-150V6 FEA Simulation Data," ed: Parker, 2015.
[131] X. Chen, J. Hu, K. Chen, and Z. Peng, "Modeling of electromagnetic torque considering saturation and magnetic field harmonics in permanent magnet synchronous motor for HEV," *Simulation Modelling Practice and Theory,* vol. 66, 05/01 2016, doi: 10.1016/j.simpat.2016.02.012.
[132] HBM, "T40B Universal Digital Torque Transducer," ed, pp. https://www.hbm.com/en/3004/t40b-universal-torque-transducer-for-test-benches/.
[133] J. E. Vrancik, "Prediction of windage power loss in alternators," 1971.
[134] S. Bearings. "The SKF model for calculating the frictional moment." https://www.skf.com/binary/144-299767/0901d1968065e9e7-The-SKF-model-for-calculating-the-frictional-movement_tcm_12-299767.pdf (accessed 18/02, 2020).
[135] K. Bearings. "Frictional coefficient (reference)." https://koyo.jtekt.co.jp/en/support/bearing-knowledge/8-4000.html (accessed 12/02, 2020).
[136] D. R. Ridley. (2005) Proximity Loss in Magnetics Windings. *Switching Power Magazine*.
[137] J. H. T. Guillod, F.Krismer, J.W.Kolar, "Litz Wire Losses: Effects of Twisting Imperfections," in *COMPEL 2017*, Stanford, California, 2017: IEEE.
[138] Cogent. *Typical data for SURA M235-35A*.
[139] A. Krings, "Iron Losses in Electrical Machines: Influence of Material Properties, Manufacturing Processes and Inverter Operation," PhD, School of Electrical Engineering, KTH Royal Institute of Technology, 2014.
[140] "FS450R120E4_B81." Infineon. www.infineon.com (accessed 2020).
[141] "HYBRID KIT DRIVE." Infineon Technologies AG. https://www.infineon.com/cms/en/product/evaluation-boards/hybrid-kit-drive/ (accessed 29/03, 2020).
[142] *DC link Capacitor for new IGBT modules*. (2016). TDK Electronics. Accessed: 29/03/202. [Online]. Available: https://www.tdk-electronics.tdk.com/en/374108/tech-library/articles/products---technologies/products---technologies/dc-link-capacitor-for-new-igbt-modules-/1857600
[143] TDK. *EPCOS Product Brief 2016: Film Capacitors*. (2016). Accessed: 29/03/2020. [Online]. Available: https://www.mouser.com/datasheet/2/400/pb-ppc-e-mobility-1511805.pdf
[144] L. Jin. (2013). Modeling of DC Link Capacitor Current Ripple for Electric Vehicle Traction Converter.

[145] C. J. Lodge and S. C. Burgess, "An investigation into the selection of optimum chain and sprocket size," *Journal of Engineering Design,* Article vol. 15, no. 6, pp. 563-580, 2004, doi: 10.1080/09544820410001731128.
[146] S. Burgess and C. Lodge, "Optimisation of the chain drive system on sports motorcycles," *Sports Engineering,* journal article vol. 7, no. 2, pp. 65-73, June 01 2004, doi: 10.1007/bf02915918.
[147] C. J. Lodge and S. C. Burgess, "A model of the tension and transmission efficiency of a bush roller chain," *Proceedings of the Institution of Mechanical Engineers, Part C: Journal of Mechanical Engineering Science,* Article vol. 216 (4), pp. 385-394, 4 2002, doi: 10.1243/0954406021525179.
[148] R. Wragge-Morley, J. Yon, R. Lock, B. Alexander, and S. Burgess, "A novel pendulum test for measuring roller chain efficiency," *Measurement Science and Technology,* Article vol. 29, no. 7, 7 2018, doi: 10.1088/1361-6501/aaa239.
[149] D.I.D. 2019 Chain Specification Sheet [Online] Available: https://didchain.com/wp-content/uploads/2019/10/2019-Chain-Spec-Sheet.pdf
[150] R. PLC. Transmission Chain: Product catalogue [Online] Available: https://www.renold.com/media/165414/transmission-chain-ren1-eng-07-14.pdf
[151] *Renold Roller Chain Catalogue*, pp. 91-117. Accessed: 25/02/2020.
[152] G. Saldaña, J. I. San Martín, I. Zamora, F. J. Asensio, and O. Oñederra, "Analysis of the Current Electric Battery Models for Electric Vehicle Simulation," *Energies,* vol. 12, no. 14, p. 2750, 2019.
[153] H.-G. Schweiger *et al.*, "Comparison of several methods for determining the internal resistance of lithium ion cells," *Sensors (Basel),* vol. 10, no. 6, pp. 5604-5625, 2010, doi: 10.3390/s100605604.
[154] C. G. Motloch *et al.*, "High-Power Battery Testing Procedures and Analytical Methodologies for HEV's," *SAE Transactions,* vol. 111, pp. 797-802, 2002.
[155] T. Hu, B. Zanchi, and J. Zhao, "Simple Analytical Method for Determining Parameters of Discharging Batteries," *IEEE Transactions on Energy Conversion,* vol. 26, no. 3, pp. 787-798, 2011, doi: 10.1109/TEC.2011.2129594.
[156] R. Jackey, M. Saginaw, P. Sanghvi, J. Gazzarri, T. Huria, and M. Ceraolo, "Battery Model Parameter Estimation Using a Layered Technique: An Example Using a Lithium Iron Phosphate Cell," 2013, doi: 10.4271/2013-01-1547.
[157] T. Huria, M. Ceraolo, J. Gazzarri, and R. Jackey, "High fidelity electrical model with thermal dependence for characterization and simulation of high power lithium battery cells," in *2012 IEEE International Electric Vehicle Conference*, 4-8 March 2012 2012, pp. 1-8, doi: 10.1109/IEVC.2012.6183271.
[158] D. Casanova, "On minimum time vehicle manoeuvring: the theoretical optimal lap," PhD Thesis, School of Mechanical Engineering, Cranfield University, 2000.
[159] H. Scherenberg, "Mercedes-Benz Racing Cars—Design and Experience," *SAE Transactions,* vol. 66, pp. 414-420, 1958.
[160] ESRI. "Choose the right projection." https://learn.arcgis.com/en/projects/choose-the-right-projection/ (accessed 09/06, 2021).
[161] K. von Laven. Spherical To Azimuthal Equidistant [Online] Available: https://www.mathworks.com/matlabcentral/fileexchange/28848-spherical-to-azimuthal-equidistant
[162] P. G. M. Mekenkamp, "Using map projections without changing the world: Projection accuracy analyses," in *International Cartiographic Conference*, A Coruña, Spain, 2005.
[163] H. Wang, J. Kearney, and K. Atkinson, "Arc-Length Parameterized Spline Curves for Real-Time Simulation," 2003.

[164] R. d. O. Santos, "FROM LAP TIME SIMULATION TO DRIVER-IN-THE-LOOP: A SIMPLE INTRODUCTION TO SIMULATION IN RACING," vol. 28/09/21, R. C. Dynamics, Ed., ed.
[165] www.iomtt.com. "FASTEST SECTOR TIMES - 'THE PERFECT LAP'." https://www.iomtt.com/tt-database/tt-records/perfect-lap-fastest-sectors (accessed 14/09/2021.
[166] www.iomtt.com. "PokerStars Senior TT - PokerStars Senior TT - Positions By Sector." https://www.iomtt.com/~/media/Files/2015/Race-results/PokerStars-Senior-TT/Senior%20Sector%20by%20SectorLR.pdf (accessed 14/09, 2021).
[167] motorcyclespecs.co.za, "BMW HP4 Race." [Online]. Available: https://www.motorcyclespecs.co.za/model/bmw/BMW_HP4_Race.htm.
[168] C. Voicu, "2020 IOM TT: Dunlop Will Race a Ducati Panigale V4 R at the TT. 230hp & 210mph." [Online]. Available: https://riders.drivemag.com/news/2020-iom-tt-dunlop-will-race-a-ducati-panigale-v4-r-at-the-tt-230hp-210mph/
[169] A. Rohatgi. "WebPlotDigitizer." Ankit Rohatgi. https://automeris.io/WebPlotDigitizer/ (accessed 02/02, 2020).
[170] L. Flanagan, "Aerodynamic Design and Optimisation of TT Zero electric motorcycle," University of Bath - Masters Thesis, 2016.
[171] S. Kakaç, R. Oskay, and H. Y. Zhang, "Correlations for Forced Convection in Ducts," in *Two-Phase Flow Heat Exchangers: Thermal-Hydraulic Fundamentals and Design*, S. Kakaç, A. E. Bergles, and E. O. Fernandes Eds. Dordrecht: Springer Netherlands, 1988, pp. 123-158.
[172] EMRAX. "EMRAX 268." https://emrax.com/e-motors/emrax-268/ (accessed 02/01, 2022).
[173] *CAS325M12HM2 1.2kV, 3.7mΩ All-Silicon Carbide High-Performance, Half-Bridge Module C2M MOSFET and Z_Rec™ Diode*.
[174] Cree. *CAS480M12HM3 1200V, 480 A All-Silicon Carbide High Performance, Switching Optimised, Half-Bridge Module*.
[175] "bamocar d3," ed. UniTek Industrie Elektronik GmbH, pp. https://www.unitek-industrie-elektronik.de/bamocar-d3-en.

Appendix A – Timeline of Electric Motorcycle Racing Activities

The University of Nottingham electric race team was founded in 2014 by a group of postgraduate students, a research associate and a professor, Prof. Pat wheeler. This team began by building an electric motorbike powered by two Agni DC motors, as was the norm at the time. The team raced this machine at the 2014 Moto-E championship.

Following this, the team developed a more advanced powertrain featuring a permanent magnet alternating current (PMAC) motor, custom motor drive and custom 500 Vdc lithium-polymer battery pack. This machine was developed over the next two seasons winning multiple races at the Moto-E championship and steadily improving its performance elsewhere.

This thesis deals with the events attended by the University of Nottingham electric motorcycle racing machine from 2017 onwards. To add context to the activities, a summary of the events is included here. This outlines the motorcycle design changes and specifications used at these events as well as the results achieved.

2017

This machine competed at the Isle of Man TT Zero achieving a 109.209 mph average lap and 3rd place. This was 10 mph faster than the team's result the previous year. This machine was the first Nottingham machine to use a commercial drive and battery pack voltage over 700 Vdc. This machine featured a Bamocar D3 motor drive and a battery pack with 168 cells in series, 4 in parallel. The change to commercial technology for the motor drive was due to a desire to prioritise reliability and data acquisition but initially lead to a reduction in ultimate power levels Figure A.1 and Figure A.2 show the machine and team that year.

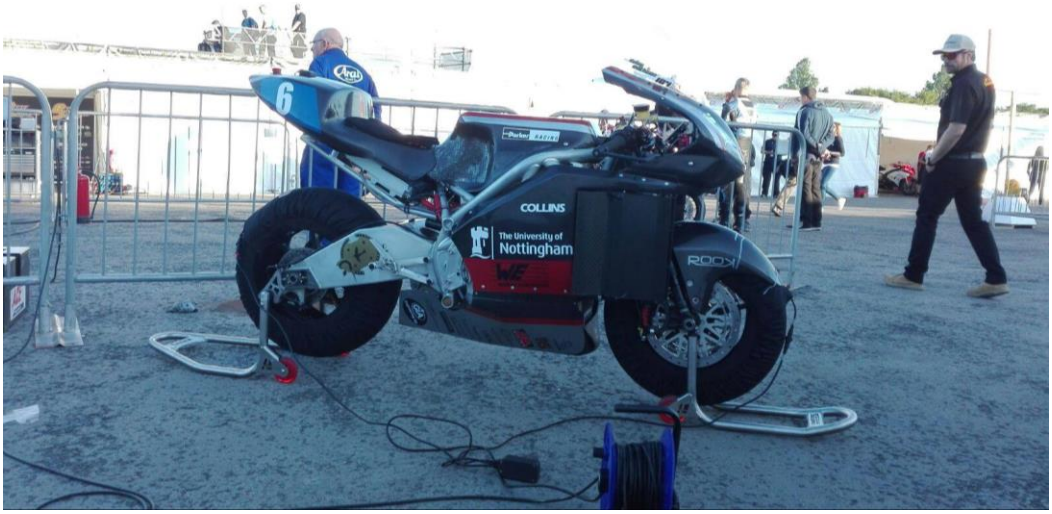

Figure A.1 – Picture of the UoN TT Zero motorcycle in 2017 specification

Figure A.2 – Picture of the 2017 team and riders at the Isle of Man TT Zero 2017

The other event attended in 2017 was Pikes Peak International Hillclimb (PPHIC) this event was held two weeks after the TT in Colorado Springs USA. As the team was unable to fly their battery pack to the race it was necessary to remove this and build another at the race event. Additionally, as the event was originally intended for motocross-style motorcycles the requirement to fit one-piece handlebars and remove the fairings lead to a significantly different appearance as can be seen in Figure A.3.

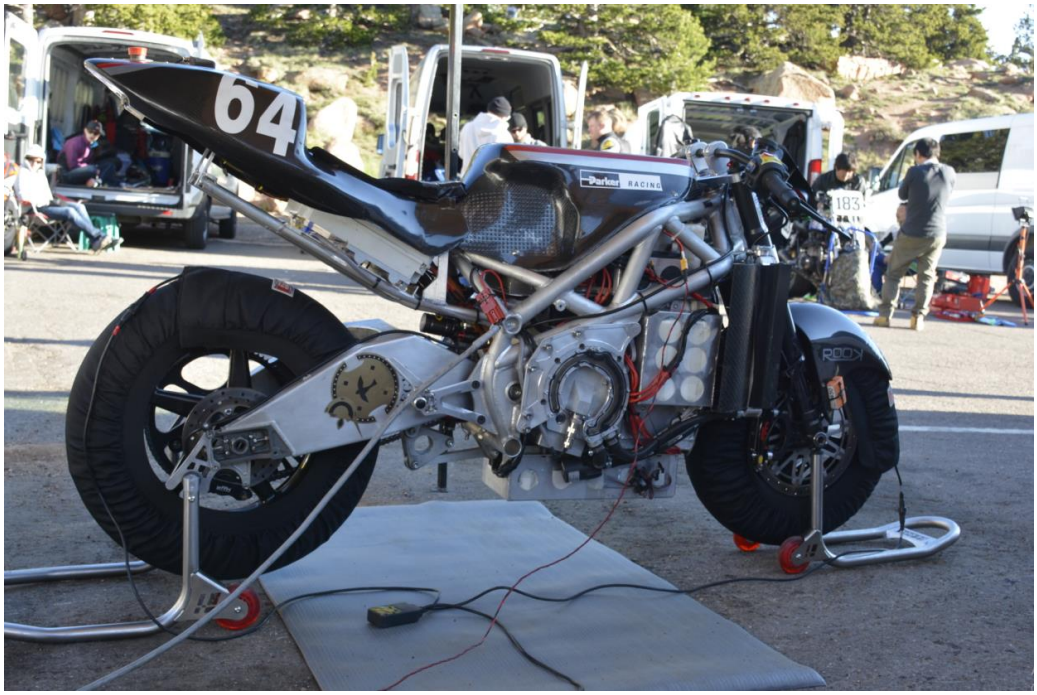

Figure A.3 - UoN 2017 Pikes Peak contender

In addition to the requirement to build a battery at the race event, it was also decided to attempt to fit a different motor drive that promised increased power levels. This was tuned at a local drag racing track with success however the combination of significant changes in a short period of time resulted in a lack of powertrain reliability and a lap time of 13 m 5 s for the race event.

2018

Learning from the previous season's rapid development and subsequent reliability issues, increased focus was put on testing. In addition, the team expanded. This led to the development of an entirely new aerodynamics package, motor drive integration into the rear subframe and the increase to 171 cells in series. The aerodynamic package included relocating the radiators to the nose of the machine. This work on reliability and aerodynamics paid off at the TT Zero 2018. Beating the previous lap record set by Team Mugen by 0.02 mph average lap speed with a speed of 119.294 mph. However, Team Mugen also beat the lap record that year resulting in second place for the University team at that year's event. This machine can be seen in Figure A.4 below. Note the extensive revisions to the fairing design.

Figure A.4 – Picture of the 2018 TT Zero contender

This year also involved competition at PPHIC. This was a much more successful venture than the previous year with the team winning the electric class with a time of 11 m 13 s and recording a 10.02 s quarter-mile drag racing run while preparing for the event. An NHRA record for 700 V electric motorbikes at the time.

Another notable achievement was the first use of the motor developed by Blisset in [16], this was raced in the Moto-E championship race held at Donnington Park Raceway that year against internal combustion machines with great success. A picture of the rider Daley Mathison overtaking a competing IC machine during this race can be seen below in Figure A.5. Sadly, the motor seized shortly after the race due to an issue with the design of the bearing preload method and associated rotor clearances.

Figure A.5 - Daley Mathison overtaking an internal combustion machine in a race at Donnington

2019

Further work was put into the aerodynamic design of the motorcycle for the following season with the rotor in the Blisset motor redesigned by the author and another team member. This was successful in eliminating the original problem and was on course to be raced at the TT Zero 2019 until tragic circumstances prevented the team's competitive appearance at the event.

Unwilling to risk the new powertrain at an event in the USA with limited facilities the previous season's powertrain was refitted. The machine was flown to PPHIC where the rider managed to record the team's fastest time in the race at 10 m 19 s. Setting the fastest ever speed for a motorcycle through the PPHIC picnic grounds speed trap of 133 mph in the process.

This machine was also raced at Elvington airfield achieving multiple world records. Figure A.6 was the final iteration of this machine as raced in 2019. The project concluded after this point.

Figure A.6 - Final iteration of the UoN superbike

The final pictures are of Daley Mathison, our dear friend and rider, doing what he did best and enjoying the machine at various events. These are included, in his memory, as a thank you to his hard work in development and endless faith in our abilities to build him a machine capable of challenging for victories.

Appendix B – Nottingham Electric Motorcycle Parameters

Multibody Model Data

Notations as per Sharp 71 model which can be found in:

R. S. Sharp, "The Stability and Control of Motorcycles," *Journal of Mechanical Engineering Science,* vol. 13, no. 5, pp. 316-329, 1971, doi: 10.1243/jmes_jour_1971_013_051_02.

Variable	Value
M_f	26.3 kg
M_r	348.6 kg
Z_f	-1850 N
I_{rx}	24.5611 kgm^2
I_{rz}	29.8356 kgm^2
I_{fz}	0.193 kgm^2
i_{fy}	0.453 kgm^2
$i_{ry} + \lambda i$	1.364 kgm^2
a	0.7804 m
b	0.6663 m
e	0.0223 m
f	0.1197 m
h	0.6186 m
R_f	0.2886 m
R_r	0.3200 m
t	0.0924 m
ϵ	0.4189 rad
C_{f1}	11173.9 N/rad
C_{f2}	938.6 N/rad
C_{r1}	15831.2 N/rad
C_{r2}	1325.6 N/rad
K	6.78 Nm/rad s
σ_f	0.2470 m
σ_r	0.3406 m
l	0.7537 m

Lap simulation model parameters – TT Zero 2018

The reference point for lengths is the front tyre centre patch (FTCP)

Variable	Value	Units	Description
m_{mc}	380	kg	Vehicle Mass
l_{wb}	1.42	m	Wheelbase
l_{cg}	0.7057	m	FTCP longitudinal distance to the centre of
h_{cg}	0.612	m	Centre of gravity height
l_b	0.758	m	FTCP longitudinal distance to body centre of
h_b	0.612	m	Height of body centre of pressure
M_{yb}	0		Body aerodynamic pitching moment
$C_{lb}A$	0.335	m^2	Body drag coefficient times cross-sectional
$C_{db}A$	0	m^2	Body lift coefficient times cross-sectional
l_w	0.3	m	FTCP longitudinal distance to winglet centre
h_w	1.0	m	Height of winglet centre of pressure
M_{yw}	0		Winglet aerodynamic pitching moment
$C_{lw}A$	0	m^2	Winglet lift coefficient times cross-sectional
$C_{dw}A$	0	m^2	Winglet drag coefficient times cross-sectional
R_{t0}	0.347	m	Rear tyre rolling radius
$\lambda_{\mu xf}$	0.8		Front tyre longitudinal friction modifier
$\lambda_{\mu yf}$	0.9		Front tyre lateral friction modifier
$\lambda_{\mu xr}$	0.8		Rear tyre longitudinal friction modifier
$\lambda_{\mu yr}$	0.9		Rear tyre lateral friction modifier
I_{rw}	0.90	kgm^2	Rear-wheel inertia
I_{fw}	0.4532	kgm^2	Front-wheel inertia
N_1	18		Motor sprocket teeth
N_2	83		Rear-wheel sprocket
R_{DC}	0.03	Ω	DC link resistance
	171		Cells in series
	4		Cells in parallel
	10	Ah	Cell capacity
C_p	890		Cell specific heat capacity
M_0	0	V	Cell instantaneous hysteresis voltage
M_1	0.03	V	Cell exponential hysteresis voltage term
γ_{hyst}	10		Cell voltage hysteresis decay constant
I_{mot}	0.0233	kgm^2	Electric motor rotor inertia
p_e	6		Number of pole pairs
N_{turns}	16.5		Electric motor winding turns
l_{rotor}	150	mm	Electric motor rotor length
R_s	0.0061	Ω	Motor winding resistance per phase

$\psi_{e,a}$	-1.032x10^{-8}		ψ_e coefficient for scaling with i_s^2
$\psi_{e,b}$	3.917x10^{-6}		ψ_e coefficient for scaling with i_s
$\psi_{e,c}$	0.0481		ψ_e zero offset coefficient
$L_{d,a}$	3.405x10^{-14}		L_d coefficient for scaling with i_s^3
$L_{d,b}$	-6.684x10^{-11}		L_d coefficient for scaling with i_s^2
$L_{d,c}$	3.932x10^{-8}		L_d coefficient for scaling with i_s
$L_{d,d}$	9.511x10^{-5}		L_d zero offset coefficient
$L_{q,a}$	-1.085x10^{-13}		L_q coefficient for scaling with i_s^3
$L_{q,b}$	1.400x10^{-10}		L_q coefficient for scaling with i_s^2
$L_{q,c}$	-6.176x10^{-8}		L_q coefficient for scaling with i_s
$L_{q,d}$	1.202x10^{-4}		L_q zero offset coefficient
k_1	9.860x10^{-9}		$T_{l,rot}$ coefficient with rotor speed ω^2
k_2	0.007		$T_{l,rot}$ coefficient with rotor speed $\omega^{0.6}$
k_3	0		$T_{l,rot}$ coefficient
μ_{frict}	0.0012		Mu Bearing
D_{IDb}	0.05		ID bearing
B_{max}	1.8	T	Core flux density at full load
B_{nl}	1.4	T	Core flux density at no load
K_{hyst}	0.4722		Iron Hysteresis constant
K_{eddy}	0.0006		Iron eddy current loss constant
β	1.6045		Steinmetz constant
λ_{mod}	0.95		V mod
f_{sw}	12	kHz	Drive Switching frequency
$N_{parallel}$	2		Switching devices in parallel per phase
u_{CE0}	0.8	V	IGBT on-state zero-current collector-emitter
u_{D0}	0.8	V	Diode on-state zero-current collector-emitter
r_C	0.0027	Ω	collector-emitter on-state resistance
r_D	0.0020	Ω	anti-parallel diode resistance
E_{on}	0.0404	J	Switching module switch on energy
E_{off}	0.0567	J	Switching module switch off energy
E_{Don}	0.0395	J	Diode switch on energy
V_{ref}	600	V	Switching device test reference voltage
I_{ref}	450	A	Switching device test reference current

Motor torque-speed map used for 2018 battery temperature limitation strategy, note this is desired torque pre-saturation.

Speed (rpm)	0	5,842	6,576	7,620	8,768	9,370	9,530	10,100	10,500
Torque (Nm)	260	260	227	190	162	152	62	50	0

Battery map coefficients for TT Zero 1RC model

Coefficients for R_{0-1RC} map:

Variable	Value
$a_{1,R0}$	0.005552
$a_{2,R0}$	0.02541
$a_{3,R0}$	0.001943
$a_{4,R0}$	1
$a_{5,R0}$	-0.0001049
$a_{6,R0}$	0.0004931
$a_{7,R0}$	0.0008159
$a_{8,R0}$	2.512×10^{-7}

Coefficients for R_{1-1RC} map:

Variable	Value
$a_{1,R1}$	0.001941
$a_{2,R1}$	0.03033
$a_{3,R1}$	0.001426
$a_{4,R1}$	1
$a_{5,R1}$	-4.957×10^{-5}
$a_{6,R1}$	-8.605×10^{-5}
$a_{7,R1}$	0.002015
$a_{8,R1}$	1.433×10^{-6}

Coefficients for τ_{1-1RC} map:

Variable	Value
$a_{1,\tau 1}$	40.64
$a_{2,\tau 1}$	0.05861
$a_{3,\tau 1}$	0.03481
$a_{4,\tau 1}$	0.4286
$a_{5,\tau 1}$	-0.3828
$a_{6,\tau 1}$	3.073
$a_{7,\tau 1}$	-0.4285
$a_{8,\tau 1}$	0.9268

Pikes Peak 2019 Motorcycle

Variable	Value	Units	Description
m_{mc}	305.5	kg	Vehicle Mass
l_{wb}	1.42	m	Wheelbase
l_{cg}	0.7057	m	FTCP longitudinal distance to the centre of
h_{cg}	0.612	m	Centre of gravity height
l_b	0.758	m	FTCP longitudinal distance to body centre of
h_b	0.612	m	Height of body centre of pressure
M_{yb}	0		Body aerodynamic pitching moment
$C_{lb}A$	0.335	m^2	Body drag coefficient times cross-sectional
$C_{db}A$	0	m^2	Body lift coefficient times cross-sectional
l_w	0.3	m	FTCP longitudinal distance to winglet centre
h_w	1.0	m	Height of winglet centre of pressure
M_{yw}	0		Winglet aerodynamic pitching moment
$C_{lw}A$	0	m^2	Winglet lift coefficient times cross-sectional
$C_{dw}A$	0	m^2	Winglet drag coefficient times cross-sectional
R_{t0}	0.347	m	Rear tyre rolling radius
$\lambda_{\mu xf}$	0.8		Front tyre longitudinal friction modifier
$\lambda_{\mu yf}$	0.9		Front tyre lateral friction modifier
$\lambda_{\mu xr}$	0.8		Rear tyre longitudinal friction modifier
$\lambda_{\mu yr}$	0.9		Rear tyre lateral friction modifier
I_{rw}	0.90	kgm^2	Rear-wheel inertia
I_{fw}	0.4532	kgm^2	Front-wheel inertia
N_1	17		Motor sprocket teeth
N_2	83		Rear-wheel sprocket
R_{DC}	0.03	Ω	DC link resistance
	171		Cells in series
	2		Cells in parallel
	8	Ah	Cell capacity
C_p	890		Cell specific heat capacity
M_0	0	V	Cell instantaneous hysteresis voltage
M_1	0.03	V	Cell exponential hysteresis voltage term
γ_{hyst}	10		Cell voltage hysteresis decay constant
I_{mot}	0.0233	kgm^2	Electric motor rotor inertia
p_e	6		Number of pole pairs
N_{turns}	20.5		Electric motor winding turns
l_{rotor}	150	mm	Electric motor rotor length
R_s	0.0075	Ω	Motor winding resistance per phase
$\psi_{e,a}$	-1.282×10^{-8}		ψ_e coefficient for scaling with i_s^2
$\psi_{e,b}$	4.865×10^{-6}		ψ_e coefficient for scaling with i_s

$\psi_{e,c}$	0.0597		ψ_e zero offset coefficient
$L_{d,a}$	5.256×10^{-14}		L_d coefficient for scaling with i_s^3
$L_{d,b}$	-1.032×10^{-10}		L_d coefficient for scaling with i_s^2
$L_{d,c}$	6.069×10^{-8}		L_d coefficient for scaling with i_s
$L_{d,d}$	1.468×10^{-4}		L_d zero offset coefficient
$L_{q,a}$	-1.675×10^{-13}		L_q coefficient for scaling with i_s^3
$L_{q,b}$	2.161×10^{-10}		L_q coefficient for scaling with i_s^2
$L_{q,c}$	-9.533×10^{-8}		L_q coefficient for scaling with i_s
$L_{q,d}$	1.856×10^{-4}		L_q zero offset coefficient
k_1	9.860×10^{-9}		$T_{l,rot}$ coefficient with rotor speed ω^2
k_2	0.007		$T_{l,rot}$ coefficient with rotor speed $\omega^{0.6}$
k_3	0		$T_{l,rot}$ coefficient
μ_{frict}	0.0012		Mu Bearing
D_{IDb}	0.05		ID bearing
B_{max}	1.8	T	Core flux density at full load
B_{nl}	1.4	T	Core flux density at no load
K_{hyst}	0.4722		Iron Hysteresis constant
K_{eddy}	0.0006		Iron eddy current loss constant
β	1.6045		Steinmetz constant
λ_{mod}	0.95		V mod
f_{sw}	12	kHz	Drive Switching frequency
$N_{parallel}$	2		Switching devices in parallel per phase
u_{CE0}	0.8	V	IGBT on-state zero-current collector-emitter
u_{D0}	0.8	V	Diode on-state zero-current collector-emitter
r_C	0.0027	Ω	collector-emitter on-state resistance
r_D	0.0020	Ω	anti-parallel diode resistance
E_{on}	0.0404	J	Switching module switch on energy
E_{off}	0.0567	J	Switching module switch off energy
E_{Don}	0.0395	J	Diode switch on energy
V_{ref}	600	V	Switching device test reference voltage
I_{ref}	450	A	Switching device test reference current

Appendix C – Description of Electric Motor Torque Equations

The peak phase voltage in the 'q' and 'd' axes is determined from the 'd' and 'q' axis currents as follows [58]. It is given in terms of the stator resistance (R_s), flux linkage (ψ_e), inductances (L_d, L_q) and the rotor electrical frequency ($\omega_e = \omega p_e$). Where 'p_e' is the number of pole pairs in the motor.

$$V_q = R_s i_q + \omega_e (L_d i_d + \psi_e) \quad (C.1)$$

$$V_d = R_s i_d - \omega_e L_q i_q \quad (C.2)$$

$$V_s = \sqrt{V_q^2 + V_d^2} \quad (C.3)$$

To simplify the control model the influence of the stator resistance R_s on V_d and V_q is commonly neglected. The effect of R_s on motor conduction losses is included in the motor loss model as this is important in the system energy balance. The motor torque is given by the following equation.

$$T_{mot} = \frac{3}{2} p_e \left[\psi_e i_q + \left(L_d - L_q\right) i_d i_q\right] \quad (C.4)$$

The optimal motor current vectors vary depending on the motor operation region. The motor output torque is constant below the start of field weakening, leading to Region 1 (the region below base speed) to be commonly referred to as the constant torque region. In Region 1, the Maximum Torque Per Amp (MTPA) distribution of 'i_q' and 'i_d' currents are as follows. Here 'i_s' is the maximum stator current visualised as the hypotenuse in Figure 5.2 [63].

$$i_q = \sqrt{\frac{\psi_e i_d}{L_d - L_q} + i_d^2} \quad (C.5)$$

$$i_d = \frac{-\psi_e + \sqrt{{\psi_e}^2 + 8\left(L_d - L_q\right)^2 i_s^2}}{4\left(L_d - L_q\right)} \quad (C.6)$$

As the system is closed V_{DC} is the highest peak line to line voltage that the drive can apply. Using the battery and motor drive model V_{DC} can be determined. Using peak phase convention base speed 'ω_{base}' is given as follows. Note λ_{mod} is an additional

coefficient introduced to ensure the motor drive retains sufficient voltage headroom to maintain stator current control under dynamic loading.

$$V_{s,lim} = \frac{V_{DC}\lambda_{mod}}{\sqrt{3}} \tag{C.7}$$

$$V_s^2 = \left(-\omega_e L_q i_q\right)^2 + (\omega_e(L_d i_d + \psi_e))^2 \tag{C.8}$$

$$\omega_{base} = \frac{V_{s,lim}}{\sqrt{\left(-L_q i_q\right)^2 + (L_d i_d + \psi_e)^2}} \tag{C.9}$$

As the distribution of currents in the field weakening region initially follow the current limiting trajectory where $i_s^2 = i_d^2 + i_q^2$ and $V_s^2 = V_d^2 + V_q^2$ it follows that:

$$V_s^2 = \left(-\omega_e L_q i_q\right)^2 + (\omega_e(L_d i_d + \psi_e))^2 \tag{C.10}$$

$$i_q^2 = i_s^2 - i_d^2 \tag{C.11}$$

$$V_s^2 = \omega_e^2\left(L_q^2 i_s^2 + \left(L_d^2 - L_q^2\right)i_d^2 + 2L_d i_d \psi_e + {\psi_e}^2\right) \tag{C.12}$$

$$0 = \left(L_d^2 - L_q^2\right) + 2L_d i_d \psi_e + L_q^2 i_s^2 + {\psi_e}^2 - \frac{V_s^2}{\omega_e^2} \tag{C.13}$$

For an SPM motor $L_d = L_q$ and for an Induction machine $\psi_e = 0$. An IPM machine typically comes between the two and can have differing L_d and L_q by design, this can be used to tailor the machine characteristics. As the model is concerned with both SPM and IPM designs the $i_q$and i_d currents in the initial field weakening region are given as follows.

$$\begin{cases} L_d = L_q & i_d = \dfrac{L_q^2 i_s^2 + {\psi_e}^2 - \dfrac{V_s^2}{\omega_e^2}}{2L_d\psi_e} & i_q = \sqrt{i_s^2 - i_d^2} \\ L_d \neq L_q & i_d = \dfrac{L_d\psi_e - \sqrt{(L_d\psi_e)^2 - \left(L_d^2 - L_q^2\right)\left({\psi_e}^2 + L_q^2 i_s^2 - \dfrac{V_s^2}{\omega_e^2}\right)}}{L_d^2 - L_q^2} & i_q = \sqrt{i_s^2 - i_d^2} \end{cases} \tag{C.14}$$

As the motor speed increases there comes a point where the optimal current vector no longer follows the MTPA trajectory. This is called the Maximum Torque Per Volt

region (MTPV). In this operation region the optimum current vector is below the maximum limit but increasing the current would only serve to increase losses and reduce the output torque. Here the stator current and voltage vectors are determined as follows [64]:

$$V_q = \frac{\psi_e - \sqrt{{\psi_e}^2 + 8V_{s,lim}^2\left(\frac{L_d - L_q}{L_q\omega_e}\right)^2}}{-4\left(\frac{L_d - L_q}{L_q\omega_e}\right)} \qquad (C.15)$$

$$V_d = -\sqrt{V_{s,lim}^2 - V_q^2} \qquad (C.16)$$

$$\begin{Bmatrix} L_d = L_q & i_d = -\dfrac{-\psi_e}{L_d} & i_q = \dfrac{V_{s,lim}}{L_q\omega_e} \\ L_d \neq L_q & i_d = \dfrac{\left(\frac{V_q}{\omega_e} - \psi_e\right)}{L_d} & i_q = -\dfrac{V_d}{L_q\omega_e} \end{Bmatrix} \qquad (C.17)$$

Appendix D – IGBT Loss Calculations

The IGBT conduction losses are modelled via a DC voltage source (u_{CE0}) representing the IGBT on-state zero-current collector-emitter voltage with a series connection to the resistance of the IGBT (r_C). 'i_C' is the instantaneous IGBT current.

$$P_{CT} = \frac{1}{T_{sw}} \int_0^{T_{sw}} P_{CT}(t)dt = \frac{1}{T_{sw}} \int_0^{T_{sw}} \left(u_{CE0} i_C(t) + r_C i_C^2(t)\right) dt \qquad (D.1)$$

A similar process is employed for the diode conduction losses with similar coefficients representing similar terms (U_{D0}, r_D, i_D):

$$P_{CD} = \frac{1}{T_{sw}} \int_0^{T_{sw}} P_{CD}(t)dt = \frac{1}{T_{sw}} \int_0^{T_{sw}} \left(u_{D0} i_D(t) + r_D i_D^2(t)\right) dt \qquad (D.2)$$

Utilising the peak output current (I_o), the drive amplitude modulation index (m_a) and the motor power factor ($\phi 1$) the average IGBT conduction losses can be expressed as the following. Were the average IGBT current value is I_{Cav} and the RMS IGBT current value is I_{Crms}.:

$$P_{CT} = u_{CE0} I_{Cav} + r_C I_{Crms}^2 = u_{CE0} I_o \left(\frac{1}{2\pi} + \frac{m_a \cos(\phi 1)}{8}\right) + r_C I_o^2 \left(\frac{1}{8} + \frac{m_a \cos(\phi 1)}{3\pi}\right) (D.3)$$

$$P_{CD} = u_{D0} I_{Dav} + r_D I_{Drms}^2 = u_{D0} I_o \left(\frac{1}{2\pi} - \frac{m_a \cos(\phi 1)}{8}\right) + r_D I_o^2 \left(\frac{1}{8} - \frac{m_a \cos(\phi 1)}{3\pi}\right) (D.4)$$

Where the inverter amplitude modulation index (m_a) is derived from the difference between the input DC voltage (V_{batt}), peak output line-line voltage (V_s).

$$m_a = \frac{2\sqrt{3} V_s}{V_{batt}} \qquad (D.5)$$

The switching losses are a product of the sum of the device switching losses (E_{on}, E_{off}) for the diode and IGBT and the switching frequency. The diode switch-off energy is commonly neglected and the loss simply $E_{Don} f_{sw}$. A simple solution for the switching loss calculation for AC motor drives is that the losses generated in one half-wave of the output frequency ($1/2f_o$) correspond to the losses generated if an equivalent DC output is applied [68]. For a three-phase AC motor drive the output current ripple and equivalent DC are determined as follows where the equivalent stator inductance is given by (L).

$$I_{ripple} = \frac{\left(V_{batt} - V_s\sqrt{2}\right)V_s}{2LV_{batt}f_{sw}} \quad (D.6)$$

$$I_{DC} = \frac{I_o}{\pi} \quad (D.7)$$

$$I_{DCon} = I_{DC} - \frac{I_{ripple}}{2} \quad (D.8)$$

$$I_{DCoff} = I_{DC} + \frac{I_{ripple}}{2} \quad (D.9)$$

The switching energy loss is a function of the change in current and voltage of the device as it switches. To simplify the model this can be roughly approximated to a linear relationship within the normal operating region of the drive as can be seen in [140].

$$P_{sw} = \frac{\left(E_{on}I_{DCon} + E_{off}I_{DCoff} + E_{Don}I_{DC}\right)f_{sw}V_s}{I_{ref}V_{ref}} \quad (D.10)$$

The total power loss in the switching devices and diodes is then given by the equation:

$$P_{loss} = 6(P_{sw} + P_{CD} + P_{CT}) \times N_{parallel} \quad (D.11)$$

Where $N_{parallel}$ is the number of IGBTs in parallel, this is particularly relevant as the Sevcon G4S10 in the UoN motorcycle uses two Infineon FS450 power modules in parallel per phase. The resulting drive is simply modelled as if two drives were operating separately at half the total current. This method scales for a higher number of devices in parallel. The power loss is included in the powertrain losses as a motor input power loss.